Abstract

Title of Dissertation: Extragalactic X-ray Surveys of ULXs and AGNs

Lisa M. Winter, Doctor of Philosophy, 2008

Dissertation directed by: Professor Christopher S. Reynolds, Advisor
Dr. Richard F. Mushotzky, Co-advisor
Department of Astronomy

Extragalactic X-ray studies provide unique opportunities for studying accreting black holes. In particular, they are necessary for studying phenomena not easily selected or observed in other wavelengths. Among these objects, ultra-luminous X-ray sources (ULXs) emit the vast majority of their luminosity in the X-ray band and are very faint or confused in other wavebands. Similarly, heavily obscured active galactic nuclei (AGN) with absorbing columns $> 10^{24}\,\mathrm{cm}^{-2}$ are rarely detected in optical surveys, due to the extreme reddening. In my thesis, I study both phenomenon in the local universe.

At ULX luminosities [L_X (0.3 – 10 keV) $> 3\times10^{39}\,\mathrm{erg\,s}^{-1}$], the European Space Agency's *XMM-Newton* satellite provides the spectral resolution and sensitivity necessary to study the population of local ULXs. Thus, we conducted an *XMM-Newton* archival study of a complete sample of the ULXs located within 8 Mpc. Our study confirmed key predictions of the intermediate mass black hole (IMBH) hypothesis for local ULXs. We then followed-up this study by investigating high signal-to-noise *XMM-Newton* observations of 14 ULX sources – studying their spectral shape, testing the validity of different accretion disk and power law models, and then using absorption of their spectra to measure the oxygen and iron abundances of the interstellar medium of their host galaxies.

New breakthroughs are expected in the study of heavily obscured AGN from SWIFT. The SWIFT satellite, launched in 2004, has detected a sample of 153 AGN with the Burst Alert Telescope (BAT) in the first 9-months of data. The BAT is sensitive in the 14 – 195 keV band and the selected sources have an average redshift of ≈ 0.03. Thus, it detects local AGN without bias towards all but the most obscured sources ($n_H > 10^{24}$ atoms cm^{-2}). The BAT AGN sources are the result of an all-sky survey with a flux limit of $F_{BAT} > 10^{-11}$ erg s^{-1} cm^{-2}. I analyze and present the results of X-ray data from *XMM-Newton*, ASCA, as well as SWIFT's XRT (0.3 – 10 keV) and BAT, in order to understand the properties of obscured and unobscured AGN in the local universe. Among our results, we show that the new class of "hidden"/buried AGN are a significant population of local AGN ($\approx 20\%$). We also find that our data supports the need for a modified AGN unified model – one which includes a luminosity dependence.

Extragalactic X-ray Surveys of ULXs and AGNs

by

Lisa M. Winter

Dissertation submitted to the Faculty of the Graduate School of the
University of Maryland at College Park in partial fulfillment
of the requirements for the degree of
Doctor of Philosophy
2008

Advisory Committee:

Professor Christopher S. Reynolds, Advisor
Dr. Richard F. Mushotzky, Co-advisor, chair
Professor M. Coleman Miller
Professor Sylvain Veilleux
Professor Edward Sion
Professor Gregory Sullivan, Dean's Representative

Preface

Much of the work presented in this thesis has been published or presented at a professional conference. The work presented in Chapter 2 of this thesis has been published in the *Astrophysical Journal* as *XMM-Newton Archival Study of the ULX Population in Nearby Galaxies* (Winter et al. 2006b). Preliminary results from this study, as well as additional work not presented in the thesis, were presented as an oral talk at the 2004 Winter American Astronomical Society Meeting in San Diego, CA, as *Investigating The Ultraviolet Environment of Ultraluminous X-ray sources* (Winter et al. 2004). Additionally, work from this Chapter was presented as an oral talk at the 2005 Winter American Astronomical Society Meeting in Washington, D.C., as *Bolstering the IMBH hypothesis: Evidence for "Low" and "High" State ULX Sources from XMM-Newton* (Winter et al. 2005).

The work presented in Chapter 3 has been published in the *Astrophysical Journal* as *Elemental Abundances of Nearby Galaxies through High Signal-to-Noise Ratio XMM-Newton Observations of Ultraluminous X-Ray Sources* (Winter et al. 2007b). The results were also presented as a poster presentation (as well as in the conference proceedings) entitled *Oxygen and Iron Abundances in nearby Galaxies Using Ultraluminous X-ray Sources* at the 2005 European Space Agency's The X-ray Universe Conference in El Escorial, Spain (Winter et al. 2006a).

The work presented in Chapter 4 has been published in the *Astrophysical Journal* as *X-ray Properties of an Unbiased Hard X-ray Detected Sample of AGN* (Winter et al.

2008). Portions of this work were presented in an oral presentation at the 2006 Chandra Extragalactic Surveys meeting in Boston, MA, as *Early Results from the SWIFT BAT survey: XMM follow-up Observations for 22 Sources*. Additionally, portions of this work were presented in a poster presentation at the 2007 Summer meeting of the American Astronomical Society Meeting in Honolulu, HI, as *Early Results From Swifts BAT AGN Survey* (Winter et al. 2007c).

The work presented in Chapter 5 has been submitted for review to the *Astrophysical Journal* on April 30, 2008. A portion of this work as well as parts of Chapter 4 were presented as an oral dissertation presentation at the 2008 Winter American Astronomical Society Meeting in Austin, TX, as *X-ray and Optical Properties of an Unbiased Sample of Local AGN* (Winter et al. 2007a).

Acknowledgements

As I finish my over 20 years of formal education, there are many people that I would like to thank for helping me along the way. First of all, as the people who helped me through the largest part of these years, I'd like to thank my parents. They have offered me support in many ways and have made countless sacrifices to give me and my sisters and brother the opportunities that we have. In a special way, I'd like to thank my dad for being a shining example of hard work and commitment and my mom for always believing in me and always being incredibly optimistic.

I would also like to thank my husband, Eric Barron, for his help and support. He introduced me to the Python programming language, which greatly improved my sanity in allowing me to easily manipulate and plot the data shown. He also helped to keep me grounded throughout the thesis writing process.

My undergraduate years are especially dear to me and for that I'd like to thank the faculty and staff of the Villanova University Astron-

omy/Astrophysics Department, as well as my fellow classmates. I received a truly excellent education from an excellent group of people. In a special way, I'd like to thank Edward Sion for being a wonderful role model as well as advisor. I'd also like to thank Drs. Ambruster, Fitzpatrick, Guinan, Maloney, and McCook, in addition to Larry DeWarf, Dr. Elizabeth Jewell, and Dr. Morgan Besson (Physics).

At the University of Maryland, I would first like to thank all of my teachers, especially Derek Richardson who always went above and beyond his duties. I also thank my fellow classmates, particularly Elyse Casper, who I struggled together with from Radiative Processes through Math Methods, as well as Katie McGleam and Ashley Zauderer. Without your moral support, homework as well as studying for the qualifiers, would have been even more exhausting. Additionally, I would like to thank Cole Miller, for encouragement as well as reading multiple second year project drafts, and both Sylvain Veilleux and Karen Lewis, for help with optical proposals and observations. Further, I would like to thank the staff at the Astronomy Department, particularly Mary Ann Phillips and Adrienne Newman, for all of their help in filling out the various required forms.

Finally, I am especially grateful to my advisors, Richard Mushotzky and Chris Reynolds for their guidance. Richard's enthusiasm, creativity, and extensive knowledge of 25+ years of X-ray astronomy (as well as nearly any other astronomy question I ask him) is a constant inspiration. I would like to thank Chris for his willingness to fit me into his extremely busy schedule, his patience in answering and explaining my questions, and his constant optimistic support.

Contents

List of Tables

List of Figures

Chapter 1

Introduction

1.1 Motivation

The X-ray band provides one of the clearest views of the most powerful phenomena in astronomy; accreting black holes. As well as being produced in copious quantities, X-rays can easily penetrate surrounding matter and arrive at our detectors millions of trillions of kilometers away. Therefore, systematic studies of extragalactic X-ray sources supply the framework necessary for studying objects that are too faint or difficult to identify in other wavelength bands. Two such classes of objects are the ultra-luminous X-ray sources (ULXs) and obscured active galactic nuclei (AGN).

ULXs are bright, non-nuclear X-ray sources with X-ray luminosities (0.3–10 keV) $> 3 \times 10^{39}\,\mathrm{erg\,s^{-1}}$ (Miller et al. 2004a). The Eddington luminosity, the luminosity at which radiation force and gravitational force are exactly matched for an object, is approximately $1.3 \times 10^{38}\,\mathrm{M/M_{\odot}\,erg\,s^{-1}}$. If the X-ray luminosities observed for the ULXs are both the Eddington luminosity and isotropic, i.e. not the product of a beaming effect, the ULXs have masses $> 20\,\mathrm{M_{\odot}}$. If the ULXs are scaled-up versions of Galactic black hole X-ray binaries, which typically have

masses ranging from 3 – 15 $M_\odot$ (Remillard & McClintock 2006), we would expect their typical luminosities to be much lower, 0.01 – 0.1 L_{Edd} (Gierliński & Done 2004). Thus, ULXs could represent a class of intermediate mass black holes (IMBHs). As such, their masses are too high to be the product of normal stellar evolution but well below those of the supermassive black holes residing in the centers of most galaxies.

Despite their high X-ray luminosities, little progress has been made in identifying optical counterparts of ULXs. Of the known ULXs (well over 50), optical counterparts were discovered for only a handful of sources at the closest distances (NGC 5204 X-1 by Liu et al. (2004), M81 X-6 by Liu et al. (2002), and M101 X-1 by Kuntz et al. (2005)). Unlike AGN, which typically have optical/X-ray flux ratios of 1 (Anderson et al. 2003), $F_{opt}/F_X < 0.1$ for ULXs (Winter et al. 2006b). The optical faintness of a ULX counterpart coupled with the distance to the source makes optical studies extremely difficult. Thus, X-ray observations are the best tools for studying these interesting sources.

Similar challenges exist for heavily obscured AGNs. While optical studies reveal the strong narrow and broad emission lines indicative of AGN activity, X-ray and optical surveys fail to select the same AGN samples (see the discussion in Mushotzky (2004)). X-ray surveys in the soft (0.5 – 2 keV) and hard (2 – 10 keV) bands identify more sources that are obscured by high column density absorbing material in the line of sight. However, even 2–10 keV X-rays are affected by this absorption, making it difficult to detect sources with column densities $> 10^{24}\,\mathrm{cm}^{-2}$ (Compton thick sources). This provides a major question for AGN surveys: how many Compton thick sources exist? Matt et al. (2000) estimated that the number could be as high as an order of magnitude more than unobscured sources which are easily detected in optical and softer X-ray surveys. In order to

account for these additional heavily obscured sources and determine their contribution to the cosmic X-ray background, very hard X-ray (> 10 keV) surveys are needed. At these wavelengths, the AGN emission is penetrating enough to pass through much of the gas and dust surrounding the AGN.

With the launch of the SWIFT satellite, we expect to gain much insight on the nature of AGN sources. The Burst Alert Telescope (BAT), sensitive in the 14 – 195 keV band, detects unobscured high energy emission from AGNs throughout the entire sky. With a much larger sample than other very hard X-ray missions (such as HEAO-1 and Integral), BAT is the first sensitive, all-sky, very hard X-ray survey in 28 years. The 9 month BAT AGN catalog consists of 153 AGN with an average redshift of 0.03 (Tueller et al. 2008). Thus, analysis of the X-ray properties of these sources will provide a new picture of the population of AGN in the local universe, including sources that were not selected in previous surveys.

This dissertation consists of two parts: 1) an X-ray survey of ULXs and 2) an X-ray study of the SWIFT BAT-detected AGNs. The structure of the thesis is as follows: a summary of the observed X-ray spectra of black holes and the instruments used to examine them, as well as a description of AGN and associated problems, is discussed in Chapter 1. The survey on ULXs and results are discussed in Chapter 2. Chapter 3 presents an application of this survey: using ULXs to study the properties of the ISM in their host galaxy. The next two chapters (4 and 5) examine the properties of the SWIFT BAT-detected AGN in the 9-month survey. Chapter 4 is specifically a study of *XMM-Newton* spectra of a representative sample of 22 sources whose X-ray spectra had never before been studied. Chapter 5 is a larger study of the X-ray properties of the entire 9-month BAT AGN catalog. Conclusions are then presented in Chapter 6, discussing both the ULX and AGN studies.

1.2 X-ray spectra of Accreting Black Holes

Observationally, the main feature of an accreting black hole's X-ray spectrum is a **power law**. This is represented as $N(E) \propto E^{-\Gamma}$, where Γ is the *photon index* and $N(E)$ has units of photons per unit area per unit time. Alternatively, this is represented as energy flux per unit area per unit time:

$$F(E) \propto E \times E^{-\Gamma} = E^{-\Gamma+1} = E^{-(\Gamma-1)} \tag{1.1}$$

Here, the value $\Gamma - 1$ is sometimes referred to as α, the *spectral index*.

The power law could be the result of either synchrotron emission from a jet or inverse Compton scattering of the blackbody photons from the accretion disk. In the first scenario, accelerated electrons spiraling in a magnetic field create the synchrotron emission. In the second scenario, the power law continuum is produced in the hot corona of the accretion disk. The photons from the accretion disk are up-scattered to higher energies from interactions with the hot corona electrons.

Typically, accreting black holes have photon indices of $\Gamma = 1.5 - 2.5$. For the Galactic X-ray binaries (stellar mass black holes), these values vary from $\Gamma \approx 1.7$ in the "low/hard" state to $\Gamma \approx 2.5$ in the "very high" state (Remillard & McClintock 2006). The low/hard state is associated with a lower accretion rate ($L \leq 0.1 L_{Edd}$) (Done & Gierliński 2003). Meanwhile, the very high state, as its name suggests, corresponds to higher luminosities ($> 0.1 L_{Edd}$). Thus, Γ seems to be correlated with L/L_{Edd} (the Eddington ratio). Similar relations between Γ and Eddington ratio are claimed for AGN spectra (Piconcelli et al. 2005; Porquet et al. 2004b; Shemmer et al. 2006).

In addition to the power law component, X-ray spectra may exhibit other

spectral features such as a soft excess, a reflection component, emission lines, and absorption features. We discuss these spectral features below.

(1) **Soft Excess** – A soft excess is an excess of emission above the extrapolated hard X-ray power law. Since this excess occurs below 1 keV, it is referred to as 'soft' emission. Some possible causes are outlined below:

Accretion Disk: Thermal emission (blackbody emission) from the inner regions of an accretion disk is observed in the high/soft or thermal dominated state of X-ray binaries (accreting stellar mass black holes). For a black hole system, the accretion disk emission is more likely the combination of blackbody emission from multiple temperature regions in the inner disk. The peak temperature of this emission is related to the mass of the central black hole, since the mass of the black hole determines the inner radius of the disk ($R \propto M$).

For a black hole, a simple calculation can be made to estimate the disk temperature expected for a given black hole mass. Equating the black body luminosity ($L = 4\pi R^2 \sigma T^4$) with the Eddington luminosity ($L = 1.3 \times 10^{38} M/M_\odot \,\mathrm{erg\,s^{-1}}$) shows that $T \propto M^{-1/4}$ for a black hole. In units appropriate for X-ray observations, the temperature for a stellar mass black hole accretion disk is $kT \approx 1\,\mathrm{keV}$, while a $1000\,\mathrm{M}_\odot$ black hole has $kT \approx 0.1\,\mathrm{keV}$. Extending this to supermassive black holes, the peak disk temperature is lower and thus in the ultraviolet.

Therefore, it is unlikely that the soft excess seen in AGN, thought to be accreting supermassive ($M > 10^5 M_\odot$) black holes, is from the disk. Here, the measured temperature of the soft excess ($kT \approx 0.1\,\mathrm{keV}$) is too hot, the shape is much more gradual than a Wien rollover, and the same effective temperature component is seen for many AGN ($kT = 0.12 \pm 0.02\,\mathrm{keV}$) (Gierliński & Done 2004). A few alternate possibilities are discussed in the literature. One possibility is that the thermal emission is from the disk, as a result of Compton up-scattering of ther-

mal emission. In other words, the disk blackbody emission is up-scattered from the optical/UV in a hotter region of the disk's corona. Other possibilities include the soft excess being the result of partially ionized material close to the disk moving at relativistic speeds. This can be explained as blurred absorption from a wind above the accretion disk (Gierliński & Done 2004) or blurred emission from matter reflected off of the disk.

Ionized gas from circumstellar matter/star formation: For AGN, a soft excess could be the result of ionized gas from circumstellar matter or star formation. A soft excess from this phenomenon is more likely in the X-ray spectrum of low luminosity AGN (LLAGN). In this case, the emission lines from the hot, ionized gas around young stars can compete with the LLAGN emission. If the AGN were more luminous, the spectral contribution from the hot gas (with $L_X \leq 10^{41}\,\mathrm{ergs\,s^{-1}\,cm^{-2}}$) would be lost to the much more powerful AGN emission.

A soft excess could also be seen if the host galaxy is undergoing very active star formation. Here, the lines produced would be strong enough to compete with the AGN emission. With lower spectral resolution, the emission lines from hot ionized gas are indistinguishable and blend to appear as a thermal spectrum. In addition to spectral resolution, the angular resolution of the telescope also plays a part in viewing a soft excess. If the angular resolution is insufficient to separate the AGN point source from nearby galaxy/star burst emission, a soft excess will be seen.

(2) **Reflected Emission**: In addition to the more or less direct emission, which is well-modeled by a power law, some portion of the direct emission may be blocked but reflected into our line of sight. Thus, the emission we see is from photons which are reflected from matter surrounding the black hole. Some of the main features of the resultant reflection spectrum include an iron line from flu-

orescence, the iron edge, and a Compton hump resulting from Compton down-scattering of photons due to electron recoil. There is also a thermal cutoff which is related to the temperature of the corona (thought to be at about 200 keV). This cutoff occurs due to the reduction in energy exchange as the photon energy approaches the average energy of the electrons in the corona. In Figure 1.1, an example is given for a model including reflection. The most prominent features include the Fe emission line at 6.4 keV, the Compton hump, and the cutoff at 200 keV. In the figure, a power law model is also shown to illustrate more clearly the significant differences between the models at higher energies (above 10 keV).

In the model, the Fe emission line is clearly a very prominent feature in the spectrum below 10 keV. The Fe lines typically observed are 6.4 keV (from cold Fe I reflection), 6.67 keV (Fe XXV), and 6.97 keV (Fe XXVI). The last two Fe lines are both from reflection of thermally excited or photoionized material. The process which produces the 6.4 keV line is known as fluorescence. Fluorescence is the phenomena in which the absorption of a higher-energy photon results in re-emission of a lower energy photon. Here, an inner level electron (at X-ray energies this is often the K shell or innermost level) is given enough energy from a photon to leave the atom. An electron from a higher energy shell cascades down to take its place, losing energy in the form of a photon. Since iron has a high fluorescent yield and relatively high cosmic abundance, this is the element commonly seen.

(3) **Absorption**

Cold/neutral Photoelectric absorption: Cold or neutral photoelectric absorption is the result of absorbing material in the line of sight. This material can be from the interstellar medium (ISM) in our own galaxy, the ISM of the host galaxy (if the object is extragalactic), and also absorbing material local to the X-ray source.

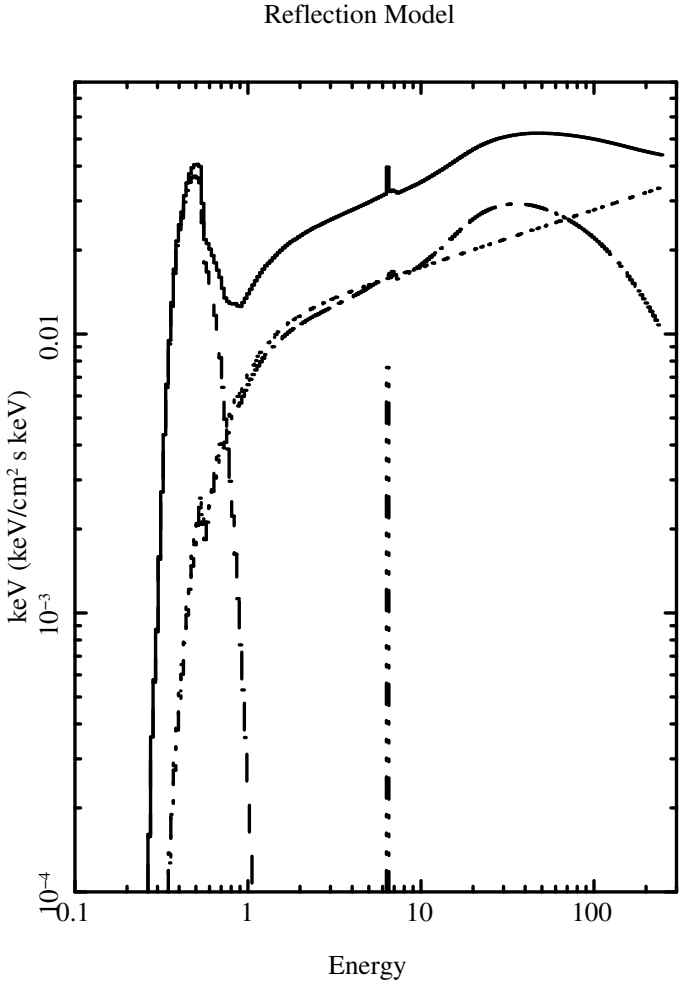

Figure 1.1: Shown is a model fit to an X-ray spectrum. Included in this model is a thermal component at soft energies (blackbody emission) along with direct power law emission and a reflection spectrum, all modulated by photoelectric absorption. The reflection spectrum has a characteristic hump, the Compton hump, and a cutoff energy at 200 keV.

The primary effect it has on the X-ray spectrum is to cut off the emission at low energies. This cutoff is determined by the amount of material, corresponding to higher energies for higher absorbing columns. In Figure 1.1, the effect of absorption is shown on the power law and reflected emission. In this example, a column density of $n_H = 10^{21}$ atoms per cm^2 is shown.

Ionized/warm absorption: Warm ionized gas, from optically-thin photo-ionized

gas in the line of sight, is seen in the spectra of some type 1 AGN. From observations with the ASCA X-ray satellite, Reynolds (1997) and George et al. (1998) found that half of their samples of unabsorbed AGN (type 1) spectra statistically preferred a warm ionized absorber model. The main signatures of a warm absorber are the O VII and O VIII K edges at 0.74 keV and 0.87 keV. However, with higher quality grating data, more features (in particular, resonance absorption lines of ionized oxygen and other elements) are distinguished and photoionization models can be used to determine the temperature and ionization parameters.

The origin of the warm absorber is unclear, but may be matter blown off the accretion disk by radiation pressure. High resolution data, including UV spectra from the *Hubble Space Telescope* and X-ray grating data from Chandra and *XMM-Newton* have led to great advances in understanding the warm aborber properties. These observations have revealed that the gas is from an outflowing wind with column densities from $10^{21-23}\,\mathrm{cm}^{-2}$ and many different ionization states (Crenshaw et al. 2003).

1.3 The X-ray Observing Tools

Having described the various features of black hole X-ray spectra, it is now necessary to discuss the tools used to obtain the spectra. The bulk of this dissertation relies on observations from *XMM-Newton* and *SWIFT*. Therefore, these observatories are discussed in the greatest detail. Additionally, *ASCA*, *Chandra*, and *Suzaku* are discussed.

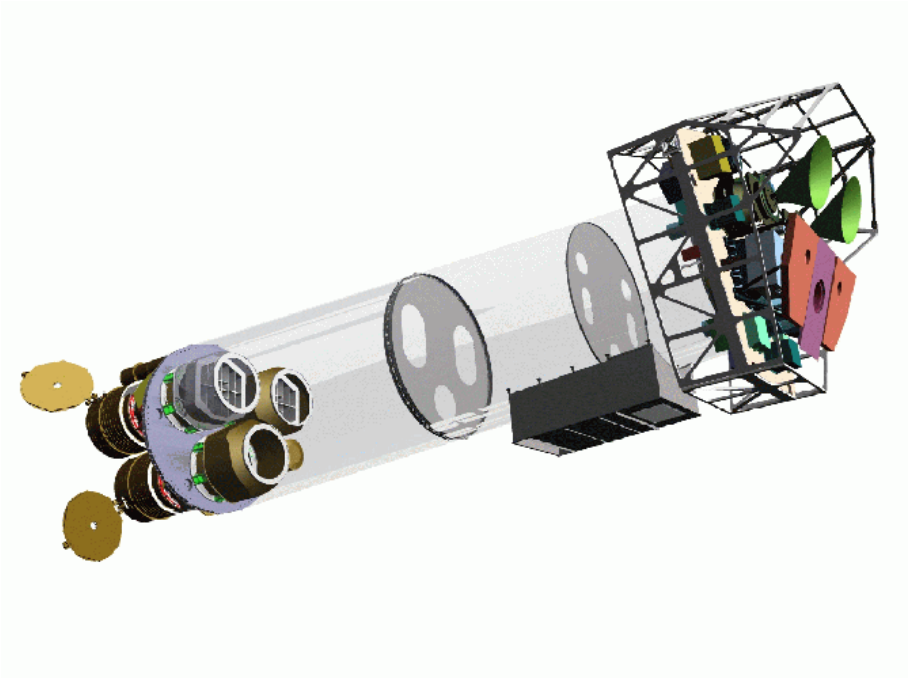

Figure 1.2: Shown here is the *XMM-Newton* payload. This image was obtained from the *XMM-Newton User's Guide* and is credited to Dornier Satellitensysteme GmbH.

1.3.1 *XMM-Newton*

A majority of the observations analyzed in this thesis, particularly the data in Chapters 2–4, come from the European Space Agency's (ESA's) *XMM-Newton*, X-ray Multi-Mirror Mission. The observatory was launched in December of 1999 as a part of ESA's Horizon 2000 Program. *XMM-Newton* is truly a multi-wavelength observatory, consisting of 4 co-aligned telescopes: three high-throughput 7.5m focal length X-ray telescopes and a 30-cm optical/UV telescope. A sketch of the payload, obtained from the *XMM-Newton User's Manual*[1], is shown in Figure 1.2.

Three types of science instruments are included: the European Photon-Imaging Camera (EPIC), the Reflection Grating Spectrometer (RGS), and the Optical Monitor (OM). EPIC includes 3 CCD cameras for moderate resolution X-ray spec-

[1] `http://heasarc.nasa.gov/docs/xmm/uhb/XMM_UHB.html`

troscopy and X-ray photometry. These CCDs include one pn camera (shown in violet towards the upper right in Figure 1.2) and two MOS cameras (shown as the green and black "horns"). Two RGS are included (shown in pink) for high resolution X-ray spectroscopy. Finally, the OM provides optical/UV photometry (with filters centered at 5430Å, 4500Å, 3440Å, 2910Å, 2310Å, and 2120Å) and grism spectroscopy. Since the X-ray observations are the main focus of this work, particularly using EPIC, the focus now turns to the X-ray capabilities.

To begin, since X-rays are absorbed and not reflected in normal incidence, X-ray telescopes use a 'grazing' incidence design. The critical angle, θ_c, for total external reflection is proportional to both X-ray wavelength and the square root of the density of atoms in the material used. Typically, gold is used for the mirrors (θ_c corresponds to 3.72°at 1 keV for both), but iridium is used for the Chandra X-ray Observatory mirrors. For *XMM-Newton*, the reflective surface is gold and the mirrors are most efficient between energies of 0.1 – 10 keV with a $30'$ field of view. One of the telescopes is arranged such that all of the light reflected from the mirrors is focused to the pn CCD. For each of the remaining two telescopes, 44% of the light is focused on the primary focus, a MOS CCD. Further, 40% passes through an array of gratings before being focused on a CCD strip (RGS). The remaining light is absorbed by the support structures. The biggest advantage of this set-up is that it allows for simultaneous observations with all 5 of the X-ray instruments (as well as the OM).

For the EPIC detectors, the cameras perform imaging in energies from 0.15 – 15 keV with a FWHM of $6''$ and a $30'$ field of view. The spectral resolution is $E/\Delta E \approx 20 - 50$. In Figure 1.3, the configuration of the MOS and pn CCD chips is shown. The pn consists of 12 CCDs that are $13.6' \times 4.4'$. Each of the MOS cameras consist of 7 $10.9' \times 10.9'$ chips. Although, due to a micrometeoroid event, CCD6

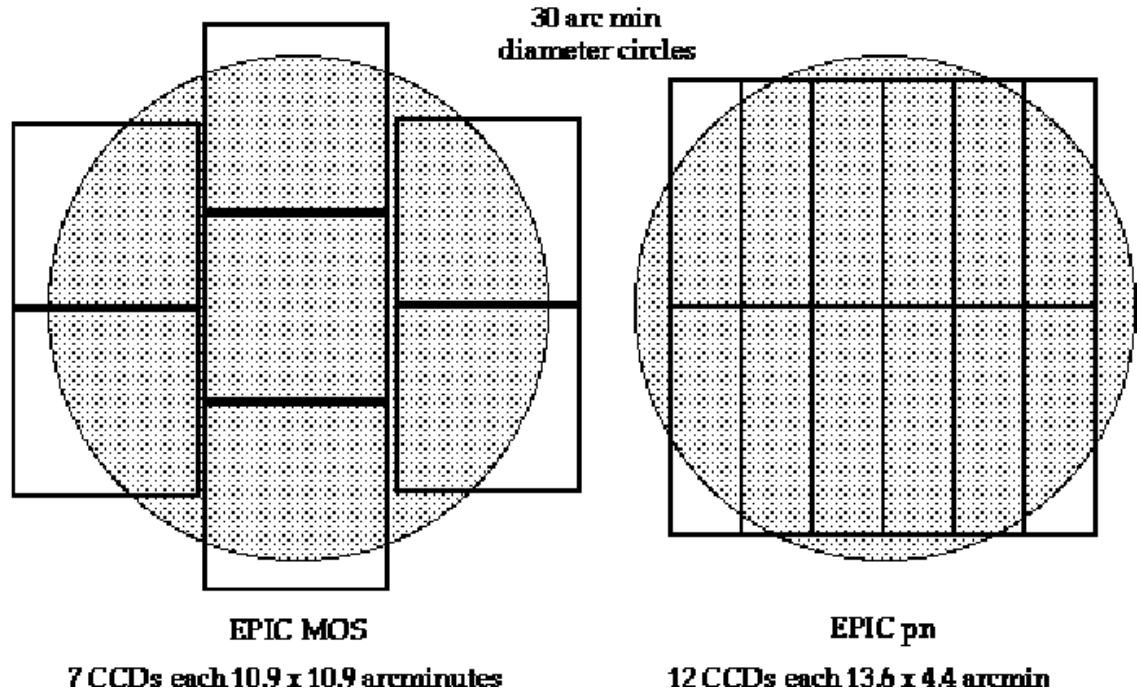

Figure 1.3: The configuration of the MOS and PN CCD arrays are shown. The figure is taken from the *XMM-Newton User's Manual*.

on MOS1 is no longer operational as of March 9, 2005.

The RGS, unlike the EPIC detectors, are geared towards high resolution spectroscopy ($E/\Delta E \approx 100$ to 500). However, it is sensitive in a far narrower energy band (0.33 – 2.5 keV). The field of view is also smaller, $5'$, as determined by the width of the 9 MOS CCDs used for the readout of the dispersed spectra. In Chapter 3, two RGS spectra are examined. However, the bulk of the analysis relied on EPIC spectra (≈ 100 spectra described in Chapters 2 – 4).

1.3.2 The SWIFT Gamma-ray Observatory

The SWIFT Gamma-ray Burst Observatory was launched into low-Earth orbit on November 20, 2004. Like *XMM-Newton*, SWIFT is a multi-wavelength observatory. However, since the main science mission is to detect and follow-up the incredibly powerful gamma-ray bursts, SWIFT includes a very hard X-ray detector with a large field of view. This allows SWIFT to scan much of the sky in search of bright triggers, which can then be rapidly followed up by additional instruments onboard as well as on the ground.

The very hard X-ray detector, the Burst Alert Telescope (BAT), is sensitive from 14 – 195 keV. The field of view is 1.4 steradians with $\approx 4'$ accuracy in source positions, depending on the source signal-to-noise. The aperture used is a coded aperture mask, consisting of ≈ 54000 lead tiles ($5 \times 5 \times 1$ mm). Below this, the detector consists of 256 modules of 128 elements (CdZnTe). BAT runs in two operational modes, burst mode and survey mode. In burst mode, BAT reads data in a photon counting mode. When not triggered on a burst, the instrument collects data by count rate in 64 energy bins. Every five minutes, a new detector plane map is made.

The technique for producing spectra with BAT (high quality imaging is not possible) is very different from the lower energy X-ray telescopes. The lead tiles in the coded aperture mask block light from bright very hard X-ray sources, casting a "shadow". The patterns formed by the shadow (really multiple shadows since multiple sources are typically in the field of view) are then separated to determine the position of the source. Depending on the brightness of the source, it may take many observations to construct a spectrum. The spectra constructed for the BAT AGN survey, for example, were made using data from

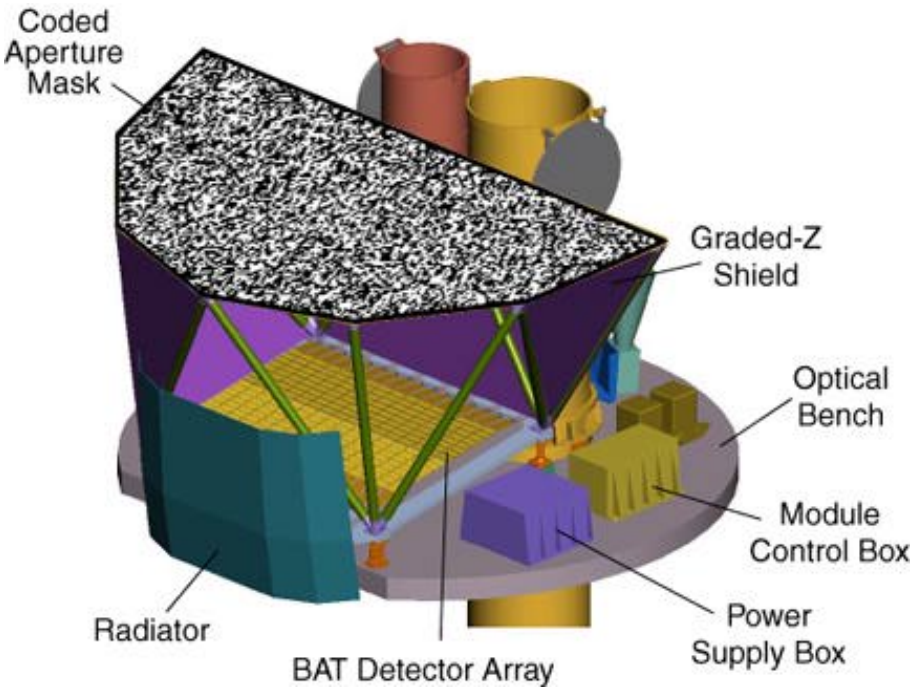

Figure 1.4: Image from the SWIFT BAT website on *HEASARC* showing a cut-away view of the BAT instrument.

22 months of observations (Tueller et al. 2008). These analyses are done by scientists at NASA Goddard Space Flight Center, particularly Drs. Craig Markwardt and Jack Tueller.

In addition to BAT, SWIFT also consists of an X-ray telescope (XRT) and an optical/ultra-violet telescope (UVOT). UVOT is essentially a copy of the *XMM's* OM. It allows for rapid optical/UV follow-ups of bursts as well as redshift determinations with the optical grism. The XRT is a grazing-incidence telescope with a focal length of 3.5 m and a $23'$ field of view. XRT is sensitive in the 0.2 – 10 keV energy band, providing X-ray imaging, spectroscopy, and timing. The CCD is an EEV CCD-22, with a 600×600 pixel area. Since the XRT position accuracy of $3''$ is very good, this allows for accurate positions for BAT-detected sources. This is essential for obtaining proper follow-ups with additional instruments (for instance ground based optical spectroscopy).

1.3.3 Additional X-ray Observatories

In addition to *XMM-Newton* and SWIFT, in Chapter 5 we describe X-ray spectra from additional observatories. The Chandra X-ray Observatory is perhaps the most famous, as the X-ray observatory of NASA's four Great Observatories. Chandra was launched July 23, 1999, only several months before *XMM-Newton*. The Chandra X-ray Observatory consists of an X-ray telescope with 4 different X-ray instruments. Unlike *XMM-Newton*, all of the science instruments can not be used simultaneously. These instruments include the Advanced CCD and Imaging Spectrometer (ACIS) and the High Resolution Camera (HRC), which are used in the primary focal-plane, and both the High Energy Transmission Grating (HETG) and Low Energy Transmission Grating (LETG), which are used in combination with either of the focal plane instruments.

In many ways, the Chandra and *XMM-Newton* observatories are complementary. The mirror effective area is much higher for *XMM-Newton*, $4650\,\mathrm{cm}^2$ at $1\,\mathrm{keV}$ to Chandra's $555\,\mathrm{cm}^2$. This allows *XMM-Newton* to collect more photons in a given amount of time, obtaining a higher quality spectrum. Meanwhile, the full-width half maximum point spread function for Chandra's mirrors is much smaller, $0.2''$ compared to *XMM-Newton*'s $6''$. This gives Chandra superior spatial resolution.

The Suzaku X-ray Observatory is another complementary observatory, not only for *XMM-Newton* but particularly for SWIFT. This Japanese mission, launched July 10, 2005, is sensitive from 0.2 – 600 keV. The observatory consists of two instruments, the X-ray Imaging Spectrometer (XIS) and the hard X-ray detector (HXD). Unfortunately the third instrument, the X-ray Spectrometer (XRS), an X-ray micro-calorimeter which would have provided superior spectral resolution,

lost its cryogen soon after launch. Four co-aligned foil X-ray telescopes focus X-rays onto each of the four XIS CCDs, each with a $19'$ field of view. A fifth is used for the non-functioning XRS, which was the primary instrument. A key advantage of this satellite is that it can obtain simultaneous X-ray (0.2–12 keV) and very hard X-ray (10–600 keV) spectra. However, the field of view for the HXD is rather large (0.56°), so it is important to select sources where source confusion will not be an issue.

The final X-ray observatory from which we obtained X-ray spectra is another Japanese satellite, the Advanced Satellite for Cosmology and Astrophysics (ASCA). ASCA was launched on February 20, 1993, and was operational into 1999. ASCA consisted of four 3.5 m X-ray telescopes with effective area of 1300 cm^2 at 1 keV, a $24'$ field of view, and $2.9'$ spatial resolution. The detectors include 2 Gas Imaging Spectrometers (GIS) and 2 sets of Solid-state Imaging Spectrometers (SIS). The SIS are CCDs while the GIS are proportional counters. We used ASCA data in this study because there are many papers detailing the ASCA X-ray spectra of AGN in a uniform way, using simple models that we employ in Chapters 4 and 5. Additionally, a very nice database (Tartarus[2]) exists with processed spectra and images available for many of the observed AGNs.

1.3.4 Analysis of the X-ray Spectra

In modern day X-ray astronomy (≈ 0.1–12 keV), the main detectors used in contemporary missions are CCDs. Since the photon energies are significant but count rates are small for cosmic X-ray sources (a count rate of 1 X-ray photon per second is considered a strong source), much information can be garnered with the CCD observations. In particular, the energy, arrival time, and position are mea-

[2] `http://tartarus.gsfc.nasa.gov/`

sured for each incoming photon. This allows for the generation of time-averaged spectra, light curves, and images. However, the analyses of X-ray spectra are not altogether straightforward since the observed spectrum is really the source spectrum convolved with the instrumental response. Further, the tools used to extract and analyze the data differ by the satellite.

The general X-ray data analysis procedure begins with an examination of the image. The source is identified and both a source and background region are specified. Next, the observed source and background spectra are extracted. These spectra consist of the raw number of counts in detector channels (the observed spectrum, $C(I)$). In order to convert the counts per detector channels into flux per discrete energy, a response file is necessary. Typically, the instrumental response consists of two files: the auxilary response file (arf, or $A(E)$) and the redistribution matrix file (rmf, or $R(E, I)$). The arf file contains efficiency versus energy, which is a combination of the telescope effective area, filter transmission efficiency, and detector quantum efficiency as a function of energy. Meanwhile, the rmf file contains the detector response.

In general, the observed spectrum can be described as:

$$C(I) = \int S(E)R(E, I)A(E)dE. \tag{1.2}$$

Since the response matrices are really the probability that a photon of a given energy is registered in a given channel, it makes more sense to fold a model spectrum through the telescope response than trying to deconvolve the response and obtain the "true spectrum" ($S(E)$). Therefore, this is the method employed for fitting X-ray spectra. The standard analysis software, which folds the model spectrum through the response and fits it to the data, is called `XSPEC` (Arnaud 1996).

In `XSPEC`, the observed spectrum is computed as the background subtracted spectrum, corrected for differences in the area and exposure time between

the source and background spectra. The fitting algorithm used is a modified Levenberg-Marquardt algorithm (Bevington 1969). Use of the algorithm involves an iterative procedure. The user provides a set of initial guesses for the model parameters ($M(E,p)$), which are changed by an indicated step size. Additionally, lower and upper limits are also supplied. At each iteration, the parameters are varied within the allowed range and a statistic is calculated to indicate the goodness of fit. Typically, the χ^2 statistic is used, however, other statistics can also be chosen (e.g. C-statistic). The definition of this statistic is:

$$\chi^2 = \sum (C(I) - M(I))^2/\sigma(I)^2, \tag{1.3}$$

where M(I) is the model folded through the instrumental response and σ is the error in the given channel, often $\sqrt{C(I)}$. The process is continued until a minimum is found in χ^2-space. The best-fit parameters are then returned, as well as the fit statistic.

In order to determine goodness of fit, the reduced χ^2 value is computed as χ^2/ν. Here, ν is the degrees of freedom or the number of free model parameters subtracted from the number of data points. A good fit is indicated by χ^2/ν close to 1. If the value is much higher, the model is not a good fit to the data. Alternatively, very low values indicate poor sampling or over-estimated errors on the data points.

Once the best fit model is obtained, it is important to also find the associated errors on each free parameter. In `XSPEC`, this is calculated with the `error` command. Here, the fitting procedure is again repeated in order to find the range of values corresponding to a user supplied confidence interval. For instance, a user may calculate the range of values corresponding to the 0.68, 0.90, or 0.99 confidence level for the change in one parameter. This involves calculating the values corresponding to $\Delta\chi^2$ of 1.00, 2.71, or 6.63 (Avni 1976), respectively, depending

on the number of model parameters. So, if the 0.90 confidence level is chosen, the model parameters will be changed, both above and below the best-fit value, and the χ^2 statistic computed until the $\Delta\chi^2$ value is 2.71.

Often, it is also important to compare the goodness of fit between multiple models for the same observed spectrum. If both models have the same degrees of freedom, the comparison is trivial – the lowest χ^2 corresponds to the best statistical fit. If one model is an extension of the other, for example a power law and blackbody model as an extension of a power law model, the F-test may be used. Here, the F statistic for the addition of a co-efficient to a model (Bevington 1969) is computed as:

$$F_\chi = \frac{\chi^2(n-1) - \chi^2(n)}{\chi^2(n)/(N-n-1)} = \frac{\Delta\chi^2}{\chi^2/\nu}. \tag{1.4}$$

In this case, the extended model (i.e. blackbody + power law model) has $n+1$ parameters (n coefficients and 1 constant term), whose χ^2 value corresponds to $\chi^2(n)$. The original model (i.e. power law model) has a χ^2 value of $\chi^2(n-1)$. Finally, there are N data points and a Gaussian or normal distribution ($G(x) = \frac{1}{\sigma\sqrt{2\pi}} \exp -\frac{1}{2\sigma^2}(x-\mu)^2$) is assumed for the χ^2 distributions of each model. A probability is then computed for the given F-statistic, indicating the probability that the two distributions come from the same distribution. Potential problems associated with using the F-test are identified by Protassov et al. (2002). However, if the threshold of significance is required to be sufficiently high (i.e. 99%), the effects are minimal.

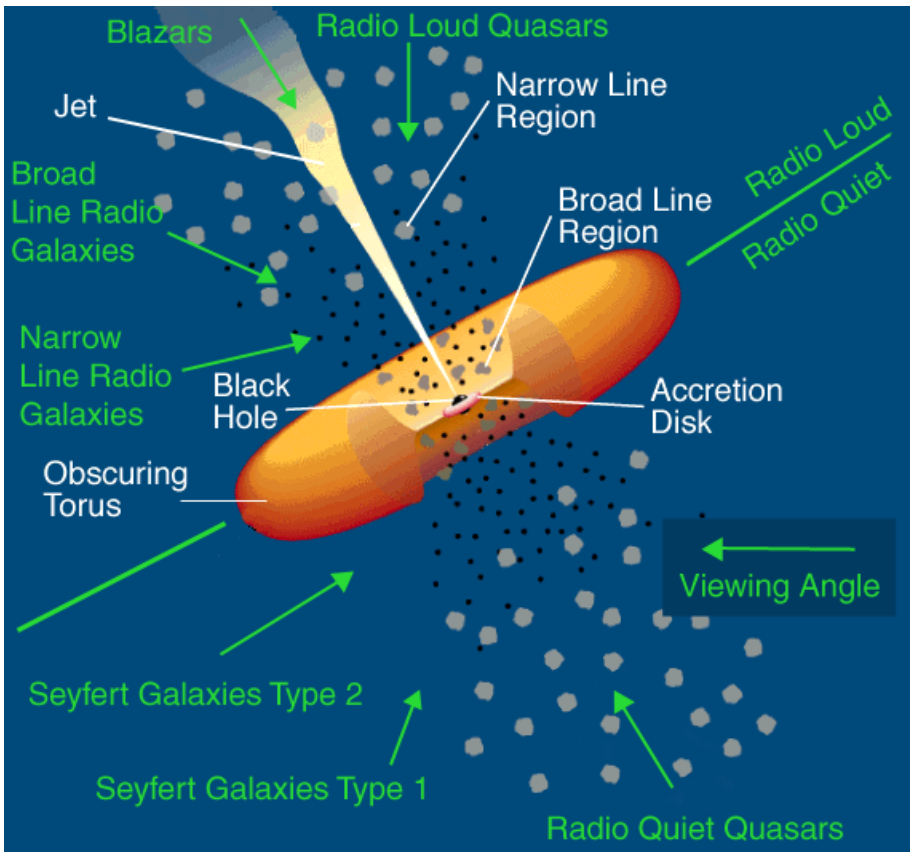

Figure 1.5: A schematic model of the AGN unified model is shown. Image credit: NASA.

1.4 The Multiple Types of AGN

Classifications of AGN can be confusing, with different terminologies used based on the wavelength through which they are viewed. In the optical, AGN are classified as broad-line Seyfert 1s, blazars, or narrow line Seyfert 2s, among others. In the X-ray, there are type 1/unabsorbed and type 2/absorbed sources. Further, in the radio bands some sources are discovered to output huge amounts of energy in jets, others show evidence of giant radio lobes. Connecting the properties in various bands can be a daunting task, which in some instances brings challenges to the standard unified AGN model.

The AGN unified model predicts that changes in the properties of AGN are the result of differences in our viewing angle to the central source. An illustration is shown in Figure 1.5. In the model, the central supermassive black hole is surrounded by an accretion disk. As previously mentioned, the source of the X-ray emission is believed to be either synchrotron emission from a jet or inverse Compton scattering of the accretion disk emission in a hot corona above the disk. Beyond the disk, there is a broad line region (widths of $\approx 10000\,\mathrm{km\,s^{-1}}$) composed of clouds of gas or a wind from the accretion disk. Since the broad line region is relatively close to the central black hole, these clouds/matter in the wind are/is affected by Doppler motions causing the resultant emission lines from gas in the region (particularly hydrogen and helium) to be broadened.

At parsec scale distances from the black hole, the AGN is thought to be surrounded by an optically thick obscuring torus (Krolik & Begelman 1988). In the X-ray band, it is the torus which is believed to contribute much of the X-ray obscuration. The term covering fraction is typically used to distinguish the amount of toroidal material that blocks the central source. As such, the covering fraction measures the probability that our line of sight to the source is obscured. Thus, a heavily obscured source most likely has a large covering fraction while an unobscured source typically has a small covering fraction. However, since this is a probability, there are some sources that are obscured along our line of sight which have small covering fractions and unobscured sources with large covering fractions. In the optical band, the presence or absence of the broad emission lines, from the broad line region, is associated with a viewing angle that is not/is blocked by the torus. Finally, at distances far from the central black hole, clouds of gas comprise the narrow line region, responsible for the narrow emission lines (widths $\leq 1000\,\mathrm{km\,s^{-1}}$) seen in the optical band.

When sources are "radio quiet", with a low ratio of radio to X-ray flux and either weak or no sign of radio jets or lobes, the designation Seyfert 1 applies to optical spectra exhibiting both broad and narrow emission lines. A Seyfert 2 source is one where the narrow lines alone are seen. Radio quiet sources comprise the majority of all AGN, such that only 10% are "radio loud". For this 10%, sources are designated broad line or narrow line radio galaxies. However, sources with a featureless optical spectrum are called blazars and are thought to be sources viewed directly along the jet.

The first firm observational support for this unified theory came with the detection of polarized broad lines for a Seyfert 2 source, NGC 1068 (Antonucci & Miller 1985). The widths of these broad lines were typical for a Seyfert 1 source. Further, the polarized light comprised 16% of the AGN flux, supporting the idea that a fraction of the direct emission from a hidden Seyfert 1 nucleus was being reflected or scattered into our line of sight. Observations of this source, thus, showed that in this case, at least, a change in viewing angle would change our classification from Seyfert 2 to Seyfert 1.

However, other AGN observations have provided challenging to this model. One such challenge involves a mismatch between X-ray and optical classifications for some AGN. A discussion of this issue is found in Matt (2002). In brief, a class of broad-line QSOs with strong X-ray absorption has been identified. Similarly, there are X-ray absorbed sources with optical broad lines. This mismatch does not immediately fit with the unified model. Some theories of how this disparity is possible include the idea that the X-ray absorption originates close to the nucleus while the optical absorber is at further distances. Other ideas include a different dust/gas ratio in the host ISM from our Milky Way or differences in dust grain size (Maiolino et al. 2001).

Another challenge is posed from observations of variability in the X-ray absorbers. Variability on the scale of several $10^{21}\,\mathrm{cm}^{-2}$ was discovered to be common in a sample of 23 X-ray type 1 and type 2 sources by Malizia et al. (1997). Since changes in the absorbers take place on time scales of a month or less, this suggests the absorber is close to the black hole. Later, Risaliti et al. (2002) found that this variability is ubiquitous in Seyfert 2s on time scales of months to a year. From their study, they find that the variability time scale is too low to be explained by changes in a torus located 1–3 pc away. Instead, they find that the X-ray absorbers must be clumpy and much closer to the black hole.

Probably the most challenging observations, however, involve the relative lack of obscured AGN at high X-ray luminosities. From a sample of 41 hard X-ray sources (2–10 keV) detected by *XMM-Newton*, Piconcelli et al. (2002) found a lower fraction of absorbed sources than predicted from cosmic X-ray background (CXB) synthesis models. Further, both Steffen et al. (2003) and Ueda et al. (2003) found that the fraction of obscured AGN is lower at high 2–10 keV band luminosities. These results in particular suggest that the unified model must be modified to include a luminosity dependence. In particular, the covering fraction of the torus seems to be dependent on luminosity. This could be the result of radiation pressure changing the shape of the torus, i.e. when the source is luminous the covering fraction is small and the source is unabsorbed.

The main point to keep in mind is that recent studies on AGN uncover many remaining questions. While we know that accreting super massive black holes lie at the heart of the phenomena, the standard unified model is too simplistic. Thus, with an unbiased local AGN sample from SWIFT's Burst Alert Telescope, we hope to answer some questions and perhaps pose new ones. In Chapters 4-6, we will touch on these issues again in the context of our X-ray analyses.

Chapter 2

ULX Survey

2.1 Introduction

In this chapter, we present the results of an X-ray analysis of Ultraluminous X-ray sources (ULXs). As mentioned in § 1.1, ULXs are pointlike, non-nuclear sources with observed X-ray luminosities greater than $10^{39}\,\mathrm{erg\,s^{-1}}$ (Miller et al. 2004a). The most interesting of these sources have bolometric luminosities above the Eddington limit for a 20 $M_\odot$ black hole, or $L_{bol} > 2.8 \times 10^{39}\,\mathrm{erg\,s^{-1}}$, which is believed to be the black hole mass limit from normal stellar evolution. While the true nature of ULXs is still unclear, they are likely a composite class of several different types of objects.

One likely explanation for extremely bright X-ray sources is that they are low luminosity AGNs or bright, distant blazars. However, while this may be the case for some individual sources, there is evidence that not all ULXs are AGNs. While some ULXs are located within a few parsecs of their host galaxy's dynamical center, they do not exhibit many of the characteristics of AGN. The most important of these is the ratio of X-ray to optical flux. ULXs are fairly easy to recognize in X-ray imaging data, but finding their optical counterparts is very difficult – a

property that is typically not true for AGN (except for heavily obscured sources). In particular, the ratio of X-ray to optical flux is a factor of 10 greater than that of AGN (Anderson et al. 2003; Stocke et al. 1983), illustrating a major difference between these objects. However, there is evidence to suggest that at least some of the cataloged ULXs really are background QSOs at high redshift (Burbidge et al. 2003).

Assuming that the Eddington limit is obeyed by black hole accretion, the existence of luminous non-AGN sources presents a puzzle. Several models have been proposed to account for the high luminosities of the ULXs. Among these are relativistic and non-relativistic beaming from stellar-mass black hole systems (King et al. 2001; Körding et al. 2002; Reynolds et al. 1997) and accretion of matter into intermediate mass black holes (IMBHs).

In several ULX systems (e.g., NGC 1313 X-2, M81 X-9), detection of emission nebulae surrounding the ULX supports the claim that the emission is isotropic (Pakull & Mirioni 2003) and can therefore not be described through beaming. Further, a number of ULX (e.g., NGC1313 X-1) X-ray spectra are best fit with combined multi-component blackbody (MCD) and power law fits, similar to Galactic black holes in their high-state. Recently, Miller et al. (2004a) found that many ULX spectral fits required cool accretion disk temperatures of approximately 100 eV. Since the theoretical relationship between black hole mass and disk temperature ($T \propto M^{-1/4}$) has been observed to hold true for stellar mass (typically around 1 keV) and supermassive (around 10-100 eV) black holes (Gierliński & Done 2004; Makishima et al. 2000; Porquet et al. 2004b), application of this scaling law to these cool accretion disk ULXs would correspond to a population of high-state IMBHs with masses of $\approx 16 - 10^4\,M_\odot$.

Still, it is likely that not all ULXs obey the Eddington limit. In this case, their

extreme X-ray luminosities could be the result of an outburst, similar to those observed for low and high mass X-ray binaries within our own Galaxy. For instance, Jonker & Nelemans (2004) find evidence for approximately 5 Galactic black hole X-ray binaries which exhibit luminosities in the ULX range during outbursts. Since the typical time scale for outburst of Galactic X-ray transients is a few days to rise from quiescent level with a decline from peak brightness to quiescent value of 30 - 40 days (Chen et al. 1997), these sources would appear as transient ULXs. Another possible explanation is super-Eddington emission from accretion disks surrounding stellar mass black holes (Begelman 2002; Ebisawa et al. 2003). Sources of this type would be expected to have soft X-ray components well modeled by hot accretion disks ($\approx 1.3 - 2.0\,$keV), similar to superluminal X-ray sources in the Galaxy (e.g. Belloni et al. (1997)).

Likely, ULXs include a variety of different objects with both isotropic and non-isotropic emitters. However, if some ULXs do indeed represent a class of high-state IMBHs, similar to the high/soft (thermal dominated) state stellar mass black holes in our own Galaxy, we also expect to see their low-state counterparts. This is the main thrust of this chapter, searching for high and low state ULXs.

In Galactic black hole systems, the low-state is generally characterized by lower luminosity, with L$< 0.1\,$L$_{Edd}$ (Done & Gierliński 2003), and a power law photon spectrum, typically with index $\Gamma \approx 1.7$ (Remillard & McClintock 2006). Indeed, the existence of some ULX sources (IC 342 X-1, NGC 5204 X-1) as possible low-hard (pure power law) state IMBHs, well-fit by simple absorbed power laws, have been noted from Chandra observations by Roberts et al. (2004). In this study we seek to test a direct prediction of the IMBH hypothesis; namely, whether there is a class of sources with properties consistent with what we expect of low-state IMBHs. This requires two major assumptions: (1) that the emission from

ULXs is isotropic and (2) that IMBHs exhibit the same states (whose classification was based on luminosity and spectral form) as stellar mass black holes. Our goal is to find these "low-state" sources, if they exist, classify the properties of both high-state and low-state ULXs, and test whether these data are consistent or inconsistent with the predictions of the IMBH hypothesis.

Therefore, in this chapter we present the results of a detailed analysis of ULXs in nearby galaxies observed with the European Space Agency's *XMM-Newton* observatory. Only *XMM-Newton* provides the count rates and bandpass necessary to distinguish different spectral models for most ULXs, accurately determine both the temperature of the thermal component expected for high-state objects, and determine whether this component is required in the spectral modeling of these objects. Since the XMM-Newton X-ray spectra of ULXs are similar in quality to spectra for Galactic X-ray binaries obtained in the 1980s, our spectral classification in this chapter will remain purely schematic. Thus, our classifications as low and high state objects are a first approximation, based on the quality of the spectra available.

In § 2.2, we detail the observations examined from the *XMM-Newton* archives and explain the data analysis for the individual point sources. In § 2.3, we discuss the spectral fitting technique as well as simulations we conducted to determine their validity. We discuss the implications of our results in § 2.4. A summary of the results of this chapter are provided in § 2.5.

2.2 Observations and Data Reduction

2.2.1 Sample Selection

The data used in this investigation were drawn from the *XMM-Newton* public data archive. Assuming that low-state ULXs exist in the luminosity range of $10^{38-39}\,\mathrm{erg\,s^{-1}}$, we conducted simulations to determine the optimum criteria for observations capable of resolving point sources of this luminosity. These simulations provided a guide for choosing which of the vast number of archival *XMM-Newton* datasets we should examine. The base luminosity of $10^{38-39}\,\mathrm{erg\,s^{-1}}$ was chosen on the assumption that an approximately $100\,\mathrm{M_{\odot}}$ black hole would radiate at $\approx 10\%$ of the L_{Edd} in the low-state (Done & Gierliński 2003).

Within the luminosity range of interest ($\mathrm{L}_X > 10^{38}\,\mathrm{erg\,s^{-1}}$), there are a number of known objects that could be confused with ULX sources. One class of sources is supernova remnants (SNRs). These sources are often easy to distinguish based on their characteristic spectrum: with poor signal to noise we expect a steep power law and as the signal to noise increases, emission lines become clearly visible. Super-Eddington accreting neutron stars have been observed to have luminosities within this range for a short period of time. Neutron star X-ray binaries often have spectra well fit by a hot multi-color disk blackbody model, or with low signal to noise, by a bremsstrahlung model. Both models have similar curvature and a 0.7-2.0 keV blackbody model is indistinguishable from the bremsstrahlung model. We chose to use the bremsstrahlung model because it is the simpler model and gives an adequate qualitative description to the data. We expect that for low temperature bremsstrahlung sources, the spectrum should be easily distinguishable from a power law with $\Gamma \approx 1.7$ (as is expected for a low-

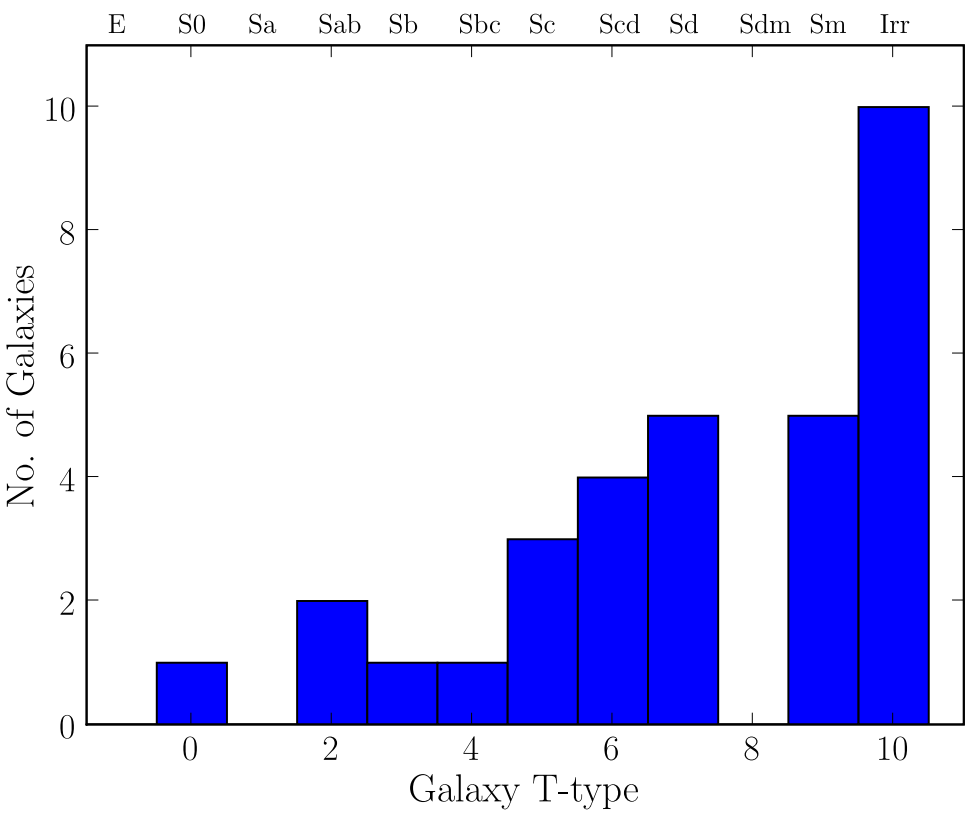

Figure 2.1: Distribution of galaxies by Hubble type among our archival *XMM-Newton* sample of nearby (< 8 Mpc) galaxies. Our sample consists of spirals and irregulars.

state object). If, however, the neutron star spectrum has kT > 5 keV, as observed for some NS X-ray binaries, our simulations show that we can not distinguish between the power law and bremsstrahlung models.

Table 2.1: *XMM-Newton* Galaxy Observations

Galaxy	Type[a]	n_H[b]	distance[c]	ref	obs id[d]	duration (s)	comments
NGC247	SAB(s)d	1.54	3.09	···	0110990301	14536	-
NGC253	SAB(s)c;HII	1.40	3.73	···	0110900101, 0152020101	30711, 110591	Starburst
NGC300	SA(s)d	3.11	2.56	···	0112800101	43967	-
NGC625	SB(s)m? sp; HII	2.15	2.62	···	0085100101	26288	-
NGC1313	SB(s)d; HII	4.0	4.17	···	0106860101	41310	-
IC0342	SAB(rs)cd; HII	30.3	3.9	1	0093640901	11217	-
NGC1569	IBm	21.7	1.6	1	0112290801	15582	Starburst
NGC1705	SA0- pec; HII	3.9	5.1	2	0148650101	58926	Starburst
MRK 71	Sm; HII	3.9	3.4	3	0141150201	45919	galaxy pair
NGC2403	SAB(s)cd; HII	4.15	3.56	···	0150651201	11415	-
Holmberg II	Im	3.42	2.70	···	0112520701, 0112520901	13528, 6860	-
Holmberg I	IAB(s)m	3.49	3.6	4	0026340101	26280	-
M81	SA(s)ab;LINER	4.12	3.6	4	0111800101	127913	Hol IX also in field of view

Continued on Next Page...

Table 2.1 – Continued

Galaxy	Type[a]	n_H[b]	distance[c]	ref	obs id[d]	duration (s)	comments
M82	I0; HII	4.14	3.9	5	0112290201	29387	Starburst
Holmberg IX	Im	4.0	3.6	4	0112521001	10350	M81 also in field of view
Sextans A	IBm	3.85	1.4	6	0026340201	21618	-
IC 2574	SAB(s)m	2.29	3.6	7	0026340301	24263	bursting star-formation
NGC 4214	IAB(s)m; HII	1.49	2.7	···	0035940201	14744	-
NGC 4258	SAB(s)bc;LINER	1.2	7.2	···	0059140901, 0110920101	16146, 21895	-
NGC4395	SA(s)m;LINER	1.33	4	···	0112521901	15842	-
NGC4449	IBm; HII	1.39	3.08	···	0112521701	15522	-
NGC4490	SB(s)d	1.78	7.8	1	0112280201	17754	interacting with NGC4485
NGC4631	SB(s)d	1.28	7.5	1	0110900201	53850	-
NGC4736	(R)SA(r)ab;LINER	1.43	4.3	1	0094360601	23461	-
NGC4945	SB(s)cd; Sy2	15.9	3.1	···	0112310301	23062	-
NGC 5204	SA(s)m; HII	1.42	4.8	1	0142770101, 0142770301	19205, 16387	-
M51	Sc; Sy2	1.55	7.2	1	0112840201	20924	Galaxy pair

Continued on Next Page...

Table 2.1 – Continued

Galaxy	Type[a]	n_H[b]	distance[c]	ref	obs id[d]	duration (s)	comments
M83	SAB(s)c;HII	3.94	6.2	···	0110910201	30627	Starburst
NGC5253	Im pec;HII	3.77	3.2	1	0035940301	47216	Starburst
M101	SAB(rs)cd	1.17	7.4	8	0104260101	43019	-
NGC5408	IB(s)m; HII	5.73	4.8	9	0112290601	7757	-
Circinus	SA(s)b; Sy2	57.8	4	10	0111240101	110496	-

[a] from the NASA/IPAC Extragalactic Database (NED)

[b] column density in units of 10^{20} cm^{-2}, obtained from the web version of the nH FTOOL

[c] distance in Mpc (if no reference is given, obtained from the distance modulus given in LEDA)

[d] *XMM-Newton* observation ids for the data examined in this survey

Table References: (1) Tully (1988); (2) Tosi et al. (2001); (3) Tolstoy et al. (1995); (4) Freedman et al. (1994); (5) Sakai & Madore (1999); (6) Sakai et al. (1996); (7) Shapley et al. (2001); (8) Kelson et al. (1996); (9) Karachentsev et al. (2002); (10) Freeman et al. (1977).

The most common sources we expected to find in this luminosity range were the analogs to Galactic black hole X-ray binaries in their high-soft (thermal dominated) state. These sources typically have spectra well fit by a blackbody with temperature of ≈ 1.0 keV combined with a power law with index $\Gamma \approx 2.5$. Our simulations sought to determine the number of photons required to distinguish between spectral fits corresponding to a power law model with $\Gamma \approx 1.7$ and a combined blackbody and power law model. These models qualitatively correspond to those of a low-state (pure power law spectrum) and high-state (thermal dominated spectrum) X-ray binary. Since we do not know the proper normalization between the blackbody and power law components for high-state objects (it varies from source to source), we tested whether each of the components separately, e.g. blackbody or a steep power law, could be distinguished from the simulated "low-state" spectrum. We chose to simulate spectra in *XSPEC* using the command `fakeit none` with generic response and ancillary response matrices. Simulating a power law model with a $\Gamma = 1.7$, we found that for 200, 400, and 1000 counts, these models were distinguishable at $> 99\%$ confidence from a blackbody source (with kT constrained to the range of 0.6 to 1.3 keV, similar to that of Galactic black holes). We found that for a lower number of counts the distribution in Γ values increases to include a larger range of Γ values (i.e. Γ = 1.3 – 2.0 compared to Γ = 1.5 – 1.7). Simulating a power law with $\Gamma = 2.5$, we find the same trend. We determined that at roughly 400 counts the distributions of Γ from a $\Gamma = 1.7$ and $\Gamma = 2.5$ power law become entirely separable at $> 99\,\%$ confidence.

In order to distinguish between the different spectral fits for objects with $L_X \sim 2 \times 10^{38}$ erg s^{-1}, we select all galaxies that were observed for at least 10 ks (with the exception of the bright ULX in NGC 5408, which had enough photons for analysis despite the low exposure time) with *XMM-Newton* and that are closer

than 8 Mpc. We estimated that these criteria would give us a minimum of 400 counts for objects with $L_X > 2 \times 10^{38}\,\mathrm{erg\,s^{-1}}$. We emphasize that the criteria quoted, based on the simulations, were used as a guide in choosing the sample of galaxies examined in this study. These simulations are not used as the statistical basis for our object-by-object analysis (discussed in § 2.3).

Our sample of galaxies is selective in that it represents objects of interest in the X-ray band. We include details on these host galaxies in Table 2.1. *XMM-Newton* spectral information of individual X-ray sources had previously been published for approximately 60% of the host galaxies. While we include references in the alternate ID column and footnotes of Table B.1, we do not compare our results with these previous studies on a source by source basis.

For 13 of the 32 galaxies examined, abstracts describing the proposals for *XMM-Newton* observations were publicly available. Of these 13, only one observation cited the motive as a study of ULXs (NGC 1313). However, 7 of the remaining 19 galaxies contained sources classified as IXOs, intermediate X-ray objects, by Colbert & Ptak (2002). If the remaining galaxies were not studied due to their ULX population, the effects of bias are small with roughly 25% of the sources studied explicitly due to their connection with ULX sources. In terms of host type, the general makeup of our host galaxy sample includes only spirals and irregulars. We show the distribution of galaxy type in Figure 2.1. Here, we find that a majority of our galaxies are irregulars (31%). Since the 2MASS galaxy survey shows a much smaller number of irregulars which are clearly not the dominating type (4% of the 100 largest galaxies) (Jarrett et al. 2003), this may introduce a bias. However, it is unclear what the nature of the bias may be.

2.2.2 Data Reduction

Data reduction of our observations proceeded using the *XMM-Newton* Science Analysis System (SAS) version 6.0.0. Since the processed pipeline products (PPS) were created with earlier versions of SAS, the observation data files (ODF) were used to produce calibrated photon event files for the EPIC-MOS and pn cameras using the commands `emchain` and `epchain`. Following this, the events tables were filtered using the standard criteria outlined in the *XMM ABC Guide*[1]. For the MOS data (both MOS1 and MOS2 cameras), good events constitute those with a pulse height in the range of 0.2 to 12 keV and event patterns that are characterized as 0-12 (single, double, triple, and quadruple pixel events). For the pn camera, only patterns of 0-4 (single and double pixel events) are kept, with the energy range for the pulse height set between 0.2 and 15 keV. Bad pixels and events too close to the edges of the CCD chips were rejected using the stringent selection expression "FLAG == 0".

Time filtering was applied as needed by editing the light curve produced in `xmmselect` for the entire observation. Flare events (distinguished by their high count rate) detected in all three cameras, were cut using the `tabgtigen` task as outlined in the *ABC Guide*. Typical count rate parameters for filtering were 'RATE < 5' for MOS detectors and 'RATE < 20' for the pn detector. Such filtering was only done as needed. Pre-filtered exposure times are listed in Table 2.1. The number of counts from the filtered net exposure times for the individual sources are listed in Table B.1. We note that the filtered data are not always sufficiently clean such that a high signal-to-noise is maintained up to 10 keV. Sources with a high background flux level, relative to the source spectrum, show poorer signal-

[1] `http://heasarc.gsfc.nasa.gov/docs/xmm/abc/`

to-noise in the spectrum above 1 keV.

Before extracting spectra of the brightest sources, contour maps of the X-ray observation were overlaid on Digital Sky Survey (DSS) images. This ensured that bright foreground stars and background AGN were easily distinguished, and thereby not included in our sample. Also, we checked the *XMM-Newton* source positions with NED and SIMBAD to determine if they coincide with any known background galaxies or QSOs. A list of these bright fore-ground or background sources is included in Table B.2.

2.3 Spectral Fitting

Spectra for the bright point sources were extracted based on their apparent brightness in the CCD images. Therefore, no explicit source detection algorithm was necessary. To extract the spectra, we used the SAS task `especget`. With this task we created spectra (for both the source and background), response matrices, and ancillary response files for all three EPIC cameras, when possible. The typical extraction radius was 20 arcseconds, but depending on both the size and proximity of a source to another source, the extraction radius ranged from 9 - 87 arcseconds. Background spectra were extracted either in an annulus centered on the source, or in a circle of appropriate size away from the source, depending on the proximity of the candidate source to other X-ray sources. Annuli were used for sources that were not located within a few arcseconds of another source, thus annular background extraction radii were not used for sources with small extraction radii. For sources in crowded regions, we used circular extraction radii close to the source. We extracted backgrounds close to the source in order to correct for emission local to the ULX. Once the spectra were obtained, they were rebinned to

require at least 20 counts per bin such that the data obey Gaussian statistics, using the command `grppha` in LHEASOFT. The list of sources, with position and count information, is included in Table B.1. We only included sources for our spectral studies that had 400 or greater pn counts (or MOS for sources in NGC 253 and M81 and NGC 4945 XMM3 and NGC 2403 XMM1, for which pn spectra were not available).

The extracted spectra were fit with standard models in XSPEC v11.3.1. For each source, we fit the pn and MOS spectra simultaneously in the 0.3-10 keV range. We allowed a free normalization constant to account for the differences in flux calibration between the three cameras (similar to Jenkins et al. (2004)). Each source was first fit with an absorbed single component model. In all cases we used the standard absorption model `wabs`, leaving the column density as a free parameter. For those sources where the hydrogen column density was unconstrained, we fixed the value to the Galactic foreground value listed in Table 2.1.

2.3.1 Single-Component Sources

Results of the single-component fits are seen in Table 2.2. We include in this table only the best-fit parameters for those sources best described by a single-component model. The addition of a blackbody component to these single-component fits changes the χ^2 value by a negligible amount and therefore is not statistically significant. More specifically, the addition of a blackbody model to the power law fit corresponds to a $\Delta\chi^2 < 2.3$, which is the $\approx 68\%$ confidence level using the F-test for two degrees of freedom.

The flux values quoted represent the unabsorbed flux in the pn spectra, in the 0.3-10 keV band. All errors quoted, here and subsequently, correspond to the 90% confidence level for one degree of freedom ($\Delta\chi^2 = 2.71$). The luminosities

Table 2.2. *XMM-Newton* best fit: single component spectral fits

	Powerlaw			Bremsstrahlung				
Source	n_H[a]	Γ	χ^2/dof	n_H[a]	kT (keV)	χ^2/dof	F_X[b]	L_X[c]
NGC247 XMM2	$1.4^{+1.8}_{-1.1}$	$2.29^{+1.02}_{-0.57}$	**47.7/54**	< 0.65	$2.55^{+6.90}_{-1.61}$	48.8/54	0.33	0.38
NGC 253 XMM2 (obs 1)	$1.6^{+0.4}_{-0.3}$	$2.51^{+0.18}_{-0.17}$	**69.1/74**	$0.5^{+0.2}_{-0.3}$	$2.12^{+0.52}_{-0.37}$	74.7/74	0.52	0.87
NGC300 XMM4[d]	2.5	9.07	90.6/45	0.27	0.14	117.6/45	-	-
NGC1313 XMM4	$1.86^{+0.5}_{-0.4}$	$1.8^{+0.07}_{-0.12}$	**141.7/149**	$1.2^{+0.3}_{-0.3}$	$6.62^{+2.3}_{-1.48}$	140.1/149	0.33	0.69
IC0342 XMM1	$5.8^{+0.6}_{-0.3}$	$1.68^{+0.08}_{-0.08}$	**159.5/185**	$4.9^{+0.5}_{-0.4}$	$10.5^{+3.3}_{-1.9}$	160/185	3.5	6.37
IC0342 XMM2	$23.9^{+4.0}_{-3.6}$	$1.85^{+0.22}_{-0.20}$	**77.5/85**	$21^{+3.0}_{-2.8}$	$8.5^{+5.0}_{-2.4}$	74.9/85	4.64	8.44
IC0342 XMM4	$5.3^{+1.4}_{-1.2}$	$2.02^{+0.20}_{-0.19}$	64/58	$4.2^{+0.99}_{-0.85}$	$4.44^{+1.68}_{-0.74}$	**56.9/58**	0.69	1.26
MRK71 XMM1	$0.47^{+0.30}_{-0.32}$	$1.69^{+0.11}_{-0.13}$	**55.3/54**	$0.04^{+0.26}_{-0.04}$	$7.98^{+4.90}_{-2.92}$	59/56	0.19	0.27
NGC2403 XMM4	$1.7^{+0.8}_{-0.7}$	$1.89^{+0.30}_{-0.25}$	**62.3/71**	$1.1^{+0.5}_{-0.3}$	$4.59^{+4.1}_{-1.5}$	62.3/71	0.31	0.48
HolmII XMM1 (obs 2)	$1.5^{+0.2}_{-0.2}$	$3.09^{+0.15}_{-0.12}$	**266.7/252**	$0.31^{+0.12}_{-0.15}$	$1.13^{+0.11}_{-0.11}$	309.4/252	3.5	3.1
Holm I XMM2	0.35[e]	$2.13^{+0.16}_{-0.15}$	**39.2/45**	0.35[e]	$2.0^{+0.57}_{-0.48}$	68.8/45	0.10	0.16
Holm I XMM3	0.35[e]	$2.05^{+0.19}_{-0.18}$	**34.4/32**	0.35[e]	$2.03^{+0.85}_{-0.56}$	42.1/32	0.12	0.19
IC2574 XMM1	$1.3^{+0.40}_{-0.30}$	$1.97^{+0.07}_{-0.10}$	120.9/103	$0.69^{+0.23}_{-0.25}$	$4.1^{+0.89}_{-0.67}$	**107.5/103**	0.35	0.47
IC2574 XMM2	$0.4^{+0.4}_{-0.3}$	$2.2^{+0.21}_{-0.09}$	**45.7/51**	0.229[e]	$1.71^{+0.33}_{-0.27}$	65.4/52	0.22	0.34
IC2574 XMM3	$0.15^{+0.35}_{-0.14}$	$2.43^{+0.27}_{-0.18}$	**40.3/49**	0.229[e]	$0.97^{+0.18}_{-0.14}$	76.5/49	0.22	0.34
NGC4214 XMM1	$1.1^{+0.52}_{-0.47}$	$1.87^{+0.26}_{-0.21}$	**41.9/38**	$0.54^{+0.41}_{-0.35}$	$4.86^{+4.52}_{-1.66}$	44.5/38	0.25	0.22
NGC4258 XMM2 (obs 2)	$6.7^{+2.6}_{-1.5}$	$2.49^{+0.44}_{-0.33}$	**83.6/57**	$4.8^{+0.9}_{-1.3}$	$2.61^{+1.22}_{-0.72}$	85.5/57	0.30	1.9
NGC4258 XMM3	$1.4^{+0.69}_{-0.64}$	$2.32^{+0.34}_{-0.24}$	**38.9/37**	$0.49^{+0.44}_{-0.38}$	$2.48^{+1.09}_{-0.74}$	41.3/37	0.20	1.2
...	3.8	1.82	**4/11**	2.7	7.14	5/11	0.077	0.48
NGC4258 XMM4	$0.68^{+0.24}_{-0.42}$	$1.97^{+0.22}_{-0.19}$	**41.1/48**	$0.06^{+0.31}_{-0.05}$	$4.07^{+1.6}_{-1.2}$	45.2/48	0.39	2.4
...	$1.9^{+0.78}_{-0.60}$	$2.24^{+0.29}_{-0.24}$	**77.03/77**	$0.9^{+0.6}_{-0.4}$	$2.82^{+1.2}_{-0.8}$	77.8/77	0.33	2.0
NGC4395 XMM2	$0.33^{+0.6}_{-0.3}$	$2.75^{+0.45}_{-0.33}$	**38.6/36**	0.133[e]	$0.79^{+0.13}_{-0.13}$	52/37	0.15	0.28
NGC4395 XMM4	$0.3^{+0.6}_{-0.3}$	$2.08^{+0.39}_{-0.30}$	**16/25**	0.133[e]	$1.97^{+0.99}_{-0.60}$	21.6/26	0.15	0.28
NGC4449 XMM2	$1.5^{+0.3}_{-0.3}$	$2.81^{+0.16}_{-0.14}$	**103.5/112**	$0.25^{+0.2}_{-0.2}$	$1.65^{+0.22}_{-0.21}$	112.1/112	0.29	0.33
NGC4490 XMM4	$10.2^{+2.3}_{-1.8}$	$2.09^{+0.23}_{-0.19}$	*51.6/50*	$8.3^{+1.3}_{-1.5}$	$4.75^{+1.82}_{-0.90}$	50.3/50	0.84	6.1
NGC4490 XMM5	$3.9^{+0.94}_{-0.81}$	$2.31^{+0.22}_{-0.20}$	**60.1/65**	$2.5^{+0.54}_{-0.59}$	$3.08^{+0.89}_{-0.62}$	61.6/65	0.41	2.98
NGC4631 XMM4[d]	7.8	9.50	261.5/74	2.9	0.17	207.8/74	-	-
NGC4631 XMM5[f]	1.3	1.03	641.8/153	1.3	199	659/153	-	-
NGC4945 XMM3	$3.3^{+1.3}_{-0.9}$	$1.82^{+0.12}_{-0.20}$	**30.1/30**	$2.5^{+0.83}_{-0.90}$	$6.07^{+4.50}_{-1.71}$	30.3/30	0.38	0.43
NGC5204 XMM2	$0.89^{+0.49}_{-0.53}$	$1.98^{+0.25}_{-0.20}$	*42.37/42*	$0.23^{+0.3}_{-0.22}$	$4.05^{+1.51}_{-0.95}$	42.2/42	0.15	0.41
...	$0.75^{+0.45}_{-0.45}$	$1.63^{+0.20}_{-0.17}$	**41.4/47**	$0.42^{+0.46}_{-0.38}$	$7.82^{+5.03}_{-2.70}$	39.4/47	0.25	0.69
M51 XMM3	$0.6^{+0.30}_{-0.40}$	$1.86^{+0.09}_{-0.15}$	**63.2/72**	$0.05^{+0.3}_{-0.02}$	$5.22^{+2.26}_{-1.41}$	69.2/72	0.18	1.1
M51 XMM4	$0.4^{+0.20}_{-0.30}$	$1.55^{+0.08}_{-0.13}$	**34.8/37**	$0.01^{+0.17}_{-0.13}$	$11.1^{+0.32}_{-0.25}$	34.8/37	0.16	0.99

[a] total column density in units of 10^{21} cm^{-2}

[b] unabsorbed flux in the 0.3-10 keV band in units of 10^{-12} erg cm^{-2} s^{-1}

[c] unabsorbed luminosity in the 0.3-10 keV band, using the distances quoted in Table 2.1, in units of 10^{39} erg s^{-1}

[d] see appendix; super-soft X-ray source best fit by single-component blackbody

[e] absorbtion column density fixed to the galactic column density found in Table 2.1

[f] source is best fit by a combined power law and *vapec* model; see appendix

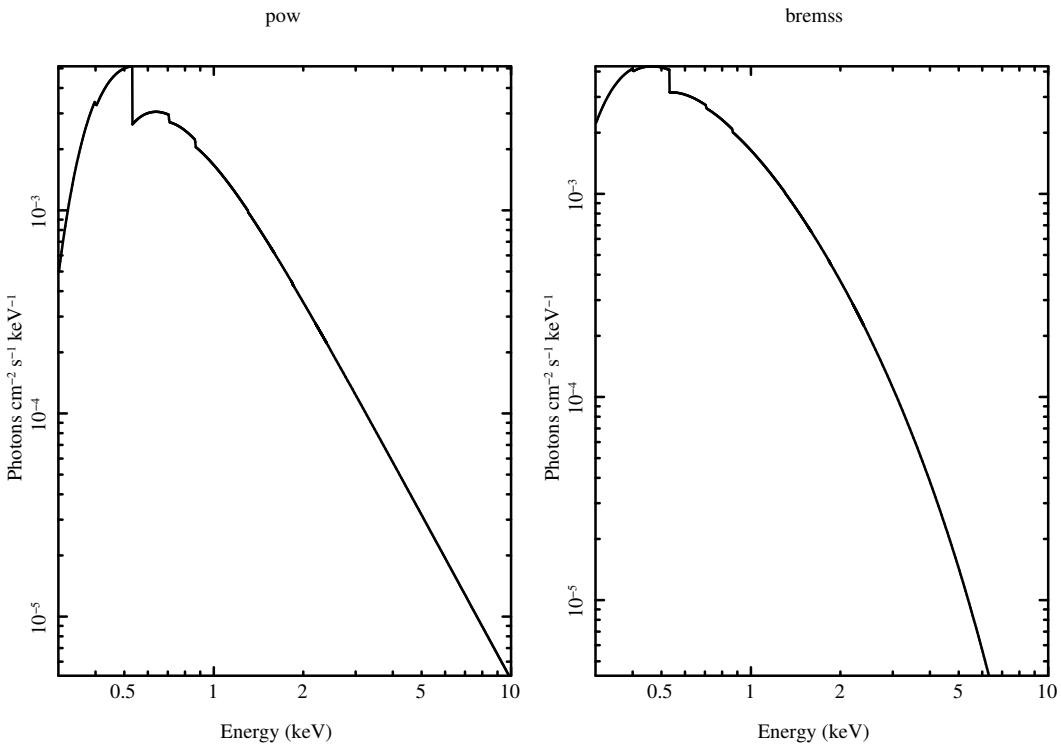

Figure 2.2: Shown are the simple single component models used: an absorbed power law and an absorbed bremsstrahlung model. Notice the difference in the curvature and cut-off of the bremsstrahlung model. Here, $\Gamma = 2.7$ for the power law model and $kT = 1.50$ keV for the bremsstrahlung model.

were calculated from the unabsorbed flux using the distances quoted in Table 2.1. Both flux and luminosity correspond to those of the best fit model (power law or bremsstrahlung). It should be noted that since our selection criteria was based on a count rate cutoff, due to the variety of spectral forms, the inferred luminosity cutoff will not be uniform.

In Table 2.2 we denote the single component model we choose as the better fit in bold. This notation also indicates the model (power law or bremsstrahlung, see Figure 2.2) used to compute the quoted flux. For $\approx 46\%$ of the power law sources, the χ^2 difference (< 2) between the power law and bremsstrahlung models is only marginally different. Of these sources, the average kT value for the bremsstrahlung fit is 5.54 keV. From our simulations we find that at high temperatures the

bremsstrahlung fit becomes indistinguishable from a simple power law. Thus, given the high temperatures of the bremsstrahlung fits for these sources, they are equally well described by the power law model. Typical kT bremsstrahlung values for accreting neutron stars are from 3.0 to 7.0 keV (Jones 1977).

"Low State" ULXs

From these single-component sources, we classify 16 sources as low-state ULX sources. This classification is based on (1) the shape of the spectrum, well-fit by an absorbed power law, (2) the luminosity of the sources (they needed to be luminous enough to be included in our sample, $L_X > 10^{38}\,\mathrm{erg\,s^{-1}}$), and (3) the X-ray location of the object within the optical galaxy (based on Digital Sky Survey (DSS) images). The third criterion was important in limiting the effects of contamination from fore-ground and background sources within our sample of ULX sources. Thus, we overlaid X-ray contours from the XMM image on the DSS images, determining the location of the X-ray source as within or outside of the optical extent of the galaxy. We note that for two of the sources classified as low-state ULXs (Holmberg I XMM2 and NGC 2403 XMM4), there is uncertainty of whether the X-ray source is in fact within the optical galaxy due to the quality of the optical DSS images. The images used to determine the third criterion are available online (http://www.astro.umd.edu/∼lwinter/second3.html). We further discuss these criteria in § 2.4.

We state that the first criterion for classification as a low/hard state ULX is a spectrum well-fit by a power law. Of the 30 sources in Table 2.2, three sources were clearly not well-fit by either the power law or bremsstrahlung model. Seven of the remaining 27 sources were clearly not within the optical extent of the host galaxy. Of the remaining sources excluded from classification as a low-hard

state object IC 2574 XMM1 was better fit with a bremsstrahlung model (with $\Delta\chi^2 = 13.4$). In an additional observation of the source NGC 4258 XMM2, a simple power law model is not an adequate fit to the data (while the X-ray luminosity of the source is below the formal ULX range of $L \geq 3 \times 10^{39}\,\mathrm{erg\,s^{-1}}$ in both observations). For the remaining sources, NGC 247 XMM2 and NGC 253 XMM2, there was sufficient doubt on the spectral form where the bremsstrahlung and power law model as well as the addition of a thermal component all yielded adequate fits to the spectra. Therefore, we excluded these sources from a classification, noting the ambiguity of the model fits for these sources.

Table 2.3: Bolometric Luminosities of ULX sources

Source	$L_{cutoffpl}$[a]	L_{bol}	[b] M_{Edd}[c]	class[d]
NGC247 XMM1	13.4258	7.07734	54	HS ULX
NGC253 XMM1	9.31469	2.44574	19	HS ULX
NGC253 XMM2	4.3701	2.15292	17	HS ULX
NGC253 XMM6	5.05828	3.92514	30	HS ULX
NGC1313 XMM3	37.0364	27.9692	215	HS ULX
NGC1313 XMM4	1.50345	···	116	LS IMBH cand.
IC0342 XMM1	14.1215	···	1086	LS ULX
IC0342 XMM2	19.8129	···	1524	LS ULX
IC0342 XMM3	114.015	95.4068	734	HS ULX
MRK71 XMM1	0.2993	···	23	LS IMBH cand.
NGC2403 XMM1	4.1497	2.14873	17	HS ULX
NGC2403 XMM4	0.57068	···	44	LS IMBH cand.
Holmberg II XMM1	0.88906	···	68	LS IMBH cand.

Continued on Next Page...

Table 2.3 – Continued

Source	$L_{cutoffpl}$[a]	L_{bol}	[b] M_{Edd}[c]	class[d]
···	16.8335	11.4543	88	HS ULX
Holmberg I XMM2	10.5158	···	809	LS ULX
M81 XMM1	15.7004	3.17932	24	HS ULX
Holmberg IX XMM1	31.0582	28.1445	216	HS ULX
NGC4214 XMM1	0.26699	···	21	LS IMBH cand.
NGC4258 XMM3	0.46503	···	36	LS IMBH cand.
NGC4395 XMM1	9.04609	2.94683	23	HS ULX
NGC4449 XMM2	2.48586	···	191	LS IMBH cand.
NGC4490 XMM1	16.8513	3.21972	25	HS ULX
NGC4490 XMM2	7.36612	4.51554	35	HS ULX
NGC4490 XMM3	240.653	176.04	1354	HS ULX
NGC4490 XMM4	1.66829	···	128	LS IMBH cand.
NGC4490 XMM5	12.7136	···	978	LS ULX
NGC4631 XMM1	10.6527	8.59661	66	HS ULX
NGC4736 XMM1	31.6561	27.3664	211	HS ULX
NGC4945 XMM3	0.44985	···	35	LS IMBH cand.
NGC5204 XMM1	22.4756	2.20492	17	HS ULX
NGC5204 XMM2	5.57769	···	429	LS ULX
M51 XMM2	4.25898	3.57502	28	HS ULX
M51 XMM3	2.10133	···	162	LS IMBH cand.
M51 XMM4	2.56064	···	197	LS IMBH cand.
M51 XMM6	46.7642	39.5189	304	HS ULX
M101 XMM1	8.04916	7.68224	59	HS ULX

Continued on Next Page...

Table 2.3 – Continued

Source	$L_{cutoffpl}$[a]	L_{bol}	[b] M_{Edd}[c]	class[d]
M101 XMM2	7.54268	4.96709	38	HS ULX
M101 XMM3	10.9792	1.03659	8	HS ULX
NGC5408 XMM1	20.9211	11.5369	89	HS ULX
Circinus XMM1	70.3579	56.1033	432	HS ULX
Circinus XMM2	208.746	0.69929	5	HS ULX
Circinus XMM3	771.157	0.212957	2	HS ULX

[a] estimation of the bolometric luminosity, determined with an exponential cut-off in the power law at high energy (see text)

[b] bolometric luminosity estimate for high-state ULXs where the power law is cut at twice kT_{in} (see text); units for both luminosity measurements in 10^{39} erg s^{-1}

[c] mass computed for objects radiating at $0.1 \times L_{Edd}$ (low-state objects) or L_{Edd} (high-state objects; using L_{bol}), in units of $M_{\odot}$

[d] classification based on the criteria set forward in the text: high-state ULX (HS ULX), low-state ULX (LS ULX), and low-state IMBH candidate (low-state object with $10^{38}\,\mathrm{erg\,s^{-1}} < L_{bol} < 3 \times 10^{39}\,\mathrm{erg\,s^{-1}}$)

For those sources we classify as ULXs, we include computed bolometric luminosities in Table 2.3. To compute the bolometric luminosities for these ULX sources, we used the exponentially cutoff power law spectrum of Magdziarz & Zdziarski (1995), model `cutoffpl` in `XSPEC`, with a cutoff energy of 10 keV. From observational studies of Galactic X-ray binaries, it has been observed that low-state objects have spectra that cut-off at high energies

($\geq 10 - 200$ keV) (Zdziarski & Gierliński 2004). Thus we chose the exponential model `cutoffpl` over a simple power law. This also minimizes the total luminosity for flat power law sources. We computed an unabsorbed bolometric flux in the $0.1 - 100$ keV range through use of the `dummyresp` command (which extends the model beyond the observation's energy range). The luminosity was then computed using the distances listed in Table 2.1. We quote these values as $L_{cutoffpl}$ (the luminosity obtained from extrapolating the power law portion of the spectrum as an exponentially cut-off power law) in Table 2.3. We note that these values represent an upper limit on the bolometric luminosity for steep power law ($\Gamma > 2$) objects, since we would expect the power law component to cutoff at some low energy. However, for shallow spectrum ($\Gamma < 2$) sources $L_{cutoffpl}$ is a lower limit. This is because, schematically, a steep power law diverges at low energies while a shallow power law diverges at high energies.

2.3.2 Two-Component Sources

For a number of sources, we found that an improvement in reduced χ^2 was achieved through fitting their spectra with an absorbed two-component blackbody and power law model. We chose a simple blackbody model over the multicomponent disk model, `diskbb`, for purely schematic reasons. Namely, observations of galactic X-ray binary systems were fit with blackbody models in the 1980s, when the signal-to-noise of these objects was comparable to that for our *XMM-Newton* data for ULX sources. We also note that the `diskbb` model does not give an entirely accurate physical description of the data as it neglects the effects of general relativity. As a schematic model, the blackbody model is simpler than `diskbb`, with the same number of degrees of freedom. In addition, for low temperatures both models yield virtually identical temperatures. For this study,

we chose the simpler model. We defer to Chapter 3 a discussion of the different models for the thermal component.

Table 2.4: *XMM-Newton* best fit: blackbody and power law fits

Source	n_H [a]	kT (keV)	Γ	χ^2/dof	$\Delta\chi^2$ [b]	F_X [c]	L_X [d]
NGC247 XMM1	$4.1^{+1.9}_{-1.5}$	$0.12^{+0.03}_{-0.02}$	$4.18^{+1.79}_{-2.52}$	86.5/93	25.7	6.2	7.1
NGC253 XMM1	$2.7^{+0.4}_{-0.4}$	$0.80^{+0.12}_{-0.09}$	$1.74^{+0.17}_{-0.14}$	225.9/230	36.7	2.7	4.5
...	$7.3^{+1.1}_{-0.9}$	$1.14^{+0.07}_{-0.10}$	$2.54^{+0.27}_{-0.22}$	567/580	44.6	3.4	5.7
NGC253 XMM2 (obs 2)	$2.0^{+0.3}_{-0.2}$	$0.71^{+0.10}_{-0.10}$	$2.14^{+0.05}_{-0.08}$	460.3/498	47.1	1.6	2.7
NGC253 XMM3	$3.1^{+4.8}_{-0.5}$	$0.75^{+0.13}_{-0.10}$	$2.47^{+2.99}_{-0.41}$	68.5/82	23.4	0.60	1.0
...	$3.2^{+0.7}_{-0.5}$	$0.67^{+0.13}_{-0.09}$	$2.07^{+0.14}_{-0.20}$	347.4/407	34.4	0.80	1.3
NGC253 XMM4	$20^{+10.8}_{-7.6}$	$0.11^{+0.03}_{-0.03}$	$2.51^{+0.49}_{-0.30}$	66.7/57	6.9	15	25
...	$4.5^{+1.2}_{-1.9}$	$0.09^{+0.02}_{-0.01}$	$2.33^{+0.27}_{-0.22}$	309.3/291	12.1	1.4	2.2
NGC253 XMM5	$1.5^{+7.2}_{-1.5}$	$0.96^{+0.24}_{-0.32}$	$2.43^{+3.06}_{-1.36}$	26.5/23	5.3	0.26	0.43
...	$4.6^{+1.1}_{-0.7}$	$0.16^{+0.02}_{-0.03}$	$1.95^{+0.14}_{-0.11}$	223.7/296	60.1	1.4	2.2
NGC253 XMM6	$6.3^{+2.1}_{-1.1}$	$0.12^{+0.02}_{-0.02}$	$2.26^{+0.18}_{-0.12}$	417.9/407	17.1	1.9	3.1
NGC253 XMM7	$6.3^{+0.9}_{-1.1}$	$0.69^{+0.11}_{-0.12}$	$2.40^{+0.41}_{-0.17}$	335.8/339	21.2	1.1	1.8
NGC300 XMM1	$1.7^{+0.20}_{-0.30}$	$0.98^{+0.14}_{-0.10}$	$3.41^{+0.06}_{-0.26}$	443.7/420	26.1	1.3	1.0
NGC300 XMM2	$3.8^{+1.7}_{-1.4}$	$0.09^{+0.01}_{-0.01}$	$2.87^{+0.34}_{-0.38}$	102.6/97	31.34	1.1	0.86
NGC300 XMM3	$4.4^{+1.0}_{-0.8}$	$0.04^{+0.25}_{-0.01}$	$1.98^{+0.1}_{-0.1}$	87.7/79	14.2	1.2	0.93
NGC300 XMM6	$2.3^{+2.6}_{-1.3}$	$0.84^{+0.25}_{-0.19}$	$4.9^{+1.97}_{-0.7}$	34.6/35	13	0.27	0.20
NGC1313 XMM1	$3.0^{+1.2}_{-0.9}$	$0.13^{+0.03}_{-0.02}$	$1.75^{+0.14}_{-0.11}$	194.1/201	35.4	0.64	1.3
NGC1313 XMM2	$3.1^{+0.4}_{-0.3}$	$0.16^{+0.04}_{-0.02}$	$2.27^{+0.10}_{-0.14}$	425.2/419	38.9	2.0	4.2
NGC1313 XMM3	$6.2^{+0.8}_{-0.6}$	$0.11^{+0.01}_{-0.01}$	$2.76^{+0.10}_{-0.11}$	441.7/424	336.6	10	22
IC0342 XMM3	$9.7^{+1.8}_{-2.1}$	$0.09^{+0.02}_{-0.01}$	$2.69^{+0.16}_{-0.23}$	129.5/107	56.3	31	56.4
NGC1705 XMM1	$0.29^{+0.39}_{-0.27}$	$1.01^{+0.41}_{-0.29}$	$2.31^{+0.89}_{-0.48}$	53/85	8.9	0.10	0.44
NGC1705 XMM3	< 1.44	$1.07^{+0.20}_{-0.15}$	$2.23^{+0.70}_{-0.56}$	69.8/65	11.1	0.15	0.48
NGC2403 XMM1	$2.3^{+1.2}_{-1.1}$	$0.66^{+0.16}_{-0.18}$	$2.18^{+0.41}_{-0.59}$	81.4/79	10.8	1.99	3.1
NGC2403 XMM2	$1.8^{+0.8}_{-0.6}$	$0.62^{+0.16}_{-0.11}$	$1.95^{+0.26}_{-0.42}$	163.1/151	16.4	1.0	1.6
NGC2403 XMM3	$1.7^{+1.1}_{-0.8}$	$0.74^{+0.23}_{-0.21}$	$2.15^{+0.66}_{-0.40}$	84.2/105	8.4	0.64	1.1
Holm II XMM1(obs 1)	$1.6^{+0.1}_{-0.2}$	$0.14^{+0.02}_{-0.01}$	$2.35^{+0.05}_{-0.11}$	997.5/976	136.7	12	10
M81 XMM1	$3.3^{+0.17}_{-0.08}$	$0.90^{+0.03}_{-0.03}$	$2.52^{+0.03}_{-0.04}$	1273.7/1243	533.1	4.5	7.0
...	$3.5^{+0.4}_{-0.6}$	$1.13^{+0.13}_{-0.14}$	$2.34^{+0.29}_{-0.36}$	203.5/204	21.4	4.8	7.4
M81 XMM2	$7.4^{+0.5}_{-0.7}$	$0.1^{+0.004}_{-0.004}$	$2.87^{+0.16}_{-0.17}$	833.9/616	524.3	13	22
M81 XMM4	$1.1^{+1.6}_{-1.0}$	$2.51^{+1.11}_{-0.73}$	$2.31^{+1.22}_{-1.05}$	48.9/50	28.2	0.43	0.70
M81 XMM5	$0.15^{+0.69}_{-0.13}$	$0.62^{+0.19}_{-0.11}$	$1.26^{+0.22}_{-0.20}$	89/80	8.5	0.38	0.59

Continued on Next Page...

Table 2.4 – Continued

Source	n_H [a]	kT (keV)	Γ	χ^2/dof	$\Delta\chi^2$ [b]	F_X [c]	L_X [d]
Holm IX XMM1	$2.1^{+0.2}_{-0.2}$	$0.17^{+0.02}_{-0.02}$	$1.72^{+0.04}_{-0.03}$	866.6/878	134.3	10	16
NGC4258 XMM1	$0.38^{+0.96}_{-0.3}$	$0.54^{+0.17}_{-0.08}$	$1.51^{+0.4}_{-0.4}$	91.1/76	10.3	0.34	2.1
NGC4258 XMM2 (obs 1)	$1.9^{+2.4}_{-0.4}$	$0.78^{+0.12}_{-0.13}$	$2.02^{+0.65}_{-1.8}$	73.4/61	24.1	0.31	1.9
NGC4395 XMM1	$2.0^{+0.08}_{-0.07}$	$0.14^{+0.02}_{-0.02}$	$3.44^{+0.54}_{-0.56}$	168.2/154	26.9	1.4	2.7
NGC4449 XMM1	$8.7^{+4.8}_{-2.1}$	$0.19^{+0.13}_{-0.07}$	$2.21^{+0.33}_{-0.29}$	111.2/116	4.3	1.56	1.8
NGC4449 XMM3	$3.5^{+1.3}_{-0.9}$	$0.15^{+0.03}_{-0.03}$	$2.52^{+0.36}_{-0.39}$	119.9/87	34.1	1.1	1.3
NGC4490 XMM1	$5.8^{+2.96}_{-2.96}$	$0.77^{+0.08}_{-0.095}$	$2.89^{+1.77}_{-0.61}$	66.5/63	35	0.88	6.4
NGC4631 XMM1	$3^{+0.9}_{-0.5}$	$0.12^{+0.03}_{-0.02}$	$2.12^{+0.03}_{-0.02}$	371.3/345	12.1	0.96	6.5
NGC4631 XMM2	$2.3^{+1.4}_{-0.3}$	$0.18^{+0.05}_{-0.06}$	$1.80^{+0.12}_{-0.09}$	107.4/97	12.1	0.25	1.7
NGC4631 XMM3	$1.1^{+1.1}_{-0.8}$	$1.01^{+0.12}_{-0.1}$	$2.45^{+1}_{-0.62}$	127.1/96	18.9	0.15	1.0
NGC4945 XMM1	$3.5^{+2.1}_{-1.1}$	$0.77^{+0.27}_{-0.10}$	$1.60^{+0.40}_{-0.31}$	96.1/120	20	0.59	0.68
NGC4945 XMM2	$3.2^{+1.1}_{-0.7}$	$1.15^{+0.28}_{-0.33}$	$1.80^{+0.20}_{-0.30}$	105.8/113	8.7	0.66	0.76
NGC4945 XMM4	$4.0^{+2.0}_{-1.1}$	$0.61^{+0.10}_{-0.10}$	$2.82^{+1.06}_{-0.58}$	58.4/60	17.1	0.38	0.44
NGC5204 XMM1	$0.66^{+0.35}_{-0.08}$	$0.16^{+0.02}_{-0.03}$	$1.92^{+0.12}_{-0.06}$	543.0/559	49.1	1.98	5.6
...	$1.1^{+0.08}_{-0.14}$	$0.16^{+0.02}_{-0.02}$	$2.03^{+0.12}_{-0.12}$	461.4/496	71.6	2.92	8.0
M51 XMM1	$0.95^{+1.10}_{-0.18}$	$0.16^{+0.03}_{-0.05}$	$2.15^{+0.42}_{-0.17}$	97/80	13.4	0.31	1.9
M51 XMM5	$10.4^{+1.7}_{-3.7}$	$0.078^{+0.01}_{-0.01}$	$2.26^{+0.26}_{-0.25}$	59.8/70	196.2	220	1900
M83 XMM4	$1.77^{+3.9}_{-1.77}$	$0.54^{+0.18}_{-0.09}$	$1.61^{+0.96}_{-0.31}$	84.8/89	6.6	0.2	0.92
M101 XMM1	$0.22^{+0.12}_{-0.15}$	$0.21^{+0.03}_{-0.04}$	$1.42^{+0.14}_{-0.05}$	249.9/231	53.1	0.45	2.9
M101 XMM2	$1.6^{+0.46}_{-0.21}$	$0.76^{+0.14}_{-0.10}$	$1.88^{+0.25}_{-0.11}$	251.6/261	37.2	0.7	4.6
NGC5408 XMM1	$0.9^{+0.21}_{-0.16}$	$0.14^{+0.01}_{-0.01}$	$2.71^{+0.16}_{-0.20}$	316.4/337	80.4	3.97	10.9
CIRCINUS XMM1	$10.1^{+1.2}_{-1.2}$	$0.10^{+0.01}_{-0.01}$	$2.30^{+0.08}_{-0.08}$	749.4/861	13.5	12	23
CIRCINUS XMM2	$11.2^{+2.4}_{-1.7}$	$0.53^{+0.03}_{-0.03}$	$4.71^{+0.94}_{-0.49}$	438.5/430	79.4	5.6	10.7
CIRCINUS XMM3	$13.5^{+5.5}_{-5.6}$	$0.67^{+0.10}_{-0.08}$	$5.77^{+2.24}_{-2.3}$	269.3/260	15.9	7.6	14.5

[a] total column density in units of 10^{21} cm^{-2}

[b] improvement in χ^2 over the single-component power law model

[c] unabsorbed flux in the 0.3–10 keV band in units of 10^{-12} erg cm^{-2} s^{-1}

[d] unabsorbed luminosity in the 0.3–10 keV band, using the distances quoted in Table 2.1, in units of 10^{39} erg s^{-1}

In Table 2.4 we present the results for the sources which are fit significantly better by the two-component model, these are sources where the improvement in χ^2 is greater than 8 (determined from our simulations in Appendix B). We include in Table 2.4 the improvement in χ^2 of the two-component fit over the simple power law. We include the power law best fits to these sources in the appendix for comparison with other analyses. In Figure 2.3, we show the PN spectrum of the two-component model fit to Holmberg II XMM1. For this source, the two component fit was clearly a better fit with $\Delta\chi^2 = 136.7$. In Figure 2.4, we also supply the ratio of data to model points for the two-component and single-component fit to this source. Here, it is clear that the disk model is a much better fit, particularly at energies below 2 keV.

In order to determine whether the blackbody component is statistically significant for all of the sources fit with a two-component model, we simulated spectra based on accurate modeling of some of the brightest sources: NGC 247 XMM1, NGC 5408 XMM1, and Holmberg II XMM1. These sources span the observed range of the ratios of the blackbody to power law component and thus represent those from our sample with a weak blackbody relative to the power law component, intermediate case, and a strong blackbody, respectively. Our simulations are described in full in Appendix B. We found that, using a $\Delta\chi^2 > 8$ criterion, which corresponds to the 99% significance level as according to the F-test for the addition of two extra parameters, we can readily detect the strong and intermediate thermal components in all spectra with more than 400 counts. The weak thermal emission cannot be detected in 400 count spectra, but is readily detected in 2000 count spectra. This gives us confidence that our results are statistically meaningful.

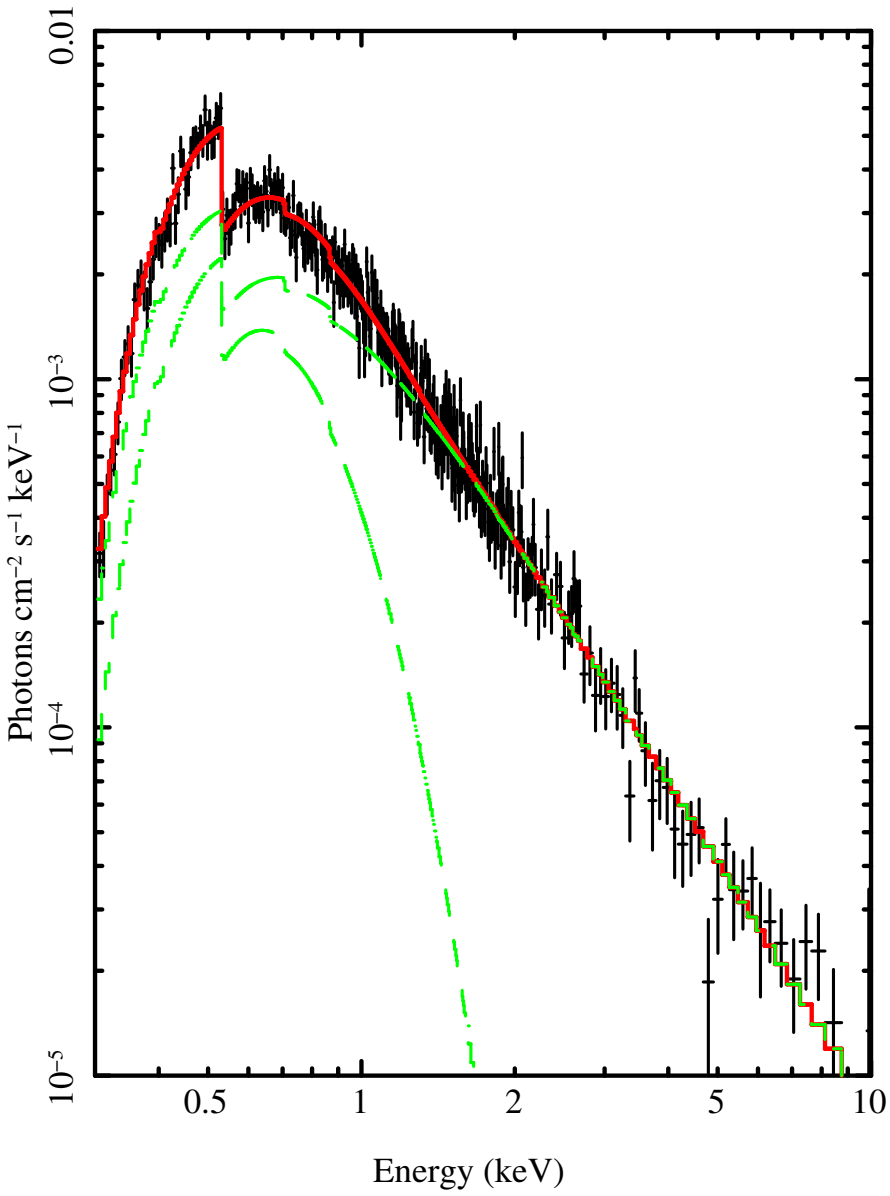

Figure 2.3: Shown is the unfolded pn X-ray spectrum of a two component model source, Holmberg II XMM1. The two-component model is shown in red. Both the absorbed power law and absorbed blackbody contributions are shown in green. This represents a source with an intermediate strength blackbody component.

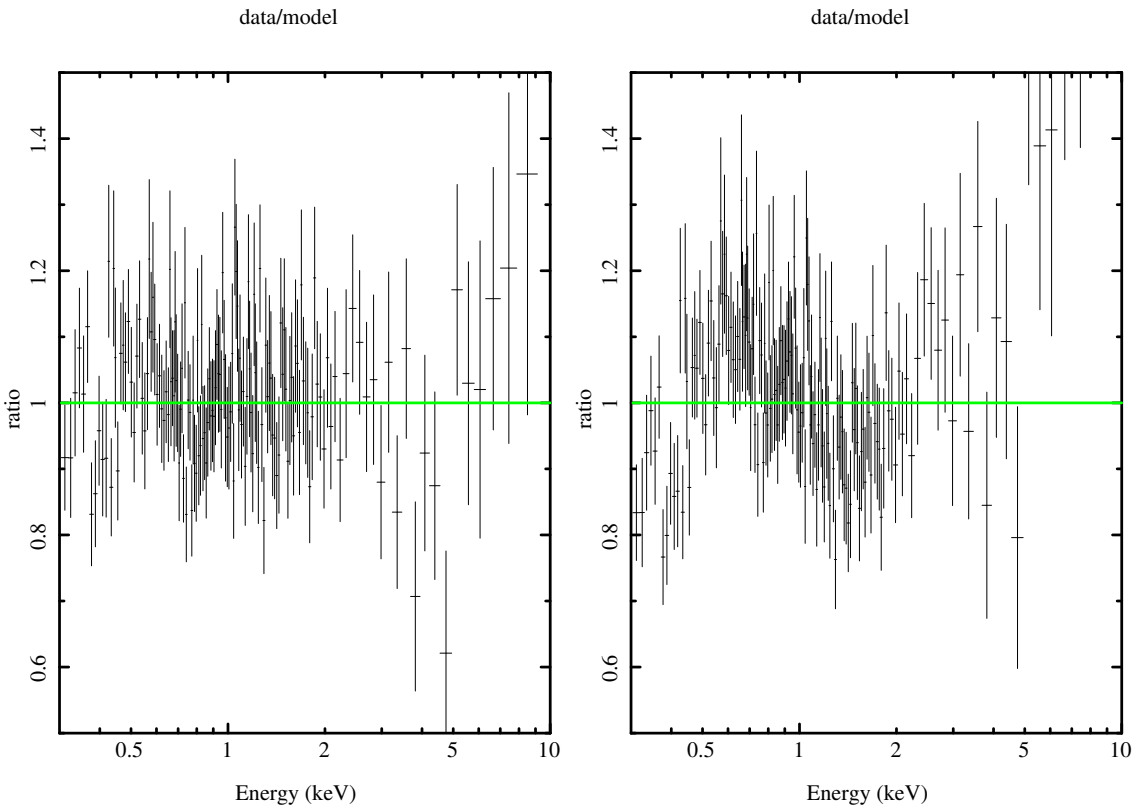

Figure 2.4: Shown is the ratio of the data to the model for the absorbed power law and blackbody model (left) and the absorbed power law model (right) for Holmberg II XMM1. Clearly, the two-component model is the better fit.

"High-State ULXs"

Of the sources in Table 2.4, we classified high-state (or thermal dominated) ULX sources based on three criteria: (1) spectra characterized by an absorbed power law and blackbody model, (2) luminosity, and (3) X-ray source within the optical extent of the host galaxy. The luminosity criteria required that these sources have unabsorbed luminosities $L_X \geq 3 \times 10^{39}\,\mathrm{erg\,s^{-1}}$ (we used $L_X = 2.7 \times 10^{39}\,\mathrm{erg\,s^{-1}}$ as our hard cutoff). If the sources are radiating at the Eddington luminosity, this cutoff luminosity corresponds to objects with masses greater than $20\,M_\odot$.

From Table 2.4, 27 observations are recorded with $L_X > 2.7 \times 10^{39}\,\mathrm{erg\,s^{-1}}$. The addition of a thermal component to these sources is statistically significant over a

pure power law model. Of the 27 observations, 3 correspond to multiple observations of a single source. From an analysis of the DSS images, all 24 of these sources are within the optical extent of their host galaxies. However, M51 XMM5 appears to be coincident with the center of its host, a dwarf companion galaxy to M51. The location, coupled with the high luminosity ($L_X = 1.9 \times 10^{42}\,\mathrm{erg\,s^{-1}}$) leads us to classify this source as an AGN. We also excluded two sources (NGC 1313 XMM2 and M81 XMM2) from our sample of high/soft state ULXs due to their previous identification as supernovae. Of the remaining 21 sources, NGC 253 XMM4 had a luminosity of $2.5 \times 10^{40}\,\mathrm{erg\,s^{-1}}$ in one observation and $2.2 \times 10^{39}\,\mathrm{erg\,s^{-1}}$ in a second. This significant change in luminosity, with one observation below our luminosity cutoff and another a factor of ≈ 10 higher than the other, led us to exclude this source as a high/soft state ULX. It is likely that this source is a stellar mass X-ray binary within its host galaxy, where one of the observations captured the source in an outburst.

In Table 2.5, we list sources that have $\Delta\chi^2$ values less than 8 for a single observation. Most of these sources have weak blackbody normalizations compared to the power law normalization. We classify these sources as being well-fit by a two-component model while acknowledging the uncertainty in the fit as determined by the simulations. The addition of the thermal component is not significant enough for these sources to be classified with certainty in either Table 2.2 or 2.4. The simple power law fits for these sources are included with those for sources in Table 2.4 in Table B.3. We note that due to their high luminosity we included six of these sources (NGC 4490 XMM2, NGC 4490 XMM3, NGC 4736 XMM1, M51 XMM2, M51 XMM6, and M101 XMM3) with uncertain fit parameters as ULX high-state sources. Two of these sources (NGC 4490 XMM3 and M51 XMM6) had unabsorbed luminosities > 10 times the $3 \times 10^{39}\,\mathrm{erg\,s^{-1}}$ cutoff used

Table 2.5. *XMM-Newton* two-component fits for sources with large uncertainty

Source	n_H[a]	kT (keV)	Γ	χ^2/dof	$\Delta\chi^2$[b]	F_X[c]	L_X[d]
NGC300 XMM5	$0.41^{+0.60}_{-0.30}$	$1.06^{+0.37}_{-0.20}$	$2.78^{+0.61}_{-0.65}$	46.6/53	7.6	0.17	0.13
NGC1705 XMM2	$0.96^{+0.97}_{-0.32}$	$0.23^{+0.10}_{-0.11}$	$1.60^{+1.97}_{-0.27}$	85.5/74	6.5	0.09	0.27
Holm I XMM1	$0.4^{+0.5}_{-0.3}$	$1.97^{+0.66}_{-0.89}$	$2.46^{+0.44}_{-0.40}$	97.4/93	5.4	0.6	0.93
M81 XMM3	$3.7^{+2.4}_{-2.1}$	$0.11^{+0.05}_{-0.02}$	$1.69^{+0.27}_{-0.33}$	77.1/78	4.25	0.53	0.82
Sextans A XMM1	$0.4^{+0.7}_{-0.1}$	$1.05^{+2.3}_{-0.07}$	$2.6^{+0.8}_{-0.2}$	269.1/271	2.3	0.60	0.14
NGC4214 XMM2	$1.8^{+1.9}_{-0.6}$	$0.81^{+0.56}_{-0.21}$	$3.95^{+1.81}_{-1.05}$	46.4/44	4.5	0.4	0.35
NGC4395 XMM3	$0.5^{+0.9}_{-0.3}$	$1.10^{+0.67}_{-0.18}$	$2.66^{+1.05}_{-0.77}$	52/56	3.9	0.29	0.56
NGC4490 XMM2	$4.4^{+1.9}_{-1.9}$	$0.60^{+0.20}_{-0.12}$	$2.13^{+0.50}_{-0.70}$	42.4/54	7.1	0.65	4.7
NGC4490 XMM3	$13^{+9.6}_{-2.5}$	$0.09^{+0.02}_{-0.02}$	$3.21^{+0.52}_{-0.17}$	72.1/78	4.6	12	87.4
NGC4736 XMM1	$6.3^{+3.0}_{-3.7}$	$0.08^{+0.03}_{-0.02}$	$2.41^{+0.34}_{-0.27}$	54.9/51	7.9	8.1	17.9
M51 XMM2	$1.3^{+0.6}_{-0.5}$	$0.26^{+0.07}_{-0.08}$	$1.80^{+0.61}_{-0.92}$	70.7/68	4.5	0.36	3.0
M51 XMM6	$8.2^{+3.5}_{-5.6}$	$0.08^{+0.05}_{-0.02}$	$3.0^{+0.37}_{-0.43}$	36.9/41	4.07	5.6	35
M51 XMM7	$2.8^{+3.4}_{-2.1}$	$0.10^{+0.03}_{-0.03}$	$1.97^{+0.43}_{-0.30}$	31.7/29	6.1	0.26	1.6
M83 XMM1	$1.6^{+0.48}_{-0.45}$	$0.74^{+0.23}_{-0.26}$	$2.58^{+0.60}_{-0.24}$	177.7/209	4.7	0.63	2.5
M101 XMM3	$1.98^{+1.0}_{-0.61}$	$0.63^{+0.22}_{-0.20}$	$2.93^{+0.15}_{-0.26}$	145.5/131	3.4	0.56	3.7
M101 XMM4	$1.8^{+0.17}_{-0.15}$	$0.54^{+0.11}_{-0.07}$	$2.22^{+0.12}_{-0.08}$	158.2/138	7.5	0.34	2.2
M101 XMM5	$1.3^{+1.2}_{-0.2}$	$0.18^{+0.05}_{-0.06}$	$1.95^{+0.3}_{-0.22}$	45.1/44	2.8	0.13	0.85

[a]total column density in units of 10^{21} cm^{-2}

[b]improvement in χ^2 over the single-component power law model

[c]unabsorbed flux in the 0.3-10 keV band in units of 10^{-12} erg cm^{-2} s^{-1}

[d]unabsorbed luminosity in the 0.3-10 keV band, using the distances quoted in Table 2.1, in units of 10^{39} erg s^{-1}

for high-state ULX classification. The other four sources had luminosities above the threshold, as well as weak blackbody components compared to the power law (see the Appendix B for simulations). We used these points to justify including these sources with the Table 2.4 sources in the following discussions with the proviso that their spectral fits do not indicate absolutely the necessity of the additional thermal component. For this reason, we denote these sources with a special symbol (a circle) in subsequent figures while including them as "high-state" ULX objects.

For our ULX sources modeled by a combined blackbody and exponentially cutoff power law, we computed bolometric luminosities using two methods. The first method is recorded as $L_{cutoffpl}$ in Table 2.3. We computed the flux from 0.1 - 100 keV using an unabsorbed blackbody and exponentially cutoff power law model using the XSPEC command `dummyresp`. For the second method, recorded as L_{bol} in Table 2.3, we estimate a more accurate bolometric luminosity calculated from the flux in the range of $2\times$ kT – 100 keV where kT is the blackbody temperature obtained from the model. In Galactic X-ray binary systems, the power law component of the X-ray spectrum is believed to be from Comptonization in a corona. The photons supplying this energy originate from the blackbody continuum emanating from the accretion disk. Thus, a natural cutoff for this power law component occurs at the peak emission of the blackbody (which is approximately $3\times$ kT). The estimated values (obtained from cutting off the combined unabsorbed blackbody and cutoff power law model at the value $2\times$ kT) differ with regard to the full estimate (flux from the fully integrated blackbody added to the separate flux from the cutoff power law from $3\times$ kT to 100 keV) depending on the normalization factors used (for both the blackbody temperature and the spectral index Γ). Choosing three sources displaying a range of blackbody to power law strength (Holmberg II XMM1, NGC 253 XMM1, and IC 0342 XMM3) we found that the estimated values were within 88.3, 95.1, and 96.8% of the more complete estimation. Given their close proximity (within approximately 90%) we quote these estimated values as a good approxmiation to the bolometric luminosity.

We note that our bolometric luminosities for all of the classified ULX sources, on average, are a factor of 1.08 greater than the X-ray luminosities in the 0.3 – 10 keV band for the objects best fit by a combined blackbody and power law. Thus, to good approximation, the X-ray luminosity is the bolometric luminosity.

However, for the objects best fit by a simple power law (low-state ULX sources), the average bolometric luminosity is roughly a factor of 7 greater than the X-ray luminosity in our band. This average is dominated by the steep power law objects, in particular Holmberg II XMM1 ($\Gamma = 3.09$), since the total luminosity depends sensitively on the lowest energy used. Excluding this object, we get an average bolometric luminosity that is 2.8 times the X-ray flux and more indicative of the general properties of these power law-fit objects.

2.3.3 Additional Sources

In addition, in this large sample of point sources, we came across a number of objects whose spectra were not well fit by the models we employed. These sources have luminosities exceeding $L_X \approx 10^{38}$ erg s^{-1}, if they are associated with the host galaxy, and are placed in Tables 2.2 and 2.4 as well as Appendix B. These sources include two supersoft sources, one possible AGN, and three sources well fit with additional absorption models (including a partial covering model and a model of hot gas). We briefly describe these sources in the appendix.

2.4 Discussion

We have determined best-fit spectral parameters of the bright X-ray sources in 32 nearby galaxies. In choosing three "standard" models for our study, we hoped to accurately separate high and low state ULXs from other types of luminous X-ray sources. We specifically chose to fit the data with the bremsstrahlung model in order to identify neutron star X-ray binaries within our sample. The models we used are purely schematic, and they do not physically explain the phenomena occurring, but are standard and qualitatively simple models often used to fit the

spectra of Galactic X-ray binaries.

We cross-referenced the X-ray positions of our sources with both NED and SIMBAD in order to identify known supernovae, galaxies, and stars. In addition, we examined the DSS optical images to place the position of our sources within their respective galaxies. Such analysis aimed to minimize contamination of our sample of ULXs with bright background and foreground sources.

Further, we examined *XMM-Newton's* Optical Monitor data in the visual bands (U, B, V). The *XMM-Newton* PPS contain point source detection files for the OM data. We overlaid these point source detections with X-ray contour maps in order to determine the **brightest possible** optical count rates for the X-ray sources, which were then converted into fluxes using the OM calibration documentation. In Figure 2.5, we plot the distribution of the logarithm of the X-ray to optical flux for the brightest possible optical counterpart inside the *XMM-Newton* error circle. Only 13 of the 32 host galaxies had visible band OM data during the observations. Of these 13 galaxies, 40 of the X-ray sources were in the range of the OM data and only 14 were coincident with an optical point source. Therefore, the majority of our sources have X-ray/optical flux ratios that are **larger** than those displayed. Figure 2.5 illustrates the lowest possible X-ray/optical flux ratios and also, by the sparsity of sources included in the diagram, it illustrates the fact that a majority of the sources have no obvious optical counterpart in the OM data, with a limiting magnitude of V ≈ 20 (Kuntz et al. 2008), and thus have very large X-ray/optical flux ratios. We estimate the point source detection limit of the OM U filter as approximately 1.24×10^{-14} erg cm^{-2} s^{-1}. For an unabsorbed X-ray flux of 1.0×10^{-12} erg cm^{-2} s^{-1}, typical of objects with $L_X \approx 2 \times 10^{38}$ erg s^{-1} located at a distance of 8 Mpc, this corresponds to $\log(f_x/f_{opt}) = 1.9$. Therefore, the average value for our sources should fall around 2 or greater. The average distribution

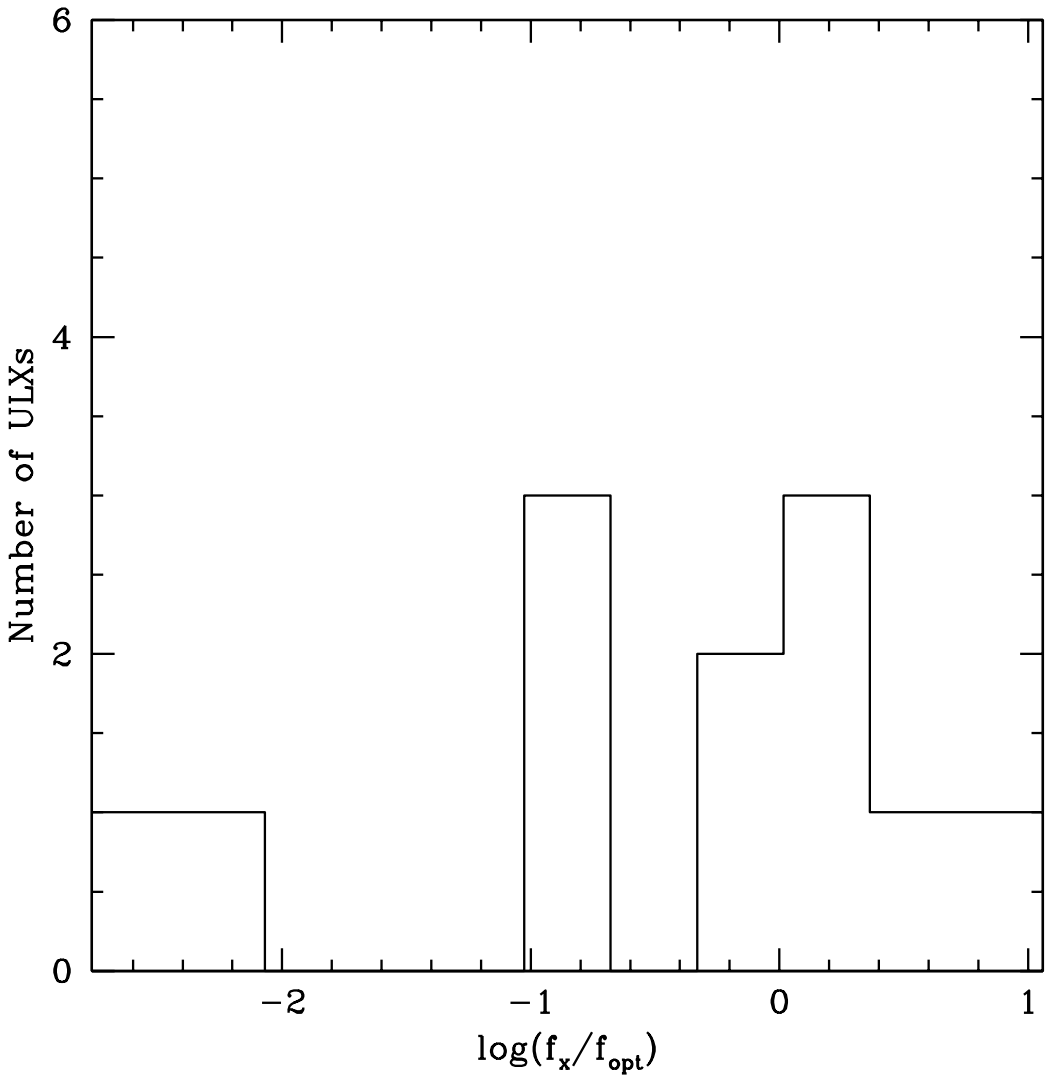

Figure 2.5: The distribution of f_x/f_{opt} for the brightest possible optical point source within the *XMM-Newton* error circle. We define f_x as the unabsorbed X-ray flux in the $0.3 - 10$ keV range and f_{opt} as the optical flux obtained from the U filter of *XMM*'s OM (as described in text). These ratios do not represent the actual f_x/f_{opt} of the sources but are an estimate of the minimum possible value. A majority of the sources had no optical point source within the X-ray contour and thus have ratios of f_x/f_{opt} far higher than those indicated in the plot.

for QSOs and AGN centers around 0 and 0.8 for BL Lacs (Anderson et al. 2003). Our objects have ratios of L_x/L_{opt} at least 10 times higher than those of AGN and 100 times greater than stars.

Recently, Gutiérrez & López-Corredoira (2005) identify six ULXs from the catalog of Colbert & Ptak (2002) as QSOs. They hypothesize that a large number of ULXs may in fact be quasars at higher redshift than their supposed host galaxy. However, unlike the objects studied in Gutiérrez & López-Corredoira (2005), our ULX sources are all spatially coincident with the optical host galaxy. In addition, a majority of our ULXs are not in the proximity of a noticeable optical point source. The X-ray/optical flux ratios of our sources are much larger, on average, than might be expected for a QSO. It is also worth noting that while some cataloged ULXs may be QSOs, optical identifications have been made associating other ULXs with a type B supergiant companion (Kuntz et al. 2005; Liu et al. 2004).

2.4.1 Classification Criteria

The spectral fits indicate that to high statistical probability (see Appendix B) we can distinguish a class of low-state ULXs from the high-state objects. This is assuming, as indicated in the introduction, that ULXs are isotropic emitters with luminosity and spectral form similar to Galactic stellar-mass X-ray binaries. In § 2.3, we stated that our ULX classification depends upon three criteria: (1) spectral form, (2) luminosity, and (3) location of the X-ray source within the optical host galaxy (as determined from the DSS images). We have chosen simple, parametric 'non-physical' models for the spectra because the signal to noise of most of the observations does not allow anything else to be constrained.

Of the sources in Table 2.2, 16 are classified as "low-state" objects or low/hard state ULXs, having unabsorbed luminosities $> 10^{38}\,\mathrm{erg\,s^{-1}}$ and spectra that are well fit by power law models. Throughout this chapter, we use the term low-state ULXs to include "low-state IMBH candidates" (sources with $\mathrm{L}_X \leq 3 \times 10^{39}\,\mathrm{erg\,s^{-1}}$

and spectra well-fit by a simple absorbed power law) and low-state sources with luminosities that clearly classify them as ULX sources ($L_X \geq 3 \times 10^{39}\,\mathrm{erg\,s^{-1}}$). These low-state ULX sources are listed in Table 2.3.

In the Spectral Fitting section, we noted that a power law and high temperature bremsstrahlung model are indistinguishable. Therefore, it is important to consider the luminosity of these sources in the claim that they are not neutron star X-ray binaries accreting at the Eddington luminosity. Of the low-state ULX sources, only two of the 16 sources have bolometric luminosities below the Eddington luminosity of a $3\,M_\odot$ object ($\approx 4 \times 10^{38}\,\mathrm{erg\,s^{-1}}$), corresponding to the maximum mass of a neutron star. All of the sources have values exceeding the Eddington limit for a $2\,M_\odot$ neutron star.

Further, 26 sources have unabsorbed $L_X \geq 3 \times 10^{39}\,\mathrm{erg\,s^{-1}}$, corresponding to $L \approx L_{Edd}$ at $M > 20\,M_\odot$ as expected for "high-state" IMBHs, and spectra that are well fit by combined blackbody and power law models. These are "high-state" objects. The spectral fits for these sources are listed in Tables 2.4 and 2.5. In a statistical sense, we find that the greater the number of counts in the observation the greater our confidence in the thermal component contributing to a better fitting model. We explain our confidence levels obtained from spectral simulations in the appendix.

In addition to these high and low state ULXs, we find a large number of sources best fit by a combined blackbody and power law model but below our threshold of $L_X \approx 3 \times 10^{39}\,\mathrm{erg\,s^{-1}}$ for a high-state ULX (listed in Table 2.4). Many of these sources may be accreting stellar mass black holes with $M < 20\,M_\odot$. Some of these non-"ULX" sources were found away from the optical extent of the targeted galaxy (from our analysis of the DSS images), and therefore may be background AGN.

2.4.2 Low-State ULXs

For Galactic black hole X-ray binaries, spectral indices of low-state (or power law dominated) objects are typically lower than those of high-state objects, with $< \Gamma >_{low} \approx 1.7$ and $< \Gamma >_{high} \approx 2.5$ (Remillard & McClintock 2006). In Figure 2.6, we plot the distribution of the spectral index for both high-state and low-state objects. The spectral index for the high-state objects is the value of Γ from the two-component fit. As in the Galactic sources, it is clear that the spectral indices of the high-state objects are indeed larger. Of further interest, the distribution of spectral index for low-state objects looks remarkably similar to the distribution of spectral index for moderate luminosity quasars, many of which are thought to be the analogs of low-state black holes (Porquet et al. 2004b). This supports the classification of these objects as accreting black holes.

For the high-state objects, we find mean values of $\Gamma = 2.46$, with a root mean square (rms) deviation of $\sigma = 0.12$ and mean $L_X = 1.4 \times 10^{40}\,\mathrm{erg\,s^{-1}}$ with $\log(\sigma) = 1.6$. This calculation excludes the 3 objects with spectral indices greater than 3.5. For the low-state objects, we find mean values of $\Gamma = 2.09$, with a rms deviation of $\sigma = 0.10$, and $L_X = 2.2 \times 10^{39}\,\mathrm{erg\,s^{-1}}$, with $\log(\sigma) = 2.1$. This value of $\Gamma = 2.1$ is softer than the typical hard-state value of ≈ 1.7, but within the $1.5 < \Gamma < 2.1$ range used to classify this state for Galactic X-ray binaries (Remillard & McClintock 2006). Computing a Kolmogorov-Smirnov two-sample test, separating the sources into the category of low-state or high-state, we find a likelihood of approximately 0.03 that the spectral indices belong to the same distribution.

The low/hard X-ray state of X-ray binaries is associated with a low accretion rate from the companion object with $L \leq 0.1\,L_{Edd}$ (Done & Gierliński 2003). There-

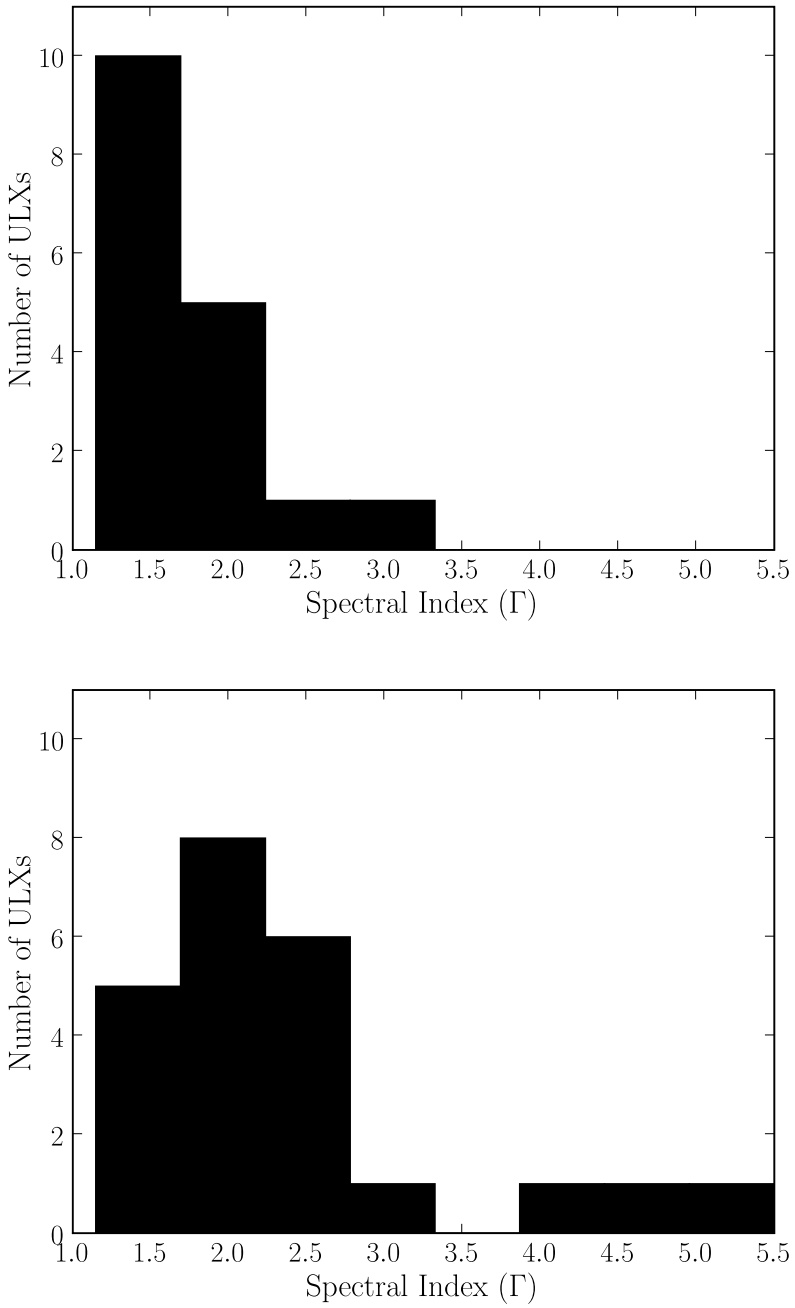

Figure 2.6: Distribution of the spectral indices (Γ) for low-state (top) and high-state (bottom) objects. For Galactic low-state objects, typically $\Gamma \approx 2.0$, similar to our sample, while the high-state objects have a steeper Γ (Remillard & McClintock 2006).

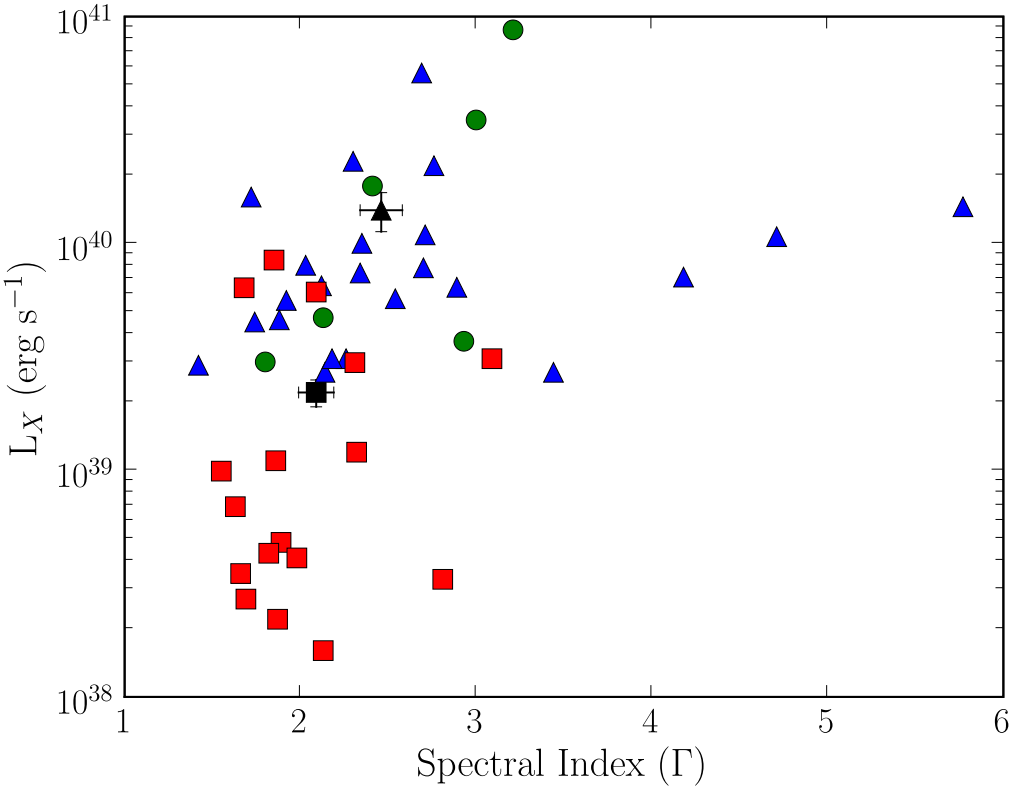

Figure 2.7: Relationship of luminosity vs. spectral index for low-state (rectangle) and high-state (triangle) objects. Sources represented by a circle are those where the $\Delta\chi^2$ value between the two-component and power law fits was very small. As expected from observations of Galactic stellar-mass black hole systems (Remillard & McClintock 2006), the classified low-state ULXs in our sample have, on average, lower X-ray luminosities than the corresponding high-state ULXs. We plot the mean values for both high-state and low-state objects with errorbars indicating the root mean square deviation. The outlying objects with spectral indices greater than 3.5 were not included in the mean or deviation calculations.

fore, on average, we expect the luminosities of the low-state objects to be lower than the high-state objects. Figure 2.7 displays the luminosity of the objects as a function of the spectral index. On average, the highest luminosity low-state objects have luminosities lower than those of the high-state objects.

The lower L_X values of the low-state objects imply that they may indeed be accreting at a lower rate than the high-state objects. This can further be seen in

the bolometric luminosities listed in Table 2.3. If these objects are accreting at a rate similar to Galactic low/hard state black holes ($0.1 \times L_{Edd}$) (Done & Gierliński 2003), we can estimate their masses as

$$\frac{M}{M_{\odot}} = \frac{L_{bol}}{0.1 \times L_{Edd}} \tag{2.1}$$

with L_{Edd} as the Eddington luminosity for a $1\,\mathrm{M}_{\odot}$ object ($1.3 \times 10^{38}\,\mathrm{erg\,s^{-1}}$). Our mass estimations, based upon our limits to the bolometric luminosities, yield masses of $20 - 1500 M_{\odot}$ (see Table 2.3), precisely what we might expect for a population of IMBHs.

2.4.3 High-State ULXs

If the high-state (thermal dominated) ULXs represent a class of intermediate mass black hole systems, their X-ray spectra should be well described by a combined blackbody and power law model. Scaling for the mass of the black hole, we would expect a relationship of $\mathrm{T} \propto \mathrm{M}^{-1/4}$ (for sources radiating near the Eddington limit) between black hole mass and blackbody temperature (Makishima et al. 2000). This would indicate a thermal component of $\sim 100\,\mathrm{eV}$ for masses of $\sim 10^3\,\mathrm{M}_{\odot}$. A few objects have been reported to display this property (Miller et al. 2004a; Roberts et al. 2005). In Figure 2.8, we graph the distribution of the thermal component for our classified high-state objects.

We find that there are two peaks in the distribution among the thermal component, one at approximately 100 eV and another centered close to 1 keV. This could indicate two different classes among the high-state objects. It is possible that those objects with blackbody components near 100 eV are indeed high-state intermediate mass black holes. We note that the soft excess in PG quasars has also been modeled as a blackbody with $\mathrm{kT}_{soft} \approx 100\,\mathrm{eV}$, but it has been suggested that this could be the result of a process not directly related to black hole

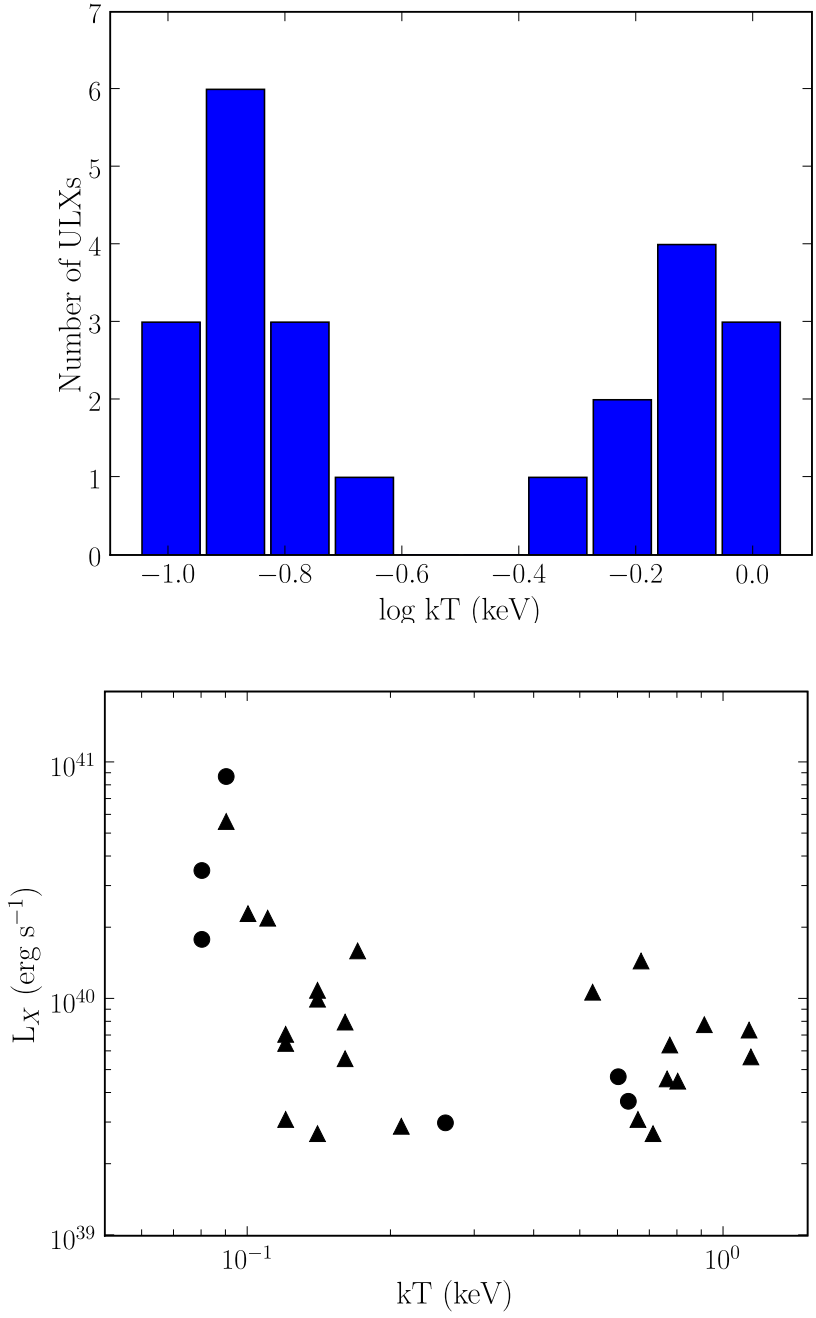

Figure 2.8: (top) Distribution of the blackbody temperature for high-state objects. (bottom) Relationship of blackbody temperature vs. luminosity (in the 0.3-10 keV band) for high-state objects. We see two peaks arise in the distribution, one centered around kT$\approx$ 0.1 and another at kT$\approx$ 1. The peak with a low disk temperature also corresponds to the highest luminosities, suggesting that these may be high-state IMBHs. The sources with higher disk temperature also have lower luminosities. The spectra of these sources were also well fit by an inverse Comptonization model (a model succesfully used to fit some of the Galactic black hole X-ray binaries in the very high state).

accretion (such as the presence of a warm absorber: Gierliński & Done (2004)). Another possible explanation is that the soft component is the result of ionized reflection from the disk (Ross & Fabian 2005). While the possibility exists that the "thermal" component of these 100 eV sources is not directly related to black hole accretion or is related in a "non-thermal" (i.e. ionized reflection) sense, as may be the case with the soft excess in PG quasars, we assume that the soft component for the objects we classify as high-state ULXs originates from a thermal disk. We use this assumption to test the IMBH hypothesis, thus speculation on the nature of the soft component is beyond the scope of this study.

The second peak, centered around 1 keV, has a temperature reminiscent of the Galactic black hole systems in our own galaxy. These systems may thus be stellar-mass black holes accreting matter near the Eddington limit. If this were the case, we would expect the luminosities of the sources exhibiting a higher blackbody temperature to be lower than those with cooler blackbody components. In the second graph of Figure 2.8, we plot the relationship between blackbody temperature and L_X in the 0.3 - 10 keV band. Once again, two groups are seen in the distribution of high-state ULXs. The most luminous objects are those with low blackbody temperatures. On average, the less luminous sources exhibit higher blackbody temperatures. For the sources with $L_X > 10^{40}\,\mathrm{erg\,s^{-1}}$, the mean blackbody temperature is 0.31 keV while the sources below this luminosity threshold have a mean blackbody temperature of 0.61 keV.

The second, low-luminosity, group in the distribution of high-state ULXs is clearly distinguishable in both plots of Figure 2.8. We found that, with the exceptions of NGC 253 XMM1, M81 XMM1, and NGC 5204 XMM1, the spectra of these objects could also be well-described by an absorbed Comptonization (`compST`) model (Sunyaev & Titarchuk 1980) used to fit galactic black holes in the "very

high" state when they are radiating at the Eddington limit. This model simulates Compton scattering of cool photons on the hot electrons of a completely ionized plasma. We present the best-fit parameters for the Comptonization model in Table B.4.

This "very high" state has been observed (Miyamoto et al. 1991) in a few Galactic black holes. Yet another rubric for the very high state emerged in Kubota et al. (2001) and Kubota & Makishima (2004), where they identify this as the "anomalous" state – a state whose spectrum can be well fit by a Comptonized scattering model. Regardless of the name, our best-fit Comptonization sources likely fit into this category. The luminosities of these sources suggest that they are stellar mass black hole systems in this anomalous/very high state.

As with the low-state, we include mass estimates for our high-state objects in Table 2.3. We assume that the high-state objects are radiating at L_{Edd} resulting in a minimum mass if there is no beaming. We find masses of $1.6-38\,M_{\odot}$, consistent with "normal" stellar mass BHs, for the sources well fit by the Comptonization model. The other high-state ULXs masses range from $17-1350\,M_{\odot}$ based on Eddington rates, analogous to the low-state ULX masses computed.

It is important to note that the initial simulations (appendix) and discussions in the Spectral Simulations section need to be considered in relation to the impact they pose to our classification scheme and the results presented in these sections. While it is indeed possible that some of the objects with a weak blackbody component and a relatively small number of counts would be mis-categorized as a pure power law spectrum, one can ask what such a possible situation would do to the correlations that we have seen. These putative objects, by assumption would have lower luminosities, however their temperatures are unknown and it is entirely unclear if they would destroy the kT–L_X correlation. As we have

shown in our simulations it is unlikely that the fitted power law index would change and thus the presence of a low state as indicated by the spectral index would not change. This would create a new type of object, one with a flat power law and a blackbody component, which is not seen in the Milky Way, nor among the high signal to noise objects.

2.4.4 Temperature Gap

In addition to the existence of ULXs with low blackbody temperatures, the temperature distribution of the high-state (thermal dominated) ULXs (Figure 2.8, left panel) displays a "gap" which is of particular interest — there is a complete absence of objects with temperatures in the range 0.26 keV to 0.50 keV. It is tempting to take this as evidence for a gap in the mass distribution of these accreting black holes. Since, for a given luminosity, we expect the temperature to vary as $T \propto L^{1/4} M^{-1/2}$, this factor of two gap in the temperature distribution translates into a factor of four gap in the black hole mass distribution.

If this result is borne out by further study, it provides an important clue to the origin and evolution of intermediate mass black holes. One popular idea is that intermediate mass black holes formed from the collapse of massive Population III stars (Madau & Rees 2001). Models suggest that Pop III stars with zero age main sequence (ZAMS) masses in the range 25–140$M_\odot$ and above 260$M_\odot$ collapse to produce black holes (Heger & Woosley 2002) whereas in the range of ZAMS masses 140–260$M_\odot$, pair-instability supernovae lead to the complete disruption of the stars (i.e., no remnant black hole remains). Hence, this model for IMBH formation predicts a gap in the IMBH initial mass function in the range of approximately 60–200$M_\odot$ (although this is uncertain on the low end due to the effect of the pulsational pair-instability on the pre-collapse core). One possibility

is that the gap in our observed temperature distribution (and hence the inferred gap in the mass function) is due to this effect of the pair instability supernovae in Pop III stars. This would require that the current IMBH mass function is approximately the same as the initial IMBH mass function. In other words, it requires that most IMBHs (especially those just below the gap) have not grown significantly due to accretion since their formation and, hence, that the ULX phase represents a short fraction of the life-time of an IMBH ($f << t_{\rm sal}/t_{\rm H}$, where $t_{\rm sal} \approx 45\epsilon_{0.1}\,Myr$ is the e-folding timescale for Eddington limited black hole growth with radiative efficiency $\epsilon = 0.1\epsilon_{0.1}$).

An alternative interpretation of the inferred mass gap is to suppose that two fundamentally different modes of formation lead to a strong bi-modality in the final black hole mass function. Black hole masses below the gap can be readily understood through normal stellar processes. A separate and distinct population of significantly more massive black holes may result from dynamical processes in the core of dense globular clusters (Gültekin et al. 2004; Miller & Hamilton 2002).

2.4.5 Comparison with Galactic HMXBs

Supposing that the Galaxy's bright X-ray population is representative of low-redshift galaxies, we expected to find a number of sources similar to Galactic X-ray binaries in our sample. In our sample, we find approximately 24 sources with luminosities below our high-state ULX cutoff ($\approx 3 \times 10^{39}\,{\rm erg\,s^{-1}}$) , X-ray positions within the optical extent of their host galaxy, and no obvious optical counterpart. The unabsorbed luminosities for these sources range from $0.4 - 2.5 \times 10^{39}\,{\rm erg\,s^{-1}}$ ($0.3 - 10\,{\rm keV}$ band). Two of these sources were transients in the *XMM-Newton* data. Of the four host galaxies with multiple observations examined, two of these galaxies contained solely ULX sources in our luminosity regime (Holmberg II and

NGC 5204). Each of the remaining two (NGC 253 and NGC 4258) had a transient source best fit by a combined blackbody and a power law.

This suggests an interesting diagnostic in terms of distinguishing our ULX sources from a normal HMXB population. In our own galaxy, most HMXBs vary on timescales of days or less and most of the black holes in the Milky Way are transients, though some HMXBs are indeed persistent. The figures in Kalogera et al. (2004), determined through detailed mass-transfer calculations, indicate that transient behavior should not be expected from a population of IMBHs. Thus, on average, our ULX sources should remain X-ray bright in multiple observations. Through a literature search, we found that 37/42 of our ULX sources are well detected in ROSAT observations and thus are luminous for greater than 10 years and therefore are not transients. Examination of the long term light curves show that most of these sources vary by less than a factor of 3 over the timescale from ROSAT to XMM. The sources that have been above the Eddington limit in the Milky Way and the Magellenic clouds do so transiently, for a small fraction of the time. As best as we can tell, from the light curves from Einstein, ROSAT, ASCA, Chandra and XMM the ULXs are, rarely, transients, and are almost always 'on', unlike Galactic "ultra-luminous" objects.

As a possible further diagnostic, we constructed a color-color diagram for our ULX sources. We adopted the colors of Done & Gierliński (2003) in order to compare our sample with their sample of Galactic X-ray sources. Thus, our colors were constructed from unabsorbed model fluxes in four energy bands: 3-4, 4-6.4, 6.4-9.7, and 9.7-16 keV. The `XSPEC` command `dummyresp` was used to calculate a flux based on the model for the 10-16 keV range. We plot colors for a pure unabsorbed power law (from $\Gamma = 1.5 - 3.0$) and an unabsorbed MCD model (`diskbb` in `XSPEC` with $\mathrm{kT}_{in} = 5.0 - 0.2$ eV) for comparison. Comparing

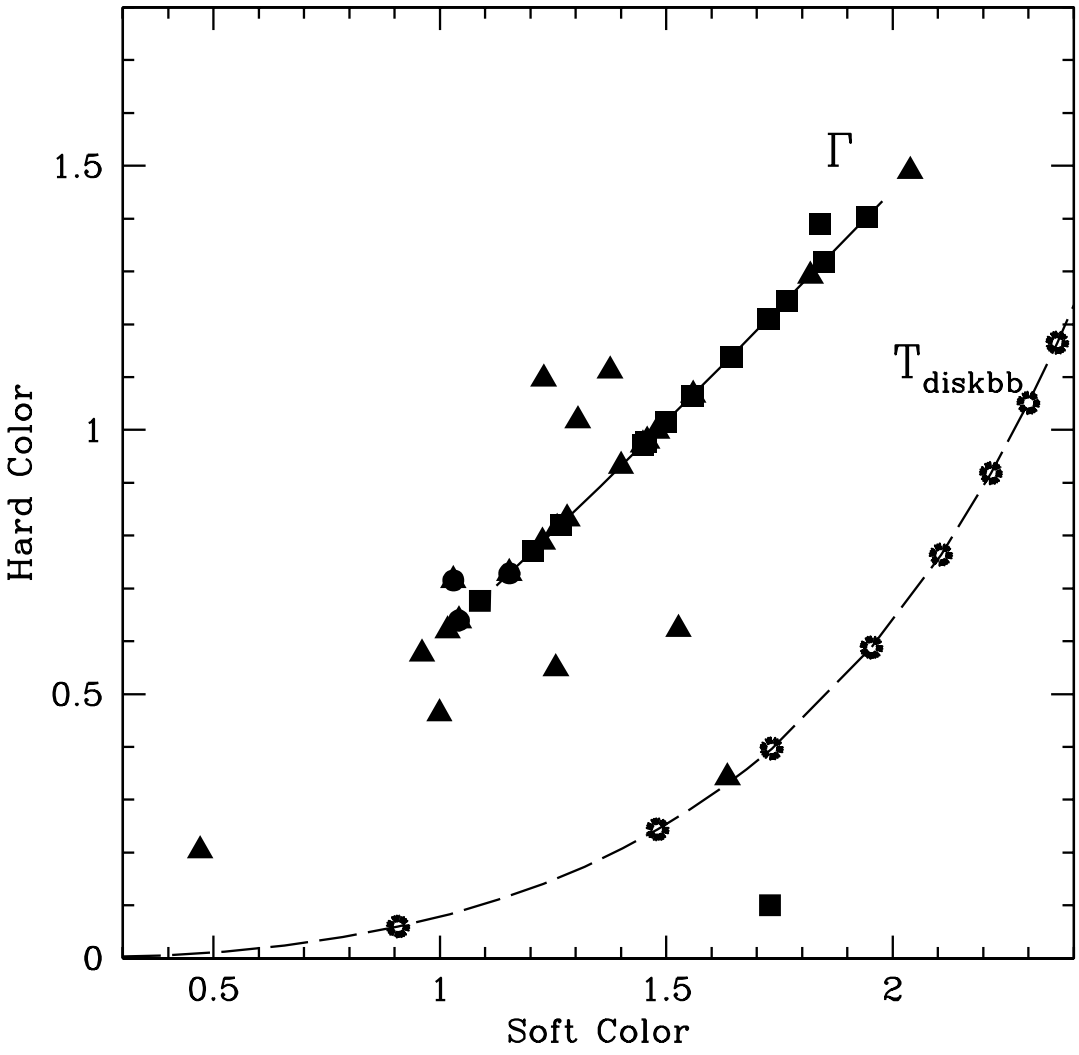

Figure 2.9: Color-Color Diagram plotting soft vs. hard colors, as outlined in Done & Gierliński (2003), for low-state (rectangle) and high-state (triangle) ULXs. The filled circles represent the sources with low $\Delta\chi^2$ values between the two-component and power law models. A large number of our sources lie in the same range of this graph as the black hole sources examined by Done & Gierliński (2003) (near the power law distribution, indicated by the solid line). The dashed line represents the color-color plot for a multi-colored disk model with different disk temperatures. The sources approaching this line were those well-fit by the Comptonization model. Done & Gierliński (2003) had no black hole sources in this region, but atolls and Z-sources, which were also well-fit by Comptonization models.

our Figure 2.9 with Figure 8 of Done & Gierliński (2003), we find that our ULX sources largely lie along the same regions as their black hole sources. A few ULX sources, however, lie in the region occupied by atoll and Z-sources in the plot of Done & Gierliński (2003). These sources were those best fit by a Comptonization model.

2.4.6 Galaxy Sample

In this section, we examine the environment in which ULX sources reside. We investigate the claim that the ULX population is proportional to the host galaxy's star formation rate (SFR) (Grimm et al. 2003; Ranalli et al. 2003). Towards this end, we use the far-infrared luminosity of the host galaxy as an indicator of the SFR. In order to compare the ULX population of a galaxy with the SFR we followed a similar approach to Swartz et al. (2004). We calculate the FIR flux from observations taken by the *Infrared Astronomical Satellite*. As in Swartz et al. (2004), the flux between 42.4 and 122.5 μm is approximated as:

$$F_{FIR} = 1.26 \times 10^{-11}(2.58S_{60} + S_{100}), \tag{2.2}$$

in units of erg cm^{-2} s^{-1}. The values of the flux at 60 μm (S_{60}) and 100 μm (S_{100}) were obtained from either Ho et al. (1997) or NED. Luminosities were calculated using the distances quoted in Table 2.1. We list these values in addition to the number of ULXs observed in individual galaxies in Table B.5. The number of ULXs includes both the objects we classify as high and low state ULX as well as those sources resolved by Chandra (see references in the Table B.1).

In Figure 2.10, we show two plots relating the number of ULXs to L_{FIR}. It has been suggested by Grimm et al. (2003) that the luminosity function in the X-ray regime from HMXBs is related to SFR. In our first plot, we find that the galaxies

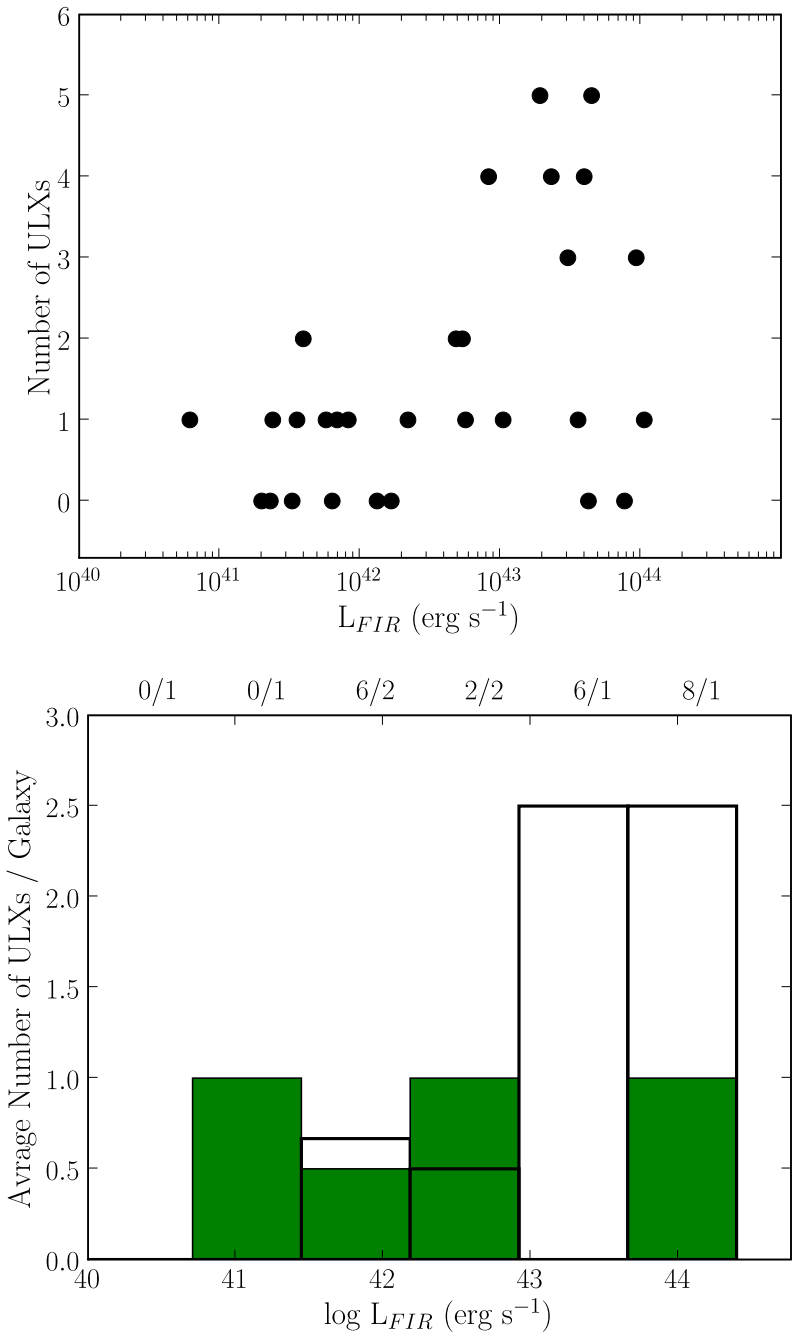

Figure 2.10: (top) Relationship of the far-infrared luminosity, as an indicator of star formation rate, vs. the number of ULXs for each galaxy. If ULXs are associated with star formation, we naively expect that the higher the FIR luminosity the more ULXs the galaxy will host. (bottom) The distribution of the average number of ULXs / L_{FIR} bin for spirals follows this expectation (marked by solid lines). The distribution of irregulars (green histogram) is not so easily interpreted. The numbers at the top indicate the number of spirals/irregulars in each of the luminosity bins. More irregulars would need to be included in this survey for meaningful statistics on this group.

with the highest L_{FIR} seem to have fewer ULXs than may be expected from the luminosity functions of Grimm et al. (2003), who present a relationship showing a scaling of the number of HMXBs with luminosities over a set threshold with the host galaxy's SFR (see equation 7; Grimm et al. (2003)). Using this relationship, we would expect that a galaxy with a SFR approximately equal to that of M51 ($\approx 4\,M_\odot\,yr^{-1}$ from their table 1) to have ≈ 4.47 objects with luminosities greater than $10^{39}\,erg\,s^{-1}$. We find 5 objects with this luminosity in M51, consistent with their result. However, for NGC 4945, a galaxy with approximately the same L_{FIR} and therefore SFR, we find only one source with a luminosity in this range. However, we note that NGC 4945 is a Seyfert, implying that the L_{FIR} may primarily be caused by the AGN and not a direct indication of SFR. In addition to high L_{FIR} sources with few ULX we find a number of sources with very small SFR but which contain a ULX. For sources with SFR $< 0.2\,M_\odot\,yr^{-1}$, which corresponds roughly to sources with L_{FIR} less than that of NGC 4736, we would expect < 0.22 sources with luminosities above $10^{39}\,erg\,s^{-1}$. However, there are a number of bright ULXs in galaxies with very low SFRs (for instance Holmberg II, Holmberg IX, NGC 5204, and NGC 5408). Thus, in a direct comparison, our results do not agree with the predictions of Grimm et al. (2003).

The second plot displays the average number of ULXs/galaxy, binned according to luminosity. This plot is extremely similar to Fig. 15 of Swartz et al. (2004) for spiral galaxies. Thus, once again, it seems that the connection between SFR and the ULX population in spirals is supported. For irregular galaxies, however, there seems to be more of a spread in the distribution. This could be the result of poor sampling — most of the bins contain only one galaxy. Another possibility is that there is no direct correlation in irregular galaxies or that the overall star formation in these galaxies is less ordered or clumpier. If the latter is the case,

the overall SFR of the galaxy is only an average over a wide range of values. We shall address this issue again in the next chapter, where we discuss the local environments of the ULXs in our sample.

In Figure 2.11 we plot the distribution of column densities among the ULXs. We subtracted the Galactic column density towards the galaxy (obtained from the nH FTOOL and listed in Table 2.1) from the values obtained through spectral fits. We note that, on average, the ULXs have large column densities. The typical Galactic column density along a line of sight is $\approx 4 \times 10^{20}\,\mathrm{cm}^{-2}$. If the ULX is located on the opposite side of its host galaxy, we might expect maximum column densities of $\approx 1.2 \times 10^{21}\,\mathrm{cm}^{-2}$. However, most of our sources have column densities well above this value. This is in agreement with the analysis of 5 ULXs by Roberts et al. (2004) and may imply, as they suggest, that the local environment of the ULXs contains an extra source of absorption. We are investigating this further, comparing the X-ray absorption column densities with HI data (see Chapter 3).

In order to better understand the relationship between SFR and the ULX population, it is necessary to extend ULX studies to other wavelengths. In particular, it becomes important to analyze UV and IR images close to the ULX.

2.5 Summary

In this chapter, we presented the results of an *XMM-Newton* archival survey of the ULX population in nearby galaxies. This study required an important assumption – that ULXs are isotropic emitters. For the sources we selected as ULX sources (which excluded transient sources and supernovae), this assumption was supported by the finding that 37/42 of our ULXs were found to be 'on' in ROSAT

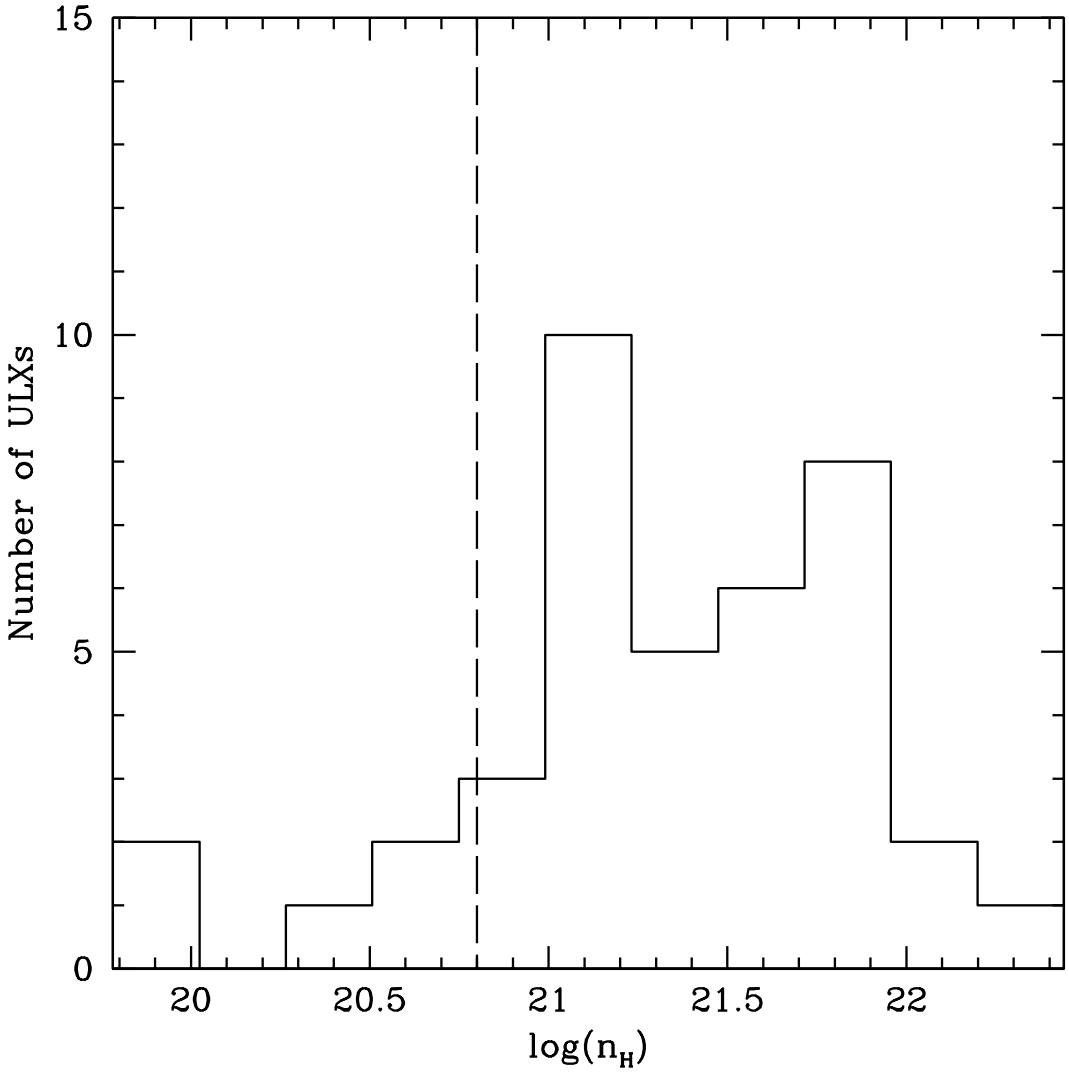

Figure 2.11: Distribution of the hydrogen column densities of ULX sources. The n_H values were obtained through spectral fits using the `wabs` model in `XSPEC`. Galactic column densities towards the host galaxy were subtracted from the spectral fit values. A majority of our ULX sources have high column densities ($> 10^{21}$ cm^{-2}), suggesting that some of this absorption originates with the local ULX environment. Bins to the left of the dashed line represent sources with column densities very close to the Galactic value and thus a simple subtraction is not statistically representative of the true value.

observations. This implies that these sources exhibited high luminosities for time scales of at least 10 years, a property that is not seen in Galactic Eddington-limit exceeding sources (such as black hole X-ray binaries undergoing an outburst). We also assumed that if some ULX sources represent a class of IMBH X-ray binaries, they would exhibit spectral states analogous to Galactic stellar mass black hole X-ray binaries. This is the hypothesis we set out to test, classifying a source as a ULX based on (1) spectral form, (2) luminosity, and (3) coincidence of the X-ray source within the optical host galaxy. Due to the quality of spectra available for these distant X-ray sources, our classification of spectral form is really a first approximation describing the basic curvature of the spectrum.

Through this study, we have found that there exists a population of objects whose X-ray spectral properties closely match the low/hard state spectra of Galactic black holes, but whose luminosities lie in the range of $L_{bol} \approx 2 \times 10^{38} - 1 \times 10^{40}$ erg s^{-1}. In the Milky Way, black holes with these spectral properties radiate at only ≈ 0.05 of the Eddington limit. If this is also true for this population, it indirectly implies that these objects have a mass greater than $\approx 30\,M_{\odot}$ ranging up to $1500\,M_{\odot}$ and thus should be IMBHs. The existence of such objects was "predicted" on the basis that the ULXs previously studied shared the X-ray spectral characteristics of high-state Galactic black holes; namely, an X-ray spectrum best fit by a combined blackbody and a power law (Miller et al. 2004a), but with much higher luminosities. If these objects are high-state IMBHs, the corresponding low-state objects should also exist.

Our survey has also uncovered a large population of objects whose X-ray spectra are well modeled by the canonical description of Galactic black holes in the high-state (thermal dominated), a black hole with a steep power law, but whose bolometric luminosities exceed 2×10^{39} erg s^{-1}, ranging up to $10^{41.5}$ erg s^{-1}

and whose blackbody temperatures are less than 0.3 keV. If these objects are radiating at $\approx 1/2$ the Eddington limit like their Milky Way counterparts their implied masses are from $30 - 3000\,M_\odot$, a range very similar to that implied by the low-state objects. Using the $M^{-1/4}$ scaling of mass to temperature, the observed spectral temperatures give masses of $500 - 10^4\,M_\odot$ a considerably larger value. In general agreement with the expectations of the IMBH hypothesis, the objects with high-state spectra are more luminous than those with low-state spectra. We note that these results have required the high signal to noise of *XMM* in order to discern the spectrum of these objects. Many of these objects have also been observed by Chandra and their spectra have been well-fitted by simple power laws.

In addition to classification of the sources, we investigated some of the properties of the ULX sources. We found a gap in the temperature distribution of high/soft state ULXs. This gap may indicate a gap in mass distribution, which may provide clues to the nature of ULXs. We also found that our ULXs are persistent sources (not transients) which occupy regions on the color-color diagram of Done & Gierliński (2003) also occupied by Galactic black hole sources. Lastly, the existence of a substantial population of ULXs in nearby dwarf and other low star formation rate galaxies argues that (in agreement with Ptak & Colbert (2004); Swartz et al. (2004)) there is more than one source term for the origin of ULXs, with at least some of them not being associated with recent star formation, at least statistically.

We conclude, from an X-ray spectral and luminosity point of view, that our data are consistent with many of these objects having the properties expected of an IMBH population. However, we also find two other populations of objects, those whose blackbody temperature and luminosity correspond to that of stellar

mass black holes with kT ≈ 1 keV and $\log L_X$ less than 2×10^{39} erg s^{-1} and a small population of objects whose X-ray spectra and luminosities are consistent with that of stellar mass black holes in the very high state, as expected from studies of the Milky Way and M31. Thus, ULX selected purely on the basis of $0.3 - 10$ keV X-ray luminosities are a composite class with $\approx 1/4$ being "normal" stellar mass black holes and the rest being consistent with a population of IMBHs.

Chapter 3

Elemental Abundances of Nearby ULX Host Galaxies

3.1 Introduction

Long exposure *XMM-Newton* observations of nearby galaxies offer new opportunities to study various properties of ULX spectra. In the previous chapter (Chapter 2), we analyzed ULX spectra from sources found in 32 nearby galaxies. Based on spectral form, luminosity, and location within the optical host galaxy, we classified a population of high/soft state and low/hard state ULXs. In our initial study, we focused on spectral fits with simple schematic models. However, for the spectra with the greatest number of counts, more detailed models can be used to glean more information from their spectra. One important investigation that such high signal-to-noise spectra can aid with is a study of absorption along the line of sight to the ULX source. Thus, in this chapter we examine the highest signal-to-noise *XMM-Newton* spectra in an attempt to understand the line of sight absorption.

Many similar studies have been done within our own Milky Way, where

X-ray absorption models have been used to determine column densities and abundances of the interstellar medium. The general procedure used in these studies is to fit absorption features in the spectra of bright, background X-ray sources. Using this method, successful determinations have been made using both background galaxy clusters (Baumgartner & Mushotzky 2006) and X-ray binaries (Juett et al. 2004). Specifically, these studies made use of a bright, X-ray source as a background through which they observed the 542 eV absorption edge produced by photo-ionization of the inner K-shell electrons of oxygen. Analogous studies have been used in the radio (see Dickey & Lockman (1990)) to optical regime, using quasars, supernovae, or stars as a background for hydrogen absorption and 21-cm emission, as a means to measure hydrogen column densities and metal abundances.

In this study, we extend the X-ray absorption studies to external galaxies using ultra luminous X-ray sources. Due to their extreme brightness in the X-ray regime and their non-nuclear location in external galaxies, these sources are ideal for probing the ISM of their host galaxies. Typical ULXs, from our Chapter 2 study, have Galactic line-of-sight column densities of a few 10^{20} cm^{-2} (Dickey & Lockman 1990) and measured X-ray column densities greater than 10^{21} cm^{-2} (Figure 2.8) for the combined ULX and host galaxy. Thus, if the local environment of the ULX contributes little absorption, the X-ray column density is dominated by the host galaxy. One goal of this study is to determine whether this absorption is that of the host galaxy or local ULX environment. Therefore, we compare the X-ray measured hydrogen column density with H I measurements from alternate methods.

In addition to the brightness of ULXs and the relatively small Milky Way contribution to their X-ray hydrogen column densities, their well characterized X-ray spectra make ULXs ideal for measuring absorption features of the ISM. Bright

ULXs (e.g. NGC 1313 X-1) typically have spectra that are well-fit by an absorbed multi-component blackbody and power law model. However, there is discussion over whether this standard model is the most physical model for the ULXs (see, for example, Stobbart et al. (2006) or Gonçalves & Soria (2006)). Different models applied to the base ULX spectra can affect the absorption measurements, particularly in the softer part of the spectrum. Thus, in this chapter we investigate the effect different soft component models have on the X-ray measured hydrogen column density and elemental abundances (through the oxygen K-shell edge at 542 eV and the iron L-shell edge at 851 eV).

We use high signal-to-noise *XMM Newton* observations of ULXs to measure hydrogen column densities and elemental abundances of oxygen and iron. Located in external galaxies, the X-ray spectral resolution of available ULX spectra is not as good as those of Galactic X-ray binaries, which often have grating spectra available (e.g. Juett et al. (2004)). Therefore, in order to be able to distinguish the oxygen K-shell edge as well as the iron L-shell edge located at 851 eV, we needed observations with a large number of counts (≈ 5000 counts). The X-ray observatory *XMM-Newton*, having a larger collecting area than Chandra, provides the counts necessary in order to conduct this study. Further, with recent 100 ks *XMM-Newton* observations available for the host galaxies of two well-studied ULXs (Holmberg II and Holmberg IX), these observations allow for the added analysis of Reflection Grating Spectrometer (RGS) spectra in addition to spectra from the European Photon Imaging Cameras (EPIC). The spectral resolution of the EPIC and RGS allow us to test different soft component models for the ULX sources, to determine the effect of the model on absorption and abundance measurements.

3.2 Source Selection and Data Reduction

In Chapter 2, we presented the results of an archival *XMM-Newton* study of ULXs in 32 nearby (< 8 Mpc) galaxies. We had extracted spectra for the brightest sources in the observations, corresponding to > 400 counts. In this study, we chose to further analyze the spectra of the objects with the highest number of counts (> 5000 counts[1]). In addition to the 11 sources from Chapter 2, we include an analysis of 3 additional sources: the two ULXs in the spiral galaxy NGC 4559 (observation 0152170501) and the bright source in M33 (observation 0102640101). A full list of the 14 ULX sources, with details of the observations (including exposure times and count rates), is found in Table 3.1.

The two ULX sources in NGC 4559 were originally studied by Vogler et al. (1997) using ROSAT and Cropper et al. (2004) with *XMM-Newton*. We follow the naming convention established in these papers. Both of these sources (X7 and X10) were not included in Chapter 2 because the host galaxy's distance is greater than the 8 Mpc limit we initially required. However, we include these sources now due to the high number of counts (> 5000 counts) in their spectra. Initially we did not include M33 X-8 in our ULX survey due to its location in the center of its host galaxy. This source, however, shows no evidence of being a low-luminosity AGN and is more likely a black hole X-ray binary (Takano et al. 1994).

Since the initial study of Chapter 2, longer exposure time *XMM-Newton* observations have become available for three of our sources from the original study.

[1]In Appendix C, we show results of simulations to determine the number of counts necessary to detect the oxygen and iron absorption edges. We found that > 40000 counts are needed to constrain iron abundance without having large errors in the measurement. For oxygen, > 5000 counts are needed to constrain the abundance without large errors. See the appendix for further details.

Table 3.1. ULX Observation Details

Source	RA (h m s)[a]	Dec (° ′ ″)[a]	n_{HGAL}[b]	Obs ID	Exposure Time (s)[c]	Count Rate (cts s^{-1})[c]
NGC247 XMM1	00 47 03.8	-20 47 46.2	1.54	0110990301	3458, 1389, 1379	0.20, 0.06, 0.06
NGC253 XMM2	00 47 22.4	-25 20 55.2	1.40	0152020101	-, 10347, 10304	-, 0.08, 0.09
NGC300 XMM1	00 55 09.9	-37 42 13.9	3.11	0112800101	6778, 2248, 2453	0.19, 0.05, 0.05
M33 X-8	01 33 50.9	+30 39 36.1	5.58	0102640101	11919, 12147, 12142	0.06, 0.02, 0.02
NGC1313 XMM3	03 18 22.5	-66 36 06.2	4.0	0106860101	6960, 2179, 1793	0.233, 0.08, 0.07
Holm II XMM1	08 19 28.8	+70 42 20.3	3.42	0112520701	31052, 1257, 10807	2.72, 0.76, 0.73
...	...	...	...	0200470101	56987,65758, 65766	3.29, 0.95, 0.94
...	...	...	...	0200470101	41816, 41802 (RGS)	0.09, 0.11 (RGS)
M81 XMM1	09 55 32.9	+69 00 34.8	4.12	0111800101	50788, -, 18988	0.51, -, 0.22
...	...	...	...	0200980101	-, 111910, 111930	-, 0.111, 0.104
Hol IX XMM1	09 57 53.3	+69 03 48.7	4.0	0112521001	14976, 6546, 6586	2.07, 0.64, 0.65
...	...	...	...	0200980101	104010, 111760, 111830	1.69, 0.51, 0.51
...	...	...	...	0200980101	103840, 103830 (RGS)	0.03, 0.04 (RGS)
NGC 4559 X7	12 35 51.8	+27 56 04	1.51	0152170501	34517, -, -	0.318, -, -
NGC 4559 X10	12 35 58.6	+27 57 40.8	1.51	0152170501	34509, -, -	0.238, -, -
NGC4631 XMM1	12 41 55.8	+32 32 14	1.28	0110900201	5093, 1969, 1762	0.13, 0.04, 0.04
NGC5204 XMM1	13 29 38.5	+58 25 03.6	1.42	0142770101	9981, 3352, 3384	0.628, 0.177, 0.179
...	...	...	...	0142770301	9231, 2284, 2349	0.855, 0.247, 0.258
M83 XMM1	13 37 19.8	-29 53 49.8	3.94	0110910201	3074, 927, 987	0.12, 0.033, 0.025
NGC5408 XMM1[d]	14 03 19.8	-41 22 59.3	5.73	0112290601	5932, 2036, 2077	0.128, 0.032, 0.033

[a]RA and Dec values quoted are the source positions from the EPIC-pn images.

[b]Milky Way hydrogen column density along the line of sight from Dickey & Lockman (1990) in units of 10^{20} cm^{-2}

[c]Exposure times and count rates are listed for the EPIC pn, MOS1, MOS2, and RGS (1 and 2), where available. Note that for sources with multiple observations, details for the additional observations are listed below the first observation. Details of the specific RGS (RGS1 and RGS2) observations are indicated with (RGS).

[d]A second observation of NGC 5408 XMM1 is referred to in § 3.4.2. This observation (0302900101) with an exposure time of 130335 s was proprietary at the time of analysis.

With the permission of Tod Strohmayer, we include data from the 100 ks *XMM-Newton* observation (0200980101) of Holmberg IX. These data include pn and MOS spectra of Holmberg IX XMM1 and MOS spectra of M81 XMM1. We also include a 100 ks *XMM-Newton* observation (0200470101) of Holmberg II XMM1 that became public after the Chapter 2 study. The EPIC and RGS spectra from this observation of Holmberg II XMM1 were first analyzed by Goad et al. (2006). For Holmberg IX XMM1 and Holmberg II XMM1, the 100 ks exposures provided us with the opportunity to extract and analyze, in addition to the EPIC spectra, spectra from the RGS detectors. Thus, we include an analysis of RGS spectra for both Holmberg II XMM1 and Holmberg IX XMM1.

For the EPIC spectra we added to our original sample, we followed the same reduction method as in Chapter 2. For observations that were processed with an earlier version of the *XMM-Newton* Science Analysis System (SAS) (we used SAS version 6.0), the observation data files (ODF) were used to produce calibrated photon event files for the EPIC-MOS and pn cameras using the commands `emchain` and `epchain`. The events tables were filtered using the standard criteria outlined in the *XMM ABC Guide*. For the MOS data (both MOS1 and MOS2 cameras), good events constitute those with a pulse height in the range of 0.2 to 12 keV and event patterns that are characterized as 0-12 (single, double, triple, and quadruple pixel events). For the pn camera, only patterns of 0-4 (single and double pixel events) are kept, with the energy range for the pulse height set between 0.2 and 15 keV. The selection expression "FLAG == 0" was used to exclude bad pixels and events too close to the edges of the CCD chips. Time filtering was applied as needed by editing the light curve produced in `xmmselect`. For the EPIC observations, time periods in the observation with high count rates (flares) in the MOS and pn were cut using the command `tabgtigen` with the 'RATE<'

command set to 5 cts s^{-1} for MOS detectors and 20 cts s^{-1} for the pn detector.

We extracted source and background spectra along with response and ancillary response matrices using the SAS task `especget`. The source spectra were extracted from circular regions, typically with radii of 20″. This region was adjusted depending on the size of the source and the proximity of the source to either another source or the edge of a CCD chip. We extracted background spectra from annular regions, except when the source was near another source or near the edge of a chip. In this case, in order to avoid source confusion, we extracted background spectra from a circular region located near the source and on the same CCD chip (as for Holmberg IX XMM1 and M81 XMM1).

For the RGS spectra we extracted first and second order spectra for the sources Holmberg IX XMM1 (0200980101) and Holmberg II XMM1 (0200470101) using the `rgsproc` command. The RA and Dec values used to extract the RGS spectra were obtained from the EPIC pn data and are the values quoted in Chapter 2. Time filtering was applied as for the EPIC data with `tabgtigen`, where the 'RATE<' command was set to 0.5 cts s^{-1} for Holmberg IX and 0.1 cts s^{-1} for Holmberg II. Once the spectra were obtained, for the RGS as well as EPIC data, they were rebinned to require at least 20 counts per bin, using the command `grppha` in LHEASOFT.

3.3 Spectral Fitting

Spectral fitting proceeded using XSPEC v11.3.1. For the RGS spectra, we simultaneously fit the first order spectra from both RGS1 and RGS2 in the RGS band (0.33 - 2.5 keV). For the EPIC spectra, we fit the pn and MOS spectra simultaneously in the 0.3-10 keV energy range. We allowed a free normalization constant

to account for the differences in flux calibration between the three EPIC cameras. Both the RGS and EPIC spectra were fit separately.

In the Chapter 2 study, we had fit all of the sources with three standard models: an absorbed power law, an absorbed bremsstrahlung model, and an absorbed combined blackbody and power law model. We used the XSPEC model `wabs` to account for absorption from the Milky Way and the host galaxy/ULX contribution. This model is a photo-electric absorption model using the cross-sections of Morrison & McCammon (1983) and the solar abundances of Anders & Ebihara (1982). We found that the spectra of the brightest ULXs were typically best-fit by an absorbed combined blackbody and power law model (fit in XSPEC as `wabs*wabs*(bbody + pow)` where the first `wabs` model was fit to the Dickey & Lockman (1990) Milky Way value and the second `wabs` model was fit to the remaining host galaxy/ULX contribution). Likewise, we began our study by fitting the additional sources (M33 X-8, NGC 4559 X-7, and NGC 4559 X-10) with the same three models noted above. We found that these sources were well fit by the absorbed blackbody and power law model with $\chi^2/\mathrm{dof} \approx 1.0$.

For M33 X-8, the source was well-fit with an absorbed blackbody and power law with best-fit parameters: $\mathrm{n}_H = 1.67^{+0.09}_{-0.08} \times 10^{21}\,\mathrm{cm}^{-2}$, kT$= 0.74^{+0.02}_{-0.02}\,$keV, $\Gamma = 2.46^{+0.06}_{-0.05}$, and $\chi^2 = 1579.8/1533$ dof, where n_H represents the host galaxy/ULX hydrogen column (the Milky Way contribution was fixed to the Dickey & Lockman (1990) value listed in Table 3.1). In Chapter 2 we noted that ULX sources well-fit with the combined blackbody and power law model with a higher disk temperature ($\approx 1\,$keV) and a lower flux were often well-fit by an absorbed Comptonization model (XSPEC model `compst`). We note that for M33 X-8 the inverse Compton scattering model also fits the data well (`wabs*compst`) but with a $\chi^2 = 1614.9/1536$ dof. Despite the larger χ^2 value, the `compst` model bet-

ter fits the residuals from the spectra's sloping high energy tail. The best-fit absorbed blackbody and power law parameters for NGC 4559 X7 (12 h 35 m 51.8 s, 27° 56′ 4″) were: $n_H = 1.51^{+0.04}_{-0.01} \times 10^{21}$ cm^{-2}, kT$= 0.13^{+0.01}_{-0.02}$ keV, $\Gamma = 2.16^{+0.10}_{-0.04}$, and $\chi^2 = 410.3/369$ dof. For NGC 4559 X10 (12 h 35 m 58.6 s, 27° 57′ 40.8″), we found: $n_H = 1.14^{+0.02}_{-0.01} \times 10^{21}$ cm^{-2}, kT$= 0.96^{+0.26}_{-0.20}$ keV, $\Gamma = 2.13^{+0.06}_{-0.05}$, and $\chi^2 = 292.3/330$ dof. X10, as noted in Cropper et al. (2004), is also well fit by a Comptonization model.

For the sources M33 X-8 and NGC 4559 X10, we noted that their spectra were well-fit by either an absorbed blackbody and power law or an absorbed Comptonization model. This brings up one issue surrounding ULX spectra. Namely, ambiguity over their spectral form. In this chapter, we assume that there is an analogy between ULXs and Galactic black hole binaries. Thus, we assume that the accurate ULX spectrum for these bright sources is a hard component (well modeled by a power law) and a soft component (which we assume as a thermal contribution from an accretion disk). The form of the soft component, in particular, will affect the measured absorption and abundance values. Thus, an investigation of this component and its affect on the absorption model is important.

The soft component of ULXs is most often modeled as a thermal component originating from an accretion disk surrounding a central black hole. There are numerous disk models applied to model this possibly thermal component. In Chapter 2, we modeled this component as a simple blackbody (in XSPEC `bbody`). While an accretion disk is expected to have a range of temperatures, empirically a single blackbody is a good fit to low signal-to-noise spectra. A simple absorbed blackbody and power law model was used for Galactic black hole X-ray binaries in the 1980s when the quality of data for these sources was analogous to that for

ULX sources today. As the next step in accretion disk models, the soft component of ULX spectra is often modeled as an optically thick, geometrically thin, multi-component blackbody disk (a multi-component disk or MCD model, `diskbb` in XSPEC) (Mitsuda et al. 1984).

Two disk models that are used to fit the soft component of ULX spectra with more physical accuracy are the XSPEC models `diskpn` and `grad`. The `diskpn` model is an extension of the MCD (`diskbb`) model which includes temperature corrections for the disk close to the black hole. The `grad` model (Ebisawa et al. 1991; Hanawa 1989) is a multi-component disk model that unlike the `diskbb` or `diskpn` model, incorporates the effects of general relativity. One of the advantages of the `grad` model is that it fits the spectra for mass (M_{grad}) and mass accretion rates ($\dot{M}$) given a few initial assumptions (distance to the source, disk inclination angle, and the ratio of the color temperature to the effective temperature).

In addition to thermal models, other models have been suggested to explain the soft component. Two of these models are ionized reflection and the warm absorber model (see § 1.2). Both of these models have been applied to low-redshift PG quasars, sources with blackbody temperatures of 150 eV. This is relevant to ULXs since many spectral fits of ULXs require cool accretion disk temperatures of approximately 100 eV (Miller et al. 2003, 2004b; Roberts et al. 2005; Winter et al. 2006b). The reflection model suggests that the soft component results from X-ray ionized reflection. In this model, back-scattering and fluorescence of X-rays in the disk, as well as radiative recombination, cause elements with smaller ionization potentials (e.g. C, O, N) to become highly ionized. Ross & Fabian (2005) note that a relativistically blurred X-ray ionization model folded through an *XMM-Newton* pn response matrix, is well-fit by a blackbody with a temperature of 150 eV, the

same value that is seen in PG quasars and many ULXs. In the warm absorber model, absorption edges and lines from an absorbing material close to the X-ray source appear as a thermal component in poorer quality spectra. With increased spectral resolution, the numerous absorption edges and lines are distinguishable. The warm absorber may be the result of a strong, mildly relativistic wind from the disk as suggested by Gierliński & Done (2004). Indeed, the presence of a warm absorber is well known and studied in many Seyfert galaxies (e.g. NGC 3783 and MCG–6-30-15).

As noted above, for subsequent spectral fits we assume a thermal model for the soft component of the ULX spectra. In the following section (§ 3.4), we will discuss the effect that different thermal models have on the measured absorption values. In order to measure the hydrogen column density, we fit the spectra of sources listed in Table 3.1 with the more sophisticated Tuebingen-Boulder ISM absorption model of Wilms et al. (2000) (`tbabs`, `tbvarabs` in XSPEC). This model accounts for X-ray absorption resulting from contributions from X-ray absorption from the gas phase of the ISM, grains, and molecules. The model uses updated solar abundances and photoionization cross-sections. For both the EPIC and RGS spectra, we accounted for Galactic hydrogen absorption by setting the column density of the `tbabs` model equal to the Milky Way hydrogen column density along the line of sight to the host galaxy. These column densities are quoted in Table 3.1 and are all less than 6×10^{20} cm^{-2}.

Since the measured X-ray column densities for ULXs are typically an order of magnitude higher than the Dickey & Lockman (1990) Milky Way values (Figure 2.8), we are confident that the additional absorption measured is not from the Milky Way. To determine the host galaxy's hydrogen column density and the abundances of elements along the line of sight (oxygen and iron), we used the

tbvarabs model. The tbvarabs model accounts for X-ray absorption due to photo-ionization. It includes the effects due to the H_2 molecule and depletion of metals in grains. The model allows for individual fits to abundant elements (He through Ni), H_2, and depletion of elements in grains. We initially allowed the hydrogen column density to vary, fixing all other tbvarabs parameters to their defaults. The Galactic column density remained fixed (using the tbabs model), while the other parameters (power law and blackbody components) were allowed to vary. This was modeled as tbabs*tbvarabs*(bbody + pow) in XSPEC, where tbabs was fixed to the Milky Way value and tbvarabs was used to fit the absorption from the ULX/host galaxy contribution. With the best-fit hydrogen column density (from tbvarabs), we allowed the oxygen abundance and then the iron abundance to vary from the solar abundances. Allowing these parameters to float provides measurements of the depth of the oxygen K-shell edge at 542 eV and the iron L-shell edge at 851 eV.

As in Baumgartner & Mushotzky (2006), we found that for our 14 sources, the oxygen absorption values from the tbvarabs model yielded different values for the EPIC pn and MOS spectra. They attribute this difference to an error in the response matrices of the MOS detectors, possibly caused by outgassing of organic material onto the surface of the MOS detectors[2]. Thus, we follow the procedure of Baumgartner & Mushotzky (2006) in adding an edge model to account for the differences. We add an extra edge component to the MOS1 and MOS2 detectors at an energy of 0.53 keV with optical depths of 0.22 and 0.20 respectively (modeled as tbabs*tbvarabs*edge*(bbody + pow)). This is the template model used for all spectral fits mentioned throughout the rest of the chapter. However, we also discuss models where we replace the simple blackbody model with the

[2]This effect is now calibrated as the MOS "patch" effect as of SAS 7.0.

other thermal models discussed (`diskpn`, `grad`).

An additional problem we note involves the hydrogen column densities along the line of sight. Baumgartner & Mushotzky (2006) note that a column density (n_H) greater than 5×10^{20} cm^{-2} is necessary to allow for good oxygen abundance measurements. We also note that at very high n_H values the oxygen edge is undetectable, where high absorption values cause the signal-to-noise to be too low to detect the edge.

3.4 Nature of the Soft Component

In the previous section we outlined three possible origins for the soft component in ULXs (X-ray reflection, thermal emission from an accretion disk, and a warm absorber model). For our purposes, we assume a thermal component origin. We chose the thermal model since, as described in Chapter 2, the spectra of ULXs are well described with models used to fit Galactic black hole X-ray binaries. To gauge the effect different disk models (i.e. `bbody`, `diskbb`, `diskpn`, `grad`) may have on the measured abundances, we discuss different disk models in § 3.4.1. In § 3.4.3, we assess the usefulness of the model (absorbed disk and power law) for measuring the galactic/ULX hydrogen column density and the oxygen and iron abundances by discussing the physical plausibility of this model.

For sources with at least 5000 counts, the 14 sources listed in Table 3.1, we fitted the `grad` model for the soft-component of the spectra (XSPEC model `tbabs*tbvarabs*edge*(grad + pow)`). Two of the additional parameters of the `grad` model include the disk inclination angle and the ratio of T_{color}/T_{eff}. We find that changing the inclination angle for Holmberg II XMM1 has a minimal change on χ^2 (< 1), Γ, and absorbing column density. Therefore, we set

the disk inclination angle to the default value of 60 °for all of the sources. The other parameter, T_{color}/T_{eff}, was set to 1.7, the conventional value adopted for stellar mass BH sources (Shimura & Takahara 1995; Sobczak et al. 1999). Here, T_{eff} is the effective temperature of the photosphere of the disk, while T_{color} is the color temperature of the disk. The color temperature is the observed temperature, which is slightly modified from T_{eff} as the photosphere spectrum is modified passing through the outer layers of the disk. We note however that there is theoretical evidence supporting a non-constant ratio T_{color}/T_{eff}, ranging from 1.7 to 3 and depending upon accretion rate (Merloni et al. 2000). Allowing the ratio to vary for Holmberg II XMM1, we found the best-fit value corresponded to 1.7. For the sake of uniformity of our models, we fixed the ratio to 1.7 for all of the ULXs.

In Table 3.2, we list the best-fit parameters for EPIC spectra using this model. Rows with no source name indicated represent an additional observation of the previous ULX (as indicated in Table 3.1). Table 3.3 provides the best-fit parameters for the RGS spectra. The important measurements to note are the host galaxy/ULX contribution to the hydrogen column density, oxygen abundance, and iron abundance from the `tbvarabs` model. All errors quoted in this paper are for the 90% confidence level for one degree of freedom ($\Delta\chi^2 = 2.76$). We provide a representative spectral fit in Figure 3.1 for the long observation of Holmberg IX XMM1.

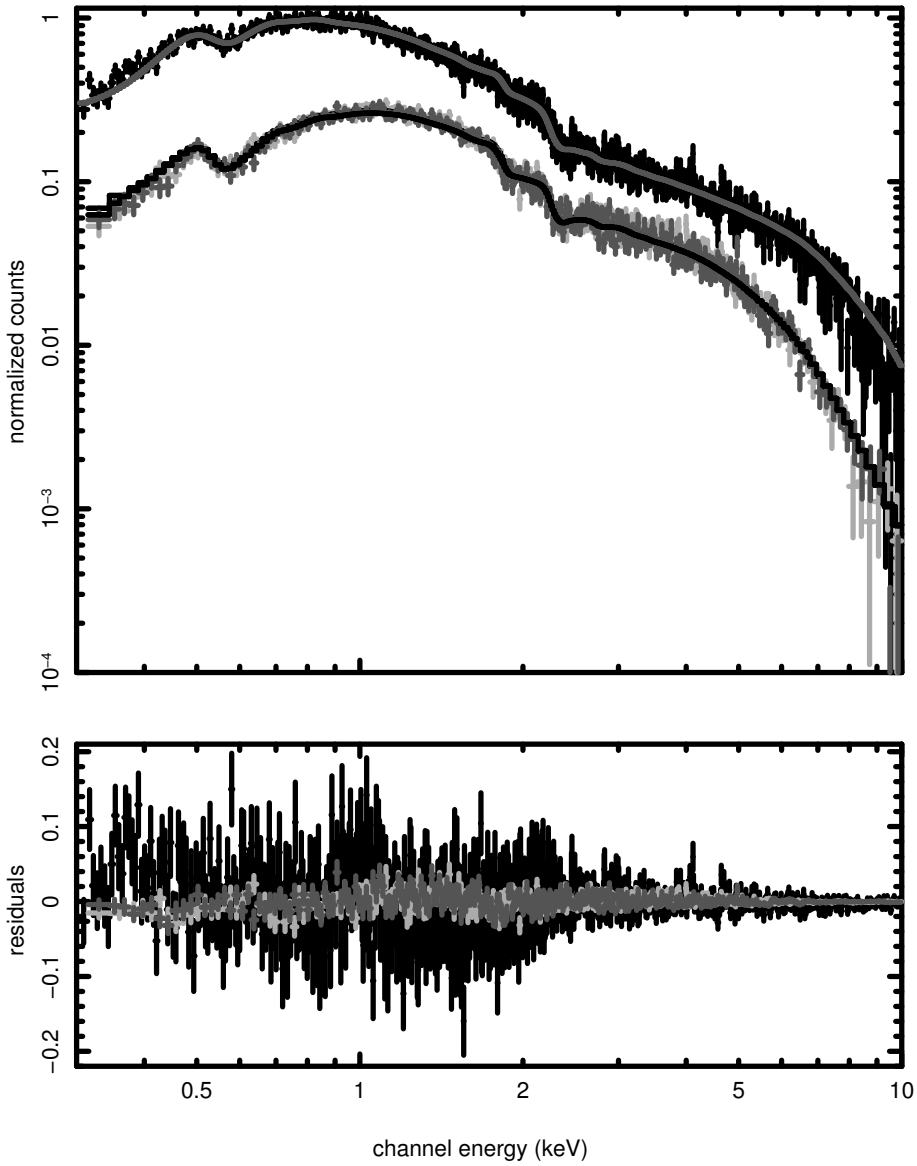

Figure 3.1: EPIC spectrum of observation 0200980101 of Holmberg IX XMM1. This plot shows the spectrum fit with the `tbvarabs*tbabs*edge*(grad + pow)` model and the residuals from this fit. The best fit parameters are listed in Table 3.2.

Table 3.2. Model Fits to EPIC spectra with the `grad` Model

Source	n_H[a]	O abund.[b]	Fe abund.[b]	Mass ($M_\odot$)	$\dot{M}/\dot{M}_{Edd}$[c]	Γ	χ^2/dof	counts[d]
HolmII XMM1	$0.12^{+0.01}_{-0.01}$	$0.90^{+0.11}_{-0.11}$	$0.0^{+0.15}_{-0.0}$	141^{+21}_{-32}	$0.15^{+0.02}_{-0.09}$	$2.36^{+0.05}_{-0.05}$	1.11	342874
...	$0.17^{+0.02}_{-0.04}$	$1.27^{+0.23}_{-0.42}$	$3.15^{+1.29}_{-1.74}$	791^{+209}_{-363}	$0.07^{+0.03}_{-0.03}$	$2.29^{+0.07}_{-0.10}$	0.98	43116
HolmIX XMM1	$0.19^{+0.02}_{-0.02}$	$1.34^{+0.12}_{-0.13}$	$2.07^{+0.12}_{-0.13}$	382^{+93}_{-76}	$0.09^{+0.02}_{-0.02}$	$1.38^{+.025}_{-.025}$	1.05	148061
...	$0.33^{+0.08}_{-0.09}$	$1.38^{+0.29}_{-0.40}$	$3.91^{+1.09}_{-1.86}$	1181^{+1516}_{-719}	$0.11^{+0.20}_{-0.07}$	$1.73^{+0.09}_{-0.09}$	0.64	28108
M33 X-8	$0.20^{+0.04}_{-0.04}$	$1.04^{+0.13}_{-0.18}$	$1.74^{+0.62}_{-0.74}$	$5.24^{+0.38}_{-0.35}$	$1.02^{+0.09}_{-0.08}$	$2.83^{+0.34}_{-0.31}$	0.97	123903
M81 XMM1	$0.66^{+0.11}_{-0.13}$	$1.20^{+0.08}_{-0.10}$	$2.04^{+0.44}_{-0.57}$	$8.61^{+33.58}_{-5.03}$	$2.32^{+44.8}_{-1.31}$	$4.84^{+0.58}_{-0.66}$	1.02	69776
...	$0.27^{+0.21}_{-0.09}$	$1.42^{+0.58}_{-0.50}$	$1.67^{+1.61}_{-1.67}$	$4.2^{+7.4}_{-1.8}$	$8.31^{+4.36}_{-5.98}$	$2.08^{+1.58}_{-0.75}$	0.91	31731
NGC253 XMM2	$0.53^{+0.07}_{-0.12}$	$1.55^{+0.20}_{-0.29}$	$2.73^{+1.17}_{-1.46}$	4140^{+860}_{-2213}	$0.05^{+0.03}_{-0.03}$	$2.32^{+0.10}_{-0.12}$	0.96	20651
NGC5204 XMM1	$0.10^{+0.04}_{-0.03}$	$1.42^{+0.55}_{-0.75}$	$0.0^{+1.84}_{-0.0}$	464^{+366}_{-219}	$0.04^{+0.08}_{-0.02}$	$1.92^{+0.08}_{-0.08}$	0.96	16717
...	$0.13^{+0.05}_{-0.03}$	$0.77^{+0.60}_{-0.77}$	$0.0^{+1.70}_{-0.0}$	449^{+490}_{-217}	$0.06^{+0.12}_{-0.03}$	$2.02^{+0.13}_{-0.14}$	0.93	13864
NGC1313 XMM3	$0.67^{+0.02}_{-0.04}$	$1.37^{+0.13}_{-0.14}$	$0.0^{+0.34}_{-0.0}$	$5000^{+0.03}_{-1160}$	$0.08^{+0}_{-0.02}$	$2.66^{+0.08}_{-0.09}$	1.02	10932
NGC300 XMM1	$0.15^{+0.05}_{-0.04}$	$2.46^{+0.45}_{-0.43}$	$0.0^{+1.77}_{-0.0}$	417^{+312}_{-175}	$0.02^{+0.03}_{-0.01}$	$2.46^{+0.10}_{-0.11}$	1.01	11479
N4559 X-7	$0.16^{+0.05}_{-0.03}$	$0.46^{+0.53}_{-0.46}$	$0.0^{+1.00}_{-0.0}$	755^{+901}_{-443}	$0.06^{+0.12}_{-0.02}$	$2.10^{+0.10}_{-0.10}$	0.83	12506
NGC4631 XMM1	$0.28^{+0.06}_{-0.06}$	$0.62^{+0.43}_{-0.58}$	$0.11^{+1.86}_{-0.11}$	$5.5^{+11.4}_{-18.6}$	$0.84^{+0.88}_{-0.42}$	$5.71^{+2.03}_{-0.31}$	1.06	8824
NGC5408 X-1	$0.09^{+0.03}_{-0.03}$	$1.99^{+0.26}_{-0.52}$	$5.0^{+0.0}_{-1.68}$	1477^{+342}_{-477}	$0.10^{+0.15}_{-0.09}$	$2.53^{+0.20}_{-0.16}$	0.96	10045
NGC4559 X-10	$0.12^{+0.05}_{-0.04}$	$1.28^{+0.61}_{-0.81}$	$0.0^{+2.30}_{-0.0}$	$5.34^{+7.88}_{-2.75}$	$2.74^{+2.52}_{-1.86}$	$2.09^{+0.52}_{-0.28}$	0.77	8837
NGC247 XMM1	$0.44^{+0.18}_{-0.12}$	$1.09^{+0.35}_{-0.28}$	$0.0^{+1.45}_{-0.0}$	1717^{+3205}_{-929}	$0.05^{+0.02}_{-0.03}$	$3.60^{+6.40}_{-6.60}$	0.60	6226
M83 XMM1	$0.13^{+0.09}_{-0.10}$	$1.70^{+1.12}_{-1.65}$	$0.0^{+3.92}_{-0.0}$	$6.34^{+13.4}_{-4.3}$	$0.92^{+0.70}_{-0.70}$	$2.64^{+0.88}_{-0.64}$	0.83	4988

[a]Hydrogen column density determined from `tbvarabs` in units of 10^{22} cm^{-2}. The Galactic value of n_H was fixed to the Dickey & Lockman (1990) value with the `tbabs` model.

[b]Element abundance relative to the Wilms solar abundance from the `tbvarabs` model

[c]Ratio of mass accretion rate from the `grad` model to Eddington accretion rate (see § 3.4)

[d]Total number of photon counts from pn and MOS detectors

Table 3.3. Model Fits to the RGS spectra with the `grad` Model

Source	n_H[a]	O abund.[b]	Fe abund.[b]	Mass ($M_\odot$)	$\dot{M}/\dot{M}_{Edd}$[c]	Γ	χ^2/dof	counts[d]
HolmII XMM1	$0.08^{+0.05}_{-0.02}$	$0.65^{+0.61}_{-0.64}$	$0.0^{+1.51}$	147^{+88}_{-83}	$0.24^{+0.11}_{-0.12}$	$1.58^{+6.75}_{-4.58}$	444.4/442	9521
HolmIX XMM1	$0.29^{+0.12}_{-0.08}$	$0.68^{+0.30}_{-0.34}$	$0.36^{+1.36}_{-0.36}$	774^{+4226}_{-570}	$0.09^{+0.16}_{-0.03}$	$1.43^{+0.45}_{-0.98}$	290.4/339	10807

[a]Hydrogen column density determined from `tbvarabs` in units of 10^{22} cm^{-2}. The Galactic value of n_H was fixed to the Dickey & Lockman (1990) value with the `tbabs` model.

[b]Element abundance relative to the Wilms solar abundance

[c]Ratio of mass accretion rate from the `grad` model to Eddington accretion rate (see § 3.4)

[d]Total number of photon counts from RGS1 and RGS2 detectors

Table 3.4. Alternative Thermal Disk Model Fits

Source	n_H[a]	Oxygen abundance[b]	Iron abundance[b]	kT	Γ	χ^2/dof	counts[c]
			`tbabs*tbvarabs*edge*(bbody + pow)`				
HolmII XMM1	$0.12^{+0.01}_{-0.01}$	$0.97^{+0.11}_{-0.12}$	$0.0^{+0.32}$	$0.24^{+0.01}_{-0.01}$	$2.41^{+0.03}_{-0.03}$	2216.5/2018	342874
...	$0.14^{+0.03}_{-0.02}$	$1.37^{+0.38}_{-0.39}$	$4.38^{+0.62}_{-1.8}$	$0.16^{+0.01}_{-0.01}$	$2.31^{+0.08}_{-0.04}$	952.7/973	43116
HolmIX XMM1	$0.14^{+0.02}_{-0.01}$	$1.51^{+0.19}_{-0.15}$	$3.37^{+0.99}_{-0.80}$	$0.19^{+0.01}_{-0.01}$	$1.40^{+0.02}_{-0.01}$	2856.7/2752	148061
...	$0.23^{+0.10}_{-0.04}$	$1.37^{+0.43}_{-0.44}$	$4.75^{+0.25}_{-1.94}$	$0.17^{+0.02}_{-0.03}$	$1.71^{+0.14}_{-0.06}$	559.5/880	28108
M33 X-8	$0.22^{+0.01}_{-0.14}$	$1.24^{+0.10}_{-0.10}$	$2.38^{+0.31}_{-0.60}$	$0.76^{+0.02}_{-0.02}$	$2.51^{+0.07}_{-0.06}$	1528.8/1533	123903
M81 XMM1	$0.39^{+0.03}_{-0.02}$	$1.13^{+0.15}_{-0.07}$	$1.78^{+0.65}_{-0.40}$	$0.90^{+0.03}_{-0.02}$	$2.70^{+0.05}_{-0.05}$	1240.2/1241	69776
...	$0.26^{+0.09}_{-0.04}$	$1.46^{+0.26}_{-0.49}$	$1.61^{+2.02}_{-1.61}$	$0.99^{+0.38}_{-0.28}$	$1.76^{+0.13}_{-0.09}$	627.4/668	31731
NGC253 XMM2	$0.22^{+0.05}_{-0.05}$	$1.21^{+0.40}_{-0.37}$	$1.53^{+1.67}_{-1.53}$	$0.73^{+0.14}_{-0.11}$	$2.16^{+0.08}_{-0.23}$	460.8/496	20651
			`tbabs*tbvarabs*edge*(diskbb + pow)`				
HolmII XMM1	$0.11^{+0.001}_{-0.01}$	$0.65^{+0.09}_{-0.05}$	$0.0^{+0.06}$	$0.34^{+0.02}_{-0.02}$	$2.38^{+0.05}_{-0.04}$	2241.8/2018	342874
...	$0.15^{+0.03}_{-0.02}$	$1.05^{+0.34}_{-0.38}$	$2.67^{+1.65}_{-1.71}$	$0.21^{+0.04}_{-0.01}$	$2.27^{+0.06}_{-0.07}$	954.2/973	43116
HolmIX XMM1	$0.19^{+0.02}_{-0.02}$	$1.38^{+0.11}_{-0.16}$	$2.39^{+0.58}_{-0.84}$	$0.24^{+0.02}_{-0.01}$	$1.39^{+0.02}_{-0.03}$	2878.9/2752	148061
...	$0.30^{+0.11}_{-0.07}$	$1.36^{+0.32}_{-0.38}$	$4.03^{+0.97}_{-1.65}$	$0.20^{+0.04}_{-0.03}$	$1.72^{+0.10}_{-0.07}$	559.8/880	28108
M33 X-8	$0.19^{+0.04}_{-0.03}$	$1.04^{+0.15}_{-0.16}$	$1.75^{+0.68}_{-0.71}$	$1.17^{+0.05}_{-0.05}$	$2.47^{+0.21}_{-0.15}$	1530.4/1533	123903
M81 XMM1	$0.63^{+0.08}_{-0.15}$	$1.19^{+0.09}_{-0.15}$	$2.07^{+0.40}_{-0.69}$	$1.38^{+0.03}_{-0.08}$	$4.08^{+0.75}_{-0.59}$	1247.7/1241	69776
...	$0.27^{+0.18}_{-0.08}$	$1.42^{+0.57}_{-0.49}$	$1.63^{+1.69}_{-1.63}$	$2.06^{+0.55}_{-0.97}$	$1.98^{+1.40}_{-0.58}$	626.9/668	31731
NGC253 XMM2	$0.21^{+0.10}_{-0.07}$	$1.16^{+0.53}_{-0.37}$	$1.64^{+1.64}_{-1.64}$	$1.27^{+0.22}_{-0.27}$	$2.27^{+0.83}_{-0.62}$	461.3/496	20651

[a]Hydrogen column density determined from `tbvarabs` in units of $10^{22}\,\mathrm{cm}^{-2}$. The Galactic value of n_H was fixed to the Dickey & Lockman (1990) value with the `tbabs` model.

[b]Element abundance relative to the Wilms solar abundance from the `tbvarabs` model

[c]Total number of photon counts from pn and MOS detectors

3.4.1 Comparison of Thermal Disk Models

We chose the general relativistic disk model, `grad`, because it is the most physically accurate of the various simple accretion disk models. Also, the `grad` model requires few initial parameters while making a direct calculation of the mass and mass accretion rate of the black hole. In order to compare the `grad` results with an alternate model, we fit the highest signal-to-noise observation of Holmberg IX XMM1 with the `diskpn` model (with the inner radius of the disk set to the radius of marginal stability or 6 times the Schwarzschild radius) in place of the `grad` model. We found that the values obtained agreed with those of the `grad` model. The mass from the `diskpn` model was slightly lower than the `grad` model value ($382\,\mathrm{M}_{sun}$ for the `grad` compared to $358\,\mathrm{M}_{\odot}$, corresponding to kT$= 0.23\,$keV for

diskpn) and the iron abundance was slightly higher at 2.33 compared to 2.07 with the grad model. Since the diskpn and grad models yield similar values, either of these disk models would be sufficient for determining the hydrogen column density and oxygen and iron abundances.

In order to test the effect the thermal model has on the tbvarabs measured parameters (i.e. n_H and abundances), we wanted to compare the results from the more physical disk model (grad) with less physical models (bbody and diskbb). In order to compare the results from these three models, we chose to examine the best-fit parameters for spectra with the highest signal-to-noise (using sources with at least 20000 counts). Thus, in Table 3.4 we list the best-fit parameters obtained using an absorbed blackbody and power law (tbabs*tbvarabs*edge*(bbody + pow)) and an absorbed diskbb and power law model (tbabs*tbvarabs*edge*(diskbb + pow)) for sources with at least 20000 counts. Subsequently in this chapter, when we refer to the bbody, diskbb, or grad models, we are referring to the model fits used in Tables 3.2- 3.4.

The curvature, or shape of the spectra at low energies, for the bbody, diskbb, and grad models is different, presumably affecting the column density and absorption values. From a comparison of these models, comparing the mean values from all of the observations with > 20000 counts listed in Tables 3.2 and 3.4, we find that the column densities obtained with the diskbb model are nearly identical to those with the grad model (the exception is the source NGC 253 XMM2). The MCD (diskbb) model hydrogen column densities are approximately 6% higher than those of the blackbody model (excluding the first M81 XMM1 observation). The average power law indices for the three models agree within a factor of 5%, with the bbody model having the lowest and the grad having the

highest average power law index (excluding the first M81 XMM1 observation). Thus, the difference in both power law index and hydrogen column density is negligible on average, with the exceptions of NGC 253 XMM2 and M81 XMM1.

For a comparison of the derived abundances, the oxygen abundance is roughly the same between the `grad` and `bbody` model. These values are approximately 10% higher than those derived from the MCD (`diskbb`) model. The iron abundances, however, vary more from model to model. The blackbody model average iron abundance is $\approx 13\%$ higher than that of the `grad` model and $\approx 18\%$ higher than that of the `diskbb` model. Thus, there are no significant changes to the model parameters in changing the base accretion disk model. The robustness of our results are verified by simulations described in the appendix.

3.4.2 Power law/Thermal disk Degeneracies

In modeling our sources with the `tbvarabs*tbabs*edge*(grad+pow)` model, we found that some of the ULX sources were well-fit by a model where the power law component dominates the low energy spectrum, also seen in Stobbart et al. (2006). This type of spectral fit typically yields a steeper power law index ($\Gamma > 3.0$) and a low mass (M$< 10\,\mathrm{M}_{\odot}$). For two sources, M33 X-8 and M81 XMM1, this model fit was a much better fit than a higher mass model with $\Delta\chi^2$ of 476 and 190 respectively. However, for some sources, there was a degeneracy between the two models (high mass and low mass/steep power law). We illustrate this degeneracy with observation 0112290601 of the source NGC 5408 XMM1, showing the high mass model and spectral fit in Figure 3.2 and the low mass model and spectral fit in Figure 3.3. For spectra exhibiting this degenerate solution, we include the low-mass/steep power law fits in Table 3.5. These fits all exhibit, in addition to low masses, solutions with $\dot{M} >> \dot{M}_{Edd}$.

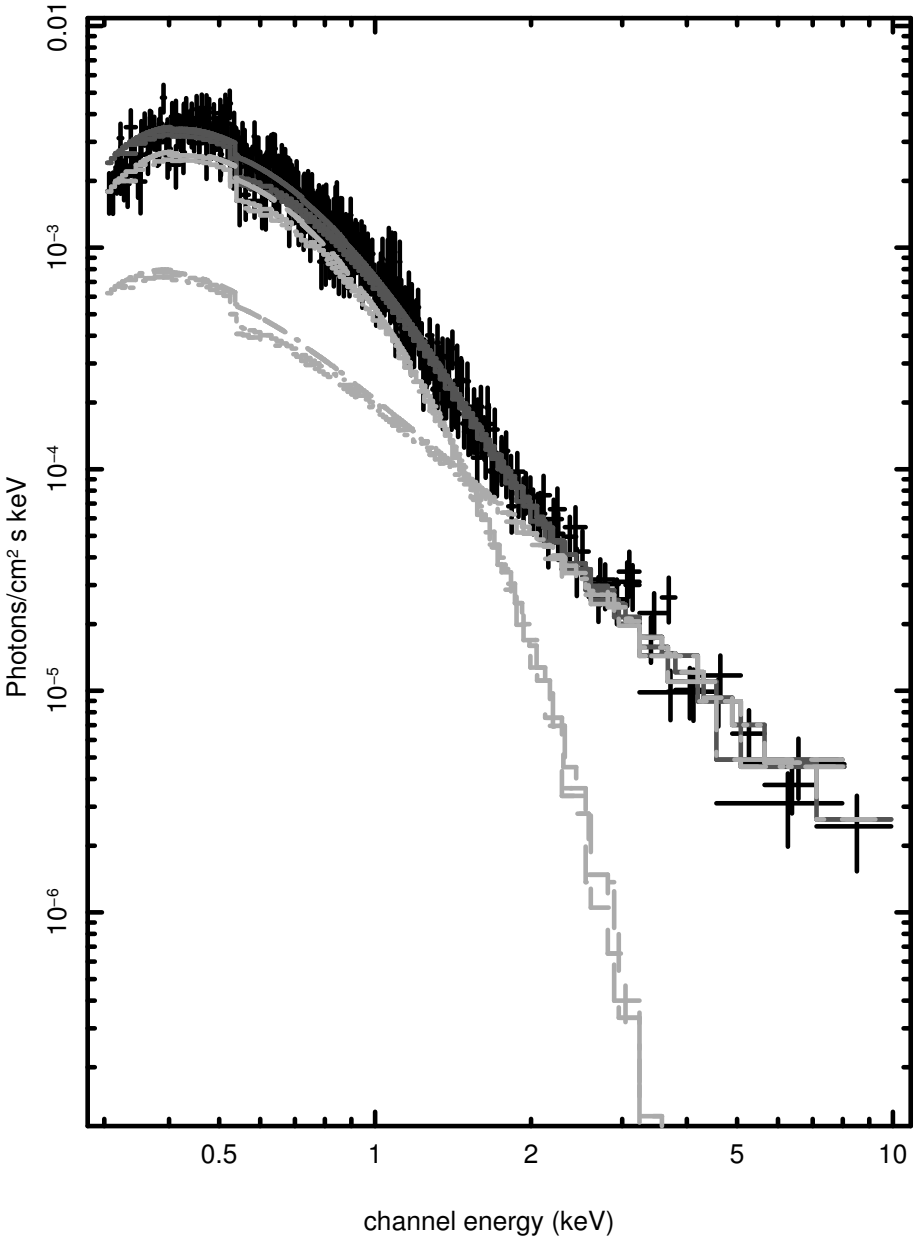

Figure 3.2: Plot of the EPIC unfolded spectrum for the NGC 5408 XMM1 ULX with the high mass solution (see Table 3.2). In the plot, the absorbed `grad` and absorbed power law model components are plotted with light gray lines while the combined model is plotted in dark gray. The thermal component clearly dominates the low energy spectrum with this model.

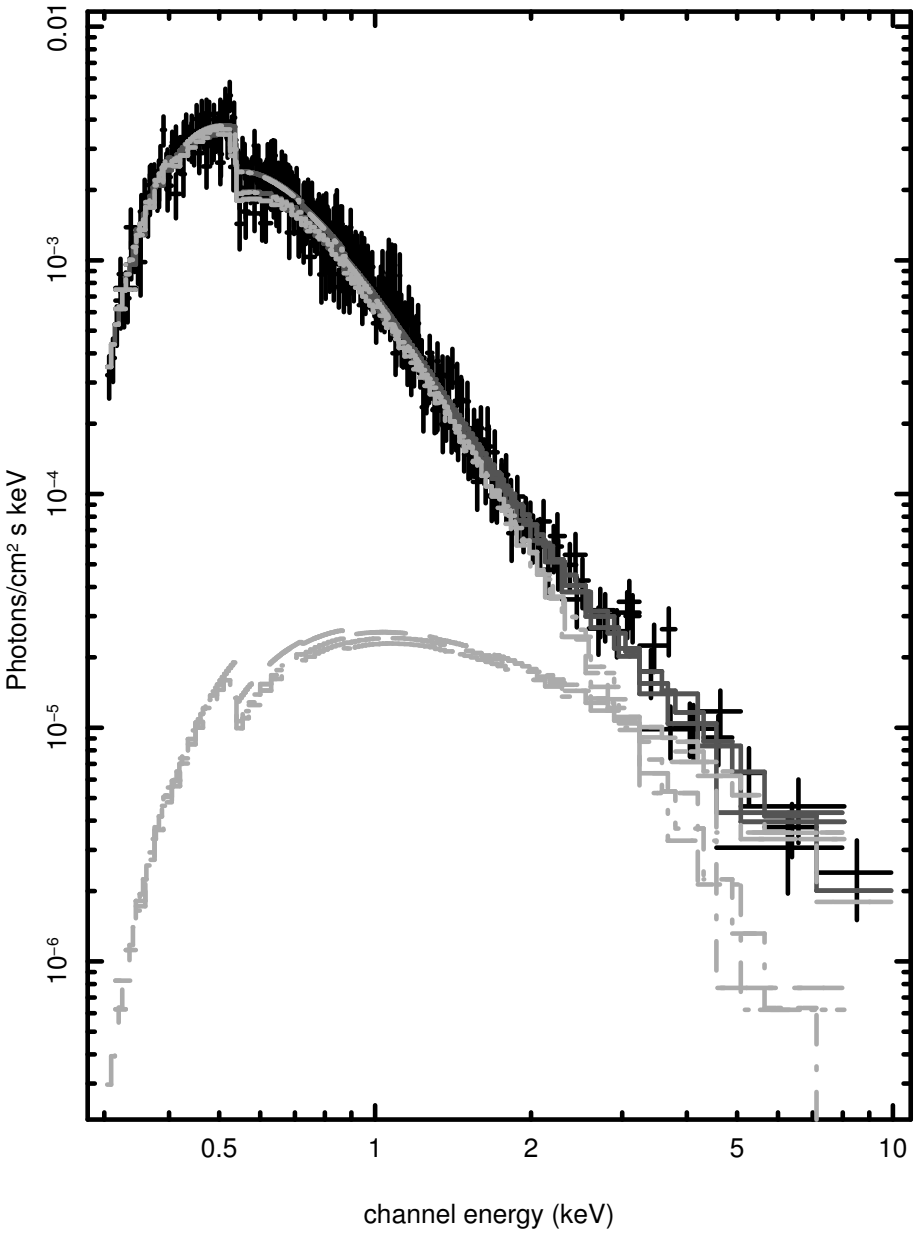

Figure 3.3: Plot of the EPIC unfolded spectrum for the NGC 5408 XMM1 ULX with the low mass solution (see Table 3.5). In the plot, the absorbed `grad` and absorbed power law model components are plotted with light gray lines while the combined model is plotted in dark gray. Notice that the low energy spectrum is dominated by the power law component with a weak contribution from the disk model (`grad`).

Table 3.5. Spectral Fits for Sources with Degenerate Solutions

Source	n_H[a]	O abund.[b]	Fe abund.[b]	Mass ($M_\odot$)	$\dot{M}/\dot{M}_{Edd}$[c]	Γ	χ^2/dof	counts[d]
HolmII XMM1	$0.20^{+0.04}_{-0.04}$	$0.83^{+0.17}_{-0.27}$	$1.11^{+0.83}_{-1.11}$	$2.24^{+1.52}_{-1.24}$	$7.79^{+1.52}_{-1.95}$	$3.10^{+0.31}_{-0.30}$	0.99	43116
HolmIX XMM1	$0.39^{+0.13}_{-0.12}$	$1.05^{+0.21}_{-0.33}$	$2.08^{+0.95}_{-1.45}$	$3.91^{+1.47}_{-1.59}$	$22.0^{+1.79}_{-2.86}$	$3.51^{+0.79}_{-0.87}$	0.64	28108
NGC253 XMM2	$0.18^{+0.17}_{-0.08}$	$1.10^{+0.42}_{-0.55}$	$1.32^{+1.90}_{-1.32}$	$6.82^{+4.19}_{-2.22}$	$1.27^{+0.71}_{-0.40}$	$2.15^{+0.84}_{-0.58}$	0.93	20651
NGC5204 XMM1	$0.18^{+0.05}_{-0.04}$	$1.00^{+0.30}_{-0.40}$	$0.0^{+0.59}_{-0.0}$	$3.21^{+0.98}_{-0.95}$	$6.86^{+0.67}_{-0.09}$	$3.28^{+0.39}_{-0.38}$	0.95	16717
...	$0.20^{+0.06}_{-0.05}$	$0.63^{+0.35}_{-0.48}$	$0.0^{+0.62}_{-0.0}$	$2.95^{+2.13}_{-1.84}$	$7.37^{+1.35}_{-2.08}$	$3.16^{+0.50}_{-0.44}$	0.94	13864
NGC300 XMM1	$0.21^{+0.05}_{-0.03}$	$1.59^{+0.22}_{-0.26}$	$0.0^{+0.53}_{-0.0}$	$1.69^{+0.85}_{-0.32}$	$0.73^{+0.18}_{-0.13}$	$3.89^{+0.21}_{-0.32}$	1.00	11479
N4559 X-7	$0.20^{+0.06}_{-0.05}$	$0.34^{+0.38}_{-0.34}$	$0.0^{+0.48}_{-0.0}$	$5.79^{+2.82}_{-2.75}$	$6.63^{+1.44}_{-2.42}$	$3.13^{+0.55}_{-0.50}$	0.83	12506
NGC5408 X-1	$0.18^{+0.05}_{-0.04}$	$0.87^{+0.28}_{-0.42}$	$0.45^{+1.75}_{-0.45}$	$2.29^{+1.57}_{-1.28}$	$4.87^{+1.23}_{-1.02}$	$4.09^{+0.28}_{-0.34}$	0.89	10045

[a]Hydrogen column density determined from `tbvarabs` in units of 10^{22} cm^{-2}. The Galactic value of n_H was fixed to the Dickey & Lockman (1990) value with the `tbabs` model.

[b]Element abundance relative to the Wilms solar abundance from the `tbvarabs` model

[c]Ratio of mass accretion rate from the `grad` model to Eddington accretion rate (see § 3.4)

[d]Total number of photon counts from pn and MOS detectors

In Stobbart et al. (2006), the authors discussed the same issues in fitting the XMM spectra of 13 ULXs. They found that two sources, M33 X-8 and NGC 2403 X-1, were best fit by the model with a power law fit to the low energy portion and thermal model at higher energy. They also indicated six sources where an ambiguity existed between the two models. To understand the spectra of the sources where both models provided good fits to the data, we further investigated the spectra of sources with multiple observations.

For Holmberg II X-1 and Holmberg IX X-1 our spectral fits include multiple observations (a shorter and a 100 kilo second observation). For each of these sources, we found that the shorter observation could be fit with either a high mass or low mass solution. When we fit the 100 kilo second observation, however, the high mass model was a much better fit. The $\Delta\chi^2$ values between the high mass and low mass solutions for the 100 kilo second observations were 135 and 88, respectively. To test this further, we also fit a 100 kilo second observation of NGC 5408 XMM1 with both of these models. This observation (0302900101)

was a proprietary observation at the time of publication for this chapter. The spectral and temporal analysis are now available in Strohmayer et al. (2007). We processed the pn data with SAS 6.5, following the same procedure as noted in the Data Reduction section. Fitting the spectrum with both models (high mass and low mass solution) we found a $\Delta\chi^2$ value of 170, favoring the high mass model.

Thus, we find that for sources that are well fit by either model (showing a degenerate solution of either high mass or low mass/steep power law) the high mass solution is the best fit when a higher count spectrum is obtained (as for Holmberg IX XMM1, Holmberg II XMM1, and NGC 5408 X-1). Though we list the alternate model column density and absorption values in Table 3.5, we use the parameters listed in Table 3.2 throughout the paper (the high mass solutions).

As noted, M33 X-8 and M81 XMM1, sources with very high number of counts, were not well-fit with a standard disk at low energy, power law at high energy model. They were best fit with the steep low energy power law and hot disk model shown in Figure 3.3. Along with these sources, NGC 4559 X-10 and M83 XMM1 were also well-fit by this model. We will further discuss these sources in the following subsection.

3.4.3 Physical Plausibility of the Accretion Disk models

In Chapter 2, we had found that ULX spectra are consistent with the high/soft and low/hard states of Galactic black holes. We had classified the sources studied in this chapter as consistent with the high/soft state. The high/soft state, as stated earlier, is characterized by emission from an accretion disk and a Comptonized power law tail. In order to investigate whether the mass and accretion rate results from the `grad` model make physical sense in terms of the X-ray binary model, we present a comparison of the derived accretion rate in Eddington

accretion rate units versus the mass in Figure 3.4. The parameter $\dot{M}_{Edd}$ was computed as $\dot{M}_{Edd} = \frac{1.3\times10^{38}M}{\eta c^2}\,\mathrm{g\,s^{-1}}$ where η, the efficiency factor, was set to 0.06 and M is the value M_{grad}. We find that for the sources with $\mathrm{M}_{grad} > 100\,\mathrm{M}_{\odot}$, the accretion rate is computed to be below 40% of the Eddington rate. This is assuming, as the `grad` model assumes, a Schwarzschild black hole. Noting that $\dot{M}/\dot{M}_{Edd}$ is equivalent to $\mathrm{L}/\mathrm{L}_{Edd}$ for most disk solutions, the $\mathrm{L}/\mathrm{L}_{Edd}$ values for the sources with $\mathrm{M}_{grad} > 100\,\mathrm{M}_{\odot}$ are consistent with those of Galactic black hole X-ray binaries in the high state ($\mathrm{L}/\mathrm{L}_{Edd} \approx 0.05 - 1.0$) (McClintock et al. 2004). Thus, the sources with $\mathrm{M}_{grad} > 100\,\mathrm{M}_{\odot}$ do have accretion rates that are predicted from scaling up (in mass) observed high state Galactic black holes. In addition, the spectral fit parameters for NGC 4631 XMM1, with an estimated mass of $5.5\,\mathrm{M}_{\odot}$ and an accretion rate $\mathrm{L}/\mathrm{L}_{Edd}$ of 0.84, are also consistent with the standard high state Galactic black hole model. This source is likely a normal stellar mass black hole X-ray binary in an external galaxy.

The remaining sources with $\mathrm{M}_{grad} << 100\,\mathrm{M}_{\odot}$ (M33 X-8, M81 XMM1, NGC 4559 X-10, and M83 XMM1) yielded $\mathrm{L}/\mathrm{L}_{Edd}$ ratios in the range of 1 – 3. These sources are also those described in the previous section where the power law component fits the low energy spectrum. They are also well fit by a Comptonization model and correspond to a sub-class of high luminosity ULXs described in § 2.4.3. Due to the luminosity and modeled disk temperature ($\mathrm{kT} \approx 1\,\mathrm{keV}$), we suggested that these sources were very high state stellar mass black hole systems. In order to be consistent with the black hole accretion model assumed in this study, the spectra of these sources should be the result of Comptonization from a thermal disk spectrum.

To test this further, we fit the spectrum of the highest count source of this type (M33 X-8) with an absorbed thermal disk and Comptonization model

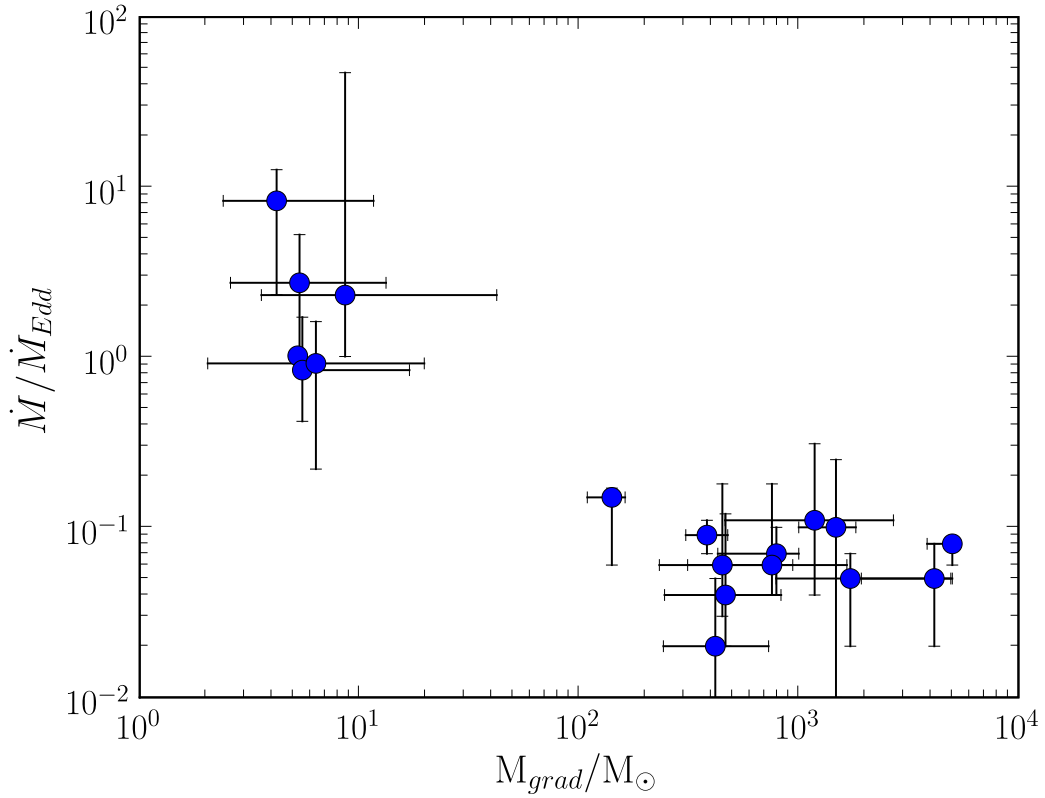

Figure 3.4: Black hole mass versus mass accretion rate (per Eddington accretion rate) obtained from the general relativistic disk model (`grad`). The sources with model parameters indicating high masses correspond to accretion rates that are below 40% of the Eddington accretion rate for the given mass. In Chapter 2, we noted a temperature gap in the range of 0.26 keV to 0.50 keV from spectral fits utilizing an absorbed blackbody and power law model. In this figure, we see that there is a gap in mass from the parameters of the absorbed general relativistic disk and power law model. The values shown are results for the EPIC spectra only, as recorded in Table 3.2 (for all sources in Table 3.2). Therefore, there are multiple points for the sources with multiple observations. We plotted these sources (Holmberg II XMM1, Holmberg IX XMM1, M81 XMM1, and NGC 5204 XMM1) twice to confirm that their masses, as determined by the `grad` model, do not vary.

(tbabs*tbabs*(diskpn + comptt)). The comptt model has the parameters: a seed temperature (keV), a plasma temperature (keV), and optical depth of the medium. We used the diskpn model in place of the grad model since the former provides a disk temperature to which the comptt seed temperature can be fixed. This provides a physical model, where the thermal disk supplies the energy for the Compton tail. M33 X-8 was well fit by this model with a $\Delta\chi^2$/dof = 1659.9/1534 (1.08). Thus, these sources are still consistent with the black hole accretion model. Replacing the tbabs model used for the galactic column density with the tbvarabs, we measured the column density, oxygen abundance, and iron abundance. With this thermal disk and Comptonization model we obtained $\mathrm{n}_H = 1.5^{+0.04}_{-0.08} \times 10^{21}\,\mathrm{cm}^{-2}$, $\mathrm{O/H} = 1.26^{+0.08}_{-0.15}$, and $\mathrm{Fe/H} = 2.83^{+0.71}_{-0.76}$, with a $\Delta\chi^2$/dof = 1577.3/1534 (1.03). Within the error bars, these results are consistent with those seen in Table 3.2.

3.5 Properties of the ISM in ULX Host Galaxies

The major question to be examined in using ULXs as probes of the ISM is whether the hydrogen column density and element abundances are primarily from the host galaxy or intrinsic to the local environment of the ULX. Before we can answer this question, it is important to understand the intrinsic spectrum of the source. In the previous section we discussed the nature of the soft component in light of the high signal-to-noise spectra of the 14 ULX sources we examined. We found that if the spectrum is due to thermal emission from a disk, modeling the spectrum with a variety of disk models (grad, diskbb, diskpn, bbody) does not significantly change the measured oxygen abundance or hydrogen column density.

Assuming the reliability of the hydrogen column density and abundance mea-

surements, based on their model independent values, we investigate the source of the absorption in ULX spectra. In order to determine whether the model n_H values suggest the necessity of extra local absorption, we compare the model values with column densities obtained from H I studies. We investigate this in § 3.5.1. The oxygen abundances (as an indication of metallicity), which we examine in § 3.5.2, can provide further clues of whether the absorption we see in the X-ray spectrum is intrinsic to the source. We also examine possible connections between the host galaxy's star formation rate and elemental abundances.

3.5.1 Column Densities

To determine whether the ULX X-ray hydrogen column densities represent largely galactic column densities or column densities local to the ULX, we compared the X-ray values to those obtained from optical and radio studies. For a comparison to hydrogen column densities from optical studies, we used interstellar reddening values. In a study of dust scattering X-ray halos surrounding point sources and supernova remnants, Predehl & Schmitt (1995) derived a relationship between hydrogen column density and interstellar reddening, using X-ray data. They found that $n_H = 5.3 \times 10^{21} cm^{-2} E_{B-V}$. They also found that these X-ray derived column densities are not affected by the intrinsic absorption of the X-ray source. Thus, the optical reddening, E_{B-V}, becomes a useful tool in checking our own X-ray derived column densities. Through a literature search, we found E_{B-V} values for the sources M33 X-8 (0.22; Long et al. (2002)) and M81 XMM1 (0.23; Kong et al. (2000)). The corresponding E_{B-V}-derived n_H values are plotted in Figure 3.5 as triangles.

For a comparison of X-ray derived hydrogen column densities with radio values, we obtained H I column densities for four objects (Holmberg II XMM1,

Table 3.6. Alternative Column Density Measurements

Source	n_H[a]	Method[b]
NGC 247 XMM1	0.316	H I
M33 X-8	0.170	E_{B-V}
HolmII XMM1	0.157	H I
M81 XMM1	0.122	E_{B-V}
M81 XMM1	0.078	H I
HolmIX XMM1	0.148	H I
NGC 4559 X7	0.357	H I
NGC 4559 X10	0.300	H I
NGC 5204 XMM1	0.182	H I

[a]Hydrogen column density (galactic, not Milky Way) determined by the method indicated in units of 10^{22} cm^{-2}.

[b]Method used to compute the corresponding column densities, either from reddening values (E_{B-V}) or from radio H I measurements, see § 3.5.1 for details.

NGC 4559 X7, NGC 4559 X10, and NGC 5204 XMM1) from the WHISP catalog (Swaters et al. 2002). These are radio H I column densities within the host galaxy (galactic), not the Galactic/Milky Way columns. Exact values of the H I column densities were computed and given to us by Rob Swaters. Additionally, we include H I column densities of NGC 247 XMM1, M81 XMM1, and Holmberg IX XMM1 from Braun (1995). We obtained the FITS files of H I column density maps from this paper (available on NED), where the pixel value corresponds to the galactic column density in units of 10^{18} cm^{-2}. The H I derived n_H values from both studies are plotted in Figure 3.5 as circles. The column densities, from the radio and reddening studies, are listed in Table 3.6.

We find that the host galaxy column densities from alternate methods (optical or radio studies) are not significantly different from the X-ray column densities.

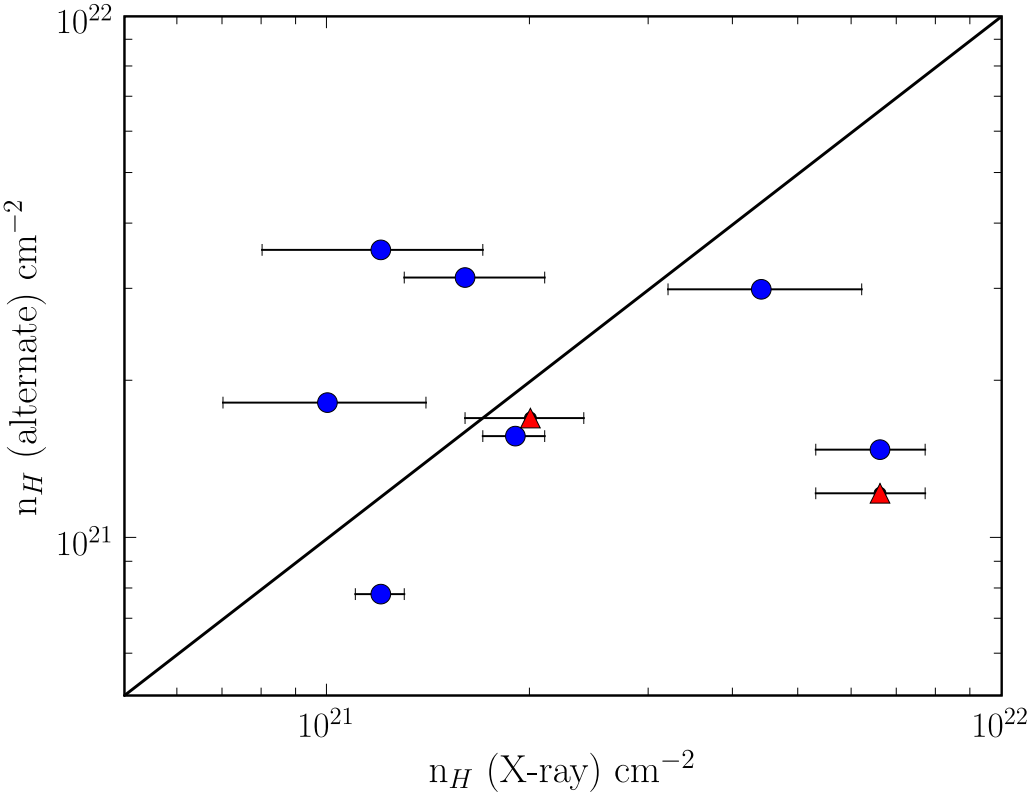

Figure 3.5: Hydrogen column density from E_{B-V} (red) or H I studies (blue) vs. the hydrogen column density obtained from the `tbvarabs` model. H I column densities were obtained for Holmberg II, NGC 5204, and NGC 4559 through the WHISP survey (Swaters *et al.* 2002). Additional H I column densities were obtained for NGC 247, Holmberg IX, and M81 through VLA data (Braun 1995). The X-ray spectral fit columns are not biased towards significantly higher values than the alternate method column densities. This implies that most of the matter in the line of sight is from H I. This is not true, however, for the source M81 XMM1 (represented by the two outlying points in the lower right portion of the graph) where the X-ray column density is much greater than those from the optical and radio.

Particularly, the X-ray values are not skewed towards substantially higher values than the optical/radio values. Thus, the X-ray columns are likely the galactic values without any additional local absorption. The exception, however, is M81 XMM1 (represented by 2 points in Figure 3.5, one for each of the methods). The E_{B-V} value (1.22×10^{21} cm^{-2}) and the H I value (0.78×10^{21} cm^{-2}) are significantly lower than the X-ray column density. This may indicate the presence of extra absorption around this source.

The result that the X-ray hydrogen column densities are in good agreement with those from H I studies and interstellar extinction values is interesting considering that the X-ray measured column densities are along a direct line of sight to the ULXs while the H I measurements are an average over a larger beam area. The agreement between the two measurements implies that the ULX sources, with the exception of M81 XMM1, lie within roughly normal areas of their local host galaxies (i.e. not in regions of higher column density such as a molecular cloud). However, this only applies to the local galaxy region surrounding the ULX and does not quantify whether the local galaxy region is different from the galaxy at large (e.g. local star formation in a galaxy undergoing little star formation on average).

3.5.2 Elemental Abundances

Test for Oxygen Ionization Level

Before discussing implications of the determined oxygen and iron abundances, we relate a test performed to determine whether we could distinguish between different ionization levels of oxygen. To do this, we used the absorption edge model, `edge`, in XSPEC (using the full model:

`tbabs*tbvarabs*edge*edge*(grad + pow)`). We first checked to see that the abundance values obtained with the edge model matched the values from the `tbvarabs` model. We fixed the oxygen abundance in the `tbvarabs` model at zero and added the edge model, allowing the threshold energy and absorption depth (τ) to float as free parameters (with an initial energy set to 0.543 keV). We fit this model to the longest observations of Holmberg II XMM1 and Holmberg IX XMM1 in addition to a source with a lower number of counts, NGC 5408 XMM1 (0112290601).

To find the oxygen column density (n_O), we used the relationship that $\tau = \sigma \times n_O$, where σ is the cross section for photoabsorption. We used the cross section values for neutral oxygen published in Reilman & Manson (1979) as an estimate. This choice is supported by the results of Juett et al. (2004), who measured the ratio of oxygen ionization states in the ISM as O II/O I≈ 0.1. In Table 3.7, the hydrogen column density, threshold energy, and optical depth are listed for the sources fit with this model. From Reilman & Manson (1979) we used the cross section values of $\sigma = 5.158 \times 10^{-19}$ cm^2 (for $E = 0.540$ keV) and $\sigma = 4.789 \times 10^{-19}$ cm^2 (for $E = 0.570$ keV). As seen in Table 3.7, the hydrogen column densities and the oxygen abundances obtained from this model are close to those from the `tbvarabs` model. The [O/H] values, where [O/H] = 12 + log(O/H) and O and H represent oxygen column density and hydrogen column density respectively, between the two models vary by less than 1%.

To test whether the threshold energy from the edge model is affected by the ionization level of oxygen, we simulated spectra of an absorbed power law model with an oxygen edge. Tim Kallmann (P.C.) provided us with an oxygen edge model incorporating the cross sections of García et al. (2005). The model allows for a variation of the ratio of O II/O I. Using the response and ancillary response

Table 3.7. Spectral Fits to the Oxygen Edge

Source	n_H[a]	E[b]	τ[c]	n_O[d]	[O/H][e]	χ^2/dof	counts[f]
HolmII XMM1	$0.16^{+0.01}_{-0.01}$	$0.566^{+0.01}_{-0.01}$	$0.35^{+0.02}_{-0.01}$	7.2	8.65/8.64	2543/2017	342874
HolmIX XMM1	$0.19^{+0.02}_{-0.02}$	$0.543^{+0.01}_{-0.01}$	$0.62^{+0.11}_{-0.12}$	12.0	8.81/8.82	2887/2751	148061
NGC 5408 XMM1	$0.17^{+0.06}_{-0.03}$	$0.538^{+0.04}_{-0.02}$	$0.37^{+0.29}_{-0.21}$	7.1	8.61/8.63	298/334	10045

[a]Hydrogen column density determined from `tbvarabs` in units of 10^{22} cm^{-2}. The Galactic value of n_H was fixed to the Dickey & Lockman (1990) value with the `tbabs` model.

[b]Threshold Energy obtained from the *edge* model in keV. Note that one `edge` model was used to correct for the difference in the oxygen edge between the pn, MOS1, and MOS2 CCDs. The other `edge` model was used to measure the oxygen abundance from the 542 eV K-shell edge.

[c]Absorption depth obtained from the `edge` model

[d]Column density of oxygen estimated from the `edge` model in units of 10^{17} cm^{-2}

[e]Abundance of oxygen relative to hydrogen from the `edge` model versus the value quoted in Table 3.2, [O/H] = 12 + log(O/H) where O is oxygen abundance and H is hydrogen abundance

[f]Total number of photon counts from the pn and MOS detectors

matrices from the long Holmberg II ULX observation, we simulated spectra with the XSPEC `fakeit` command for a $\Gamma = 2.35$ power law. We simulated spectra for O II/O I ratios of 0.0, 0.2, 0.4, 0.6, 0.8, and 1.0. The simulated spectra were binned with a minimum of 20 counts/bin. The absorption edge component of the spectrum was then fit with the `edge` model. The fits to the threshold energies for the simulated spectra yielded values ranging from 0.53-0.59 keV, with no preference of lower O II/O I ratios corresponding to lower threshold energies. Since the O I absorption edge occurs at E= 0.543 keV and the O II absorption edge occurs at E= 0.57 keV, we could not distinguish between these ionization states of oxygen. Our simulations show that the oxygen `edge` measurements will be sensitive to O I and O II but not to high ionization states (for instance O VIII which has an edge energy of 0.87 keV).

X-ray/optical [O/H] Comparison

As noted above, we tested the oxygen abundances obtained with the absorption model `tbvarabs` against the abundances obtained from adding a photo-electric absorption edge model, for three of the ULX sources. We found good agreement ($< 1\%$ difference in [O/H] values) between both models for the X-ray spectra. However, we found that it is not possible to distinguish between different low ionization states of oxygen using the edge model.

We now discuss comparisons of our X-ray oxygen absorption values with measurements in different wavelengths, based on a literature search for [O/H] ratios. In Figure 3.6 we compare our [O/H] ratios with those of a study conducted by Pilyugin et al. (2004) (black). They provide a compilation of [O/H] ratios determined through spectrophotometric studies of H II regions. Their [O/H] values are based on the radial distribution of oxygen abundance using the P-method. This method uses an abundance indicator from easily measurable oxygen lines (R_{23} =([O II]$\lambda\lambda$3727, 3729 + [O III]$\lambda\lambda$4959, 5007)/ H-β) along with an excitation parameter. Using this method, Pilyugin et al. (2004) determined [O/H] values for spiral galaxies where published spectra were available for at least 4 H II regions. In addition, they reference [O/H] values for irregulars obtained through alternate methods. Our [O/H] values are determined from the oxygen abundances listed in Table 3.2. Thus, [O/H]$= 12 + \log(O \times 0.00049)$. O is the oxygen abundance obtained from the model, which is multiplied by the Wilms relative abundance of 4.9×10^{-4} of oxygen to hydrogen. We were able to compare [O/H] values for 8 sources with the P-method values (M33, NGC 253, NGC 300, M81, Holmberg II, NGC 4559, and NGC 5408). We include the [O/H] value computed for the Holmberg IX ULX by Miller (1995) of 8.12. This value was computed from an optical study of the surrounding H II region. Also, we add the [O/H] value of 8.4 for

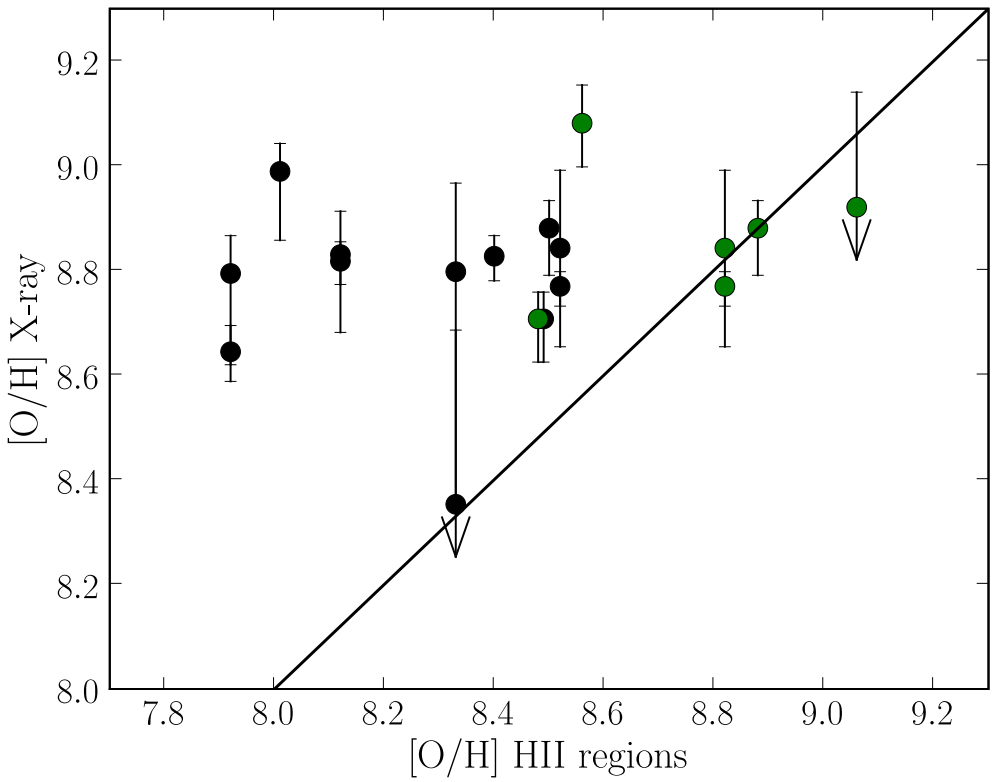

Figure 3.6: Oxygen abundances from studies of H II regions vs. oxygen abundances from the `tbvarabs` model. The [O/H] ratios are given for Holmberg II XMM1, NGC 5408 XMM1, Holmberg IX XMM1, NGC 4559 XMM1, NGC 4559 XMM2, NGC 1313 XMM3, M33 X-8, NGC 300 XMM1, NGC 253 XMM2, and M81 XMM1 using the P-calibration method (black). Also, [O/H] ratios are included for M33 X-8, NGC 300 XMM1, M81 XMM1, NGC 253 XMM2, and M83 XMM1 using the R_{23} calibration method (green). Arrows indicate that the lower limit for the [O/H] X-ray parameter is below the plotted graph region. Our values are high compared to the P-method but in good agreement with the R_{23} method. The sources with the largest difference between [O/H] values are those located in irregular galaxies.

NGC 1313, determined separately by both Calzetti et al. (1994) and Walsh & Roy (1997).

As shown in Figure 3.6, our [O/H] values are consistently high compared to those obtained from the Pilyugin et al. (2004) H II study. Pilyugin et al. (2004) include a discussion of how their values, obtained by the P-calibration method, are

significantly lower than those obtained by Garnett (2002) using the R_{23}-calibration method. This method computes O/H at the B-band effective or half-light radius of the disk. In Figure 3.6 we include [O/H] values for NGC 253, NGC 300, M33, M81, and M83 from Garnett (2002) (green). Our oxygen abundances are in much better agreement with the values from this R_{23}-calibration method.

Our [O/H] values, which are consistent in the X-ray band between two separate absorption models, (`tbabs*tbvarabs*edge*(grad + pow)` and an `tbabs*edge*edge*(grad + pow)` model), are consistent with the values of Garnett (2002). We further wish to compare them to the metallicity predicted from Sloan Digital Sky Survey (SDSS) results. As a result of a SDSS study, Tremonti et al. (2004) found a luminosity-metallicity relation for their sample of star-forming galaxies of: $12 + \log(O/H) = -0.185(\pm 0.001)M_B + 5.238(\pm 0.018)$. In Figure 3.7 we compare our values with their results (represented by the line). We obtained absolute magnitudes (M_B) for the host galaxies using the total apparent corrected B-magnitude recorded in the HyperLeda galaxy catalogue (Paturel et al. 1989)(parameter *btc*) and the distances listed in Table 2.1. For M33 and NGC 4559, which were not included in the previous study, we used the distances of 0.7 Mpc and 9.7 Mpc from Ho et al. (1997). The majority of our sources are consistent with the SDSS results. However, the sources in low luminosity irregular galaxies have metallicities much higher than predicted.

Galaxy Properties

More luminous galaxies are sometimes expected to have higher star formation rates, and thus higher metallicity. However, we found no evidence of this. Investigating further into the relationship between star formation rate (SFR) and metallicity, we chose to look at a galactic luminosity diagnostic that is less dependent

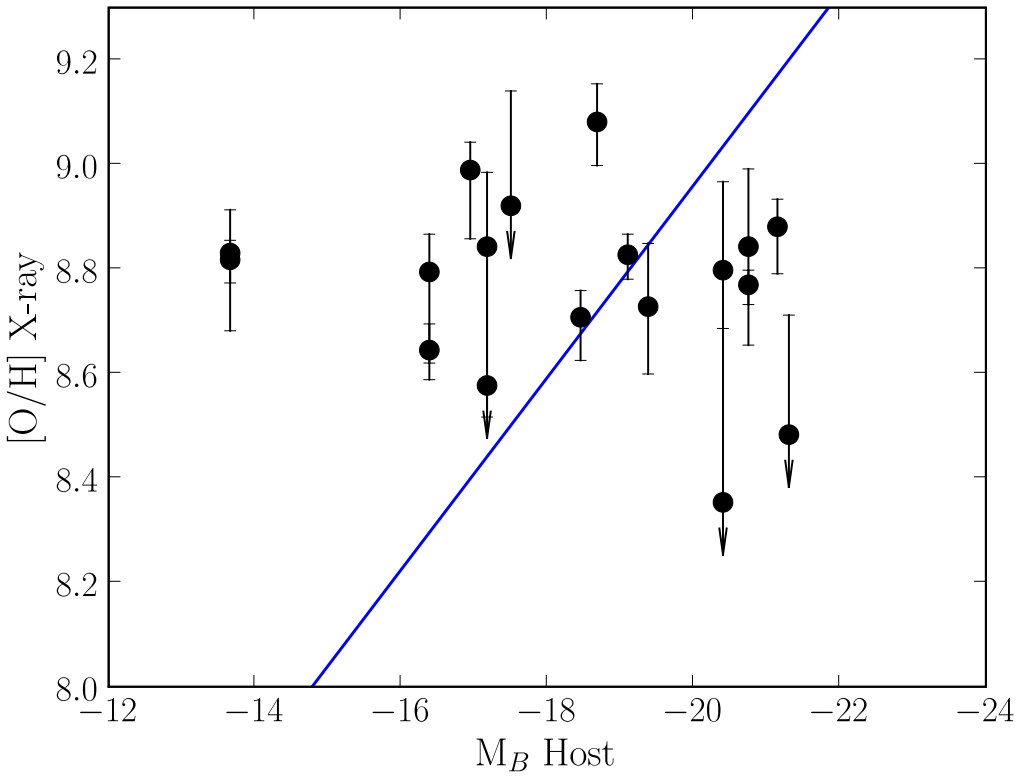

Figure 3.7: Host galaxy M_B vs. ULX X-ray [O/H] ratio. The solid line represents the SDSS results from a study of star-forming galaxies (Tremonti et al. 2004). Arrows indicate that the lower limit for the [O/H] X-ray parameter is below the plotted graph region. Our values are largely consistent with the Sloan results, with the exception of Holmberg IX and Holmberg II. Both of these galaxies are irregulars. The X-ray [O/H] ratio derived from the ULX spectra is higher than predicted for these objects.

on extinction from dust, the infrared galactic luminosity (L_{FIR}). In Chapter 2, we calculated L_{FIR} using data from the *Infrared Astronomical Satellite* and the approach of Swartz et al. (2004). We quoted values of L_{FIR} in Chapter 2. Using the same method, with IRAS fluxes obtained from Ho et al. (1997), we find M33 to have $L_{FIR} \approx 1.7 \times 10^{42}\,\mathrm{erg\,s^{-1}}$ and NGC 4559 to have $L_{FIR} \approx 7.4 \times 10^{42}\,\mathrm{erg\,s^{-1}}$. We used these L_{FIR} values to compare the SFR to both the oxygen and iron abundances.

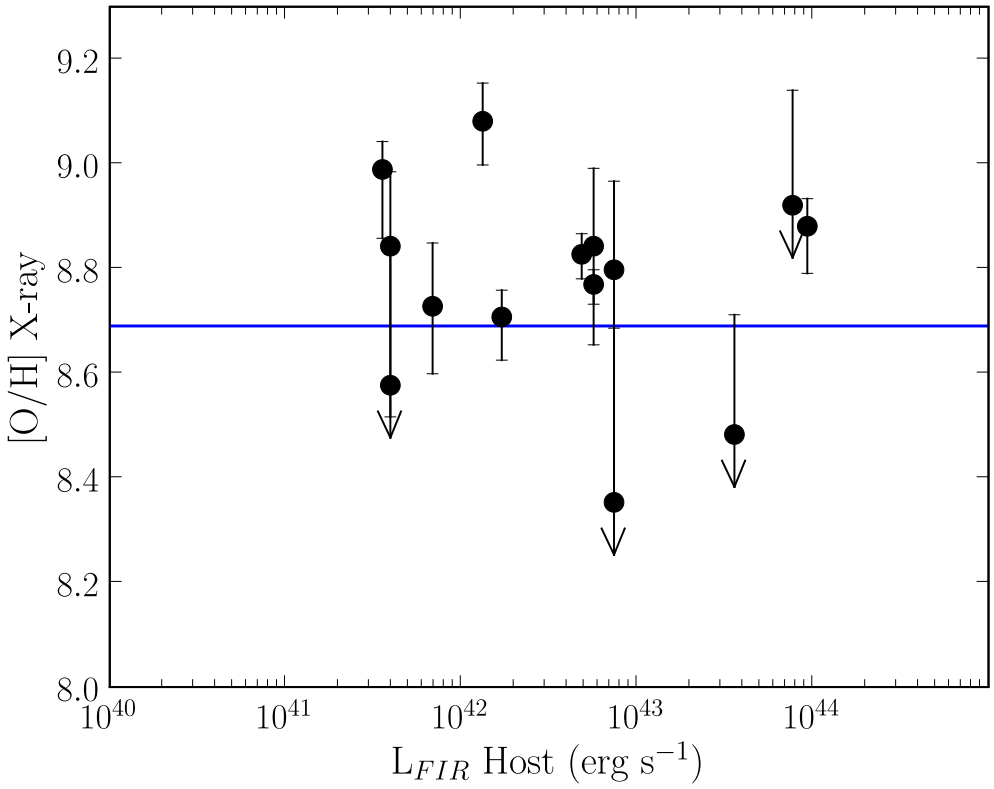

Figure 3.8: Oxygen abundance ([O/H]) as a function of the host galaxy's FIR luminosity, obtained from IRAS. The line represents the Wilms solar value of [O/H] . Arrows indicate that the lower limit for the [O/H] X-ray parameter is below the plotted graph region. There appears to be no correlation between L_{FIR} and oxygen abundance. In fact, the sources show roughly solar [O/H] abundances regardless of host galaxy.

In Figure 3.8, we plot oxygen abundance relative to SFR. All sources with the exception of Holmberg IX XMM1, which did not have available IRAS data, are plotted. We see, as was also illustrated in Figure 3.7, that the luminosity of the host galaxy does not determine the metallicity. The more luminous galaxies do not have metallicities higher than the less luminous galaxies. In fact, most sources have oxygen abundances that are roughly the Wilms solar abundances (indicated by the line).

In Figure 3.9 we see that there is no relationship between iron abundance (see

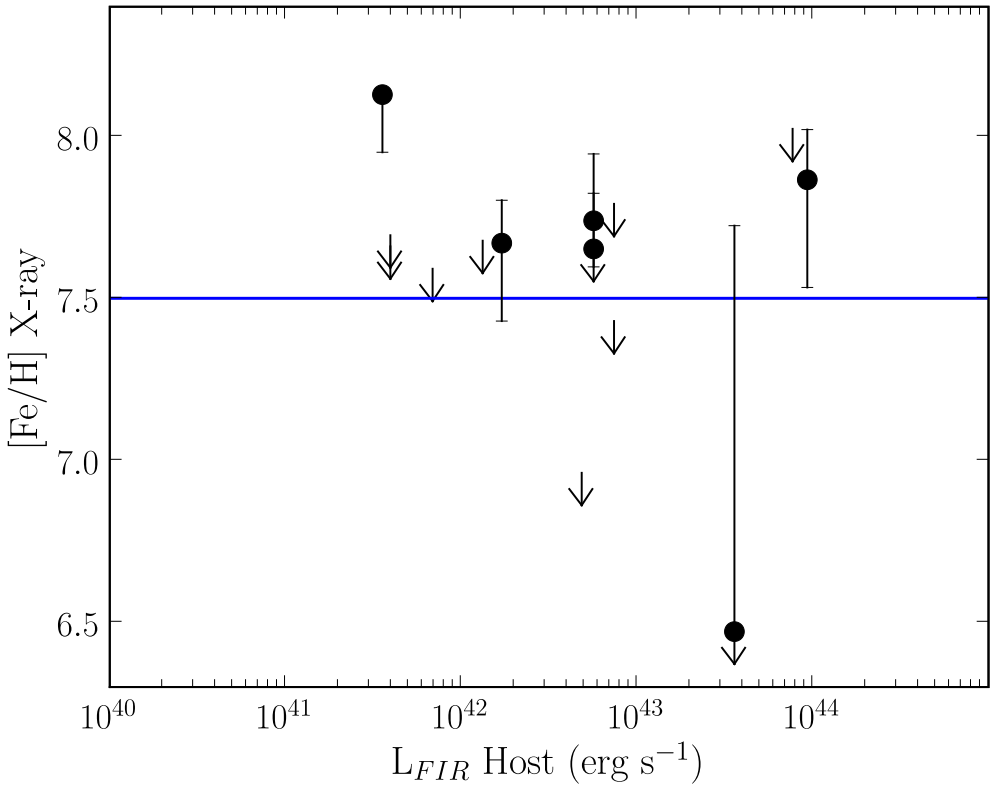

Figure 3.9: Iron abundance ([Fe/H]) as a function of the host galaxy's FIR luminosity obtained from IRAS. Holm IX did not have corresponding IR data, however, being an irregular galaxy, its L_{FIR} would probably be comparable to Holm II. The iron abundances of both of the irregulars are well above those of the ULXs in spiral galaxies. The sources in galaxies with larger L_{FIR} have roughly equal iron abundances, within the error bars. The iron abundances in all cases are well above the Wilms solar abundance. Arrows indicate that the lower limit for the [Fe/H] X-ray parameter is below the plotted graph region.

values in Tables 3.2 and 3.3 for values) and SFR. The Wilms solar abundance for iron is only 2.69×10^{-5} relative the hydrogen abundance. The plots show that the metallicity relationship is very flat, all of the sources have roughly solar abundances. This is also seen in Figure 3.10. This plot shows the [Fe/H] ratios versus the [O/H] values, both obtained through the `tbvarabs` model. The solar Wilms values are represented on the plot by the open circle symbol. It appears that the sources are slightly more abundant in iron than the solar value, however, the er-

ror bars are quite large. The oxygen abundances, as before stated, are roughly the solar Wilms value. Roughly, the abundances appear solar.

With such a flat relationship between abundance and luminosity, we tested to see if this result carried through in a comparison of abundance versus radial distance within the host galaxy. This follows upon an interesting property observed in spiral galaxies. Namely, that abundances are typically higher in the center of the galaxy and decrease with increasing radius (Searle 1971). We tested how our results compare to this result in Figure 3.11. For the sources located within spiral galaxies, we plotted the [O/H] ratio as a function of distance R from the dynamical center (as reported by NED). We used the distances quoted in Table 2.1 to translate angular distance on the sky into kpc from the galactic center. As evidenced in the plot, we do not see much variation in the [O/H] values. Clearly, the expected scaling of higher oxygen abundance towards the center is not seen. Since the sources lie in different host galaxies with different relative abundances, it is possible that this trend may be detectable with a larger sample of galaxies. However, the implication from Figures 3.7 through 3.11 is that the environment of the ULX sources is relatively uniform in terms of metallicity. The ULX sources appear to live in similar environments, with metallicities roughly solar.

3.6 Summary

Through our work, we conclude that X-ray spectral fits to ULX sources do provide a viable method of finding abundances in other galaxies. We have determined hydrogen column densities and oxygen abundances along the line of sight to 14 ULX sources. To measure these values, we assumed a connection between ULXs and Galactic black hole systems such that the ULX spectra used in this

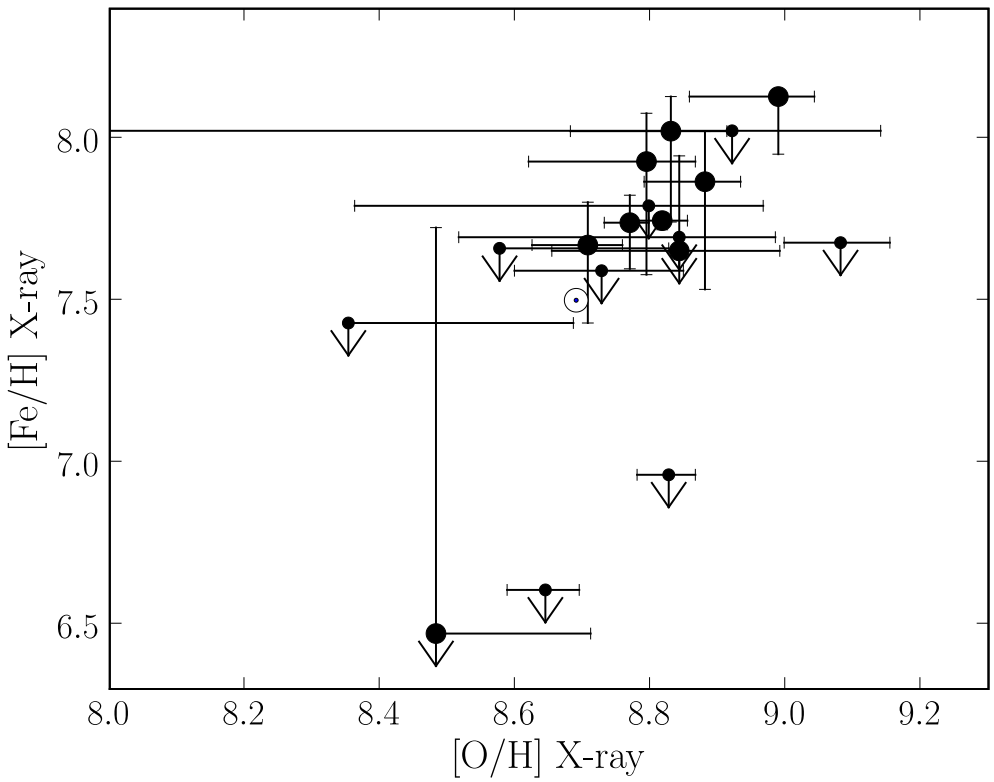

Figure 3.10: [Fe/H] as a function of [O/H] from the `tbvarabs` model, using the `grad` and power law fit. The Wilms solar abundance is indicated with an open circle. The ratio of Fe/O abundances obtained through the X-ray spectral fits are approximately the Wilms solar values. Arrows indicate that the lower limit for the [Fe/H] X-ray parameter is below the plotted graph region.

study correspond to a high/soft state. Therefore, we modeled the sources with an absorbed disk model and power law (in XSPEC `tbabs` *`tbvarabs`*(*accretion disk model* + `pow`)). We tested the effect different accretion disk models have on the measurement of the host galaxy's hydrogen column density and elemental abundance with the disk models: `grad`, `diskpn`, `diskbb`, and `bbody`. We found that the measured hydrogen column density and abundances are model independent.

We also tested the physical plausibility of this model by comparing the mass and mass accretion rates obtained from the `grad` model with expected results based on Galactic black hole systems. We found that the ULX spectra were con-

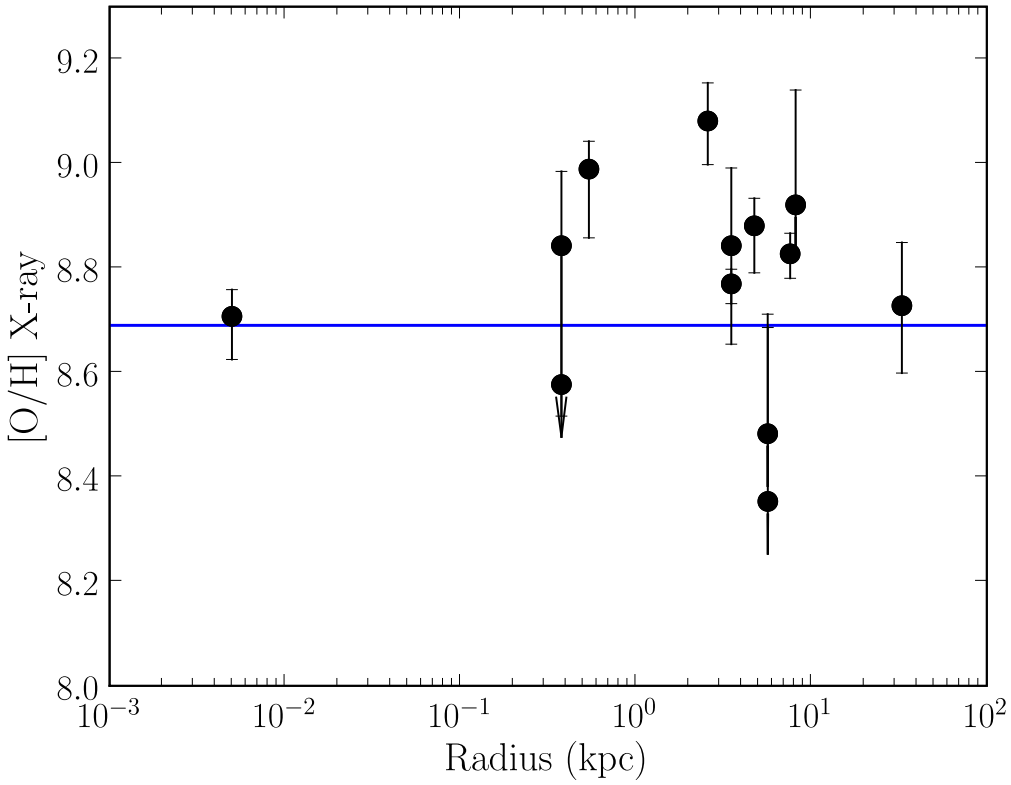

Figure 3.11: Oxygen abundances from the `tbvarabs` model vs. distance of the ULX from the host galaxy's dynamical center. The [O/H] ratios are given for spiral galaxies only. There is no correlation between radius and oxygen abundance in our sample. However, since the sources originate in different host galaxies with different abundances, there is no conclusion that can be drawn from this data. The host galaxy NGC 4559, containing two ULX sources studied, does appear to show a possible correlation (the source nearer the center has a higher oxygen abundance), however, the error bars on the oxygen abundance are large for both sources.

sistent with the high/soft state, with L/L_{Edd} values < 1.0 for sources with a standard thermal model at low energies and power law dominated higher energy spectrum. For four sources, the spectra were consistent with a heavily Comptonized spectrum. These sources are more likely stellar mass black hole systems in a very high state of accretion. We modeled their spectra with a power law at low energy and disk model around 1 keV. This model provided similar col-

umn density and abundance values to a more physical absorbed disk and Comptonization model.

Comparing our X-ray measured column densities with those from optical and H I studies for 8 of our sources, we find that 7 of the sources have X-ray column densities approximately equal to those of the alternate methods. This implies that the hydrogen columns towards most of our ULX sources represent that of their host galaxy. Since the H I studies represent averages over a large beam area where the X-ray column densities are directly along the line of sight to the ULX source, this implies that the ULX sources lie within roughly normal areas of their host galaxies, locally. However, without comparison with other lines of sight in the galaxy, we can not determine whether the local galaxy regions are different from the galaxy on average. The exception in this study was M81 XMM1, whose X-ray hydrogen column density was large relative to the H I study. This suggests that there is extra absorption intrinsic to this source.

The oxygen abundances appear to be roughly the Wilms solar values. For five sources, the count rates were sufficient to determine iron abundances without large error bars (see Figures 3.9 and 3.10). We found that iron abundances for these sources were slightly overabundant relative to the solar Wilms value. However, within error bars, the abundances appear solar. X-ray derived [O/H] values are comparable to those from an optical study by (Garnett 2002), indicating that the X-ray derived values are the same as the [O/H] values of H II regions within the host galaxy. Luminosity-metallicity relationships for the ULX host galaxies show a flat distribution, as does a radius-metallicity plot. Therefore, it appears that the ULX sources exist in similar environments within their host galaxy, despite the wide range of host galaxy properties.

Chapter 4

A Representative Sub-Sample of the SWIFT BAT AGN Survey

4.1 Introduction

Breaking with the focus of the previous two chapters, ULXs, the following two chapters discuss X-ray surveys of the SWIFT Burst Alert Telescope AGN survey. AGN surveys are typically dominated by two selection effects: (1) dilution by starlight from the host galaxy and (2) obscuration by dust and gas in the host galaxy and/or the AGN itself (see Hewett & Foltz (1994); Mushotzky (2004)). These factors previously kept an unbiased AGN sample from reach. However, with the capabilities of SWIFT's Burst Alert Telescope (BAT), this has changed. The BAT surveys the sky in the hard X-ray range of 14-195 keV. As of early 2006, BAT detected 153 AGN with a median redshift of 0.03 (Markwardt et al. 2005; Tueller et al. 2008). These AGN were selected purely by their hard X-ray flux, and thus, all but the most heavily absorbed sources ($n_H > 3 \times 10^{24}\,cm^{-2}$) are not affected by obscuration from gas and dust, which prevents them from being easily detected in UV, optical, or soft band X-ray surveys. Thus, the BAT survey

will provide the information necessary to derive the true distribution of AGN characteristics across the entire electromagnetic spectrum.

The 9-month BAT detection limit is $\approx 2 \times 10^{-11}\,\mathrm{erg\,s^{-1}\,cm^{-2}}$. Thus, the BAT AGNs are more powerful sources than the ULXs, with X-ray luminosities over the full range of AGN luminosities. For the closest Seyfert galaxies ($z \approx 0.01$), the BAT flux limit corresponds to a 14 – 195 keV luminosity of roughly $3 \times 10^{42}\,\mathrm{erg\,s^{-1}}$. Most of the sources ($\approx 97\%$) have been optically detected as relatively bright nearby objects with $< z > \approx 0.03$, while most of the sources without bright optical counterparts are blazars, of which there are 17 in the sample (Tueller et al. 2008). Since the BAT sources are mostly bright and nearby, they are good sources with which to study multi-wavelength properties.

Before delving into the survey and its results, it is important to understand the importance of the BAT survey. Therefore, in § 4.1.1, we elaborate on the selection effects in various wavelength bands. We then discuss other very hard X-ray surveys (HEAO-1 and Integral) and BAT's advantages in § 4.1.2. Finally, in § 4.1.3, we outline the study presented in this chapter – the X-ray properties of 22 previously unobserved (in X-rays) BAT AGN.

4.1.1 Selection Effects

As mentioned, selection effects are a common hazard in AGN surveys. The first effect, dilution by starlight from the host galaxy, is most important in the optical/UV and infrared bands – where stars output most of their energy. This dilution can even be present in the soft X-ray ($< 2\,\mathrm{keV}$). Here, the contributions of stars, particularly hot, young stars, supernova remnants, and ionized gas in star forming regions, can dominate over comparatively weaker AGN emission. In the optical/UV through IR, this becomes increasingly more important for a

galactic stellar luminosity of $L \geq 10^{44}\,\mathrm{erg\,s^{-1}}$. In the soft X-rays, luminosities up to $L_{0.5-2} \approx 10^{41}\,\mathrm{erg\,s^{-1}}$ from stellar processes (Ranalli et al. 2003) can rival the AGN emission in a low luminosity source. Observationally, this has the effect of reducing the equivalent width of AGN emission lines and masking the contribution of the AGN to the measured flux/color (Mushotzky 2004).

The second important selection effect is the result of obscuration along our line of sight to the AGN. Particularly for sources located in the Galactic plane, dust and gas in our own Galaxy provides obscuration. Above the Galactic plane, this obscuration largely comes from dust and gas in the AGN's host and/or more local to the AGN. From AGN models of the Cosmic X-ray background (CXB), Fabian & Iwasawa (1999) found that the observed CXB can be replicated if we assume that 85% of the direct X-ray emission from AGN is obscured. This suggests that obscuration is an important effect, present in the majority of AGN.

In X-ray astronomy, a frequently used definition is that obscured sources are those with $n_H \geq 10^{22}\,\mathrm{atoms\,cm^{-2}}$. As the column density goes to higher values, the photoelectric cut-off from absorption shifts to higher energies (see Figure 1.1). Therefore, the direct emission from the AGN is cut-off and the corresponding soft flux ($< 2\,\mathrm{keV}$) is low. Thus, soft X-ray surveys are extremely sensitive to the effects of obscuring material. Even above 2 keV, the effect of obscuration can make it difficult to impossible to select an unbiased sample of highly obscured sources. In particular, AGN with columns $n_H \geq 1.5 \times 10^{24}\,\mathrm{atoms\,cm^{-2}}$, become extremely difficult to find. Such sources, termed Compton thick, have an optical depth $\tau > 1$ towards inverse Compton scattering. Therefore, the only emission that reaches us is scattered or reflected emission, estimated to be ≈ 50–100 times weaker than the direct emission (Comastri 2004).

Not only are Compton-thick sources faint, due to the lack of direct emission,

but a further complication arises in that obscured AGN are less luminous than unobscured AGN. We already mentioned this in § 1.4, as a challenge to the unified AGN model. In short, there are few luminous absorbed AGN in the 2–10 keV band (Steffen et al. 2003) and a larger fraction of absorbed AGN at lower luminosities (Ueda et al. 2003). Since all X-ray surveys are flux limited, this makes it even more difficult to obtain an unbiased sample at a given redshift – the true ratio of absorbed to unabsorbed sources could be skewed by missing the lower luminosity absorbed AGN.

Of course, the effect of obscuration is not limited to the X-ray bands. In fact, it has a much stronger affect in the UV, optical, and near-IR. One evidence of this is the fact that there are X-ray selected AGN showing none of the optical properties of AGN. This can be because of dilution or obscuration. In the case of obscuration, the source is obscured to such a degree that none of the AGN emission lines can be seen. As Mushotzky (2004) points out, columns above $10^{22}\,\mathrm{cm}^{-2}$ atoms cm^{-2} correspond to extinction of $A_V > 5$, high enough that the UV/near-IR flux from the AGN would not be seen.

Other effects that we have not yet mentioned include both those from separating out star burst/AGN contributions and aperture size. In the optical/UV, line diagnostics are effective at distinguishing between H II regions and AGN emission (see Veilleux (2002) for a review). However, in the IR, it is difficult to separate out the AGN and stellar components without very high signal to noise spectra (see Meléndez et al. (2008)). As for aperture size, Veilleux et al. (1995) show the significant effects aperture sizes have in the IR. Such effects are also important in other bands (i.e. optical) and are somewhat related to the dilution effect. For instance, a small aperture may include mostly light from the bulge region where a large aperture may include the entire galaxy. This effect is also sensitive to the

redshift of the target, since redshift affects the angular size of the host galaxy.

In the radio band, a different kind of selection effect is at work. Namely, only 10% of AGN are radio-loud, i.e. have luminous radio emission (White et al. 2000). Thus, while finding AGN in the radio is easy, based on the presence of radio jets or lobes, the majority of AGN are radio-quiet. Therefore, to examine the radio properties of an unbiased sample, the sample must first be identified in an alternate band and then followed up with radio observations.

Therefore, assuming that very hard X-rays (> 10 keV) are present in all AGN, they provide one of the best means to select an "unbiased" sample. At these high energies, there is no detectable emission from normal stars. Also, obscuration plays a minimal effect for columns of $n_H \leq 10^{24}$ atoms cm^{-2}. Further, AGN emission in the hard X-ray band is closely tied to the accretion processes, originating from a compact region very close to the black hole. While, most other AGN signatures detected in other bands are from indirect or reprocessed emission.

4.1.2 Other Hard X-ray Surveys

Beginning in 1977, NASA launched a series of High Energy Astronomy Observatories (HEAO). HEAO-1 was the first of these, surveying the sky ≈ 3 times in the 0.2 keV–10 MeV band over its 1.5 year lifetime. Among its achievements, HEAO-1 provided a measurement of the 3–50 keV X-ray background (Marshall et al. 1980) and a complete flux limited survey of high Galactic latitude sources (Piccinotti et al. 1982). The HEAO-1 X-ray survey covered 8.2 sr at a sensitivity of $\approx 3.1 \times 10^{-11}$ erg s^{-1} cm^{-2} in the 2–10 keV band. In the survey, 85 sources were detected, including ≈ 30 AGN (9 sources were unidentified).

More recently, Chandra and *XMM-Newton* have conducted deep X-ray surveys in the 2–10 keV band for relatively small regions of the sky. Unlike HEAO-1,

however, many of the detected sources are at much higher redshifts ($z \geq 1$) than the BAT AGN. A good review of these surveys can be found in Brandt & Hasinger (2005). Based on redshift, the $z \approx 1$ sources provide a good comparison with the BAT AGN survey, particularly to search for evolutionary differences between the two populations.

Yet another contemporary mission is Integral. The International Gamma-ray Astrophysics Laboratory (INTEGRAL) is a European Space Agency led satellite launched in October 2002. The main goals are spectroscopy, at a resolution of $E/\Delta E = 500$, and imaging, with angular resolution of 12′, in the 15 keV to 10 MeV range. The satellite consists of four science instruments: the spectrometer (SPI), imager (IBIS), an X-ray detector sensitive in the 3–25 keV band – Joint European X-ray Monitor (JEM-X), and an optical monitoring camera (OMC) with a V band filter (500–850 nm). The Key Project of INTEGRAL is a study of gamma-ray sources located in the Galactic plane. Therefore, the sky-coverage is particularly good in this region and much poorer in other regions.

An INTEGRAL all-sky survey of AGN has now been completed in the 17–60 keV band (Sazonov et al. 2007) to a limiting flux of $F_{17-60} \approx 1.4 \times 10^{-11}\,\mathrm{erg\,s^{-1}\,cm^{-2}}$. There are a few clear advantages the BAT survey can claim. For one, BAT is truly all-sky with a much higher sensitivity over a wider range of the sky. Due to its larger field of view, BAT detects many more AGN than INTEGRAL. After a 4 year survey, INTEGRAL detected 127 AGN. In the 9-month survey, BAT has already detected more sources (153). Further, the BAT survey continues to detect more sources with the 22-month survey adding an additional ≈ 100 AGN (Tueller *et al.*, in prep). However, INTEGRAL clearly has the advantage in the Galactic plane. A second advantage of BAT is that it covers a larger and higher energy range (14–195 keV) than INTEGRAL. Thus, it can potentially

detect more absorbed sources.

4.1.3 This Chapter

Despite the X-ray brightness of the BAT AGN, a number of these sources had yet to be observed spectroscopically in the X-rays. In this chapter, we present an analysis of *XMM-Newton* EPIC spectra of 23 sources, 2 of which correspond to a pair of interacting galaxies where the BAT source is confused, i.e. likely a combination of the AGN, for which spectra were obtained through discretionary project scientist time. These sources had no previous X-ray spectrum, were clearly detected by the BAT, and had clear optical counterparts from Digital Sky Survey (DSS) images. Many of these sources now also have SWIFT X-ray Telescope (XRT) spectra available. Thus, we are able to compare the XRT spectra with the EPIC spectra. In § 4.2, we detail the observations and data analysis for the XMM-Newton and SWIFT observations. In § 4.3, we describe spectral fits to the X-ray spectra, including a search for variability between the XRT and *XMM-Newton* observations. We discuss our results in § 4.4. Finally, we summarize our results in § 4.5. Through this chapter, we make the claim that the properties of this sample are representative of the larger 9-month AGN catalog. Thus, the results become more interesting as a first look at the BAT AGN properties, which is then expanded on with the entire sample in Chapter 5.

4.2 Observations and Data Analysis

4.2.1 XMM-Newton and SWIFT XRT Spectra

We obtained proprietary *XMM-Newton* observations of 22 out of 26 proposed BAT AGN sources through discretionary project scientist time. These particu-

lar BAT AGNs were selected based on: their detection in BAT with high significance ($\sigma > 5$), a clear optical counterpart to the BAT source in Digital Sky Survey images, and no previous X-ray spectrum. A list of these sources, whose X-ray spectra were observed for the first time, is in Table 4.1. Here we list the source name, co-ordinates, redshift, Galactic column density towards the source, AGN type, and host galaxy type. For one of the BAT sources, the "BAT source" is an interacting galaxy system with two AGNs, MCG +04-48-002 and NGC 6921. In addition to the *XMM-Newton* observations, we downloaded archived SWIFT XRT observations (48) for the 22 BAT AGNs from the NASA HEASARC archives. In Table 4.2 we include details on the observations examined.

We reduced the *XMM-Newton* data using the Science Analysis System (SAS) version 7.0. We created calibrated photon event files for the EPIC-MOS and pn cameras using the observation data files (ODF) with the commands `emchain` and `epchain`. Following this, the events tables were filtered using the standard criteria outlined in the *XMM-Newton ABC Guide*[1]. For the MOS data (both MOS1 and MOS2 cameras), good events constitute those with a pulse height in the range of 0.2 to 12 keV and event patterns that are characterized as 0-12 (single, double, triple, and quadruple pixel events). For the pn camera, only patterns of 0-4 (single and double pixel events) are kept, with the energy range for the pulse height set between 0.2 and 15 keV. Bad pixels and events too close to the edges of the CCD chips were rejected using the stringent selection expression "FLAG == 0".

Light curves of the observations were produced with `xmmselect` and examined for flaring events (distinguished by high count rates). Time filtering was required only for the sources SWIFT J0641.3+3257, SWIFT J0911.2+4533, MCG +04-22-042, MRK 417, WKK 1263, and NGC 6921/MCG +04-48-002 (the interact-

[1] `http://heasarc.gsfc.nasa.gov/docs/xmm/abc/`

Table 4.1. Details on the Sub-sample of 22 Sources

Source	RA (h m s)	Dec (° ′ ″)	Redshift	$n_{H(GAL)}$[1]	Type[2]	Host Galaxy[2]
MRK 352	00 59 53.28	31 49 36.87	0.014864	5.59	Sy1	SA0
NGC 612	01 33 57.74	-36 29 35.70	0.029771	1.85	Gal	SA0+ pec
SWIFT J0216.3+5128	02 16 29.84	51 26 24.70	?	1.57	–	?
NGC 1142	02 55 12.196	-00 11 00.81	0.028847	6.00	Sy2	S pec
SWIFT J0318.7+6828	03 18 18.98	68 29 31.42	0.090100	35.1	Sy2	S?
ESO 548-G081	03 42 03.72	-21 14 39.70	0.014480	3.04	Sy1	Sba
ESO 362-G018	05 19 35.82	-32 39 27.90	0.01264	1.78	Sy1.5	S0/a
ESO 490-G026	06 40 11.69	-25 53 43.30	0.024800	11.7	Sy1.2	Pec
SWIFT J0641.3+3257	06 41 23.04	32 55 38.60	0.017195	11.6	Sy2	E?
MRK 18	09 01 58.39	60 09 06.20	0.011088	4.49	Sy2	S
SWIFT J0904.3+5538	09 04 32.94	55 38 30.63	0.037142	2.78	Sy1	?
SWIFT J0911.2+4533	09 11 29.97	45 28 05.00	0.026782	1.64	Sy2	S?
MCG +04-22-042	09 23 43.00	22 54 32.50	0.032349	3.37	Sy1.2	E
MRK 417	10 49 30.93	22 57 51.90	0.032756	2.06	Sy2	Sa
UGC 6728	11 45 16.02	79 40 53.42	0.015300	4.49	Sy1.2	SB0/a
SWIFT J1200.8+0650	12 00 57.92	06 48 23.11	0.036045	1.43	Sy2	S?
ESO 506-027	12 38 54.59	-27 18 28.20	0.025024	6.60	Sy2	S pec s
WKK 1263	12 41 25.74	-57 50 03.50	0.024430	35.5	Sy2[3]	Sc
MCG +09-21-096	13 03 59.47	53 47 30.10	0.02988	1.53	Sy1	SABb
NGC 4992	13 09 12.95	11 38 45.32	0.025137	2.09	Gal	Sa
NGC 6860	20 08 46.89	-61 06 00.70	0.014884	4.19	Sy1.5[4]	SB ab
NGC 6921	20 28 28.86	25 43 24.30	0.014287	26.0	Sy2	SA 0/a
MCG+04-48-002	20 28 35.0	25 44 00.0	0.013900	26.0	Sy2	S

[1]Galactic column density towards the source, in units of 10^{20} cm^{-2}, as obtained from the web version of the n_H FTOOL. These are the values from Dickey & Lockman (1990).

[2]AGN type and host galaxy type from Tueller et al. (2008). For AGN types, optical identifications are listed, where available. Where "Gal" is indicated, there are no optical emission lines indicative of the presence of an AGN. The optical spectrum looks like a galaxy spectrum. Additional host galaxy classifications were obtained from the LEDA database. Where "?" is indicated, there is no available classification.

[3]While WKK 1263 is classified as a Sy2 in NED, we could find no optical spectrum to confirm this.

[4]NGC 6860 is classified as a Sy1.5 by Lipari et al. (1993) contrary to NED's classification as a Sy1.

ing system). The light curves were filtered using the task `tabgtigen`, as outlined in the SAS ABC guide, with the parameters 'RATE< 50' counts/s for the pn and 'RATE< 10' counts/s for MOS observations.

Spectra of the sources were extracted using the SAS task `especget`. This routine extracts source and background spectra from a defined region as well as response and ancillary response matrices. We extracted the source spectra from circular regions with radii between $\approx 30 - 125''$. The extraction radius depended upon the location of the source with respect to other sources and the edge of a

CCD chip. Background regions were extracted from annular regions surrounding the source, where possible. In cases were the source was near the edge of a chip or another source, circular regions near the source were used, of the same size as the source region and on the same chip.

Of the 22 target observations, there were a few cases where the position of the source fell within a gap in the CCD chip (for either the pn or a MOS detector). This occurred for the MOS1 observation of SWIFT J0641.3+3257 and the pn observation of SWIFT J0911.2+4533. Thus, there are no corresponding spectra from these CCDs. Also, the position of source SWIFT J0904.3+5538 was located such that a large fraction of the light (66%) was located in a gap in the pn CCD. Due to a problem with the ODF files for NGC 6860, the pn observation of this source could not be extracted.

Table 4.2: *XMM-Newton* EPIC and SWIFT XRT Observation Information

Source	Telescope	Observation ID	Start Date	Exposure Time (s)[1]	Total Counts[1]
MRK 352	XMM	0312190101	2006-01-24	9773, 12382, 12360	71296, 23572, 23175
MRK 352	XRT	00035243001	2006-05-29	11527	3456
MRK 352	XRT	00035243002	2006-05-30	19385	3983
NGC 612	XMM	0312190201	2006-06-26	9744, 12456, 12457	1164, 285, 352
NGC 612	XRT	00035627001	2006-06-02	6743	20
NGC 612	XRT	00035627002	2006-06-12	4875	20
SWIFT J0216.3+5128	XMM	0312190301	2006-01-24	8921, 11485 ,11495	14412, 6454, 6053
SWIFT J0216.3+5128	XRT	00035247001	2006-01-08	8291	1516
SWIFT J0216.3+5128	XRT	00035247002	2006-01-10	5559	982
SWIFT J0216.3+5128	XRT	00035247003	2006-02-05	2113	288
NGC 1142	XMM	0312190401	2006-01-28	8921, 11485, 11496	2481, 847, 907
NGC 1142	XRT	00035248001	2006-06-29	6808	245
NGC 1142	XRT	00035248002	2006-07-07	5434	201
NGC 1142	XRT	00035248003	2006-07-08	4670	145
NGC 1142	XRT	00035248004	2006-07-11	1888	40
SWIFT J0318.7+6828	XMM	0312190501	2006-01-29	6578, 11163, 11170	9654, 4512, 4491

Continued on next page ...

Table 4.2 – Continued

Source	Telescope	Observation ID	Start Date	Exposure Time (s)[1]	Total Counts[1]
SWIFT J0318.7+6828	XRT	00035249001	2006-03-29	9247	413
SWIFT J0318.7+6828	XRT	00035249002	2006-04-05	8061	385
ESO 548-G081	XMM	0312190601	2006-01-28	8924,11485, 11499	106660, 32699, 32404
ESO 548-G081	XRT	00035250001	2006-01-28	3561	3632
ESO 548-G081	XRT	00035250002	2006-03-19	6605	7821
ESO 362-G018	XMM	0312190701	2006-01-28	8921, 11483, 11498	8497, 2905, 2884
ESO 362-G018	XRT	00035234001	2005-10-29	1379	772
ESO 362-G018	XRT	00035234002	2005-11-26	6979	2587
ESO 490-G026	XMM	0312190801	2006-03-07	9192, 11812, 11823	52246, 21057, 19713
ESO 490-G026	XRT	00035256001	2005-12-16	8246	4448
ESO 490-G026	XRT	00035256002	2006-03-23	2809	1434
ESO 490-G026	XRT	00035256003	2006-03-28	2747	954
SWIFT J0641.3+3257	XMM	0312190901	2006-03-11	10696, -, 13507	2686, -, 786
SWIFT J0641.3+3257	XRT	00035257002	2005-12-18	7784	20
SWIFT J0641.3+3257	XRT	00035257003	2005-12-26	14864	82
SWIFT J0641.3+3257	XRT	00035257006	2006-01-07	20008	60
MRK 18	XMM	0312191001	2006-03-23	9910, 13387, 13402	4990, 1089, 1029
MRK 18	XRT	00035259001	2005-12-18	5353	50
MRK 18	XRT	00035259002	2005-12-26	3088	20
SWIFT J0904.3+5538	XMM	0312191101	2006-03-31	7142, 12072 , 12089	10830, 10980, 11221
SWIFT J0904.3+5538	XRT	00035260001	2005-12-15	5706	916
SWIFT J0904.3+5538	XRT	00035260002	2006-01-06	6211	736
SWIFT J0911.2+4533	XMM	0312191201	2006-04-10	-, 11530, 11531	-, 615, 515
SWIFT J0911.2+4533	XRT	00035261001	2006-01-04	5487	21
SWIFT J0911.2+4533	XRT	00035261002	2006-01-22	8875	80
MCG +04-22-042	XMM	0312191401	2006-04-18	9012, 11809, 11824	126070, 39777 39220
MCG +04-22-042	XRT	00035263001	2005-12-10	8564	4986
MRK 417	XMM	0312191501	2006-06-15	7437, 348, 351	1075, 348, 351
MRK 417	XRT	00035264001	2005-12-12	6306	41
MRK 417	XRT	00035264002	2006-03-03	3534	20
MRK 417	XRT	00035264003	2006-06-24	16130	140
UGC 6728	XMM	0312191601	2006-02-23	7220, 11404, 11415	30705, 11420, 11109
UGC 6728	XRT	00035266001	2006-06-24	6331	3090
UGC 6728	XRT	00035266002	2006-06-29	3017	994
UGC 6728	XRT	00035266003	2006-07-07	1433	463

Continued on next page ...

Table 4.2 – Continued

Source	Telescope	Observation ID	Start Date	Exposure Time (s)[1]	Total Counts[1]
SWIFT J1200.8+0650	XMM	0312191701	2006-06-26	9777, 12495, 12507	4543, 1590, 1751
SWIFT J1200.8+0650	XRT	00035267001	2005-12-11	14961	638
SWIFT J1200.8+0650	XRT	00035267002	2005-12-21	3156	120
ESO 506-G027	XMM	0312191801	2006-01-24	8162, 11139, 11150	2114, 630, 645
ESO 506-G027	XRT	00035273002	2005-06-15	3209	60
ESO 506-G027	XRT	00035273003	2005-08-15	1938	20
ESO 506-G027	XRT	00035273004	2005-08-28	10808	242
WKK 1263	XMM	0312191901	2006-02-01	8902, 11482, 11495	24195, 10198, 10120
WKK 1263	XRT	00035268001	2005-12-15	3253	564
WKK 1263	XRT	00035268002	2005-12-29	8690	1346
SWIFT J1303.8+5345	XMM	0312192001	2006-06-23	8408, 11470, 11490	86597, 27942, 27492
SWIFT J1303.8+5345	XRT	00035269001	2005-12-19	7468	7723
SWIFT J1303.8+5345	XRT	00035269004	2006-07-02	4752	3986
NGC 4992	XMM	0312192101	2006-06-27	12849, -, -	1756, -, -
NGC 6860	XMM	0312192201	2006-03-19	-, 11815, 11823	-, 5485, 4910
NGC 6860	XRT	00035275001	2005-12-12	3536	632
NGC 6921	XMM	0312192301	2006-04-23	8789, 11235, 11249	2243, 554, 513
NGC 6921	XRT	00035276001	2005-12-16	4071	41
NGC 6921	XRT	00035276002	2006-03-23	4600	40
NGC 6921	XRT	0003072201	2006-06-03	6885	65
MCG +04-48-002	XMM	0312192301	2006-04-23	8789, 11235, 11249	845, 180, 163
MCG +04-48-002	XRT	00035276001	2005-12-16	4071	41
MCG +04-48-002	XRT	00035276002	2006-03-23	4600	40
MCG +04-48-002	XRT	0003072201	2006-06-03	6885	65

[1]For the XMM observations, the exposure times and total counts are listed for the EPIC pn, MOS1, and MOS2 respectively.

For the XRT data, we extracted spectra of target sources from the cleaned photon counting event files downloaded from the public High Energy Astrophysics Science Archive Research Center (HEASARC) archive. We extracted spectra for

observations that had XRT exposure times of at least 1000 s, following the instructions outlined in *The SWIFT XRT Data Reduction Guide*[2]. Spectra were extracted for the sources using the FTOOL XSELECT. With this tool, a source region was created in DS9, with a radius of $\approx 50 - 70''$. A background region was created in a source free region close to the source, with a radius of $95''$. We used the standard response and ancillary response files available for the photon counting event files with grades 0 to 12. These are publicly available in the SWIFT XRT calibration database (CALDB).

For all of the spectra, we binned the source and background spectrum and response files for each observation with the Ftool `grppha`. All spectra were binned with 20 counts/bin. We then fit the spectra in the 0.3-10 keV range with XSPEC version 11. The details of these fits are described in the following section.

4.2.2 SWIFT BAT Spectra

BAT is a wide field (≈ 2 steradians) coded aperture hard X-ray instrument. During normal operations, it usually covers $\approx 60\%$ of the sky each day at < 20 milliCrab sensitivity. The BAT spectra were derived from an independent all sky mosaic map in each energy bin, averaged over 22 months of data, beginning on Dec 5 2004 (Tueller in preparation). The survey was processed using the BAT Ftools and additional software to make mosaic maps. The energy bin edges are 14, 20, 24, 35, 50, 75, 100, 150, 195 keV. The energies are calibrated in-flight for each detector using an on-board electronic pulser and the 59.5 keV gamma and La L and M lines from a tagged 241Am source. The average count rate in the map bin that corresponds to the known position of the counterpart was used. Due to the strong correlation of the signal in adjacent map bins of the over-

[2] `http://heasarc.nasa.gov/docs/swift/analysis/xrt_swguide_v1_2.pdf`

sampled coded aperture image, it is not necessary to perform a fit to the PSF. Each rate was normalized to the Crab nebula rate using an assumed spectrum of $10.4 \times E^{-2.15}\,\mathrm{ph\,cm^{-2}\,s^{-1}\,keV^{-1}}$ for the BAT energy range. Due to the large number of different pointings that contribute to any position in the map, this is a good approximation of the response. This has been verified by fitting sources with known spectra (Cas-A compared to BeppoSax and Integral, PSR1509-589 compared to Integral, NGC2110 and Cen-A compared to Suzaku) and generally produces a good connection to X-ray spectra in sources that do not vary much with time. Error estimates were derived directly from the mosaic images using the RMS image noise in a region around the source of roughly 3 degrees in radius. This is the optimum procedure due to the residual systematic errors of 1.2 to 1.8 times statistical values in the current BAT mosaics. Analysis of the noise in the images suggests that the variations in noise are small on this scale. Analysis of negative fluctuations shows that the noise is very will fit by a Gaussian distribution and that this normalization is very accurate on average. All fitting of the BAT data was performed on this normalized data using a diagonal instrument response matrix. This procedure correctly accounts for instrumental systematics in sources with spectral indices similar to the Crab. While there may be significant systematic errors for sources with spectra that are much flatter than the Crab, this is not a significant problem for most of the sources presented in this chapter (the exceptions being NGC 612 and MRK 417).

4.3 Spectral Fitting

In examining the X-ray spectra of these BAT AGNs, there are two main goals: to determine how the sources vary between observations and to determine the spectral properties of the source (the hydrogen column density, spectral shape, and properties of the Fe K line and/or other lines if present). Since the extracted *XMM-Newton* spectra have, on average, ten times the number of counts from the XRT spectra, we will focus on the *XMM-Newton* spectra for a more detailed analysis. The effective spectral resolution for the XRT is lower, since there are fewer counts and at 20 cts per bin there are few data points, such that Fe K lines which are clearly visible in 10 ks *XMM-Newton* observations are not resolved in comparable XRT observations (see Figure 4.1). Thus, in order to examine the variability between the XRT and *XMM-Newton* observations we need to rely on simple models for the AGN spectra.

As a first fit to the spectra and as a means to compare variability between XRT and *XMM-Newton* observations, we fit each observation separately with a simple absorbed power law (absorption model * `pow`). In XSPEC, we used the absorption model `tbabs` to account for cold absorption in the Milky Way. Thus, we fixed the `tbabs` model hydrogen absorption to the Dickey & Lockman (1990) value (see Table 4.1). We allowed the parameter of a second `tbabs` model to float in order to account for the combination of absorption from the AGN host galaxy and local environment.

To apply this model to the *XMM-Newton* EPIC observations, we simultaneously fit the pn and MOS observations, using a constant value to account for differences in flux calibration. The best-fit spectral parameters for these observations are recorded in Table 4.3, including the observed flux values at soft (0.3-

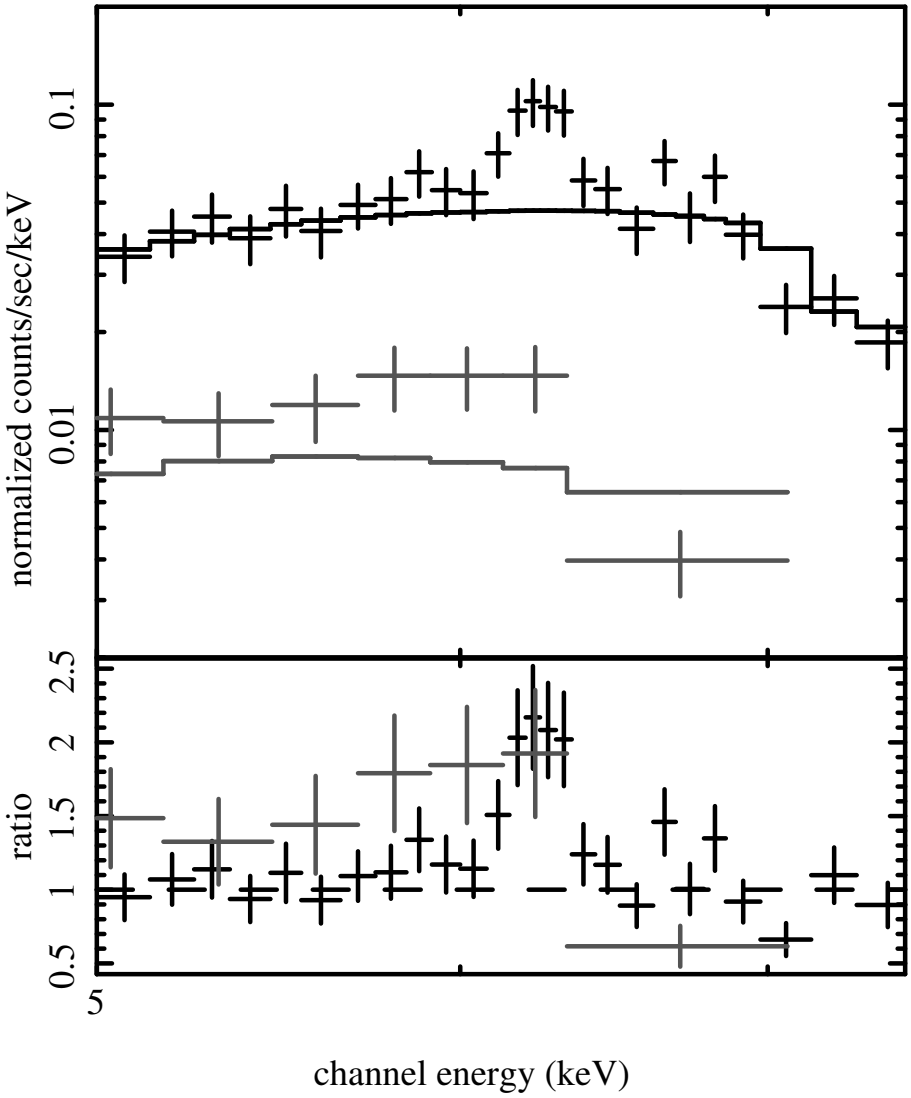

Figure 4.1: *XMM-Newton* pn and the highest quality XRT spectrum for NGC 1142 centered on the 6.4 keV fluorescent Fe K line. The lines represent a simple absorbed power law model. In the $\approx$ 10 ks pn, the Fe K line is clearly distinguishable requiring the addition of a Gaussian component. However, the $\approx$ 7 ks XRT spectrum, binned as the pn spectrum with 20 photons/bin, does not have the spectral resolution required to distinguish this feature. We found this to be the case with all of the XRT spectra examined for these 22 BAT AGNs.

2 keV) and hard (2-10 keV) energies. We include the best-fit spectral parameters for the XRT observations in Table 4.4. All quoted errors represent the 90% confidence level. We excluded from our spectral fits any observation with ≤ 50 counts. Also, we note that this simple power law model is a very poor fit to the *XMM-Newton* spectra of NGC 612, NGC 1142, ESO 362-G018, MRK 417, ESO 506-G027, and MCG +04-48-002. For each of these five sources the reduced χ^2 value indicates that the simple power law fit was not a good description of the data. Thus, no errors were calculated for the spectral parameters. We will discuss the spectra of these sources and more acceptable models below.

4.3.1 Detailed Spectral Properties

From our initial examination of the spectra, we found that simple power law models (see Table 4.3) were not sufficient in describing the spectra of all of our sources. In particular, there are three main features that were not accounted for by a simple absorbed power law: a soft excess, line emission, and additional complexity from emission with varying column densities. A "soft excess" in an AGN may be the result of thermal emission (for instance, from star formation), low temperature Comptonization, blurred reflection (Czerny et al. 2003; Ross & Fabian 2005), or blurred absorption (Gierliński & Done 2004). Line emission can be produced by a number of mechanisms, in particular from fluorescent, photo-ionized or collisionally ionized gas. Most importantly for AGN, is fluorescence from lowly ionized iron, with the strongest feature being the Fe K line at 6.4 keV. The final type of "feature", a complex spectrum with different column densities, is difficult to interpret. Such spectra, which appear to have a "double power law" shape, could be the result of contamination of the AGN light by a less absorbed X-ray binary spectrum, a dusty environment where the AGN emis-

sion is partially covered by absorbing material, or scattering of some of the AGN light.

In order to better characterize our sources, we first grouped our sources in basic categories: (1) pure power law sources (with or without absorption beyond the Galactic Milky Way values), (2) power law sources with a soft excess (with or without absorption), and (3) more complex "double power law" shaped spectra. Based on the F-test, any additional components added to our spectral models improved the fit by a χ^2 of at least 8 (this is the 99% level for 2 additional degrees of freedom). The only exception is the addition of a gaussian line (`zgauss` in XSPEC) to characterize the Fe K-α line at 6.4 keV. Where the addition of the line was not significant, we derived upper limits on the strength and intensity (indicated by the normalization which is the integrated photon flux of the line) of a possible emission line. Therefore, for all of our sources, we fixed the energy of a gaussian line to 6.4 keV in the source's rest frame with a fixed width (FWHM) of 0.01 keV, corresponding to an unresolved line.

Table 4.3. XMM-Newton Spectral Analysis: Absorbed Power Law Fits

Source	Observation ID	n_H [1]	Γ	χ^2/dof	F_{soft} [2]	F_{hard} [2]
MRK 352	0312190101	–	$1.95^{+0.01}_{-0.01}$	3104.4/1569	6.87	9.76
NGC 612 [3]	0312190201	79.90	0.31	274.2/83	0.00	1.66
SWIFT J0216.3+5128	0312190301	$1.74^{+0.06}_{-0.07}$	$1.77^{+0.04}_{-0.04}$	1069.7/985	0.90	8.44
NGC 1142 [3]	0312190401	65.68	1.63	942.8/197	0.00	3.00
SWIFT J0318.7+6828	0312190501	$3.20^{+0.31}_{-0.34}$	$1.36^{+0.10}_{-0.11}$	812.3/772	0.23	7.43
ESO 548-G081	0312190601	–	$2.03^{+0.01}_{-0.01}$	2943.5/1642	11.34	13.48
ESO 362-G018 [3]	0312190701	–	1.47	2534.6/549	0.69	1.83
ESO 490-G026	0312190801	$0.24^{+0.01}_{-0.01}$	$1.59^{+0.02}_{-0.02}$	1634.2/1757	5.30	19.79
SWIFT J0641.3+3257	0312190901	$12.11^{+3.08}_{-1.79}$	$0.98^{+0.30}_{-0.20}$	218.4/154	0.00	3.38
MRK 18	0312191001	$13.06^{+7.20}_{-3.52}$	$1.26^{+0.72}_{-0.38}$	413.4/327	0.00	1 .60
SWIFT J0904.3+5538	0312191101	–	$1.79^{+0.01}_{-0.02}$	1126.3/865	3.19	5.41
SWIFT J0911.2+4533	0312191201	$27.63^{+27.50}_{-9.43}$	$1.34^{+2.21}_{-0.43}$	19.9/17	0.00	1.55
MCG +04-22-042	0312191401	–	$2.00^{+0.01}_{-0.00}$	1835.8/1819	12.45	15.52
MRK 417 [3]	0312191501	41.76	0.56	565.6/82	0.00	1.52
UGC 6728	0312191601	$0.01^{+0.00}_{-0.01}$	$1.78^{+0.02}_{-0.02}$	1207.0/1160	3.59	6.49
SWIFT J1200.8+0650	0312191701	$9.31^{+0.72}_{-0.67}$	$1.30^{+0.11}_{-0.10}$	484.0/357	0.02	5.17
ESO 506-G027 [3]	0312191801	75.91	1.14	543.4/172	0.00	3.73
WKK 1263	0312191901	$0.06^{+0.01}_{-0.02}$	$1.53^{+0.03}_{-0.02}$	1257.3/1248	2.32	9.99
MCG +09-21-096	0312192001	–	$1.76^{+0.01}_{-0.00}$	1291.2/1626	9.27	15.85
NGC 4992	0312192101	$76.20^{+16.36}_{-8.73}$	$1.69^{+0.58}_{-0.30}$	139.6/82	0.00	1.91
NGC 6860	0312192201	$0.00^{+0.01}_{-0.00}$	$0.28^{+0.04}_{-0.03}$	523.5/406	0.57	9.84
NGC 6921	0312192301	$98.33^{+14.57}_{-12.91}$	$1.95^{+0.40}_{-0.37}$	287.3/168	0.00	2.58
MCG +04-48-002[3]	0312192301	0.0	1.98	146.0/56	0.02	0.06

[1]Cold hydrogen column density in units of $10^{22}\,\mathrm{cm}^{-2}$ from the `tbabs` model. This accounts for absorption beyond the Galactic values which are listed in Table 4.1. A dash in this column indicates that no extra absorption was necessary.

[2]The observed soft flux (0.3-2 keV) and hard flux (2-10 keV) are given in units of $10^{-12}\,\mathrm{erg\,cm^{-2}\,s^{-1}}$.

[3]Errors at the 90% confidence range are not meaningful when $\Delta\chi^2/\mathrm{dof} > 2.0$.

Table 4.4: SWIFT XRT Spectral Analysis: Absorbed Power Law Fits

Source	Observation ID	n_H[1]	Γ	χ^2/dof	F_{soft}[2]	F_{hard}[2]
MRK 352	00035243001	$0.01^{+0.02}_{-0.01}$	$1.75^{+0.07}_{-0.06}$	181.3/133	4.04	7.75
MRK 352	00035243002	$0.00^{+0.01}_{-0.00}$	$1.65^{+0.04}_{-0.04}$	152.0/152	2.69	5.95
SWIFT J0216.3+5128	00035247001	$2.37^{+0.33}_{-0.29}$	$2.15^{+0.18}_{-0.17}$	56.1/67	1.35	10.75
SWIFT J0216.3+5128	00035247002	$1.15^{+0.25}_{-0.23}$	$1.77^{+0.21}_{-0.20}$	46.0/44	1.30	11.10
SWIFT J0216.3+5128	00035247003	$1.29^{+0.75}_{-0.65}$	$1.88^{+0.59}_{-0.55}$	15.7/11	1.06	9.17
NGC 1142[3]	00035248001	83.45	3.88	35.5/9	0.00	5.07
NGC 1142	00035248002	$28.19^{+20.59}_{-10.99}$	$1.51^{+1.89}_{-1.18}$	9.3/7	0.00	7.36
NGC 1142	00035248003	$95.73^{+84.77}_{-36.88}$	$3.11^{+4.44}_{-2.08}$	2.8/4	0.00	6.59
SWIFT J0318.7+6828	00035249001	$3.70^{+1.74}_{-1.83}$	$1.73^{+0.48}_{-0.55}$	17.4/17	0.15	4.11
SWIFT J0318.7+6828	00035249002	$3.66^{+1.44}_{-1.41}$	$1.44^{+0.40}_{-0.46}$	11.6/16	0.13	4.78
ESO 548-G081	00035250001	–	$1.92^{+0.04}_{-0.05}$	131.7/136	13.91	19.62
ESO 548-G081	00035250002	–	$2.06^{+0.03}_{-0.02}$	332.6/225	16.19	18.34
ESO 362-G018	00035234001	$0.00^{+0.01}_{-0.00}$	$1.79^{+0.09}_{-0.09}$	36.6/33	7.66	12.69
ESO 362-G018	00035234002	–	$1.45^{+0.05}_{-0.05}$	159.7/108	4.38	12.16
ESO 490-G026	00035256001	$0.27^{+0.04}_{-0.03}$	$1.88^{+0.07}_{-0.07}$	143.8/177	7.07	18.91
ESO 490-G026	00035256002	$0.27^{+0.09}_{-0.09}$	$1.70^{+0.14}_{-0.13}$	59.2/62	6.32	21.07
ESO 490-G026	00035256003	$0.49^{+0.15}_{-0.14}$	$1.88^{+0.19}_{-0.18}$	27.2/42	4.28	14.49

Continued on Next Page...

Table 4.4 – Continued

Source	Observation ID	n_H[1]	Γ	χ^2/dof	F_{soft}[2]	F_{hard}[2]
SWIFT J0904.3+5538	00035260001	$0.00^{+0.01}_{-0.00}$	$1.54^{+0.08}_{-0.08}$	39.9/40	2.04	5.02
SWIFT J0904.3+5538	00035260002	$0.00^{+0.02}_{-0.00}$	$1.49^{+0.09}_{-0.09}$	34.2/32	1.51	4.01
MCG +04-22-042	00035263001	$0.01^{+0.00}_{-0.01}$	$1.90^{+0.05}_{-0.05}$	173.9/185	7.99	11.69
MRK 417[3]	00035264003	–	-1.78	38.5/4	0.00	2.16
UGC 6728	00035266001	$0.01^{+0.02}_{-0.01}$	$1.82^{+0.07}_{-0.07}$	106.6/117	6.88	11.78
UGC 6728	00035266002	$0.00^{+0.04}_{-0.00}$	$1.76^{+0.15}_{-0.08}$	62.4/42	4.58	8.37
UGC 6728	00035266003	$0.04^{+0.08}_{-0.04}$	$1.74^{+0.25}_{-0.20}$	19.6/19	4.80	9.67
SWIFT J1200.8+0650	00035267001	$11.23^{+3.50}_{-2.62}$	$1.60^{+0.48}_{-0.41}$	39.5/28	0.01	4.99
SWIFT J1200.8+0650	00035267002	$4.48^{+13.37}_{-4.48}$	$1.12^{+2.03}_{-1.27}$	2.7/3	0.00	5.68
ESO 506-G027[3]	00035173004	36.38	-0.22	33.7/9	0.00	5.02
WKK 1263	00035268001	$0.04^{+0.22}_{-0.04}$	$1.63^{+0.27}_{-0.17}$	26.8/24	2.09	7.79
WKK 1263	00035268002	$0.12^{+0.11}_{-0.10}$	$1.63^{+0.14}_{-0.13}$	55.1/59	1.73	6.98
MCG +09-21-096	00035269001	$0.00^{+0.01}_{-0.00}$	$1.80^{+0.04}_{-0.03}$	250.2/240	13.67	22.13
MCG +09-21-096	00035269004	$0.00^{+0.02}_{-0.00}$	$1.72^{+0.05}_{-0.04}$	143.9/151	11.41	21.09
NGC 6860	00035275001	$0.28^{+0.15}_{-0.11}$	$1.17^{+0.20}_{-0.18}$	30.9/27	1.55	11.54

[1]Cold hydrogen column density in units of 10^{22} cm^{-2} from the `tbabs` model. This accounts for absorption beyond the Galactic values which are listed in Table 4.1. A dash in this column indicates that no extra absorption was necessary.

[2]The observed soft flux (0.3-2 keV) and hard flux (2-10 keV) are given in units of 10^{-12} erg cm^{-2} s^{-1}.

[3]Errors at the 90% confidence range can not be calculated for sources when $\Delta\chi^2/\mathrm{dof} > 2.0$.

Simple Power Law Sources

A total of five of our sources (5/22) had *XMM-Newton* spectra best-fit by simple power law models. None of these sources showed evidence of a strong Fe K line (EW < 150 eV for all of these sources). We record the equivalent width and normalization value for these lines in Table 4.5. Since the redshift for the source SWIFT J0216.3+5128 is unknown and there is no evidence for a strong line, we exclude this source from the analysis. We attempted to obtain an optical spectrum for this source as part of our BAT AGN follow-up program with the 2.1-m telescope at Kitt Peak National Observatory (Winter *et al.* in preparation). We found, however, that the probable Digital Sky Survey optical counterpart within the BAT and *XMM-Newton* error circles was a star. Likely, the true optical counterpart of this source is faint and below the DSS detection limit. Based on the lack of a bright optical counterpart and the featureless X-ray power law spectrum, this source is probably a blazar, based on its similarity to other BAT blazars which have a high X-ray/optical ratio.

Soft Excesses

Four sources (4/22) had *XMM-Newton* spectra best represented by a power law with a soft excess. Since the spectra do not have the counts necessary to distinguish between a reflection or absorption model, we used a simple blackbody (`bbody` in XSPEC) model to characterize this component. The best-fit spectral parameters are shown in Table 4.6. The soft excess is significant for all of these sources with $\Delta\chi^2$ values, between the simple power law and the power law with a blackbody model, from $\approx 220 - 1400$. As with the pure power law sources, we

Table 4.5. XMM-Newton Detailed Fits For Power Law Sources

Source	n_H[1]	Γ	Fe K EW[2]	Fe K norm.[2]	χ^2/dof	F_{soft}[3]	F_{hard}[3]
MCG +04-22-042	–	$2.01^{+0.01}_{-0.01}$	$130.38^{+33.95}_{-38.60}$	$21.0^{+5.50}_{-6.20}$	1801.9/1818	12.44	15.65
UGC 6728	$0.01_{-0.01}$	$1.78^{+0.03}_{-0.02}$	$83.33^{+56.58}_{-45.66}$	$5.73^{+3.89}_{-3.14}$	1198.8/1159	3.59	6.51
WKK 1263	$0.06^{+0.01}_{-0.02}$	$1.54^{+0.02}_{-0.02}$	$31.23^{+32.35}_{-23.67}$	$3.69^{+3.83}_{-2.80}$	1253.0/1247	2.32	9.99
MCG +09-21-096	–	$1.77^{+0.01}_{-0.01}$	$55.94^{+31.09}_{-29.09}$	$9.83^{+5.47}_{-5.11}$	1281.6/1625	9.26	15.89

[1]Cold hydrogen column density in units of 10^{22} cm^{-2} from the `tbabs` model. This accounts for absorption beyond the Galactic values which are listed in Table 4.1. A dash in this column indicates that no extra absorption was necessary.

[2]Equivalent width (in eV) and flux normalization for an inserted Gaussian line at 6.4 keV (redshifted) with a set FWHM of 0.01 keV. The flux normalization is in units of $10^{-6}\times$ total photons cm^{-2} s^{-1} in the line.

[3]The observed soft flux (0.3-2 keV) and hard flux (2-10 keV) are given in units of 10^{-12} erg cm^{-2} s^{-1}.

Table 4.6. XMM-Newton Detailed Fits for Power Law + Blackbody Sources

Source	n_H[1]	kT[2]	Γ	Fe K EW[3]	Fe K norm.[3]	χ^2/dof	F_{soft}[4]	F_{hard}[4]
MRK 352	–	$0.096^{+0.003}_{-0.003}$	$1.70^{+0.02}_{-0.01}$	$60.29^{+28.09}_{-27.89}$	$7.78^{+3.62}_{-3.60}$	1695.2/1566	6.50	11.89
ESO 548-G081	–	$0.087^{+0.003}_{-0.003}$	$1.85^{+0.01}_{-0.01}$	$114.35^{+38.41}_{-22.56}$	$18.7^{+4.60}_{-4.70}$	1760.8/1639	10.84	15.83
ESO 490-G026	$0.33^{+0.04}_{-0.02}$	$0.074^{+0.005}_{-0.006}$	$1.67^{+0.03}_{-0.02}$	$59.37^{+23.36}_{-23.28}$	$13.3^{+5.20}_{-5.23}$	1542.9/1754	5.31	19.49
SWIFT J0904.3+5538	$0.06^{+0.03}_{-0.02}$	$0.070^{+0.004}_{-0.006}$	$1.71^{+0.06}_{-0.03}$	$40.71^{+71.76}_{-40.71}$	$2.79^{+4.92}_{-2.79}$	903.2/862	3.05	5.96

[1]Cold hydrogen column density in units of 10^{22} cm^{-2} from the `tbabs` model. This accounts for absorption beyond the Galactic values which are listed in Table 4.1. A dash in this column indicates that no extra absorption was necessary.

[2]Temperature of the blackbody component (kT) in keV units.

[3]Equivalent width and flux normalization for an inserted Gaussian line at 6.4 keV (redshifted) with a set FWHM (in eV) of 0.01 keV. The flux normalization is in units of $10^{-6}\times$ total photons cm^{-2} s^{-1} in the line.

[4]The observed soft flux (0.3-2 keV) and hard flux (2-10 keV) are given in units of 10^{-12} erg cm^{-2} s^{-1}.

fit an Fe K line at 6.4 keV with a Gaussian. The results are recorded in Table 4.6.

Warm Absorbers

In our models for AGN spectra, we assume that the absorption along the line of sight is cold, neutral hydrogen (with the `tbabs` model). However, signatures of warm, optically-thin absorption from photo-ionized gas, have been detected in half of an ASCA Seyfert 1 AGN sample studied by Reynolds (1997) and 13/18 of the ASCA Seyfert 1 AGN sample of George et al. (1998). The main signatures of a warm absorber are the O VII and O VIII K edges at 0.74 keV and 0.87 keV. Since warm absorbers are seen in such a large fraction of ASCA observations of Seyfert 1 sources and our data are of high enough quality to distinguish the warm absorber signatures, or at least constrain upper limits, we looked for these signatures among the sources with a high number of counts below 2 keV (with the exception of possible blazar SWIFT J0216.3+5128).

Following Reynolds (1997), we added two edge models (`zedge` in XSPEC) to account for the O VII and O VIII K edges. We fixed the edge at the energies of these warm absorber signatures (0.74 keV and 0.87 keV), allowing the optical depth to vary. In Table 4.7, we record the errors on optical depth and the change in χ^2. In the Reynolds (1997) sample, optical depths for clearly detected edges ranged from $\approx 0.10-1.5$. From our spectral fitting, half of the sources have upper limits of $\tau < 0.10$ for O VII and 7/8 have upper limits of $\tau < 0.10$ for O VIII. In fact, the only source with a clear detection of both edges is ESO 490-G026. Clearly, much less than half of our low absorption/simple X-ray model sources show evidence of warm absorbing material in their spectra. We will discuss our results further in § 4.4.

Table 4.7. XMM-Newton Warm Absorber Model

Source	τ O VII [a]	τ O VIII[a]	$\Delta\chi^{2}$[b]
MRK 352	0.017	0.005	-12.3
ESO 548-G081	0.032	0.005	-0.06
ESO 490-G026	$0.233^{+0.048}_{-0.083}$	$0.095^{+0.047}_{-0.043}$	25
SWIFT J0904.3+5538	$0.186^{+0.098}_{-0.091}$	0.039	9.9
MCG +04-22-042	$0.063^{+0.022}_{-0.029}$	$0.035^{+0.026}_{-0.025}$	41.5
UGC 6728	0.072	0.023	0.8
WKK 1263	$0.046^{+0.087}_{-0.046}$	0.020	1.0
MCG +09-21-096	$0.036^{+0.023}_{-0.025}$	0.008	5.7

[a]Optical depth with errors or upper limits for the additions of edge models (`zedge`) at 0.74 keV and 0.87 keV.

[b]The χ^2 from the best fit model in Table 4.5 or 4.6 minus χ^2 from the warm absorber model.

Complex X-ray spectra sources

The remaining 13 sources ($\approx 1/2$) had spectra we classified as "double power law" spectra, similar to Turner et al. (1997). Earlier, we mentioned three scenarios that could create this type of a spectrum. Based on these three possibilities (viewing another source(s) such as X-ray binaries/diffuse galactic emission along with the absorbed AGN, cold gas partially covering the AGN light, and scattering of the AGN light from regions of different column densities) we decided to fit the spectra of these sources with the partial covering model, `pcfabs` in XSPEC. The partial covering model (see: Holt et al. (1980)) has two parameters: the hy-

drogen column density and the covering fraction. In addition to describing a partial absorber spectrum, this model is also useful for describing a spectrum where AGN light has been scattered, where the power law index of the direct, heavily absorbed spectrum is the same as that of the scattered component (which is not heavily absorbed). This model, to summarize, allows for flexibility in the soft spectrum which can fit all of the three physical origins mentioned for a complex spectrum (assuming the X-ray binary/diffuse emission has the same power law slope as the AGN emission, which is not expected). Thus, we fit the spectra of the remaining 13 sources with the model `tbabs*pcfabs*(pow + zgauss)` (Table 4.8).

As we noted, the partial covering model gives an equivalent result to a model with a power law modified by different amounts of absorption and two flux normalizations. We also wanted to test whether the power law spectral indices for these two components are the same or differ. To this end, we fit the sources with the model `tbabs*(tbabs*pow + tbabs*(pow + zgauss))`. This model allows the power law indices, normalizations, and column densities to vary for two separate power laws. The results do not differ significantly for half of the sources between the partial covering model (Table 4.8) and the separate power laws model (Table 4.9), with $\Delta\chi^2 < 8$. Each of these seven sources show a ratio of the low absorption power law to the more highly absorbed power law flux ($N_{\Gamma_1}/N_{\Gamma_2}$) less than 0.14 with an average value of 0.03. These results could be consistent with any of the three possible physical models, where the portion of scattered light or additional non-AGN emission or unabsorbed AGN light is very small. This is true of all of the sources, with the exception of ESO 362-G018 and NGC 6860, whose spectra are more complicated.

For the BAT source corresponding to the interacting system (NGC 6921 and

MCG +04-48-002), both sources are clearly absorbed. For MCG +04-48-002, the absorbed power law component in the double power law model was not well constrained due to the weak contribution from the low absorption power law component. This source was weaker by an order of magnitude than NGC 6921 in the *XMM-Newton* observation. Thus, throughout the remainder of the paper we will distinguish NGC 6921 as "the BAT source". This will not change any results, since both sources are absorbed sources with similar spectral results. We added MCG +04-48-002 to the spectral fits because, though it is clearly the weaker source in the XMM observations, it is brighter than NGC 6921 in the XRT observations. Further, in recently obtained Suzaku observations, which we are currently analyzing, we found that MCG +04-48-002 was the brighter source. These findings and a detailed analysis will be discussed in a future paper.

Based on reduced χ^2, three of the "double power law" sources (NGC 1142, ESO 362-G018, and ESO 506-G027) require additional/alternative models. For NGC 1142, a soft excess is clearly present (see Figure 4.2). The addition of a blackbody component with a temperature kT$= 0.123$ keV improved the separate power laws fit (Table 4.9), yielding an acceptable fit with χ^2/dof of 217.13/191. We note that this blackbody temperature, kT$= 0.123$ keV, is similar to the values seen in Table 4.6 for the sources fit with simple blackbody and power law models. The spectrum of ESO 362-G018, however, is still even more complicated. This spectrum appears to have well defined lines, particularly a strong line measured with an energy of 0.56 keV, which is consistent with O VII and improves the separate power laws fit by $\Delta\chi^2 = 50$. However, the power law spectral index for this source is still extremely flat ($\Gamma = 0.67$) where the typical value for Γ is ≈ 1.80 (Mushotzky 1982). This is also true of NGC 612, MRK 417, ESO 506-G027, and NGC 6860.

Flat power law indices have been noted, in addition to high column densities ($n_H \geq 10^{24}\,\mathrm{cm}^{-2}$) and strong Fe K lines (EW greater than a few hundred eV), as indicators of Compton-thick AGN (Matt et al. 1996). For NGC 612, MRK 417, and ESO 506-G027, all of these factors are met. However, even though ESO 362-G018 has a strong Fe K line and a flat spectrum, the fitted column density is only $6.3 \times 10^{22}\,\mathrm{cm}^{-2}$. The spectrum of NGC 6860 is even odder, with both power law components (see Table 4.9) having a flat slope with very low hydrogen column densities ($\mathrm{n}_H < 10^{22}\,\mathrm{cm}^{-2}$) and no strong Fe K line.

Though high column densities are possible indicators of Compton-thick sources, it is also possible for the X-ray spectrum of a Compton-thick source to have a lower measured column density. Such a model, as was proposed for the Seyfert 1 source MRK 231 by Maloney & Reynolds (2000), could be applicable for ESO 362-G018 and NGC 6860. In this model, the central power law source is blocked by Compton-thick material. The resulting reflection component is then scattered and absorbed elsewhere, outside the Compton-thick region. As a result, the measured X-ray column density is from this second absorbing region. Therefore, we include ESO 362-G018 and NGC 6860 in our list of Compton-thick candidates, despite their low column densities.

For our Compton-thick candidates, the sources with flat power law indices (ESO 362-G018, NGC 6860, NGC 612, MRK 417, and ESO 506-G027), we simultaneously fit the 8-channel BAT spectrum along with the XMM-Newton spectra, allowing a constant factor to vary for the BAT data, as we did for the MOS spectra. Increasing the energy range to 195 keV allows for better constraints on the power law component at high energies. Also, since a Compton-thick source spectrum should be a heavily reflected spectrum, it is extremely important to have higher energy data to determine the cutoff energy of the power law. This is evident con-

Table 4.8. XMM-Newton Detailed Fits: Partial Covering Model

Source	n_H [1]	fraction[1]	Γ	Fe K eqw[2]	Fe K norm.[2]	χ^2/dof	F_{soft} [3]	F_{hard} [3]
NGC 612	$129.70^{+12.90}_{-8.30}$	$0.999^{+0.001}_{-0.002}$	$2.12^{+0.06}_{-0.33}$	$108.10^{+63.74}_{-62.83}$	$17.9^{+10.6}_{-10.4}$	116.7/81	0.02	1.50
NGC 1142	$79.75^{+5.81}_{-3.05}$	$0.996^{+0.001}_{-0.001}$	$2.27^{+0.09}_{-0.17}$	$219.21^{+57.30}_{-40.87}$	$39.0^{+10.2}_{-7.27}$	260.5/195	0.08	3.01
SWIFT J0318.7+6828	$4.10^{+0.48}_{-0.41}$	$0.967^{+0.009}_{-0.009}$	$1.52^{+0.12}_{-0.11}$	$44.15^{+41.58}_{-39.43}$	$5.35^{+5.04}_{-4.78}$	775.9/770	0.24	7.31
ESO 362-G018	$26.64^{+2.72}_{-2.49}$	$0.913^{+0.005}_{-0.011}$	$2.13^{+0.04}_{-0.04}$	$421.82^{+35.15}_{-105.96}$	$28.6^{+2.38}_{-7.18}$	824.1/547	0.63	3.34
SWIFT J0641.3+3257	$16.01^{+2.68}_{-2.28}$	$0.982^{+0.007}_{-0.009}$	$1.24^{+0.26}_{-0.23}$	$7.76^{+46.01}_{-7.76}$	$0.51^{+3.00}_{-0.51}$	176.9/152	0.02	3.31
MRK 18	$18.25^{+3.64}_{-2.71}$	$0.97^{+0.02}_{-0.02}$	$1.62^{+0.31}_{-0.22}$	$178.09^{+109.77}_{-107.72}$	$5.47^{+3.37}_{-3.31}$	322.4/325	0.03	1.57
SWIFT J0911.2+4533	$33.02^{+11.01}_{-12.76}$	$0.994^{+0.004}_{-0.009}$	$2.47^{+0.98}_{-1.20}$	$582.76^{+425.24}_{-317.37}$	$23.7^{+17.3}_{-12.9}$	9.3/15	0.01	1.45
MRK 417	$85.69^{+12.73}_{-6.96}$	$0.995^{+0.002}_{-0.002}$	$2.25^{+0.15}_{-0.17}$	$114.77^{+75.78}_{-80.97}$	$10.8^{+7.11}_{-7.60}$	88.1/80	0.06	1.44
SWIFT J1200.8+0650	$10.80^{+0.68}_{-0.82}$	$0.991^{+0.002}_{-0.003}$	$1.47^{+0.10}_{-0.11}$	$84.18^{+47.13}_{-27.15}$	$7.69^{+4.31}_{-2.48}$	340.3/355	0.04	5.08
ESO 506-G027	$76.82^{+7.37}_{-6.79}$	$0.986^{+0.006}_{-0.003}$	$0.91^{+0.23}_{-0.18}$	$428.89^{+50.01}_{-85.01}$	$72.0^{+8.40}_{-14.3}$	228.9/170	0.03	3.87
NGC 4992	$69.05^{+7.39}_{-2.38}$	$0.9974^{+0.0015}_{-0.0016}$	$1.61^{+0.13}_{-0.41}$	$320.22^{+80.93}_{-72.56}$	$29.8^{+5.55}_{-5.39}$	120.8/132	0.01	1.93
NGC 6860	$4.53^{+1.33}_{-1.30}$	$0.60^{+0.07}_{-0.10}$	$0.79^{+0.11}_{-0.15}$	$75.64^{+62.90}_{-64.48}$	$9.45^{+7.86}_{-8.06}$	483.5/404	0.54	8.99
NGC 6921	$97.42^{+19.08}_{-3.78}$	$0.9984^{+0.0007}_{-0.0012}$	$2.34^{+0.11}_{-0.21}$	$54.56^{+47.68}_{-53.02}$	$11.9^{+9.8}_{-10.3}$	190.7/154	0.03	2.53
MCG +04-48-002	$96.00^{+51.97}_{-27.77}$	$0.9963^{+0.0023}_{-0.0133}$	$2.47^{+0.32}_{-0.44}$	811^{+1219}_{-329}	$42.3^{+63.7}_{-17.2}$	62.8/52	0.025	0.31

[1]Cold hydrogen column density in units of $10^{22}\,\mathrm{cm}^{-2}$ from the `pcfabs` model. This accounts for absorption beyond the Galactic values which are listed in Table 4.1. The fraction column is the partial covering fraction.

[2]Equivalent width (in eV) and flux normalization for an inserted Gaussian line at 6.4 keV (redshifted) with a set FWHM of 0.01 keV. The flux normalization is in units of $10^{-6}\times$ total photons $\mathrm{cm}^{-2}\,\mathrm{s}^{-1}$ in the line.

[3]The observed soft flux (0.3-2 keV) and hard flux (2-10 keV) are given in units of $10^{-12}\,\mathrm{erg\,cm}^{-2}\,\mathrm{s}^{-1}$.

Table 4.9. XMM-Newton Detailed Fits: Double Power Law Model

Source	n_H[1]	Γ_1	n_H	Γ_2	$N_{\Gamma_1}/N_{\Gamma_2}$[2]	Fe K eqw[3]	Fe K norm.[3]	χ^2/dof	Flux[4]
NGC 612	$0.32^{+0.09}_{-0.18}$	$4.27^{+1.78}_{-1.15}$	$79.79^{+19.47}_{-12.30}$	$0.28^{+0.21}_{-0.19}$	0.215	$177.00^{+86.96}_{-74.36}$	$12.8^{+6.25}_{-5.37}$	82.0/79	1.69
NGC 1142	$0.15^{+0.07}_{-0.06}$	$3.10^{+0.31}_{-0.71}$	$62.94^{+10.87}_{-5.72}$	$1.49^{+0.31}_{-0.17}$	0.028	$268.10^{+62.48}_{-52.50}$	$35.4^{+8.31}_{-6.90}$	245.8/193	3.19
SWIFT J0318.7+6828	$1.11^{+1.42}_{-1.11}$	$1.51^{+2.63}_{-0.72}$	$6.10^{+8.15}_{-6.10}$	$1.74^{+1.10}_{-0.24}$	0.139	$45.29^{+62.89}_{-37.03}$	$5.63^{+5.36}_{-4.79}$	772.8/768	7.41
ESO 362-G018	$0.00^{+0.01}_{-0.00}$	$2.30^{+0.07}_{-0.06}$	$6.30^{+2.32}_{-2.66}$	$0.67^{+0.18}_{-0.23}$	1.753	$432.23^{+110.50}_{-32.59}$	$22.1^{+3.31}_{-3.40}$	736.0/545	4.26
SWIFT J0641.3+3257	$0.00^{+0.04}_{-0.00}$	$0.82^{+1.38}_{-0.76}$	$16.96^{+9.75}_{-3.30}$	$1.45^{+0.78}_{-0.42}$	0.012	$1.58^{+55.02}_{-1.58}$	$0.20^{+3.37}_{-0.20}$	176.5/150	3.30
MRK 18	$0.36^{+0.57}_{-0.29}$	$3.74^{+2.79}_{-1.67}$	$18.28^{+7.22}_{-5.71}$	$1.78^{+0.65}_{-0.56}$	0.048	$188.57^{+113.34}_{-109.56}$	$5.91^{+3.33}_{-3.49}$	315.4/323	1.53
SWIFT J0911.2+4533	$3.84^{+9.73}_{-3.84}$	$2.56^{+7.44}_{-5.52}$	$48.03^{+28.32}_{-24.61}$	$3.35^{+6.59}_{-2.04}$	0.002	$695.56^{+1213.04}_{-437.52}$	$32.0^{+55.8}_{-20.1}$	8.2/13	1.36
MRK 417	$0.00^{+0.04}_{-0.00}$	$2.36^{+0.16}_{-0.16}$	$54.15^{+25.04}_{-11.30}$	$0.88^{+0.97}_{-0.42}$	0.101	$179.20^{+87.71}_{-86.64}$	$9.65^{+4.72}_{-4.67}$	78.8/78	1.62
SWIFT J1200.8+0650	$0.00^{+0.06}_{-0.00}$	$1.75^{+0.93}_{-0.43}$	$10.57^{+0.79}_{-0.98}$	$1.43^{+0.10}_{-0.08}$	0.009	$94.46^{+35.70}_{-35.96}$	$8.58^{+3.24}_{-3.27}$	338.9/353	5.14
ESO 506-G027	$0.00^{+0.08}_{-0.00}$	$0.81^{+0.28}_{-0.31}$	$80.37^{+7.77}_{-8.68}$	$0.99^{+0.48}_{-0.24}$	0.011	$418.22^{+69.39}_{-59.66}$	$73.6^{+12.2}_{-10.5}$	228.1/168	3.89
NGC 4992	$0.32^{+0.73}_{-0.31}$	$2.68^{+3.73}_{-1.69}$	$68.47^{+14.94}_{-9.62}$	$1.41^{+0.53}_{-0.14}$	0.006	$318.31^{+90.94}_{-74.91}$	$27.9^{+7.96}_{-6.56}$	70.4/78	1.97
NGC 6860	$0.00^{+0.01}_{-0.00}$	$0.47^{+0.10}_{-0.06}$	$0.60^{+9.45}_{-0.13}$	$0.48^{+1.56}_{-0.08}$	0.745	$65.36^{+60.57}_{-62.15}$	$8.17^{+7.57}_{-7.77}$	459.7/402	9.97
NGC 6921	$0.57^{+0.20}_{-0.21}$	$5.08^{+2.53}_{-1.25}$	$90.25^{+10.75}_{-10.63}$	$1.71^{+0.53}_{-0.25}$	0.025	$89.01^{+54.93}_{-58.37}$	$14.7^{+9.11}_{-9.67}$	149.3/164	2.64
MCG +04-48-002	$0.13^{+0.36}_{-0.13}$	$3.06^{+1.07}_{-0.78}$	$223.58^{+48.06}_{-88.16}$	$10.00_{-6.63}$	1.6e-9	496^{+954}_{-279}	$34.2^{+66.6}_{-19.1}$	58.4/50	0.26

[1]Cold hydrogen column density in units of $10^{22}\,\mathrm{cm}^{-2}$ from the `tbabs` model. This accounts for absorption beyond the Galactic values which are listed in Table 4.1. In this model, there is a separate column density component for each of the two power laws.

[2]Ratio of the flux normalization value for power law one versus power law two. For nearly all of these sources, the low absorption power law is much weaker.

[3]Equivalent width (in eV) and flux normalization for an inserted Gaussian line at 6.4 keV (redshifted) with a set FWHM of 0.01 keV. The flux normalization is in units of $10^{-6}\times$ total photons $\mathrm{cm}^{-2}\,\mathrm{s}^{-1}$ in the line.

[4]The observed total flux (0.5 – 10 keV) in units of $10^{-12}\,\mathrm{erg\,cm}^{-2}\,\mathrm{s}^{-1}$.

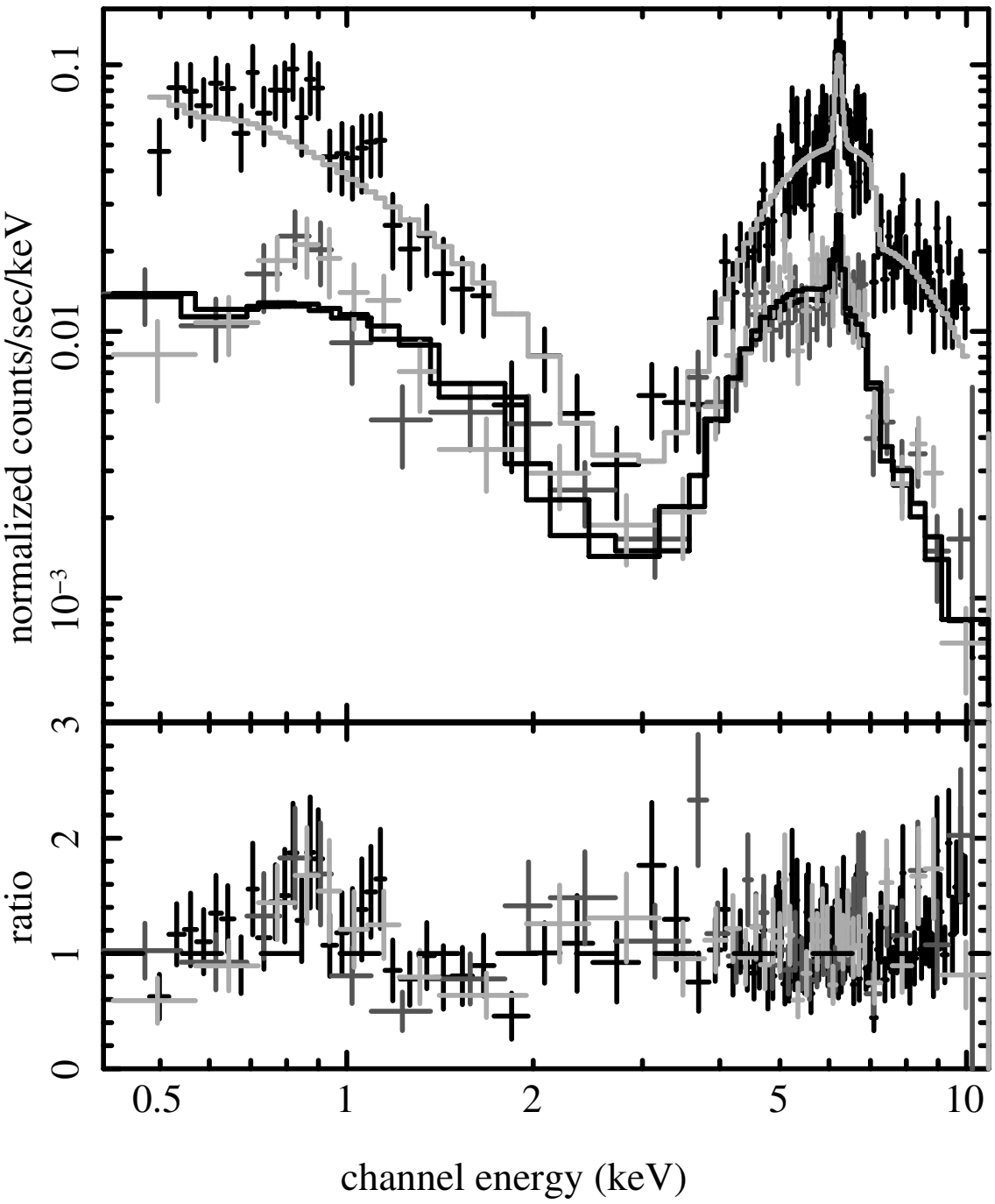

Figure 4.2: *XMM-Newton* spectrum (pn, MOS1, and MOS2) of NGC 1142 fit with the model `tbabs*pcfabs*(pow + zgauss)*const`. There is a clear soft excess with possible unresolved lines (in pn). We find that a better fit to this source is obtained with the addition of a blackbody model.

sidering that the reflection spectrum (`pexrav` in XSPEC (Magdziarz & Zdziarski 1995)) depends upon the cutoff energy of a power law, in addition to iron abundance, reflection factor, and geometry of the system. When we use this model, we fixed the iron abundance to the solar value and the inclination angle of the system to the default (60°).

We note that in using the BAT spectra we are assuming that the individual 14 – 195 keV spectra do not vary over the period of 22 months used to create the BAT spectrum. Future AGN observations with Suzaku, which can obtain simultaneous spectra from 0.3–200 keV, will allow us to test the accuracy of this assumption. To this end, we have obtained and are processing the Suzaku spectrum for one of our Compton-thick candidates, MRK 417. A paper is in preparation.

i. Low column density Compton-thick candidates

ESO 362-G018 The X-ray spectrum of ESO 362-G018 was not well-fit by either the partial covering or double power law model. While the double power law model provided the best fit, with a reduced χ^2 value of 1.35, this is not satisfactory. In the residuals from the fit, at least two emission line features were present. Adding gaussians for these lines, the fit improved by $\Delta\chi^2 = 72$. The energies of these lines (0.56 keV and 0.90 keV), which have fluxes on the order of the Fe K line flux, correspond to helium-like oxygen and possibly helium-like neon lines.

The flat power law and strong Fe K line suggest a reflection spectrum. Simultaneously fitting the *XMM-Newton* spectra with the BAT spectrum, we replaced the heavily absorbed power law model with a reflection model (`pexrav`). This model is an acceptable fit to the data with a reduced χ^2 of 1.14. However, though the reflected power law component is more typical of AGN ($\Gamma = 1.99^{+0.15}_{-0.27}$), the column density is extremely low for a Compton-thick source ($n_H = 6.2^{+9.0}_{-2.6} \times$

10^{21} cm^{-2}). As mentioned earlier, the observed low column density could be the result of scattering of the reflection spectrum through a second absorbing region of lower column density. The details of this fit are listed in Table 4.10 along with the other Compton-thick candidates.

From the HST observation of this source, Das et al. (2006) describe the image as showing dusty lanes that are interspersed with star-forming regions. This complex environment could partially cover some of the X-ray emission as well as contribute line-emission from young stars. Similarly, ESO 362-G018 could be a very Compton-thick source whose flat, reflection-dominated spectrum is scattered and viewed through an absorber (Maloney & Reynolds 2000). From the $\approx$ 10 ks *XMM-Newton* exposure, it is clear that the spectrum is complex. For a more accurate description of the source spectrum, a longer observation with higher signal-to-noise is necessary.

NGC 6860 From a literature search, we found that NGC 6860 is well studied in the optical and IR. Bennert et al. (2006) find optical emission line diagnostics of this source indicative of an intermediate state between an AGN and starburst galaxy. Indeed, they state that the AGN dominates only in the inner 10″ in the IR/optical. While it is unclear whether this is also true in the X-ray band, we necessarily extracted a spectrum from a much larger, 85″ region. The Optical Monitor pipeline processed images (U, UVW1, UVM2) also confirm the presence of star formation, where the nucleus is seen surrounded by a ring of star forming regions. From the evidence of the optical and IR observations, it is likely that the spectral form of NGC 6860 is composite, with both star burst/star formation and AGN contributions.

From the double power law model, we found that residuals to the fit indi-

cated a soft excess. Given the optical and IR evidence of star formation, we added an `apec` model to fit this excess. The `apec` model in XSPEC is a model for collisionally-ionized diffuse gas. Since the quality of the *XMM-Newton* spectra is too low to distinguish between collisionally and photo-ionized gas, we used the simpler, collisionally ionized model. As input parameters, the `apec` model requires a plasma temperature, metal abundance, redshift, and normalization. We fixed the redshift to the source's value and set the abundance to the solar value. Adding this model, with a best-fit plasma temperature of kT$= 0.14$ keV and normalization of 2×10^{-4}, improved the double power law fit by $\Delta\chi^2 = 6$. Therefore, this is not significant at the 90% level. One thing to note, however, is that the addition of the `apec` model causes Γ_1, the low absorption power law component, to steepen from 0.47 to 3.60. The higher absorption power law model components, column density and power law index, do not change.

Adding a reflection model to this fit (double power law with an `apec` model), improves the fit by $\Delta\chi^2 = 10$. With this model, we could not constrain the reflection factor or folding energy. We then added the BAT data to the *XMM-Newton* spectra. Still, the reflection factor and folding energy were not constrained (they continued to increase to unphysical values). We fixed these values to a folding energy of 100 keV and complete reflection. Though this model does not make physical sense, since a strong Fe K line is expected in a reflection dominated spectrum, it was clear from the fitting that a high reflection factor is preferred statistically. This reflection dominated model obtains a good statistical fit to the data with $\Gamma_1 = 1.14$ and $\Gamma_2 = 2.31$ and $\chi^2/dof = 444.5/408$ (see Table 4.10). However, we stress that since there is no strong Fe K line and the column density is low, we do not believe that this model is a good physical description of the data.

For this source, we also fit the data with a double partial covering model

(which could possibly be justified in a clumpy, dusty environment) and a model where we replaced the neutral absorption model, `tbabs`, with an ionized absorber, `absori`. Both models fit the data with similar χ^2 values as the reflection model (reduced χ^2 of 1.02 and 1.08, respectively). Both models also cause the fitted power law indices to steepen to values typical of AGN sources. We conclude that the spectrum of this source is too complicated (see Figure 4.3) to quantify with the data available. A better signal-to-noise spectrum is required to understand this source's X-ray spectrum.

ii. High column density Compton-thick candidates

As mentioned, we simultaneously fit the BAT spectra with the *XMM-Newton* spectra for sources with flat power law indices. Our three additional Compton-thick candidate sources are NGC 612, MRK 417, and ESO 506-G027, all with $n_H > 5 \times 10^{23}\,cm^{-2}$. For each of these sources, we replaced the heavily absorbed power law component in the double power law model (Table 4.9) with the reflection model (`pexrav`). We record the absorbed column density, power law index for the reflection component, cutoff energy (which was not constrained for ESO 506-G027), normalization factor for the BAT spectrum, and goodness of fit in Table 4.10.

Allowing the BAT flux normalization to vary by a constant multiplicative factor, we found that the values of the factors for NGC 612 and MRK 417 were very low ($<< 0.50$). Examining the BAT spectra, there is clear curvature in the BAT energy spectrum of these two sources, which is not well fit by the `pexrav` model (see Figure 4.4). This curvature is not seen in the other three Compton-thick candidate spectra (see Figure 4.3 for the spectrum of NGC 6860). Of particular note, the BAT spectrum of NGC 612 appears flat (well-modeled by a power law index

Table 4.10. Compton-thick Reflection Model

Source	n_H[1]	Γ	cutoff E[2]	BAT norm[3]	χ^2/dof
NGC 612[4]	$62.55^{+11.90}_{-23.92}$	$0.95^{+0.36}_{-0.80}$	$48.58^{+83.42}_{-24.18}$	$0.08^{+0.09}_{-0.05}$	81.7/85
ESO 362-G018	$0.62^{+0.90}_{-0.26}$	$1.99^{+0.15}_{-0.27}$	100	$0.782^{+0.27}_{-0.22}$	622.8/547
MRK 417[4]	$18.19^{+9.00}_{-13.57}$	$0.73^{+0.34}_{-0.53}$	$106.7^{+112.10}_{-54.70}$	$0.19^{+0.12}_{-0.09}$	114.6/83
ESO 506-G027	$65.49^{+11.93}_{-10.40}$	$1.88^{+0.22}_{-0.26}$	100	$0.94^{+0.24}_{-0.10}$	226.7/174
NGC 6860	$0.00^{+1.04}$	$2.31^{+0.14}_{-0.17}$	100	$1.21^{+0.32}_{-0.19}$	444.5/408

[1]Cold hydrogen column density in units of 10^{22} cm^{-2} from the `tbabs` model. This accounts for absorption beyond the Galactic values which are listed in Table 4.1. In this model, there is a separate column density component for each of the two power laws. The column densities listed are for the more heavily absorbed source.

[2]Cutoff energy for the `pexrav`/reflection model. For this model, we assumed that this component was a pure reflection component and allowed the cutoff energy to vary. Where the cutoff energy could not be constrained (the model parameter increases to very large, unphysical values), we fixed this parameter at the default value of 100 keV.

[3]Using the constant model, we allowed the BAT normalization to vary by a multiplicative factor. The recorded value is the factor variation of the BAT flux to the pn flux (normalized at 1), except for NGC 6860 which has no pn data (normalized to MOS1).

[4]For NGC 612 and MRK 417, the best fit to the data, in terms of reduced χ^2, was a model with low BAT normalization. Both of these sources showed curvature in the BAT spectrum, which was not well fit by the `pexrav` model. We include, in the text, a discussion of this as well as a description of the fits with BAT normalization set to 1 (similar to the best fits for the remaining 3 Compton-thick candidates).

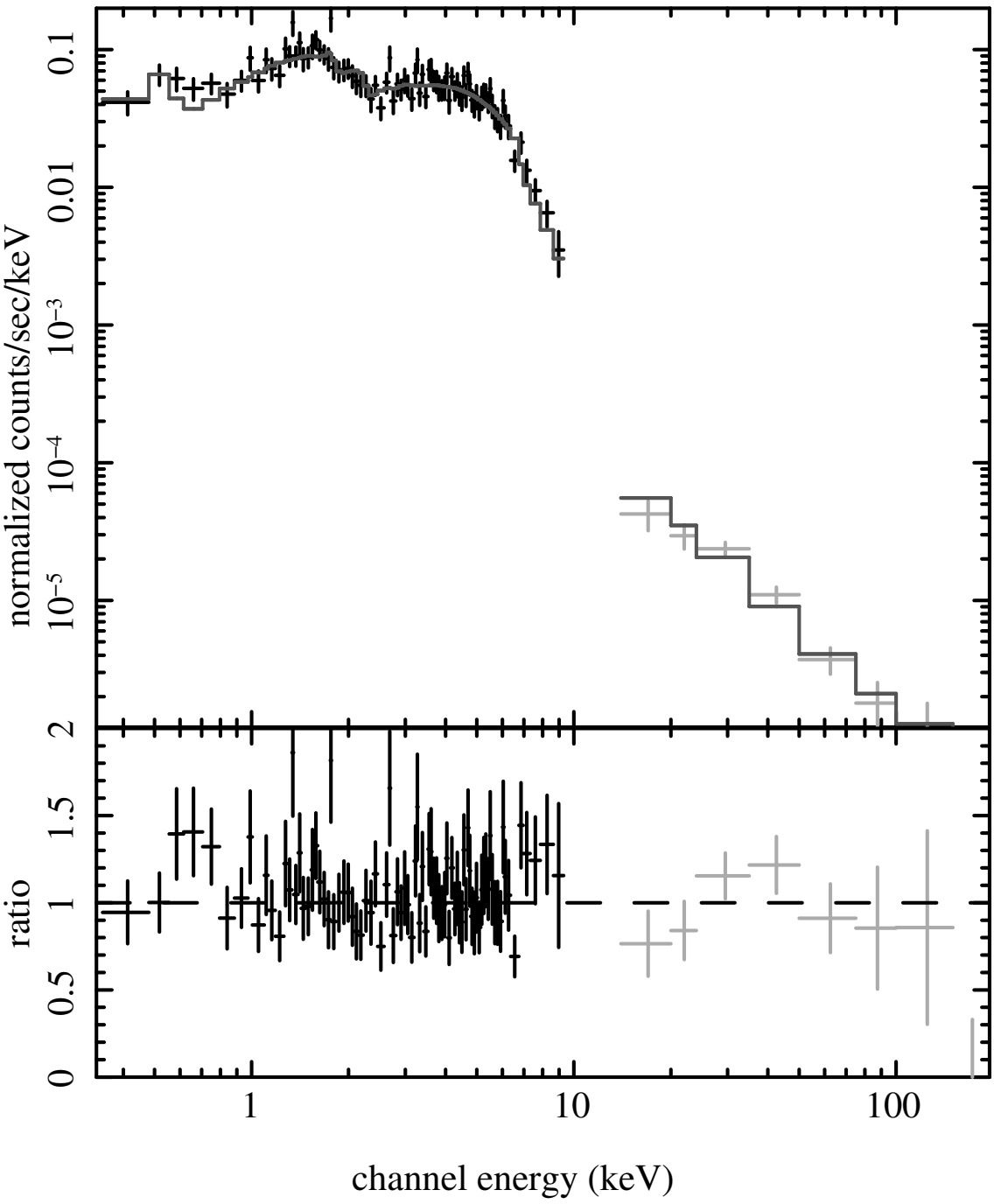

Figure 4.3: *XMM-Newton* MOS1 (no pn data was available for this source) and SWIFT BAT spectra of NGC 6860 fit with a reflection model. The spectrum of this source is very complex and could be adequately fit by a few different models (such as a reflection model, ionized absorption in place of neutral absorption, and a double partial covering model). However, residuals in the model point to complexity that can not be explained without higher signal-to-noise observations.

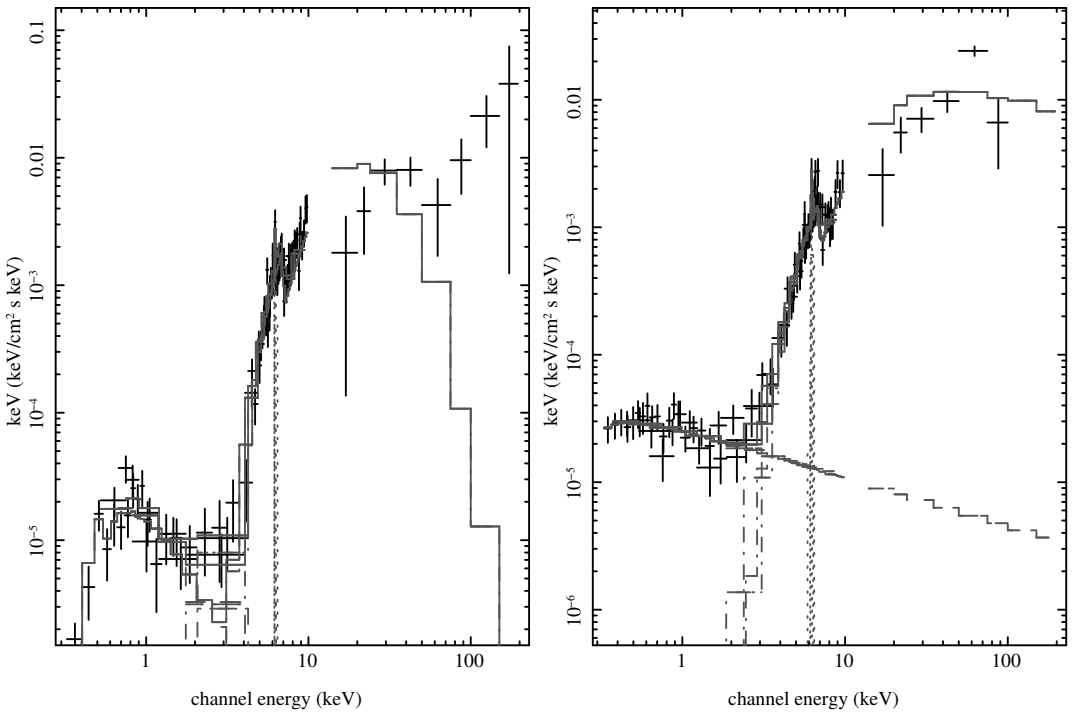

Figure 4.4: *XMM-Newton* and BAT spectra of the Compton-thick candidate sources NGC 612 (left) and MRK 417 (right). The model used is `tbabs*(tbabs*pow + tbabs*(pexrav + zgauss))*const`. The unfolded spectrum is plotted (E^2 f(E) vs. E, where f(E) is the model). The fits to the sources are described in the text. These fits were obtained with the constant factor set to 1.0 (normalized to the pn spectrum). The BAT spectra show some curvature and are not well fit by this model. This was not true of the remaining 3 Compton-thick candidates.

$<< 1.0$). For MRK 417, fixing the BAT multiplicative factor to 1.0 (the same as the pn spectrum) leads to a worse fit to the data with $\chi^2/\mathrm{dof} = 144.7/85$. With this fit, the cutoff energy for the `pexrav` model becomes unconstrained while the column density and power law index increase ($n_H = 3.4^{+0.9}_{-0.8} \times 10^{23}\,\mathrm{cm}^{-2}$ and $\Gamma = 1.85^{+0.12}_{-0.12}$). The same effect happens with the spectrum of NGC 612, where the best fit gives $\chi^2/\mathrm{dof} = 126.4/86$ with $n_H = 8.2^{+0.9}_{-2.6} \times 10^{23}\,\mathrm{cm}^{-2}$ and $\Gamma = 1.09^{+0.34}_{-0.45}$. It is possible that the curvature seen in the BAT spectrum is a real feature of the spectrum above 10 keV. Since the BAT diagonal response matrix is based on the harder spectrum of the Crab ($\Gamma \approx 2$), it is invalid in this case. Further, since the

BAT spectra are time averaged over months of observations, simultaneous observations for the 2 – 10 keV and 15 – 200 keV bands are needed to determine whether the BAT spectra correctly represent the very hard X-ray spectrum. We have already obtained Suzaku spectra for MRK 417 and are in the process of analyzing the data, which will be presented in an upcoming paper.

4.3.2 Variability

The main focus of our variability study is determining how the sources vary between the *XMM-Newton* and XRT observations, on a timeframe of hours to months. However, with 10 ks *XMM-Newton* observations, we also looked for shorter variability by examining the light curves of our sources. To this end, we extracted light curves from the filtered pn (or MOS1 where there was no pn data available) event files with the FTOOL XSELECT. We extracted light curves from the same regions used to extract spectra, binned by 100 s. We also extracted a background light curve from a region of the same size on the same chip as the source. We excluded SWIFT J0911.2+4533 from our analysis due to the low average count rate in the MOS1 observation (the source is located in a gap in a chip for the pn observation), $< 0.1 \mathrm{ct\,s^{-1}}$, which is on the order of the count rate in the background spectrum.

For the remaining 21 sources, following the analysis of Nandra et al. (1997), we computed the normalized excess variance and χ^2 values, for the assumption that the flux was constant, to quantify variability. We list these values as well as the average count rate in Table 4.11. Within our sample, 8 sources were flagged as possibly variable during the *XMM-Newton* observation, with reduced $\chi^2 > 1.5$, corresponding to a probability of $< 1\%$ of the count rates corresponding to constant count rates. For each of these 8 sources, we examined both the source

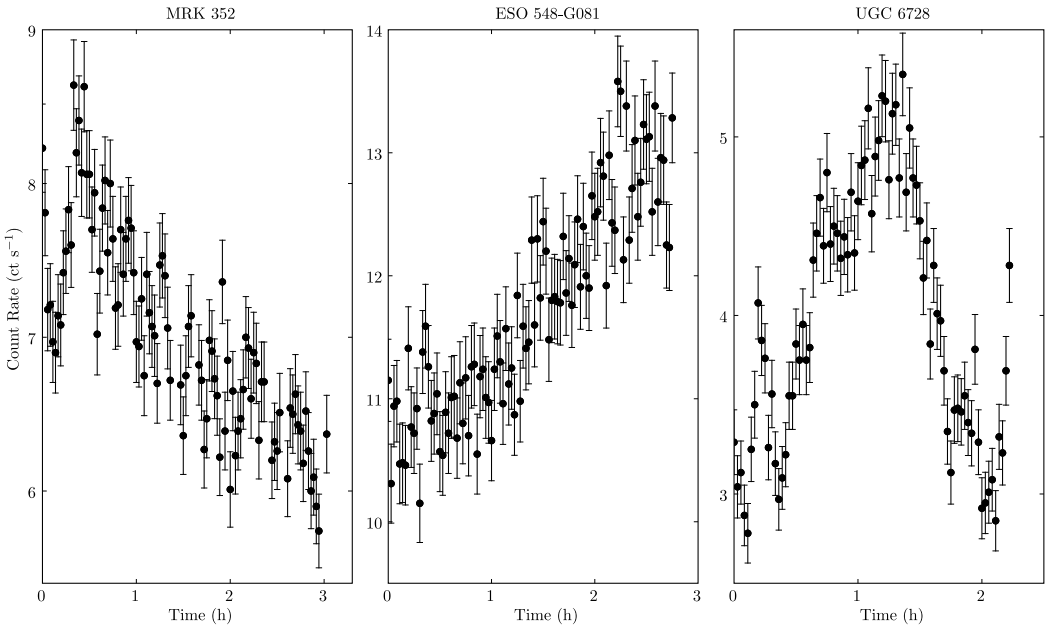

Figure 4.5: Light curves binned by 100 s for the *XMM-Newton* pn observations of MRK 352, ESO 548-G081, and UGC 6728. These two were the only sources to show significant variability above the background level($\chi^2/dof > 1.5$ compared to a constant flux model). Each of these sources are among the brightest flux sources in our sample (though not the three brightest), all are optical Seyfert 1 sources.

and background light curves. We found that for 5 of the sources the source and background light curves showed identical variability. For each of these sources, the ratio of average background count rates to average source count rates was relatively large, between 0.2 and 0.8. Thus, the background rates were significant compared to the source rates. The variability, also seen in the background light curve, was not intrinsic to the source for these sources. This was not the case for MRK 352, ESO 548-G081, and UGC 6728. The variability for these bright, Seyfert 1 sources is measured source variability.

In Figure 4.5, we include the light curves for each of the 3 sources with variability during the *XMM-Newton* observation. From the light curves, we estimated

Table 4.11. Variability in individual *XMM-Newton* Observations

Source	<Ct Rate>[a]	σ^2_{rms}[b]	χ^2/dof[c]
MRK 352	7.023	7.010 ± 0.0014	576.71/99
NGC 612	0.119	8.583 ± 5.640	123.93/107
SWIFT J0216.3+5128	1.470	1.043 ± 0.0048	82.57/100
NGC 1142	0.283	6.755 ± 0.8434	82.51/100
SWIFT J0318.7+6828	1.166	49.05 ± 0.5085	727.06/71
ESO 548-G081	11.730	$4.497 \pm 3 \times 10^{-4}$	620.33/100
ESO 362-G018	0.949	1.067 ± 0.01185	107.24/100
ESO 490-G026	5.128	$0.00523 \pm 2 \times 10^{-6}$	105.16/103
SWIFT J0641.3+3257	0.243	62.76 ± 8.863	273.35/120
MRK 18	0.507	94.36 ± 3.251	995.16/113
SWIFT J0904.3+5538	0.960	$0.7704 \pm 7 \times 10^{-4}$	133.70/121
MCG +04-22-042	13.151	$0.08061 \pm 6 \times 10^{-5}$	88.10/80
MRK 417	0.145	19.83 ± 12.28	103.53/77
UGC 6728	3.982	29.45 ± 0.02293	1069.19/81
SWIFT J1200.8+0650	0.430	1.860 ± 0.09154	100.27/110
ESO 506-G027	0.268	4.805 ± 0.6714	117.02/100
WKK 1263	2.446	$0.1615 \pm 3 \times 10^{-4}$	94.24/89
MCG +09-21-096	9.348	$0.02412 \pm 3 \times 10^{-6}$	96.63/99
NGC 4992	0.136	9.399 ± 3.531	163.66/143
NGC 6860	0.478	49.60 ± 1.823	377.40/119
NGC 6921	0.268	105.8 ± 12.07	500.70/122

[a]Average count rate for the *XMM-Newton* observation in the 0.3 – 10 keV band.

[b]Corresponding excess variability measurements, as defined in Nandra et al. (1997) $\times 10^{-3}$.

[c]χ^2 value divided by the number of bins for variability.

an average change in count rate/time, or Δ R/ΔT, where ΔR=$R_{max}-R_{min}$ and ΔT is the corresponding change in time. These values are $2.5\,\mathrm{ct\,s^{-1}}/2.4\,\mathrm{hr}$ (MRK 352), $2.8\,\mathrm{ct\,s^{-1}}/2.7\,\mathrm{hr}$ (ESO 548-G081), and $2.4\,\mathrm{ct\,s^{-1}}/0.8\,\mathrm{hr}$ (UGC 6728). For both MRK 352 and ESO 548-G081, these rates are minimums since the light curves are decreasing/increasing monotonically. UGC 6728, however, shows a definite maximum and is thus the most rapidly variable source, with count rate changing appreciably over less than an hour.

In order to compare variability between observations, on time scales of days to months, we compared the XRT and *XMM-Newton* spectral fits listed in Tables 4.4 and 4.3. In Figure 4.6, we plotted the hard, 2 – 10 keV, (x) and soft, 0.5 – 2 keV, (+) flux for multiple observations of our sources. We made the initial assumption that any intrinsic differences in flux between the instruments is less than 10%. From the figure, it is clear that variations greater than this level occurred for all of the 16 sources with > 100 counts in the XRT spectra. Of these, the most extreme changes are seen for ESO 362-G018, where both the hard and soft flux drop by an order of magnitude between the last two observations. However, without error bars on the flux and with a simplified model that is not satisfactory for all the sources, particularly for the high column density/complex spectra, a simple comparison of the fluxes is only a starting point for our variability study.

In addition to the flux, both the power law index and hydrogen column density introduce other sources of variation measured by the simple power law model. Changes in these parameters also affect the measured flux. Thus, we computed a statistic to quantify the flux variations between observations. To this end, we determined the value $(F_{max}-F_{min})/F_{avg}$ and the corresponding Δt_{max} ($|t_{max}-t_{min}|$ in days or the change in time for the greatest difference in observed flux between two observations) for each source in both the hard and soft bands. These values

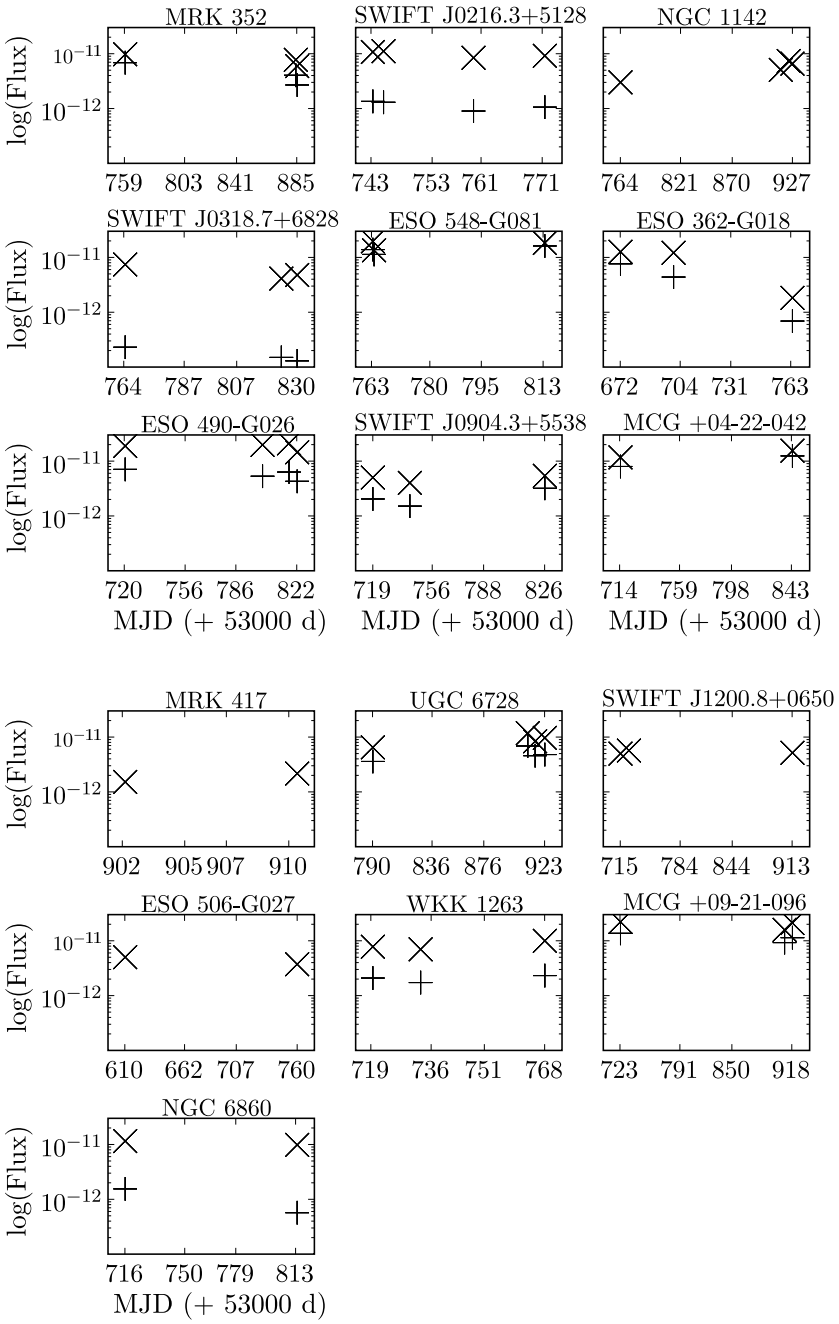

Figure 4.6: Plots of the flux variation in the soft 0.5 – 2 keV (+) and hard 2 – 10 keV (x) bands for sources with *XMM-Newton* and XRT observations ($>$ 100 counts). These flux values were obtained from simple absorbed power law fits (see Tables 4.4 and 4.3). For the sources with few/no counts in the soft band, the soft flux was unmeasurable.

are listed in Table 4.12 and the distributions of the values are plotted in Figure 4.7. From the histograms, there is no measured difference between the low column density sources (simple sources) and the high column density (complex sources). The values of $(F_{max}-F_{min})/F_{avg}$, however, are much smaller in the hard band than the soft. We note that the heavily absorbed sources, with much lower count rates in the soft band, have much less accurate soft flux measurements as well as fewer sources with observations > 100 counts. For the low column density sources, we find an average $(F_{max}-F_{min})/F_{avg}$ value of 0.52 in the soft band and 0.37 in the hard band.

Based on the $(F_{max}-F_{min})/F_{avg}$ values for our sources, our results indicate that the AGN spectra vary more in the soft band than the hard band. We tested this by performing a Kolmogorov-Smirnov test on the soft and hard band values of $(F_{max}-F_{min})/F_{avg}$, excluding the sources with values of 0 in the soft band. The maximum difference between the cumulative distributions is 0.54 with a corresponding probability of 0.028, suggesting that the distributions in the soft and hard band differ. This claim was also made based on ASCA observations of Seyfert 1 sources by Nandra et al. (1997). In addition to this result, we find that the hard flux variability for the low absorption and more complex sources is similar. Unfortunately, due to the lower number of counts in the XRT observations, we can only compare half of the complex sources to the complete sample of low column density sources.

In Figure 4.8, we plot the variability measure $(F_{max}-F_{min})/F_{avg}$ versus the change in time between the observations of F_{max} and F_{min}, Δt_{max}. From this plot, it is clear that, as already stated, the variability measurement $(F_{max}-F_{min})/F_{avg}$ is smaller in the hard band than the soft band. However, there is no significant difference in Δt_{max} for the total sample, with average values of 100.1 days for the

soft band and 81 days for the hard band.

As a next step in our analysis, we simultaneously fit the *XMM-Newton* pn spectrum with all of the corresponding XRT observations for the sources listed in Table 4.12. We began by fixing all XRT fit parameters to the best-fit *XMM-Newton* pn power law (+ gaussian where there is a strong line and blackbody where it was required) model. We accounted for absorption using the `tbabs` model for low column sources and the `pcfabs` model for the heavily absorbed/complex sources. We then allowed the flux to vary between these observations by adding a `const` model. Where the addition of this model significantly changed χ^2 ($\Delta\chi^2 > 10$) we flagged the source as having a varying flux. We then tested variability in column density and power law photon index by allowing each of these parameters, along with their normalizations, to vary. Again, we noted significant changes in χ^2.

In order to measure the amount each model parameter varied between observations, we obtained error measurements for n_H, Γ, and the 0.3 – 10 keV flux. We used the XSPEC model `pegpwrlw` in place of the `pow` model. The `pegpwrlw` model is similar to the simple power law model, however, the parameters E_{min} and E_{max} are used to indicate the energy range for the power law component. The normalization is then the flux from the pegged power law in units of 10^{-12} erg s^{-1} cm^{-2}. Since the normalization is a parameter in the model, errors are easily computed for the flux with the XSPEC command `err`. For all of the sources, we fixed $E_{min} = 0.3$ keV and $E_{max} = 10.0$ keV. We indicate variability based on our model fits in n_H, Γ, and flux (from the `pegpwrlw` model) in Table 4.12. Details on the model fitting for the individual variable sources are discussed in the appendix.

For the sources with low column densities, $n_H < 10^{23}$ cm^{-2}, and simple spec-

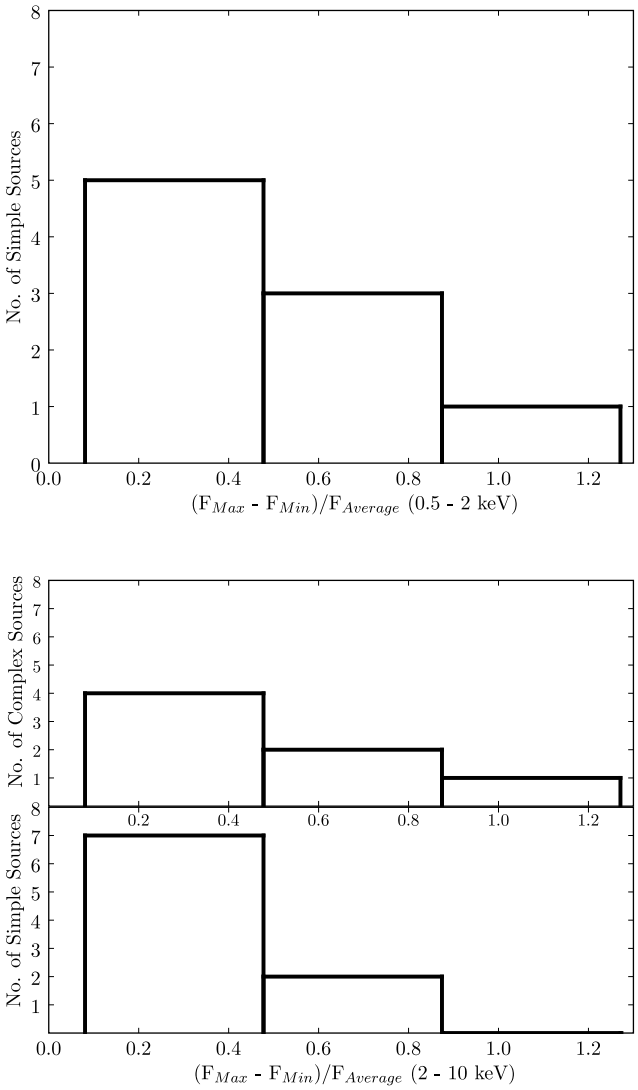

Figure 4.7: Distribution of variability measurements, $(F_{max}-F_{min})/F_{avg}$, for all of the sources listed in Table 4.12. The first histogram shows the values for the soft (0.5 – 2.0 keV) band while the second set of histograms show the distribution in the hard (2.0 – 10.0 keV) band. For the soft band, we show the distribution only for the low column density/simple model sources. The more absorbed/complex sources had fewer counts in the soft band, making the $(F_{max}-F_{min})/F_{avg}$ unreliable for most of these sources. Further, only half of the absorbed sources had XRT observations with > 100 counts over all bands, so the sample is not complete even in the hard band. For the simple model sources, we find that the variability, estimated from $(F_{max}-F_{min})/F_{avg}$, is higher for many of the sources in the soft band than the hard band.

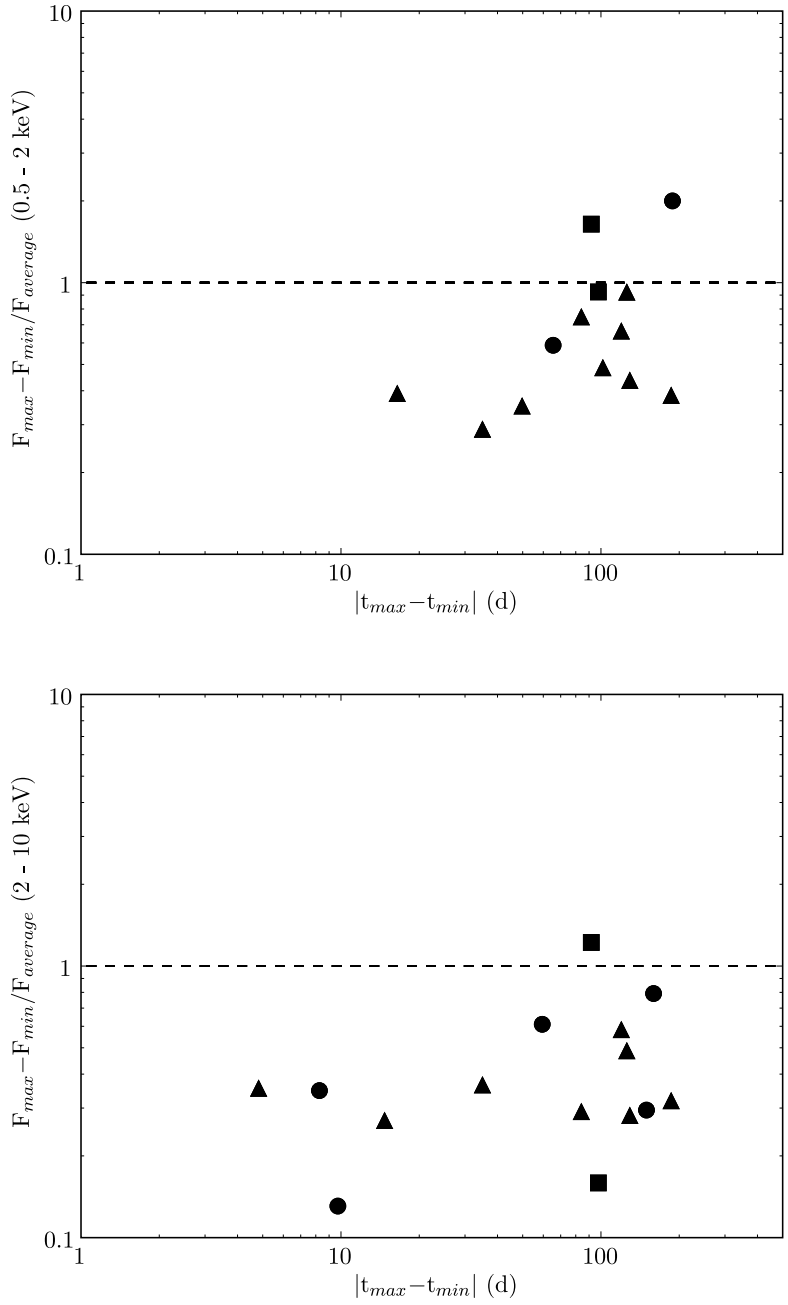

Figure 4.8: Plots of the flux variation in the soft 0.5 – 2 keV and hard 2 – 10 keV bands, measured by $(F_{max}-F_{min})/F_{avg}$, versus number of days between observations for the maximum and minimum flux. In this figure, sources with X-ray spectra best described by a simple model (triangles), complex model (circles), and the two complex sources with $n_H < 10^{23}\,cm^{-2}$ (squares) are plotted. The $(F_{max}-F_{min})/F_{avg}$ values are lower in the hard band. In the soft band, three complex sources are not plotted due to uncertainty in measuring their soft fluxes. The average value of Δt_{max} or $|t_{max}-t_{min}|$ is about 100 days for both hard and soft flux.

Table 4.12. Variability between *XMM-Newton* and XRT Observations

Source	Soft var.[1]	Δ t$_{soft}$[2]	Hard var.[1]	Δ t$_{hard}$[2]	n$_H$?[3]	Γ?[3]	Flux?[3]
MRK 352	0.92	125.7	0.49	125.7	yes	no	yes
SWIFT J0216.3+5128	0.39	16.5	0.27	14.7	no	no	yes
NGC 1142	0.00	151.9	0.79	159.4	no	yes	yes
SWIFT J0318.7+6828	0.59	65.5	0.61	59.4	no	no	yes
ESO 548-G081	0.35	49.7	0.36	49.7	no	yes	yes
ESO 362-G018	1.64	91.8	1.22	63.5	yes	no	yes
ESO 490-G026	0.49	101.7	0.35	4.8	yes	yes	yes
SWIFT J0904.3+5538	0.75	84.1	0.29	84.1	yes	yes	yes
MCG +04-22-042	0.44	129.1	0.28	129.1	yes	no	yes
MRK 417	0.00	8.3	0.35	8.3	no	no	no
UGC 6728	0.66	119.8	0.58	119.8	no	no	yes
SWIFT J1200.8+0650	2.00	188.4	0.13	9.7	no	no	no
ESO 506-G027	0.00	149.7	0.29	149.7	no	no	no
WKK 1263	0.29	35.0	0.36	35.0	no	no	yes
MCG +09-21-096	0.38	186.2	0.32	186.2	no	yes	yes
NGC 6860	0.92	97.7	0.16	97.7	yes	yes	yes

[1]Comparing soft and hard flux from the *XMM-Newton* and XRT observations listed in Tables 4.4 and 4.3. As noted in the Variability section, we used the statistic $(F_{max} - F_{min})/F_{avg}$ to compare the individual *XMM-Newton* and XRT fluxes in the soft (0.5 – 2.0 keV) and hard (2.0 – 10.0 keV) bands. For a few of the high column density sources (n$_H > 10^{23}$ cm^{-2}), the soft band flux was not able to be measured accurately due to a lack of counts. Therefore, the values in the Soft var. column are unreliable for these sources (NGC 1142, MRK 417, SWIFT J1200.8+0650, and ESO 506-G027).

[2]The corresponding value t$_{max}-$t$_{min}$ in days for the $(F_{max} - F_{min})/F_{avg}$ values in each band.

[3]Was there variability in each of the indicated parameters (n_H, Γ, Flux)? Details are given in the appendix for each individual source.

tral shapes (Tables 4.5 and 4.6), all had at least one XRT observation to compare with the *XMM-Newton* spectra. All of these sources showed some form of variability. As an example, Figure 4.9 shows the XRT and pn normalized observed and unfolded spectra with the best-fit model for MRK 352. This source showed more variability than any other low column density source. For MRK 352, the *XMM-Newton* spectrum, taken five months prior to the XRT observations, shows no absorption and is nearly double the flux level of the second XRT observation. In the XRT observations, which are taken only a day apart, the flux changes by 40%. The column densities also change between these two observations, by approximately 30%, where the XRT columns are an order of magnitude higher than the *XMM-Newton* observation's measured column density. The observations for the low column sources indicate variability in: flux for all of these sources (8), column density for half, and power law index for 3 sources.

For the sources with hydrogen column densities higher than $10^{23}\,\mathrm{cm}^{-2}$ (Table 4.8), five of the AGN had XRT observations, all with less than 100 counts, while NGC 4992 had no XRT observations. Of the remaining six sources, MRK 417, SWIFT J1200.8+0650, and ESO 506-G027 did not vary, in that, allowing n_H, the power law, and flux to vary yielded $\Delta\chi^2 < 10$. Using the `pegpwrlw` model, the errors on the flux for each observation (*XMM-Newton* and XRT) were within range of the other observations. For example, SWIFT J1200.8+0650 showed an unabsorbed flux from the power law component ranging from: 1.01 – 1.25 $\times 10^{-11}\,\mathrm{erg\,s^{-1}\,cm^{-2}}$ (XMM), 1.01 – 1.29 $\times 10^{-11}\,\mathrm{erg\,s^{-1}\,cm^{-2}}$ (XRT-1), and 1.04 – 1.50 $\times 10^{-11}\,\mathrm{erg\,s^{-1}\,cm^{-2}}$ (XRT-2) with $\chi^2/\mathrm{dof} = 235.7/241$ for the `tbabs`*`pcfabs`*(`pegpwrlw`) model.

The sources NGC 1142, SWIFT J0318.7+6828, ESO 362-G018, and NGC 6860 did show significant variability between the *XMM-Newton* and XRT observations

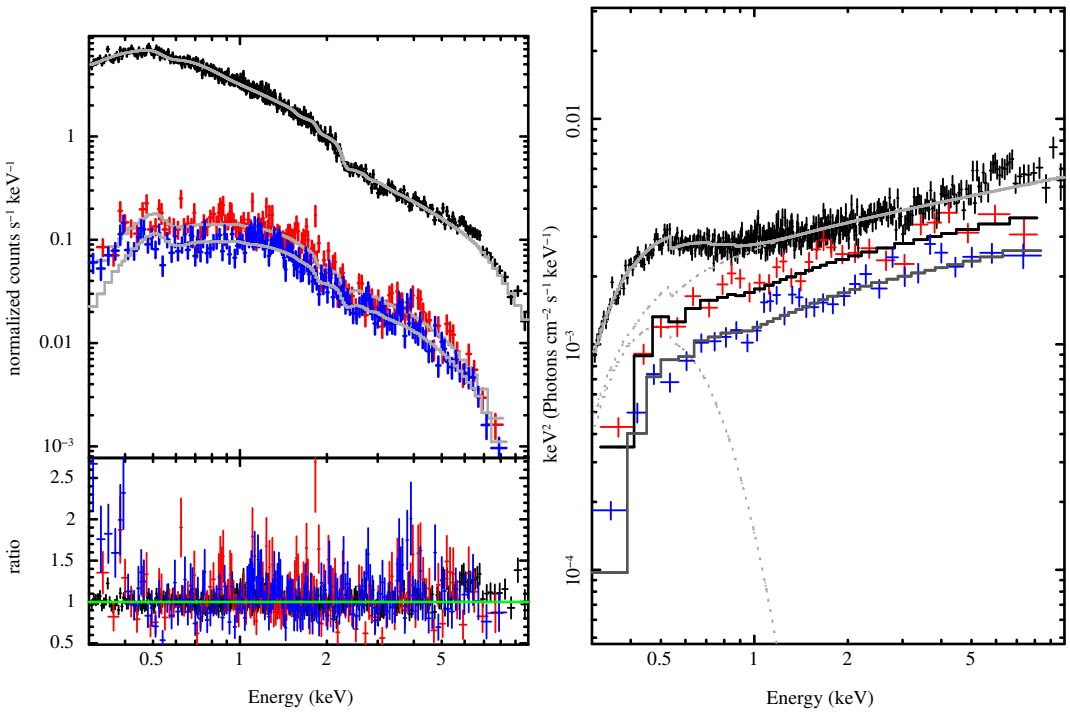

Figure 4.9: **(left)** *XMM-Newton* pn spectrum (black) with two XRT (red and blue) observations for MRK 352 fit with the model `tbabs*tbabs*(pegpwrlw + bbody)`. The best-fit model required both the hydrogen column density and flux to vary between the three spectra. **(right)** The unfolded spectrum (E^2 f(E) vs. E, where f(E) is the model) is plotted for the same source, MRK 352.

(as detailed in the appendix). To summarize the variability, 3 showed no variability, 4 had variable fluxes, 2 had varying column densities, and 3 showed varying spectral indices. Given the complex shape of the spectra of ESO 362-G018 and NGC 6860, we are uncertain of how to interpret the variability. We simply noted the sources as varying under all of our criteria, but again note their complexity.

ESO 362-G018 showed the most variability of the objects in our study. We conclude this section with a discussion of this source's spectrum. In Figure 4.10a, we plotted the observed spectra of this source. The shape of the spectra varied considerably below 2 keV for all observations. In the hard band, the XRT observations show no evidence of the Fe K line which is so prominent in the pn spectrum. In Figure 4.10b, we plot the unfolded spectra. Here the y-axis cor-

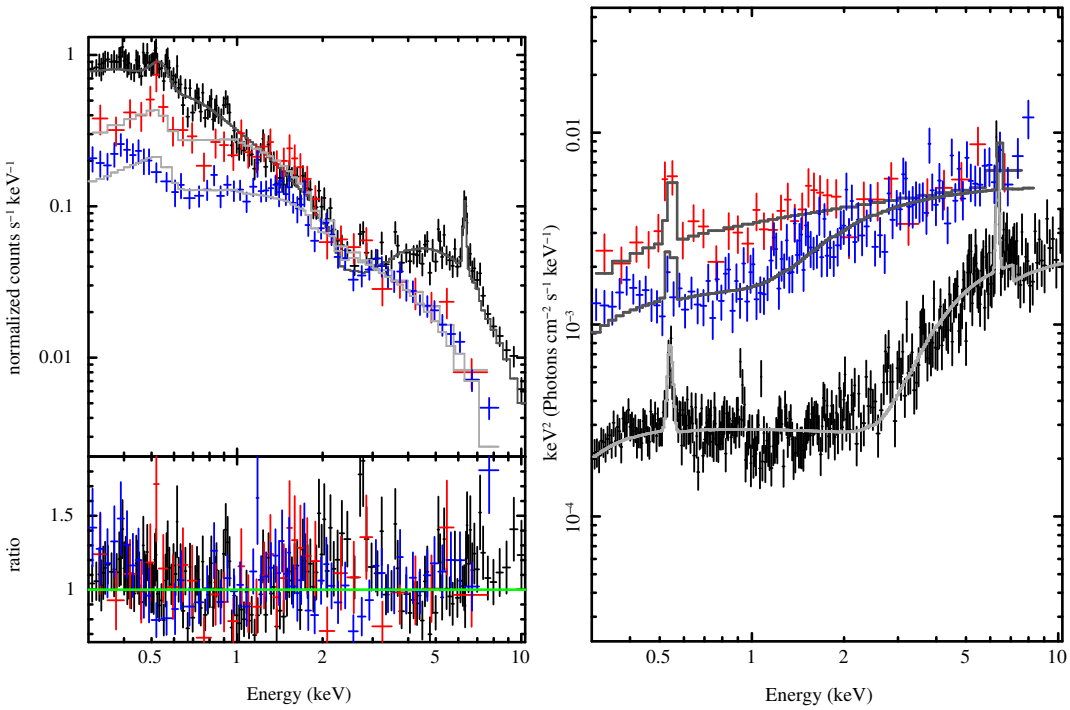

Figure 4.10: **(left)** *XMM-Newton* pn spectrum (black) with two XRT (red and blue) observations for ESO 362-G018 fit with the model `tbabs*pcfabs*(pegpwrlw + zgauss + zgauss)`. This source, with a complex spectrum, varied considerably between the XRT observations, taken approximately 2 months later, and *XMM-Newton* observation. The *XMM-Newton* observation shows a strong Fe K line and a column density 10 times that seen by the XRT observations. The flux is also lower by $\approx$ 50% in the *XMM-Newton* observation (the spectra shown are normalized and exhibit the **observed** spectrum). **(right)** The unfolded spectrum for ESO 362-G018 is plotted (E^2 f(E) vs. E). If the Fe K line remained at the same level as in the *XMM-Newton* observation, the increased flux from the power law component would dominate the line emission in the XRT observations. This is a possible explanation for the appearance of the Fe K line. The observed spectrum is shown in Figure 4.9.

responds to E^2 f(E). In this plot, we can see that the XRT spectra (taken about 2 months before the *XMM-Newton* observation) are much brighter. If the Fe K line remained at the same flux level, it would be completely dominated by the power law component. This is one possible explanation for the disappearance of the Fe K line.

To summarize our findings, only a few sources (3/21) varied appreciably

on the $\approx$ 3 hr time scale of the *XMM-Newton* observations. Those sources that did vary were bright, X-ray sources with spectra well-fit by simple power law models. From a comparison of the XRT and *XMM-Newton* spectra, taken a day through months apart, it is clear that most of the sources vary on longer time scales. In the extreme case of ESO 362-G018, the source varies drastically in flux, column density, and overall shape in two months time. All of the low column density sources varied in flux, while half showed evidence for varying column densities. Unfortunately, given the lower count rates in comparable exposure times, we have less data on the high column density sources. From a comparison of the $(F_{max}-F_{min})/F_{avg}$ distributions, they appear to vary similarly to low column sources. However, higher quality data is necessary to draw firm conclusions.

4.4 Discussion

In this study, we examined the X-ray properties of a sub-sample of BAT detected AGN from the 9-month BAT catalog. These sources, selected based on their 14-195 keV flux, probable optical identifications with the Digital Sky Survey and 2MASS, and their lack of an archival X-ray spectrum, are probably representative of the whole 9-month sample. Having a bright DSS or 2MASS counterpart does not impart a significant selection effect, considering that all but 20 of the BAT AGN 9-month sample fit this criteria. The 20 sources without a bright optical/IR counterpart are mostly blazars, of which there are only 15 in the 9-month catalog. Since blazars are less than 10% of the sample, we decided to focus on the majority, non-blazar sources. For the BAT AGN sample, Tueller et al. (2008) list 2MASS K_s magnitudes for the sources with available values from NED. The average value

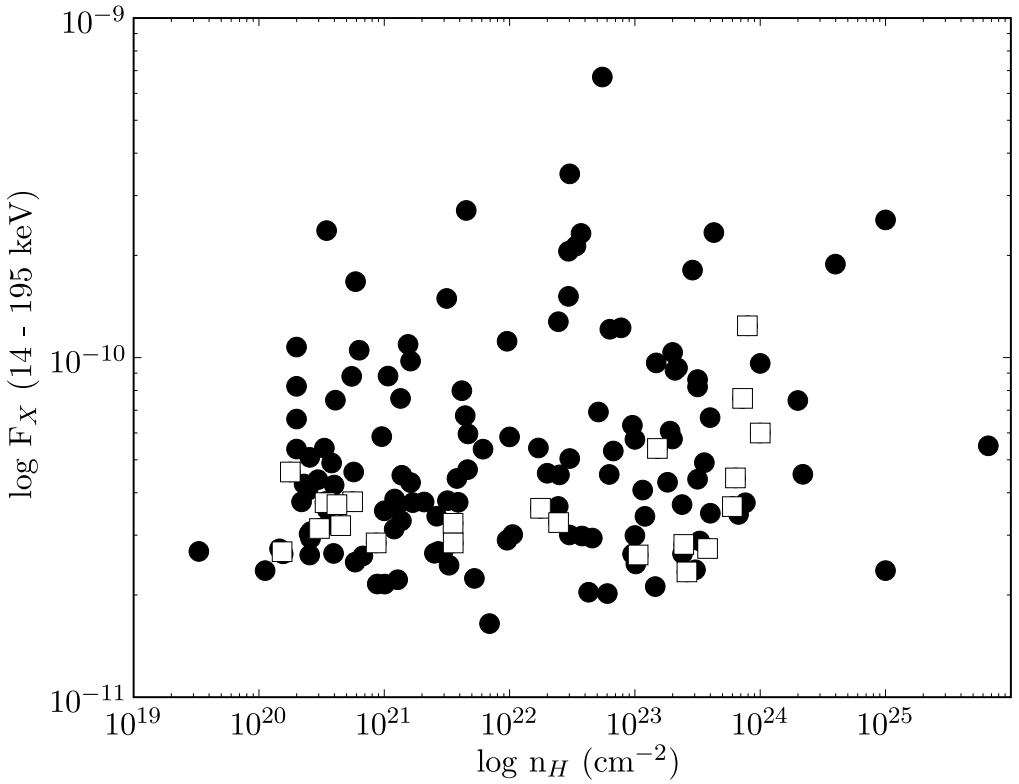

Figure 4.11: Hydrogen column density (cm^{-2}) versus the 14-195 keV flux (erg s^{-1} cm^{-2}) measured by SWIFT's BAT instrument. These values are listed in Tueller et al. (2008), with the circles representing 9-month catalog sources and the squares sources from the 9-month catalog with *XMM-Newton* follow-ups detailed in this paper. We note that for column densities higher than $\approx 10^{24}$ cm^{-2}, the spectrum is likely optically thick to Compton emission and thus there is a greater uncertainty in the measured hydrogen column density.

for the BAT sample is 11.47 with a variance of 4.04. Our sub-sample is slightly dimmer, with an average magnitude of 12.10 and a variance of 1.80, but well within the distribution of BAT AGN magnitudes.

The column density distribution of our sub-sample, shown in Figure 4.11, is representative of the larger sample. In the plot of hydrogen column density versus 14-195 keV flux (values from Tueller et al. (2008)), our 22 *XMM-Newton* follow-up sources span the range of hydrogen column densities. Roughly half

of the sources have low column densities ($n_H < 10^{23}\,cm^{-2}$), while half are more heavily absorbed. We find the same ratio of absorbed to non-absorbed sources in our *XMM-Newton* follow-up sample. While the low absorption sources in our sample span the lower range of hard X-ray fluxes (from BAT), this is expected, since the sources were not previously studied in the X-ray regime. For the absorbed sources, however, we find that our sample spans the full range of BAT X-ray fluxes.

Given that our sample of sources is a representative sample of the 9-month BAT catalog, it is worthwhile to discuss the general properties of our sources. To begin, the optical host galaxy classifications of our sources are listed in Table 4.1. Examining the host galaxy classifications, 17/22 of the hosts are classified as spirals or peculiar spirals. This result is interesting, considering that Grogin et al. (2005) found the hosts of X-ray selected, z $\approx 0.4-1.3$, Chandra Deep Field sources to be dominated by ellipticals. If the BAT AGN hosts are predominately spirals, as our sample suggests, this could imply an evolutionary effect in AGN host galaxies between the z≈ 0.03 and z $\approx 0.4 - 1.3$ universe.

4.4.1 Spectral Classification

From our detailed X-ray spectral fits, we found that 9 of the 22 sources had column densities below $10^{23}\,cm^{-2}$ and spectra well-fit by simple power law or power law with a soft excess models. Nearly half of these sources showed evidence of having a soft excess. Optically, all of these sources except for SWIFT J0216.3+5128 and WKK 1263 are Seyfert 1 – 1.2 sources. As discussed in the detailed spectral fitting section, SWIFT J0216.3+5128 is most likely a blazar. Though, WKK 1263 is identified as a Seyfert 2 in NED, no optical spectrum is available in the literature to confirm this. It is possible that this source was simply misclassified.

The remaining sources in our study had more complex X-ray spectra. For most of these sources, half of the sample, an absorbed power law component model fit is unacceptable. This was particularly true for ESO 362-G018 and NGC 6860. The column densities and power law indices computed from the simple model, for these sources, are drastically different than values from more complex models. Both of these sources, optically Sy 1.5, had optical images indicating dust clouds interspersed with star formation. Likely, the complex environment contributed to the complexity seen in the X-ray observation. However, without higher signal-to-noise observations we were unable to resolve the complex spectral components. These results illustrate the danger of using low quality data/simple models to determine the properties of complex sources.

The remaining 11 sources, half of the sample, had column densities clearly above $10^{23}\,\mathrm{cm}^{-2}$. We classified the observed spectra of these sources as having a "double power law" shape, similar to Turner et al. (1997). Optically, these sources are Seyfert 2s. The exceptions are NGC 612, a weak-lined, giant radio galaxy, and NGC 4992, which have "galaxy" spectra or optical spectra showing no emission lines indicative of AGN emission. NGC 612 was specifically classified as a "non-LINER", e.g. having non-AGN line ratios, by Lewis et al. (2003), while NGC 4992 is an INTEGRAL source whose optical spectrum led Masetti et al. (2006) to classify the source as an X-ray bright, optically normal galaxy. Considering the X-ray column densities for these sources, the optical AGN emission could be hidden or obscured by the high column of gas, $\mathrm{n}_H > 5 \times 10^{23}\,\mathrm{cm}^{-2}$, in the line of sight.

For all of the complex X-ray spectra sources, we fit the spectra with (1) a partial covering absorption model and (2) a double power law model, where each power law component had a separate absorption model. Most of the sources showed no significant difference in χ^2 between these two models. This makes it impos-

sible to determine whether the soft flux is the result of scattering of the AGN light, partial covering of the AGN light, or other X-ray sources (such as X-ray binaries or diffuse galaxy emission) contaminating the AGN spectrum. Particularly for sources, such as NGC 612, with low 0.5 – 2 keV fluxes, e.g., $F_{0.5-2keV} = 2 \times 10^{-14}$ erg s^{-1} cm^{-2} corresponding to a luminosity, $L_{0.5-2keV} \approx 4 \times 10^{36}$ erg s^{-1}, within the observed range of Galactic X-ray binaries, since the X-ray luminosity function extends to $\approx 3 \times 10^{38}$ erg s^{-1} (Grimm et al. 2002).

For sources with flat spectra (low photon index, Γ), we fit the spectra with a Compton thick model (a reflection dominated model, `pexrav`). We added the BAT spectra to the *XMM-Newton* data in order to extend the energy range to 200 keV. In addition to providing an adequate fit to the data, replacing the heavily absorbed power law component with a reflection model resulted in steeper spectral slopes more consistent with average AGN photon indices (where the BAT spectra were not curved, see Table 4.10). Based on the detailed model fits, NGC 612, ESO 362-G018, MRK 417, ESO 506-G027, and NGC 6860, are classified as Compton-thick candidates. Two of these sources, ESO 362-G018 and NGC 6860, have measured column densities $n_H << 10^{23}$ cm^{-2}. While a column density this low is not expected from reflection in a Compton-thick region, an alternate model where the reflection component is scattered and then absorbed outside of the Compton-thick region, such as employed for MRK 231 (Maloney & Reynolds 2000), could explain the spectra.

In addition to the Compton-thick candidates, four of the complex spectra sources had high partial covering fractions (> 0.99) with the partial covering model and very low ratios of the unabsorbed power law to the absorbed power law component ($N_{\Gamma_1}/N_{\Gamma_2} < 0.02$) with the double power law model. Thus, emission from the sources SWIFT J0641.3+3257, SWIFT J0911.2+4533, SWIFT

J1200.8+0650, and NGC 4992, was extremely low in the soft band (0.5 – 2 keV) compared to the hard band (2 – 10 keV). These sources are consistent with the new class proposed by Ueda et al. (2007) of hidden or buried AGN. Ueda et al. (2007) predict that these sources should have lower [O III] luminosities than typical Seyfert 2 sources. Archival optical spectra of NGC 4992 show very weak [O III], in fact, so much so that, as discussed above, the spectrum of this source appears as a typical galaxy. In our optical study (in preparation), we will explore this issue further. For now, it is important to note that more of these hidden sources exist. If our sample, showing 4/22 hidden AGN, is representative of the larger BAT sample, we expect that about 1/5th of local AGN have these same properties, making them nearly undetectable in optical samples.

4.4.2 X-ray Colors

Having classified the sources into categories, we now describe the general properties of our sample as a whole. To begin, in Figure 4.12 we plotted the column densities versus two different flux ratios (similar to a diagnostic in Malizia et al. (2007)). The column densities we used are listed in Tables 4.5, 4.6, and 4.9, where we used the column density of the more heavily absorbed power law component for the complex spectra. The flux ratios plotted are the ratios of $F_{2-10\,keV}/F_{14-195\,keV}$ (medium/hard) and $F_{0.5-2\,keV}/F_{2-10\,keV}$ (soft/medium). In the plots, we represent the three classes of objects (simple power law or power law and blackbody fit sources with low columns (triangles), complex heavily absorbed spectra (circles), and complex spectra that require more complicated models (squares)). We find that the low absorption sources have average values of medium/hard and soft/medium flux of 0.38 and 0.48, respectively. There is little change between the medium/hard and soft/medium flux ($\approx 20\%$) for the low

absorption sources. The heavily absorbed sources, however, have average values of medium/hard and soft/medium flux of 0.08 and 0.02. This is a 75% change in the values. Obviously, there is much less soft flux for the absorbed sources. The complex sources with poorly defined spectral models, have intermediate values of the medium/hard and soft/medium colors of 0.17 and 0.11.

In terms of use as a diagnostic, we find that the plot of column density versus ratio of $F_{2-10\,keV}/F_{14-195\,keV}$ (medium/hard) is a good diagnostic of column density, for $n_H < 10^{24}\,cm^{-2}$. Sources with similar column densities occupy areas close to the regions of constant power law index plotted (for $\Gamma = 1.5$ and 1.9). This is not true for the plot of column density versus ratio of $F_{0.5-2\,keV}/F_{2-10\,keV}$ (soft/medium). This appears to be a poor diagnostic, despite its wide spread use in deep X-ray surveys, with a large spread in the soft/medium color particularly seen in the sources with $n_H > 10^{23}\,cm^{-2}$. These results are not surprising, since the 2–10 keV flux is also affected by absorption.

From these color diagrams, we decided to construct a color-color diagram of the soft/medium flux ratio versus the hard/medium flux ratio in attempts to construct a better diagnostic diagram for sources with too few counts to measure column density. In Figure 4.13, we plot this diagram using the same symbols as in the previous diagram to indicate low absorption (triangle), complex (circle), and more heavily absorbed (square) sources. In this figure, it is clear that the different types of sources are clearly separated. The low absorption sources occupy the left hand upper corner, where the soft/medium and hard/medium colors are nearly equal. The heavily absorbed sources are closer to the right bottom corner, where the hard/medium flux ratio is much higher than the soft/medium flux ratio. Between these values, the complex sources as well as a source from each of the other two categories, reside. All of these sources have measured column

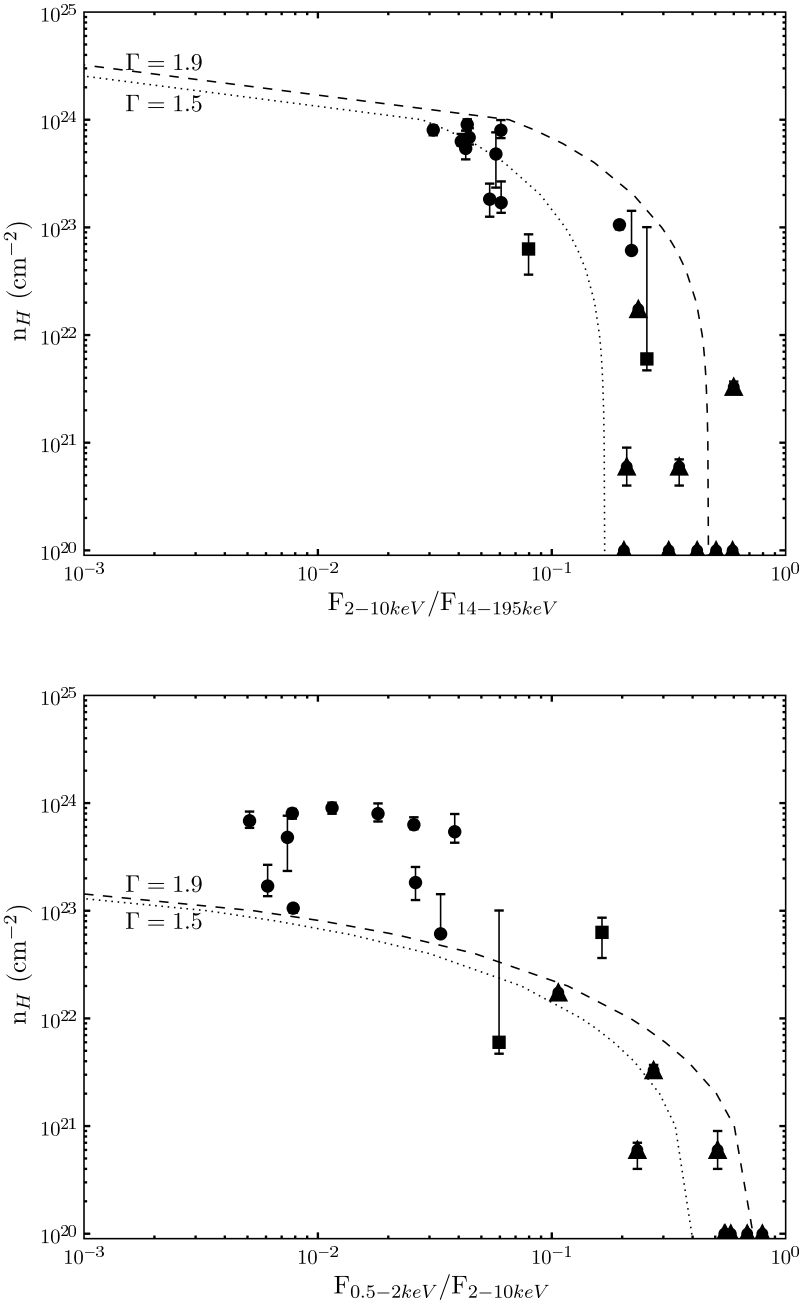

Figure 4.12: Plots of n_H vs. flux ratios for the *XMM-Newton* follow-up sources, showing the ratio of the 2 – 10 keV to 14 – 195 kev (BAT) flux (top) and 0.5 – 2 keV to 2 – 10 keV flux (bottom). The symbols represent the simple model sources (triangles), complex spectra (circles), and complex spectra we could not interpret (squares; ESO 362-G018 and NGC 6860). The unabsorbed sources are plotted as having $n_H = 10^{20}$ cm^{-2}. These sources had approximately the same ratio of hard flux/BAT flux as soft flux/hard flux. For the more heavily absorbed sources, the ratio of hard flux/BAT flux is clearly larger than the soft flux/hard flux ratio. The lines represent column density vs. flux ratio for constant power law indices ($\Gamma = 1.9$ and 1.5, as labeled).

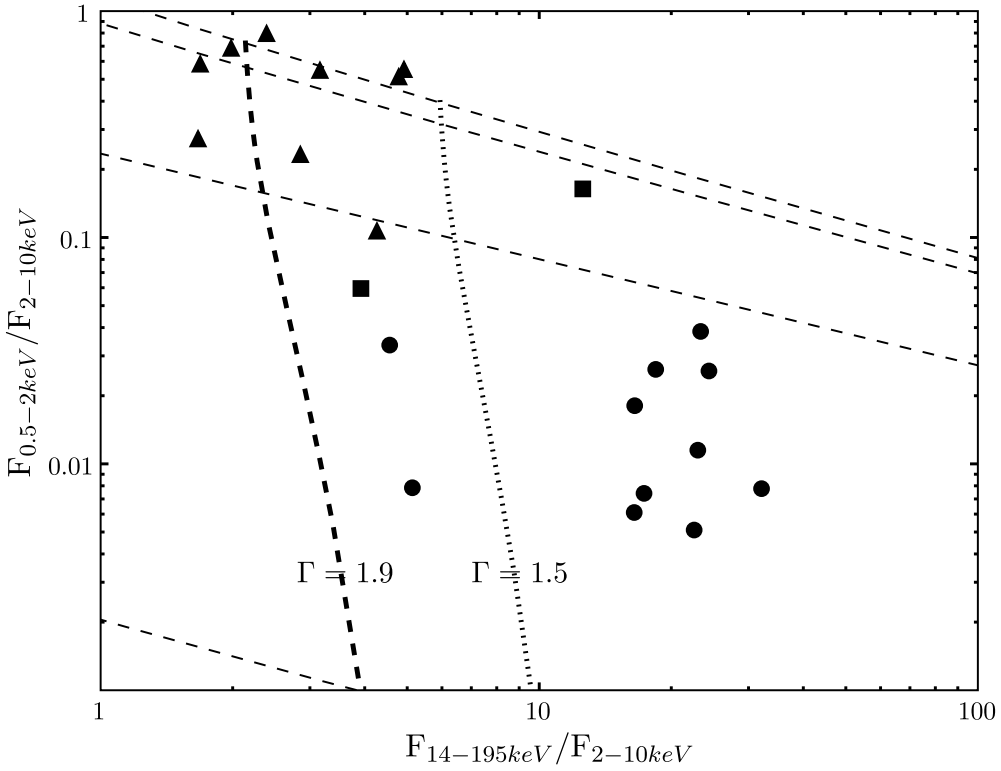

Figure 4.13: Color-color diagram of soft/medium (0.5 – 2 keV / 2 – 10 keV flux) and hard/medium (14 – 195 kev (BAT) / 2 – 10 keV flux) colors. The vertical lines represent values for constant power law indices (of $\Gamma = 1.9$ and 1.5, as labeled) with different absorbing columns. The other lines on the diagram represent constant column densities for different power law indices (from top to bottom: 10^{20}, 10^{21}, 10^{22}, and 10^{23} cm^{-2}). The symbols represent the simple model sources (triangles), complex spectra (circles), and complex spectra we could not interpret (squares; ESO 362-G018 and NGC 6860). The unabsorbed sources clearly occupy a region to the top left in the diagram while the more heavily absorbed sources lie towards the bottom right. Sources with column densities in the middle (between 10^{22} and 10^{23} cm^{-2}) lie between our unabsorbed and heavily absorbed points. From this result, we present a new diagnostic to describe spectra with low counts.

densities from $10^{22} - 10^{23}$ cm^{-2}, intermediary between the two classes. This result is very nice in that it provides a good diagnostic tool for observations with few counts, but requires data above 15 keV.

4.4.3 Properties of the Spectral Components

In addition to the flux and column density measurements, we have measured power law indices, blackbody components (where present), and Fe K equivalent widths (with the physical width of the line fixed to 0.01 keV at 6.4 keV). From our sample, we found no correlation between the hard band (2 – 10 keV) luminosity and power law indices. An important point to note is that the measured power law index for the complex spectra depends very much on the model used. Comparing the results of the partial covering model with the double power law model (Tables 4.8 and 4.9), the average power law index for the partial covering model is significantly higher ($< \Gamma >= 1.74$ compared to $< \Gamma_2 >= 1.36$) with smaller associated error bars. For the remaining 9 sources, the sources with spectra modeled by absorbed simple power law or power law and blackbody models, $< \Gamma >= 1.75$, similar to the results from the partial covering model. The values for the simple model/low absorption sources and those from the partial covering model are consistent with average photon indices for AGN (≈ 1.8 from Mushotzky (1982)).

Soft excesses, modeled with a blackbody component, were statistically significant in half of the spectra modeled by a simple power law model. We find a significantly smaller fraction compared to the ROSAT sample of Gallo et al. (2007), who find soft excesses in all of their sources, and a significantly larger fraction compared to the Lockman Hole *XMM-Newton* survey (Mateos et al. 2005), where only 11% of type 1 and 25% of type 2 sources show a soft excess. Due to the low number of counts for our heavily absorbed sources, we can not quantify with cer-

tainty how many complex/heavily absorbed sources have this component, but at least one source (NGC 1142) has a statistically significant soft excess. For the low absorption sources, $< kT >= 0.08$ keV, which is similar to but slightly lower than that seen for PG selected QSOs ($< kT_{BB} >= 0.14 \pm 0.02$ keV) (Piconcelli et al. 2005; Porquet et al. 2004b). If the soft excess is the result of a thermal process, the lower kT values in our sample could be related to the lower luminosities of our sample, compared to the PG QSOs. In fact, our average blackbody temperature is directly in the range of those found for type 1 AGN in the Lockman Hole sample, $< kT >= 0.09 \pm 0.01$ keV (Mateos et al. 2005).

The final spectral component measured for our entire sample is the Fe K equivalent width (EW) at 6.4 keV. In Figure 4.14, we plot the Fe K EW versus the hard band (2 – 10 keV) luminosity. We fit a line with the ordinary least squares bisector method to the upper limits of the EW measurements (see plot), yielding a fit of $\log EW = (-0.697 \pm 0.144) \times \log L_{2-10kev} + (32.045 \pm 6.164)$. The significance of this fit, indicated by $R^2 = 0.22$, where R^2 is the coefficient of determination, is very low. Thus, our results show no indication of the X-ray Baldwin or IT effect (Iwasawa & Taniguchi 1993), an anti-correlation of Fe K EW and hard band luminosity (see the following chapter).

For the low absorption/simple model sources, we measured the significance of the O VII and O VIII K edges to search for evidence of a warm absorber (see Table 4.7). All of the simple model sources, with the possible exception of WKK 1263, are classified optically as Seyfert 1s and thus can be directly compared with the Reynolds (1997) sample. In Figure 4.15, we plot the values of optical depth for each of the edges versus $L_{2-10keV}$ for our sources as well as the Reynolds (1997) sources with luminosities in the same range. As the figure shows, the optical depths we found for our sources are much lower than those from the Reynolds

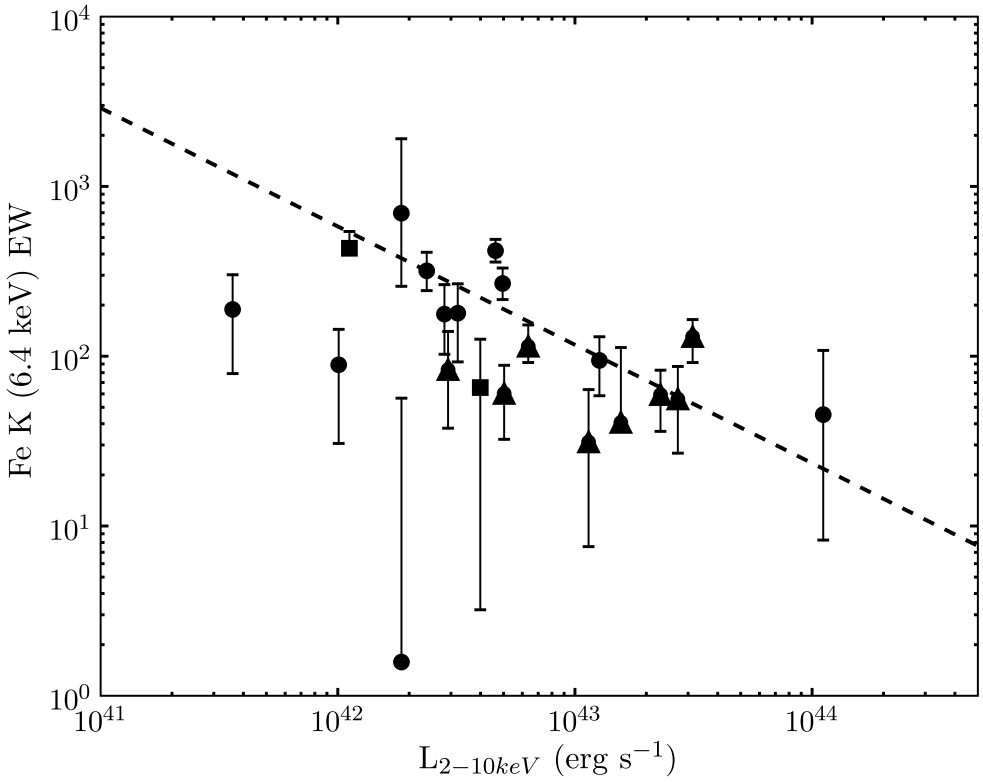

Figure 4.14: Plot of the Fe K equivalent width measurements (eV) versus the luminosity in the hard band (2 – 10 keV). The equivalent width measurements are from the best-fit models for the sources shown in Tables 4.5, 4.6, and 4.9. The simple power law/ power law and blackbody, unabsorbed/low absorption sources are plotted as triangles. The squares represent the two sources with complex spectra we could not interpret (ESO 362-G018 and NGC 6860). Finally, the circles represent the absorbed sources with complex spectra. The source SWIFT J0216.3+5128 is not plotted since there was no evidence of a line and the redshift is unknown. The line is the ordinary least squares bisector fit to the data using the upper limits on the Fe K equivalent widths.

sample. Only one source, ESO 490-G026, had a clear detection ($\Delta\chi^2 = 25$) with the optical depths of both edges having upper limits above 0.10. Thus, where half of the Reynolds sample and 13/18 of the George et al. (1998) sample showed evidence of a warm absorber in the line of sight, we find only 1/8 of our Seyfert 1 sources to show significant evidence of a warm absorber. This result could be due to an incomplete or biased sample of Seyfert 1 sources, since the sources in this study were among the low absorption sources with the lowest BAT flux in the 9-month sample. Alternatively, our result could be representative of the entire BAT sample. In this case, it is possible that the previous AGN samples showed more detections because they were from an optically selected/soft X-ray selected sample. Thus, a possibility is that the emission that ionizes the gas, creates a region of warm, ionized gas, that also destroys dust. An optical or softer X-ray survey could preferentially select these sources, missing more obscured sources. Analysis of the remaining BAT sources will allow us to verify whether our result of few warm absorbers is consistent with the properties of the entire 9-month catalog.

4.4.4 Variability

In addition to the spectral properties, we examined our sources for two types of variability: (1) during the *XMM-Newton* observations and (2) variability in spectral form and brightness between the *XMM-Newton* and XRT observations. For the first type of variability, we created binned light curves for each object in our sample. We found that 3/21 sources showed significant variability, with rates varying by 2.4 – 2.8 $\mathrm{ct\,s^{-1}}$ over time scales of 0.8 – 2.7 hr, in the pn observations. The sources that varied the most were all Seyfert 1 sources with low absorption and X-ray spectra well-fit by simple power law or power law and a blackbody

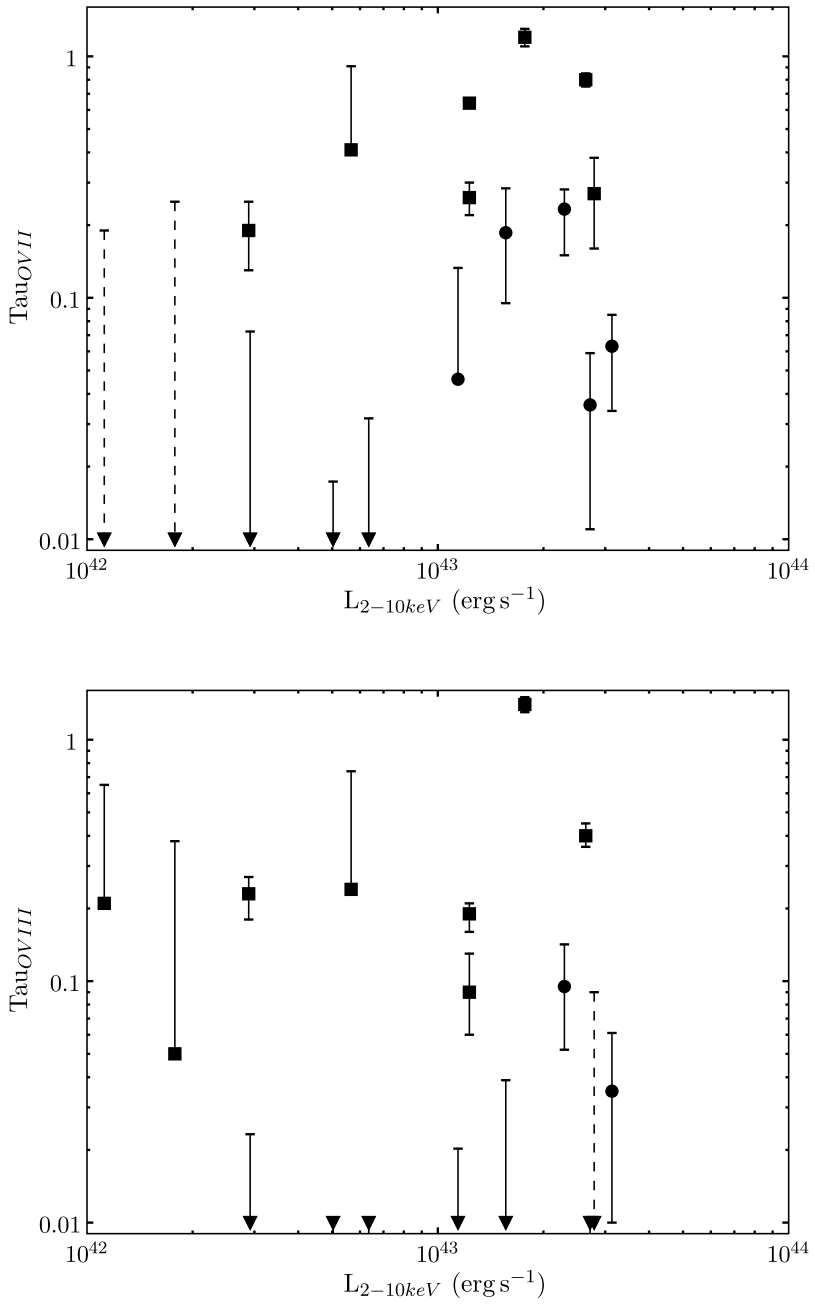

Figure 4.15: Plot of the optical depth of an added O VII, 0.74 keV, and O VIII, 0.87 keV, K edge vs. 2 – 10 keV luminosity. This model was added for the low absorption/simple model sources (circles, solid lines for upper limits), which are optical Seyfert 1 sources. We compare our values to those from Reynolds (1997) (squares, dashed lines for upper limits). We find much weaker optical depths among our sample, most noticeably for O VIII where the upper limits are well below $\tau = 0.1$ for all but one source. Further, in Table 4.7, the addition of the two edge models gives a statistically better fit ($\Delta\chi^2 > 10$) for only two sources (ESO 490-G026 and MCG +04-22-042). Only ESO 490-G026, has upper limits for both O VII and O VIII with $\tau > 0.1$.

models. These sources were among the brightest in our sample. While only three sources showed short term variability, during the *XMM-Newton* observation which lasted ≈ 10 ks, nearly all of the sources (13/16) exhibited variability on longer time scales, of hours to months, from comparisons of the *XMM-Newton* and XRT observations. This result agrees with earlier studies which found AGN more variable on long time scales than short time scales (Barr & Mushotzky 1986; Nandra et al. 1997).

From our comparison of the *XMM-Newton* and XRT spectra, we found 13/16 sources had varying fluxes, 6/16 had varying column densities, and 6/16 sources had varying power law indices. Sources tended to vary more in the soft band than the hard band (see the Variability section). Unfortunately, due to lower count rates, measuring variability for the heavily absorbed sources was more uncertain, particularly in the soft band (0.5 – 2 keV). In addition, we had fewer XRT observations with > 100 counts for these sources. Based on the result that our sources varied more in the soft than hard band, it is likely that if we had more counts in the soft band for the heavily absorbed sources, as well as more observations for comparison, our results would agree with other AGN variability studies which found $> 90\%$ of their sources to vary over the time scale of months to years (such as the AGN from the Lockman Hole (Mateos et al. 2007) and Chandra Deep Fields (Bauer et al. 2003b; Paolillo et al. 2004) studies).

In Figure 4.16, we plot column density versus flux and photon index versus flux for the sources that vary. The plots show the observed parameter for each observation/average parameter for the source, where the observed values for each source are plotted with a different symbol. In the column density figure, there is clearly no correlation seen between the column density and flux. Similar results were found by Risaliti et al. (2002) for a sample of Seyfert 2 galaxies, where they

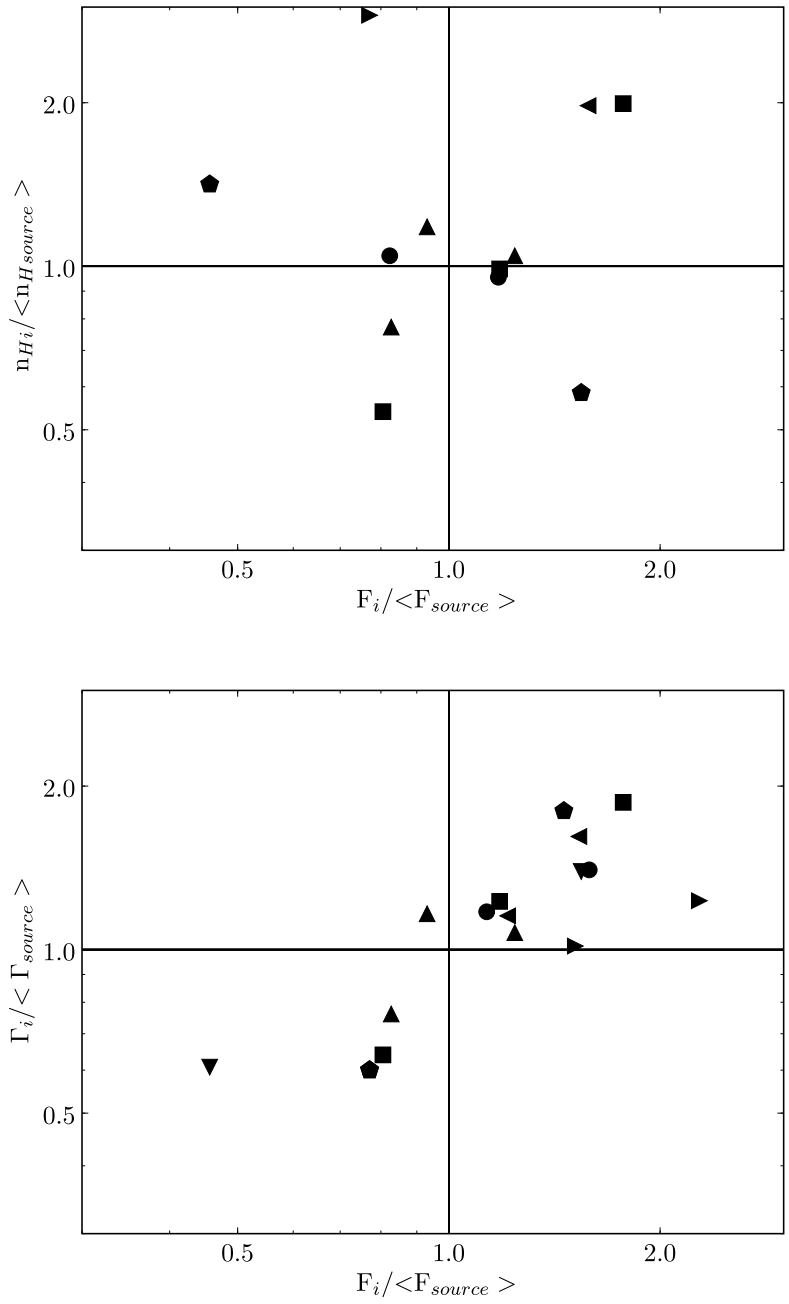

Figure 4.16: Plots of varying column density (top) and photon index (bottom) with flux. For sources that showed variations in column density or photon index, we plotted the observation's value divided by the average for the source (i.e. $F_i/ <F_{source}>$), for each individual observation. The flux is the 0.3 – 10 keV flux from the pegged power law component. The lines mark the area where each parameter is 1.0 (where the observation value is the average value). A different symbol is used for each source. No correlation is seen between column density and flux, however, there is a strong correlation between photon index and flux.

conclude that the variations in column density are not caused by varying ionization states but by a clumpy absorber. In the plot of spectral indices, however, we do find a correlation between the spectral index and the flux. Therefore, we find that higher fluxes correspond to higher spectral indices. This result has been seen before for individual sources (Mushotzky et al. 1993). Based on a variability study of the AGN sources in the Lockman Hole, Mateos et al. (2007) find no correlation between spectral variability and flux variability. Further, they find flux variability much more prevalent in their sample than spectral variability, finding spectral variability in only $14 \pm 8\%$ of Seyfert 1s and $34 \pm 14\%$ of Seyfert 2s. However, Mateos et al. (2007) note that the detection of spectral variability is related to the quality of the spectrum. When they consider this factor, they predict a higher fraction of $\approx 40\%$ to exhibit spectral variability. We do not have a complete sample for Seyfert 2 sources, due to the low number of counts in the XRT observations for heavily absorbed sources. However, we find $7/8$ classified Seyfert 1 sources to exhibit a variation in either column density or power law index, much higher than the Mateos et al. (2007) estimated value. Additionally, as we stated earlier, there is a clear correlation between changing flux and power law index for individual sources.

For the Compton-thick sources, variability or a lack thereof, gives clues to the size and location of the Compton-thick gas. For our heavily obscured Compton-thick candidates, only MRK 417 had enough counts in an XRT observation ($>$ 100 counts) to test for long term variability. We found no statistically significant evidence of variability for this source between the *XMM-Newton* and XRT observations, taken 6 months apart. This lack of variability in two observations does not give us much information. For the low absorption Compton-thick candidates, however, we find a great deal of variability between the *XMM-Newton* and XRT

observations. In particular, for NGC 6860, the flux and spectral index are higher in the XRT observations, while the column density is lower. Since the XRT observation was taken 4 months earlier, this puts a limit on the suggested change from Compton-thin to a reflection-dominated spectrum. Similarly, significant changes are seen between the XRT and *XMM-Newton* observations of ESO 362-G018. In this source, the most significant change is the disappearance of the strong Fe K line seen in the *XMM-Newton* observation. A smaller time constraint is placed on this source, 2 months between the last XRT and the *XMM-Newton* observation, for a change from a Compton-thin to a reflection-dominated spectrum.

Changes from Compton-thin to Compton-thick spectra have been noted before, particularly by Matt et al. (2003). They discuss two possible scenarios to explain the changes in spectra, a change in column density of the absorber (Risaliti et al. 2002) and a "switched-off" source, that is, a state where the emission from the central source drastically decreases below our detection threshold. For both ESO 362-G018 and NGC 6860, Seyfert 1.5 sources embedded in dusty host galaxies, a changing absorber is a more appealing explanation.

4.5 Summary

From our analysis of the *XMM-Newton* and XRT spectra of 22 BAT-selected AGN, the complexity of the spectra of a large fraction of nearby ($< z > \approx 0.03$) AGN is clear. Based on the range of X-ray column densities and BAT (14 – 195 keV) fluxes (Tueller et al. 2008), our sources are a representative sample of the 9-month BAT catalog. In analyzing their properties, we are presenting for the first time the global X-ray properties of an unbiased, local AGN sample.

Within our sample, we find half of the sources to have low absorption ($n_H <$

10^{23} cm^{-2}) and spectra well-described by simple power law models. Half of these sources statistically show evidence of a soft excess. We tested these sources for the presence of a warm absorber, finding only one statistically significant detection out of 8 low absorption sources. This is at odds with the studies of George et al. (1998); Reynolds (1997) who found half or more of their samples consistent with warm absorbers. If our result of few warm absorbers is found in the entire Seyfert 1 BAT AGN sample, the detection of a large number of warm absorbers is likely a selection effect of optical/soft X-ray AGN samples.

The remaining 13 sources, which had too few soft counts to test for the presence of a warm absorber, have more complex spectra. Within the class of complex sources, we find five Compton-thick candidates (based on a flat spectrum above 2 keV), two of these sources with spectra too complex to model successfully with the available signal-to-noise. Additionally, four other sources are consistent with the hidden/buried AGN described in Ueda et al. (2007). Since $\approx 1/5$ of our sample fits in this category, we agree with Ueda et al. (2007) that these types of sources are a significant fraction of local AGN. If these sources have weak [O III] emission, as Ueda et al. (2007) predicts, they would be easily missed in optical surveys and require very hard X-ray surveys, such as the BAT and Integral surveys, for detection.

On short time scales, during the ≈ 3 hr *XMM-Newton* observations, we found that only 3/21 sources varied significantly, all of which were bright, low absorption X-ray sources. Comparing the XRT and *XMM-Newton* observations of 16/22 sources, which were separated by hours to months, we were able to compare the spectra for longer time scale variability. Most of the sources varied in flux (13/16), such that our results agree with previous studies which found AGN to vary more on longer time scales than short time scales (Barr & Mushotzky 1986;

Nandra et al. 1997). In terms of spectral variability, nearly half of the sources varied in both column density (6/16) and power law index (6/16). We found no correlation between column density and flux between observations for the individual sources. However, there was a strong correlation between power law index and 0.3 – 10 keV flux, where steeper slopes correspond to higher fluxes. Contrary to the variability study by Mateos et al. (2007) who estimate $\approx 40\%$ of their sample to vary with respect to spectral shapes, we find 7/8 identified Seyfert 1s to vary in either column density or power law index. We note, as Mateos et al. (2007) point out, that the detection of this variability depends on the quality of the data. Thus, similar comparisons with Seyfert 2s were not plausible since the data quality was much lower.

Optically, the Seyfert type of the sources match the X-ray column densities. Thus, the Seyfert 1 sources have $n_H < 10^{22}\,cm^{-2}$ and the Seyfert 2 sources have $n_H > 10^{22}\,cm^{-2}$. The two sources with no optical AGN signatures are heavily absorbed sources with $n_H > 5 \times 10^{23}\,cm^{-2}$. The host galaxies of our sample are mostly spirals, contrasting with the results of Grogin et al. (2005), who find elliptical hosts dominating the $z \approx 0.4 - 1.3$ universe.

Chapter 5

The Complete X-ray Properties of the BAT AGN

5.1 Introduction

In Chapter 4, we analyzed the X-ray properties of a sub-sample of 22 AGN from the BAT AGN catalog. Among our results, we found that 20% of our sample had properties consistent with hidden/buried AGN, a class of object first identified through BAT and Suzaku observations (Ueda et al. 2007). In this Chapter, we present the results of an analysis of the X-ray properties of the entire 9-month catalog. We provide the compiled properties from archival data, analyses presented in the literature, and previously unanalyzed SWIFT XRT observations. Thus, for the first time we show the collective properties of a 14–195 keV band AGN sample – probing energies high enough that there is no selection effect for absorbing columns up to $\approx 10^{24}\,\mathrm{cm}^{-2}$.

Our goals in this chapter are two-fold. First, we present the X-ray properties for the entire 9-month catalog (Tueller et al. 2008). Second, we examine in more detail the collective properties of a uniform sub-sample. This sample con-

sists of non-beamed sources with Galactic latitudes $\geq 15^{\circ}$. In § 5.2, we describe the observations and the spectral fits, including data from ASCA, XMM-Newton, Chandra, Suzaku, and SWIFT XRT. In § 5.3, we describe the general properties of the entire BAT 9-month AGN sample. In § 5.4, we describe in more depth the properties of our uniform sample. In § 5.5, we present the average X-ray spectrum as well as the 2–10 keV $\log N$-$\log S$ relation. These X-ray properties can now be used as input to X-ray background models for $z \approx 0$. We then discuss the properties of the host galaxies in § 5.6. Finally, we summarize our results in § 5.7.

5.2 The Data

5.2.1 Source Selection

The sources in the 9-month BAT AGN catalog were selected based on a detection at 4.8σ or higher. This corresponds to fluxes in the 14–195 keV band of $\geq 2 \times 10^{-11}$erg s^{-1} cm^{-2}. The survey and the method of selection are described in (Tueller et al. 2008). To summarize, the BAT positions for the detected sources have an error of $\leq 6'$at 4.8σ. Therefore, the positions of identified sources were compared with available optical, radio, and X-ray observations. Where the BAT source could not be identified with a previously known AGN source, SWIFT XRT observations were obtained. With an identified XRT counterpart, the position is narrowed to an error of $\sim 4''$. The source identification was further constrained by the requirement that each of the BAT AGN sources have a clear optical/IR counterpart in the Digital Sky Survey/2MASS. Many of the sources in this entire 9-month sample have identifications based on optical spectra either from archived data, the literature, or our own follow-up data. The sample consists of 17 blazars/BL Lacs, 49 Sy 1–1.2s, 34 Sy 1.5–1.9s, and 45 Sy 2s. Of

the remaining sources, 7 are unidentified, 2 have optical spectra showing a normal galaxy (i.e. no AGN emission lines; NGC 612 and NGC 4992), and 2MASX J09180027+0425066 is identified as a type 2 quasar.

In order to study the properties of the local BAT-detected AGN, we identify a uniform sample from the 9-month catalog. This requires the exclusion of beamed sources as well as sources within the Galactic plane ($b < 15^{\circ}$). We exclude beamed sources (the 17 blazars/BL Lacs), since they make up only $\approx 10\%$ of AGN and are at higher redshifts than our sample of local sources. Further, the physics behind the spectra are different between beamed and unbeamed sources, since these sources are jet dominated. Only high Galactic latitude sources are included ($b > 15^{\circ}$), since the identification of AGN in the Galactic plane by BAT are less certain due to the higher background and large number of unidentified sources (Galactic and extragalactic). This uniform sample consists of 102 sources. Among these, 34 are Sy 1–1.2s, 28 are Sy 1.5–1.9s, and 36 are Sy2s, with none of the sources without an identification. Since the normal galaxy spectra sources and the type 2 quasar show no broad lines, we include them as Sy2s in the following discussions.

Since the 9-month survey sources are moderately bright, many of them were well-known AGN sources with archival data/published papers detailing the X-ray properties. Thus, in compiling the X-ray properties of this sample, we first searched the literature for analyses of the X-ray spectra of our sources. In the following section, we describe the X-ray data and analysis for the entire sample.

5.2.2 X-ray Data and Analysis

As discussed in Chapter 1, the X-ray emission from AGN primarily takes the form of an absorbed power law (Mushotzky et al. 1993). Additional features which are present in the 0.3–10 keV spectra of many AGN include a soft excess and an Fe K-α line. The soft excess is often modeled as a blackbody component ($kT \approx 0.1$ keV) and its origin is believed to be either thermal emission from star formation, photoionized gas, blurred reflection (Czerny et al. 2003; Ross & Fabian 2005), or blurred absorption (Gierliński & Done 2004). The Fe K-α line is a fluorescent line from lowly ionized iron at 6.41 keV. Finally, many AGN exhibit a complex spectrum indicating emission components absorbed with different column densities. This type of spectrum may be the result of scattering of direct AGN emission, a dusty environment where the AGN emission is partially covered by absorbing material, or contamination of the AGN spectrum by less-absorbed X-ray binaries. In our effort to uniformly compare the properties of our sources, we searched the literature for simple models fit to the X-ray data, based on these components (power law, absorption (simple or complex), soft excess, and Fe K line). We did not include models for reflection since higher signal-to-noise spectra would be required for the entire sample.

In our study of 22 *XMM-Newton* follow-ups of BAT AGN (Chapter 4), we had used the same components to classify the AGN X-ray spectra. We chose a simple and complex model that is well-used throughout the literature, allowing for easy comparison with other AGN studies. In this study, we adopt these same models. Our simple model is an absorbed power law model (Figure 5.1a), with an additional soft blackbody and/or gaussian (for the Fe-Kα line) model where required. Using the standard X-ray software for fitting X-ray spectral models,

XSPEC (Arnaud 1996), our simple model is represented as `tbabs`*(`pow` + `bbody` + `zgauss`). Here, `tbabs` is a standard neutral absorption model (Wilms et al. 2000). We categorize a complex spectrum as one well-fitted with either a partial covering model (Figure 5.1b) or a double power law model, both of which give similar results (in χ^2 and spectral parameters), along with an Fe-Kα line. Our complex/partial covering model is formally implemented in XSPEC as `pcfabs`*(`pow` + `zgauss`) for partial covering or `tbabs`*(`pow` + `tbabs`*(`pow` + `zgauss`)) for a double power law model. Further discussions of our choice of these models can be found in Chapter 4.

For all of the 9-month BAT AGN, we list the source, position, optical type, host galaxy type, and details of the observation in Table E.1. We include the X-ray satellite used, references, exposure time, and count rate, where available. Where count rates and exposure times are quoted, they correspond to the pn detector for *XMM-Newton* and SIS0 for ASCA. For many sources, spectra were available from many different satellites. Our preference was to choose ASCA analyses first, followed by *XMM-Newton* and Chandra. Mostly, this is due to the uniform way the spectral properties of Seyfert 1s and Seyfert 2s are presented in papers analyzing ASCA data, such as Nandra et al. (1997); Reynolds (1997); Turner et al. (1997), and the availability of a uniform database (Tartarus[1]). Also, especially with the increased resolution of the grating spectrometers and higher signal-to-noise CCD data on *XMM-Newton* and Chandra, more accurate/complicated models are often used to analyze spectra from these satellites, particularly for observations with a large number of counts. Where multiple observations were available, we chose the longest observation below 50 ks, to be comparable to the quality of spectra collected for other sources.

[1] `http://astro.ic.ac.uk/Research/Tartarus/`

Where references were not available, or comparable models were not used, we analyzed either SWIFT XRT, ASCA (downloaded from the Tartarus database), or Suzaku spectra (we obtained data for ≈ 10 sources through AO-1/AO-2 proposals). For the XRT spectra, we analyzed these data following the same procedure as in Chapter 4. In XRT observations with few counts, if there were multiple observations available, we combined the spectra from the longest observations with the FTOOL `mathpha`. The analysis of the Suzaku spectra is contained in Ueda et al. (in prep), which includes detailed analyses of the spectra. The observation and source properties for the SWIFT XRT, ASCA, and Suzaku observed sources are also listed in Table E.1.

In Tables E.2 and E.3, we list the spectral properties from the observations. Table E.2 includes our XSPEC fits to the XRT data using an absorbed power law (`tbabs*pow`) or an absorbed partial covering model (`pcfabs*pow`). For each of these fits, an additional neutral absorber (`tbabs`) was fixed to the Galactic column density. For spectra with clear residuals from these models indicating a soft component or an Fe K-α line, we added the necessary components and included the details in the appendix. Table E.3 includes the compiled properties from the literature as well as our own fits to ASCA spectra downloaded from the Tartarus database. For these spectra, the model used is clearly specified in the table. In both tables, we categorize the spectra as being simple (S: well-fit by an absorbed power law or power law and blackbody) or complex (C), as in Chapter 4. In Figure 5.2, we plot some examples of the XRT spectra from each category. Notice that the spectrum of UGC 11871 has no data points below 1 keV. For this source, as well as 3 other sources in Table E.2, we classify the source as S*. This indicates that it was best fit with a simple power law, however, with longer exposure times, and thus more data points below 1 keV, it would likely be

a complex source, showing the characteristic complex/double power law shape.

We have collected the X-ray properties for 145/154 AGN. Though there are 153 BAT sources, one BAT source (NGC 6921/MCG +04-48-002) is the combination of two interacting galaxies, each hosting AGN (Winter et al. 2008). In the appendix, we include details on each of the 9 sources excluded from this analysis. The sources are excluded due to a lack of data available (2) or complex spectra (7). For instance, Cen A, an AGN hosted in a merger galaxy, is a complex source that is excluded. In the following sections, we will describe the X-ray properties for the remaining 145 sources.

5.3 Properties of the Spectra

In Tables E.1– E.3, we provide information on the 9-month BAT AGN sources, including the X-ray spectral parameters and fluxes, all derived in a uniform way. In order to study the properties of the local BAT-detected AGN, we need to look at a uniform sample. In the following sections, we will concentrate on the properties of our uniform sample. However, it is first worth noting some of the general properties of the sources detected in the 9 month catalog.

As a means to summarize these properties, we plot a color-color plot of $F_{0.5-2keV}/F_{2-10keV}$ vs. $F_{14-195keV}/F_{2-10keV}$ (all observed fluxes), first used in Chapter 4. This plot includes all sources excepting 3 AGN (the unabsorbed sources ESO 416-G002, MCG -01-13-025, and Mrk 79) which had only broad band fluxes available, the 4 sources which had no high-quality or publicly available X-ray spectra, and the 4 very complex spectra sources (NGC 1275, Cen A, NGC 6240, and GRS 1734-292). As in Chapter 4, the unabsorbed/low absorption sources (triangles, $n_H \leq 10^{22}$ cm^{-2}) occupy the upper left portion, with one exception. Cyg A

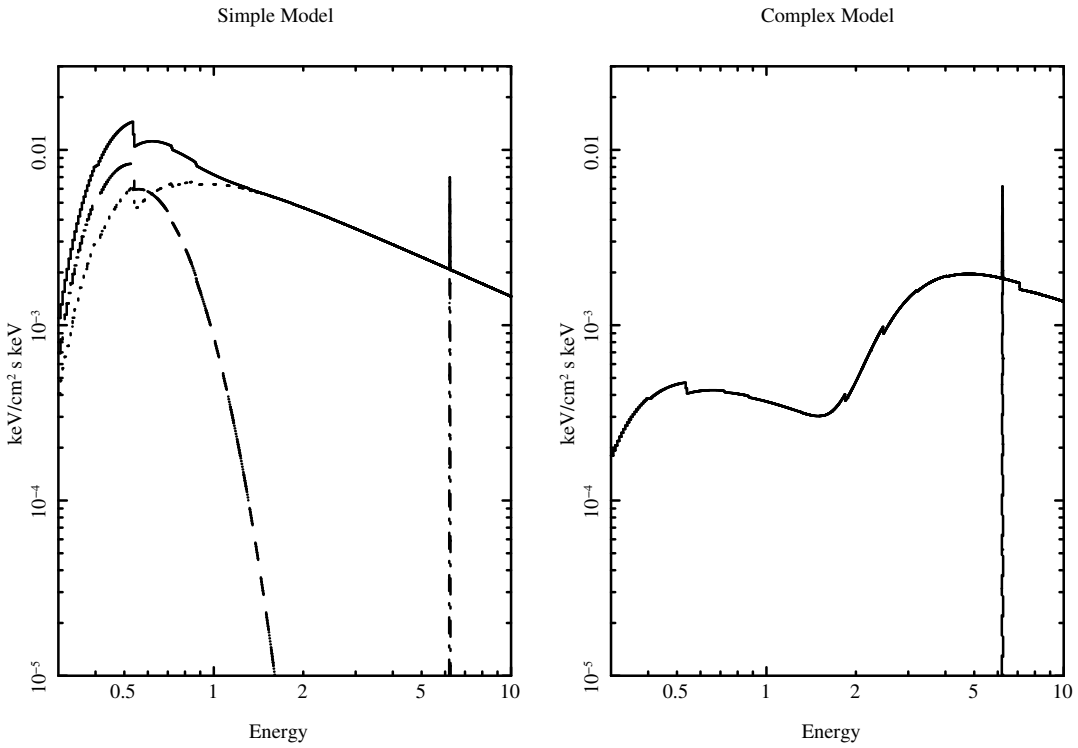

Figure 5.1: The above figures are examples of the complex and simple models used in this chapter. The simple model (left) is an absorbed power law model ($N_H = 8 \times 10^{20}\,\mathrm{cm}^{-2}$ and $\Gamma = 1.75$). In addition to the power law, we include a blackbody component ($kT = 0.1\,\mathrm{keV}$, dashed line) and a 60 EW Fe K-α line at 6.41 keV. The complex model (right) is an absorbed partial covering model (or a double power law model, which gives similar results). Here, the same power law and gaussian components are used as for the simple model, with $N_H = 1 \times 10^{23}\,\mathrm{cm}^{-2}$ and a covering fraction of 0.95.

is a complex source with a complex spectrum, the product of an AGN in a recent merger galaxy. A strong thermal component, mainly from the hot thermal emission of the rich galaxy cluster Cyg A inhabits, is seen at low energies, modeled by a Raymond-Smith thermal model (Sambruna et al. 1999). This thermal emission gives Cyg A its unique position on the diagram.

For the unabsorbed sources, the soft band mean (μ) color is 0.55 with standard deviation (σ) of 0.39. The hard color is much higher, with $\mu = 6.67$ and $\sigma = 17.50$. Many of the heavily absorbed sources (circles, $\mathrm{n}_H > 10^{23}\,\mathrm{cm}^{-2}$) are located

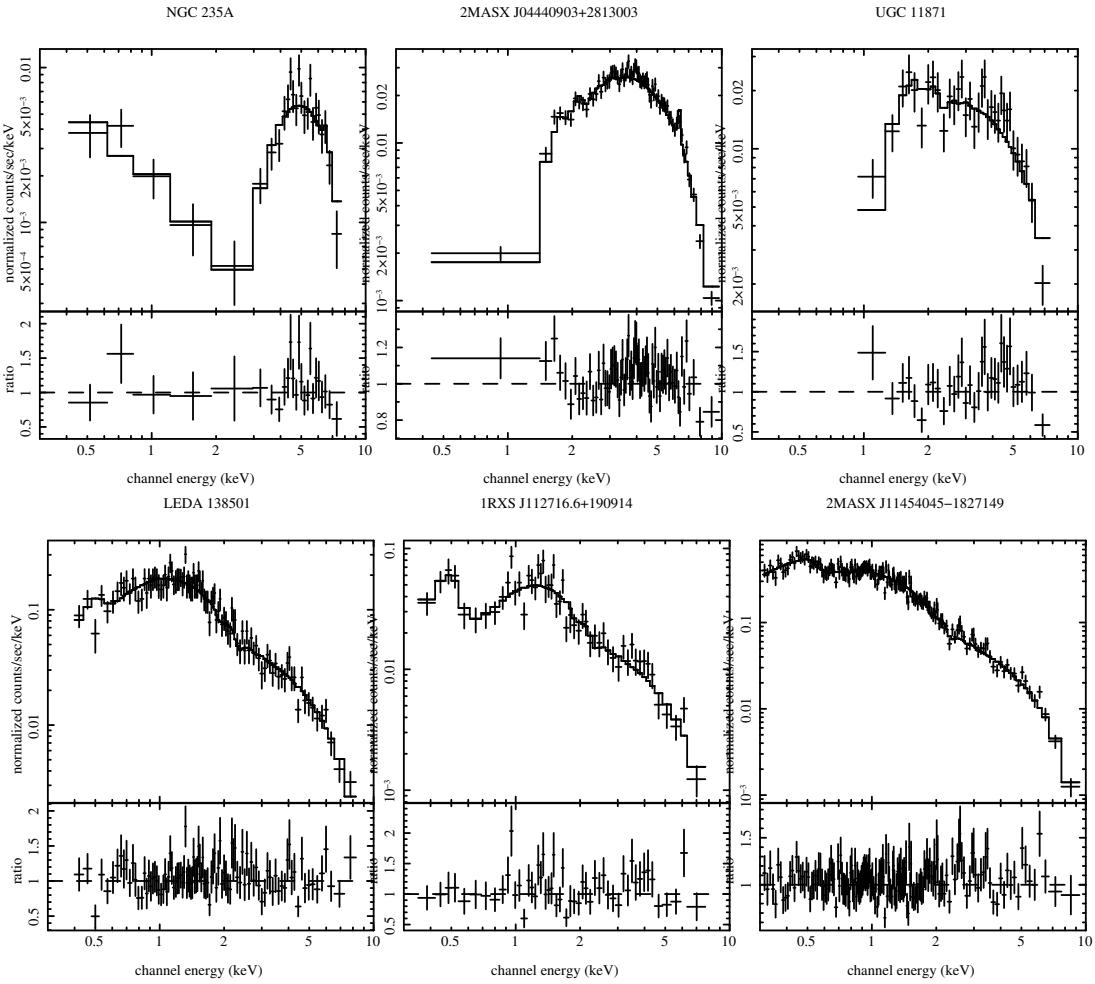

Figure 5.2: Examples of XRT spectra for sources fit with simple and complex models, along with residuals. The spectra of 2MASX J04440903+2813003 and 2MASX J11454045-1827149 were rebinned to better show the residuals from the model. Details of each of the fits are recorded in Table E.2. The sources in the top row are all well-fit with the complex model, while the lower row sources have simple spectra (see Figure 5.1).

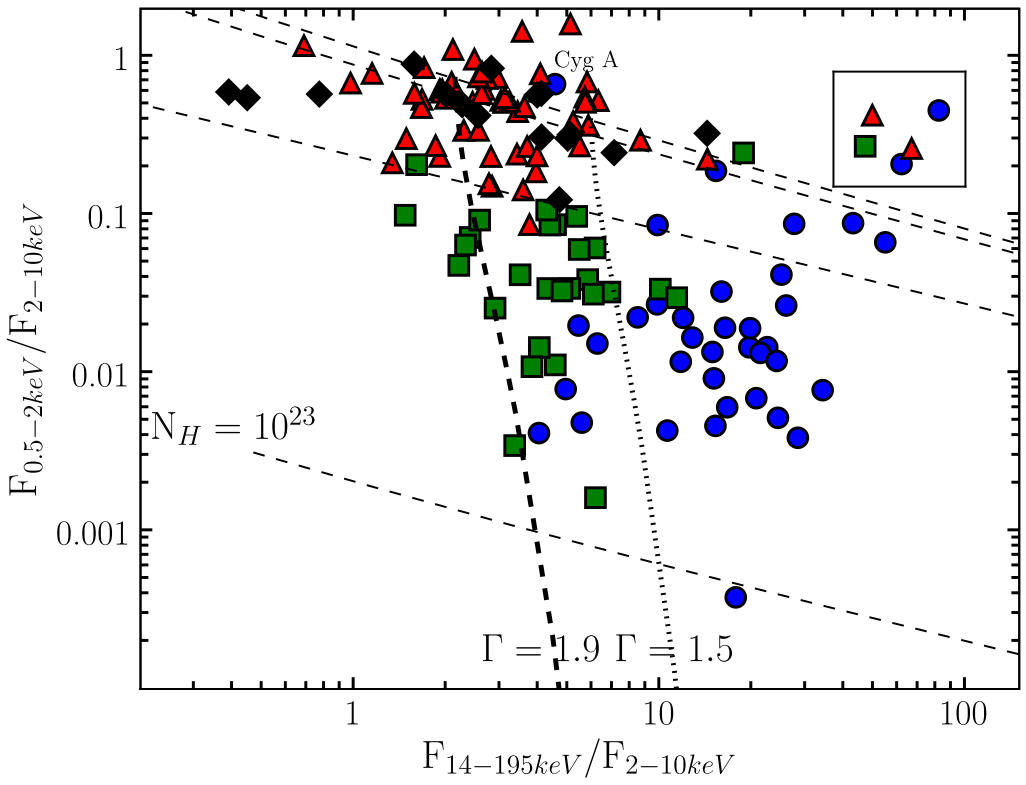

Figure 5.3: We plot all of the 9-month BAT AGN with soft and hard fluxes on the color-color plot initially presented in Chapter 4. The triangles represent sources with $n_H < 10^{22}\,cm^{-2}$, while the circles represent sources with $n_H > 10^{23}\,cm^{-2}$. Squares indicate the intermediary hydrogen column sources. Finally, diamonds are used to represent the 17 blazar/BL Lac sources, which all have low measured column densities. In the text, we describe Cyg A (the circle labeled in the plot) and 5 other sources (NGC 1365 and NGC 5728 (circles), Mrk 3 (square), and NGC 4945 and NGC 6814 (triangles), within the box) to have unusual positions.

towards the lower right corner. These sources clearly have much less flux in the soft band (with the exception of Cyg A). The mean and standard deviations are: $\mu = 0.06$, $\sigma = 0.13$ (soft) and $\mu = 20.43$, $\sigma = 16.16$ (hard). Finally, the squares represent the intermediary sources, with $10^{22}\,cm^{-2} < n_H \leq 10^{23}\,cm^{-2}$. These sources have colors clearly in the middle, with soft colors ($\mu = 0.07$, $\sigma = 0.07$) similar to the more absorbed sources and hard colors ($\mu = 6.68$, $\sigma = 8.48$) closer to the less absorbed sources.

In our color-color plot, there are some clear outliers towards the upper right. The high column density sources include the complex 'changing-look' AGN, NGC 1365, and NGC 5728, a strongly barred galaxy whose host is likely the main contributer to the soft thermal emission. The remaining sources include Mrk 3 (square) and both NGC 4945 and NGC 6814 (triangles). Among these, Mrk 3 and NGC 4945 have complex spectra. NGC 6814 is well fit by an unabsorbed power law but has a strong Fe-Kα line (EW$= 545$ eV). There is very little flux in the ASCA observation below 1 keV. The strong emission in Fe Kα and weak flux at soft energies contribute to give it an unusual location in the plot. In short, all the sources at this location have complex or atypical spectra. However, another factor which can lead to unusual positions in the color-color plot is time variability. This variability could be over the softer X-ray band (< 10 keV) or in the BAT observations. The complex source NGC 6814, for instance, is known to show X-ray variability by at least 10 times over time scales of years (Mukai et al. 2003). In the 14–195 keV band, the corresponding BAT fluxes are time averaged over months. Therefore, sources that are variable in the X-ray or BAT bands may have unusual hard colors. Analysis of the X-ray light curves, however, is beyond the scope of this thesis.

We next summarize the X-ray spectral shape of the BAT AGNs. In Tables E.2 and E.3, we included a column with the type of model used (simple or complex). Excluding the 17 blazars, 63 sources are best fit with a simple model while 65 require a more complex model. As stated earlier, our complex model referred to a better fit (over the simple power law model) with either a partial covering or double power law model. Among the complex sources, 5 corresponded to low column density sources ($n_H \leq 10^{22}$ cm^{-2}), 20 to sources with intermediate columns (10^{22} cm$^{-2} < n_H \leq 10^{23}$ cm^{-2}), and 40 to the heavily absorbed sources

($n_H > 10^{23}\,cm^{-2}$). All of the heavily absorbed sources were better fit with a complex model. This shows that our color-color plot is particularly good for selecting complex sources, which lie to the right of the constant $\Gamma = 1.5$ line (indicating colors for a fixed spectral index with an absorbed power law model).

Among the complex absorbed sources, we classify 28 AGN as "hidden"/buried sources. "Hidden" AGN were first distinguished as a new class discovered by BAT in Ueda et al. (2007). These sources are extremely obscured, possibly by a geometrically thick torus. Since the hidden sources were identified in the X-ray and only two sources were identified in the discovery paper, the multi-wavelength properties are as of yet not fully classified. The X-ray spectra are characterized by a very small scattering component ($\leq 3\%$) in the soft band. In the partial covering model, the model is a multiplicative model defined as $M(E) = f \times e^{-n_H \sigma(E)} + (1 - f)$. Here, f is the covering fraction, n_H is the neutral hydrogen column density, and $\sigma(E)$ is the photo-electric cross-section. The scattering fraction is then the value (1 - f). For our spectral fits, the partial covering model is applied to a simple power law spectrum (`pcfabs*pow` in `XSPEC`).

We adopted the criteria that a hidden source is one where the scattering component is ≤ 0.03 and the ratio of soft (0.5 – 2 keV) to hard (2 – 10 keV) flux is ≤ 0.04. Of the 28 identified, 9 are from Chapter 4. The additional sources include 5 sources with ASCA spectra (NGC 788, NGC 3081, NGC 3281, NGC 4507, and IC 5063) and 4 with Suzaku spectra (ESO 297-018, ESO 005-G004, and 2MASX J09180027+0425066, and 3C 105). The remaining 10 sources have XRT spectra (listed in Table E.2) which are identified as complex (C) or as well-fit with a simple model but with little/no soft flux (S*). The median column density of the hidden sources is $\log n_H = 23.57$ and the median soft/hard flux is 0.013, consistent with the properties of the previously identified hidden sources.

5.4 The 'Uniform' Sample

Having summarized the general properties of the entire 9-month BAT AGN sample, we now will focus on a uniform sample. Our uniform sample includes 102 Seyferts at $|b| \geq 15^{\circ}$, with 46 simple power law model sources and 56 complex model (partial covering or double power law model) sources. In this section, we present general properties of this uniform sample including the distribution of n_H, Γ, $L^{corr}_{2-10keV}$, and $\mathrm{L}^{corr}_{2-10keV}/\mathrm{L}_{Edd}$. We also discuss the existence of correlations between these properties, particularly with the Fe-Kα equivalent width. Finally, we discuss the properties of our classified simple and complex sources in more detail.

5.4.1 Distribution of z, n_H, and Γ

In this subsection, we show the distribution of redshift, column density, and spectral index for the simple model and complex model sources. The average redshift for the sample is 0.03 (Tueller et al. 2008). In Figure 5.4, we show the distribution of the logarithm of z for the simple (top) and complex (bottom) sources. The complex sources are slightly closer than the simple model sources. The mean z and standard deviations are: $\mu = 0.03$, $\sigma = 0.37$ (simple) and $\mu = 0.02$, $\sigma = 0.40$ (complex). The redshift distributions indicate very local AGN and therefore this may have an effect on differences in spectral properties/luminosities when we compare our sources with the X-ray properties derived from higher redshift ($z \approx 1$) hard X-ray selected samples (i.e., the PG quasars), which also tend to be more luminous than the BAT selected sources by 10–100 times.

In Figure 5.5, we plot the normalized column density distribution of the simple (top) and complex (bottom) sources. These column densities are the columns

in excess of the Galactic value (i.e. that from Dickey & Lockman (1990)), which is not included in the plot. Where no additional absorption was necessary, we set $n_H = 10^{20}\,\mathrm{cm}^{-2}$. From the plots, it is clear that simple model sources have much lower column densities than sources with spectra modeled with a complex model. The mean and standard deviation for these $\log n_H$ distributions are: $\mu = 20.58$, $\sigma = 0.74$ (simple) and $\mu = 23.03$, $\sigma = 0.71$ (complex). Notice that none of the complex model sources have columns of $\log n_H \leq 21$. As already noted above, none of the simple power law model sources have columns of $\log n_H \geq 23$.

With our simple model fits, we have determined the photon spectral index, Γ, best fit to the continua of our sources. We excluded a treatment of reflection, using a simpler model which is recorded more uniformly throughout the literature (absorbed power law/ partially covering absorbed power law models). This allows us to use results from the literature for most of our sources. If we had used the reflection model (`pexrav` in XSPEC), many fewer literature results could be included. In Figure 5.6, we plot the distributions for the simple power law model (top) and the more complex model (bottom). For the complex sources, we exclude 3C 452 whose flat spectrum is best characterized by reflection (Evans et al. 2006). The mean and standard deviation for the simple model is $\mu = 1.78$ and $\sigma = 0.24$. This is consistent with the $< \Gamma >= 1.75$ we obtained from our representative sample (Chapter 4). For the complex sources, 10 had been best fit by a double power law model while the rest were fit with a partial covering model. Of these 10, all but 2 had details of the corresponding best-fit partial covering model in Turner et al. (1997). We computed the average difference between the two model fits ($< \Gamma_{pcfabs} >=< \Gamma_{dbl} > /1.18$) and applied this correction to estimate Γ_{pcfabs} for the 10 applicable sources. Thus, our distribution is computed using the partial covering model spectral index. The mean and standard devia-

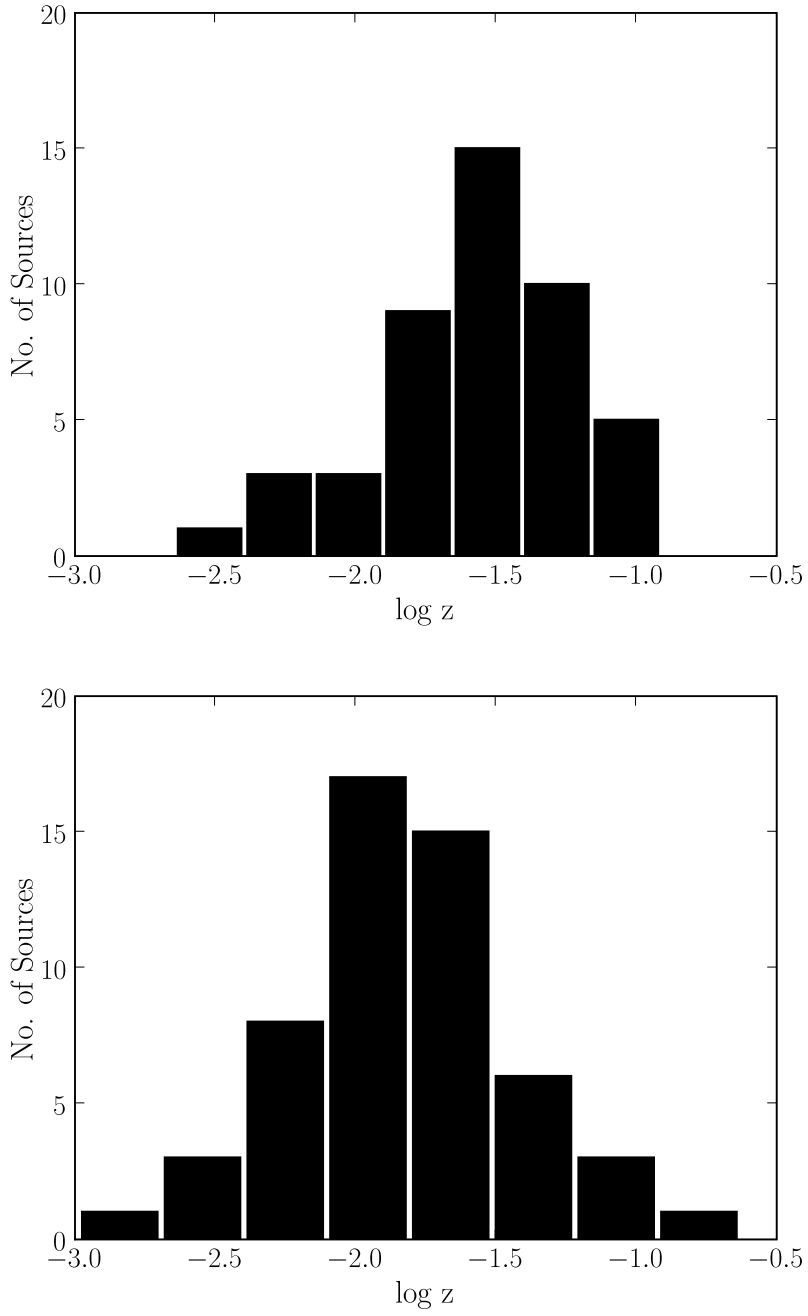

Figure 5.4: We plot the distribution of the log of redshift for our uniform sample of 102 sources. The top plot shows the simple model/power law sources, where the mean redshift and standard deviation are $\mu = 0.03$ and $\sigma = 0.37$. The bottom plot shows the distribution of complex/partial covering/double power law sources, where the mean redshift and standard deviation are $\mu = 0.02$ and $\sigma = 0.40$. As can be seen, the distribution of complex model sources has a slightly lower redshift than the simple model sources.

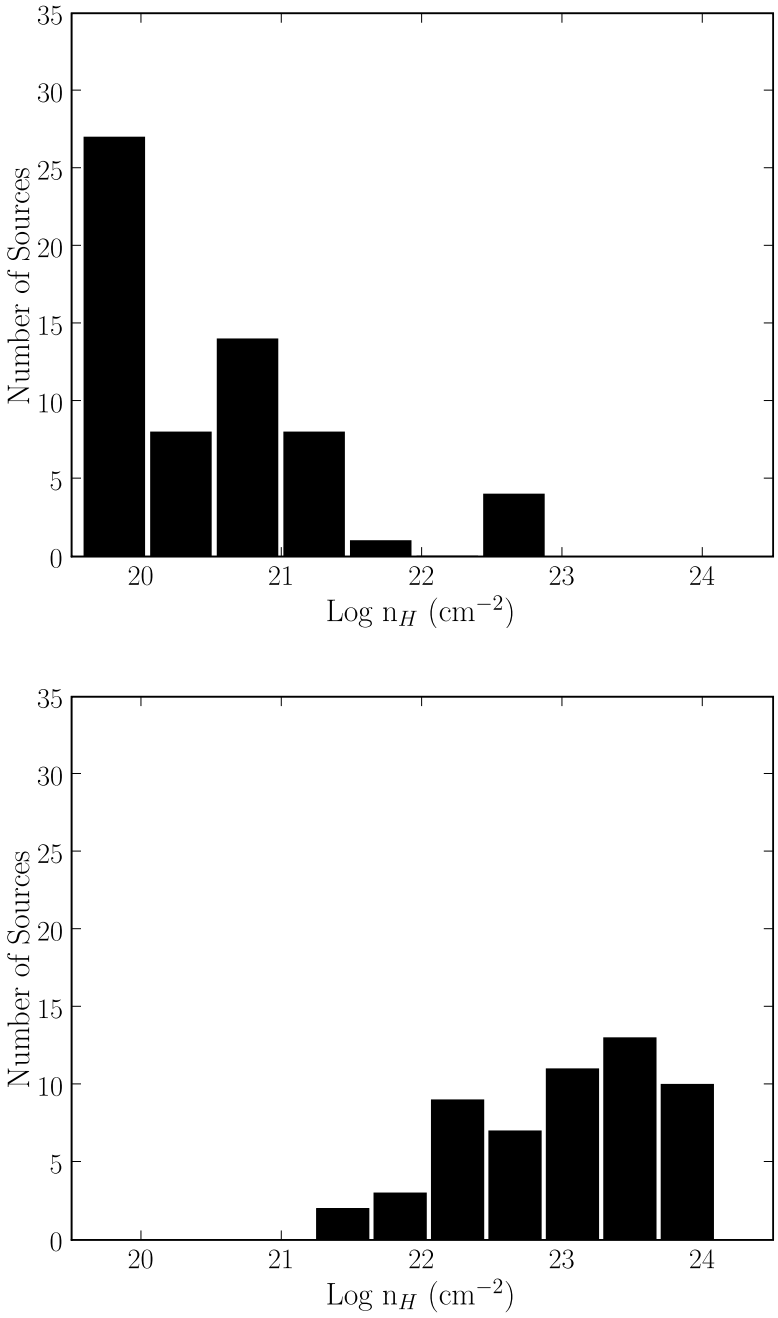

Figure 5.5: We plot the distribution of the log of column densities for our uniform sample of 102 sources. The top plot shows the simple model/power law sources, where the mean and standard deviation are $\mu = 20.58$ and $\sigma = 0.74$. The bottom plot shows the distribution of complex/partial covering/double power law sources, where the mean and standard deviation are $\mu = 23.03$ and $\sigma = 0.71$. Clearly, the simple model sources are dominated by low column density sources while the complex model sources mostly have higher column densities.

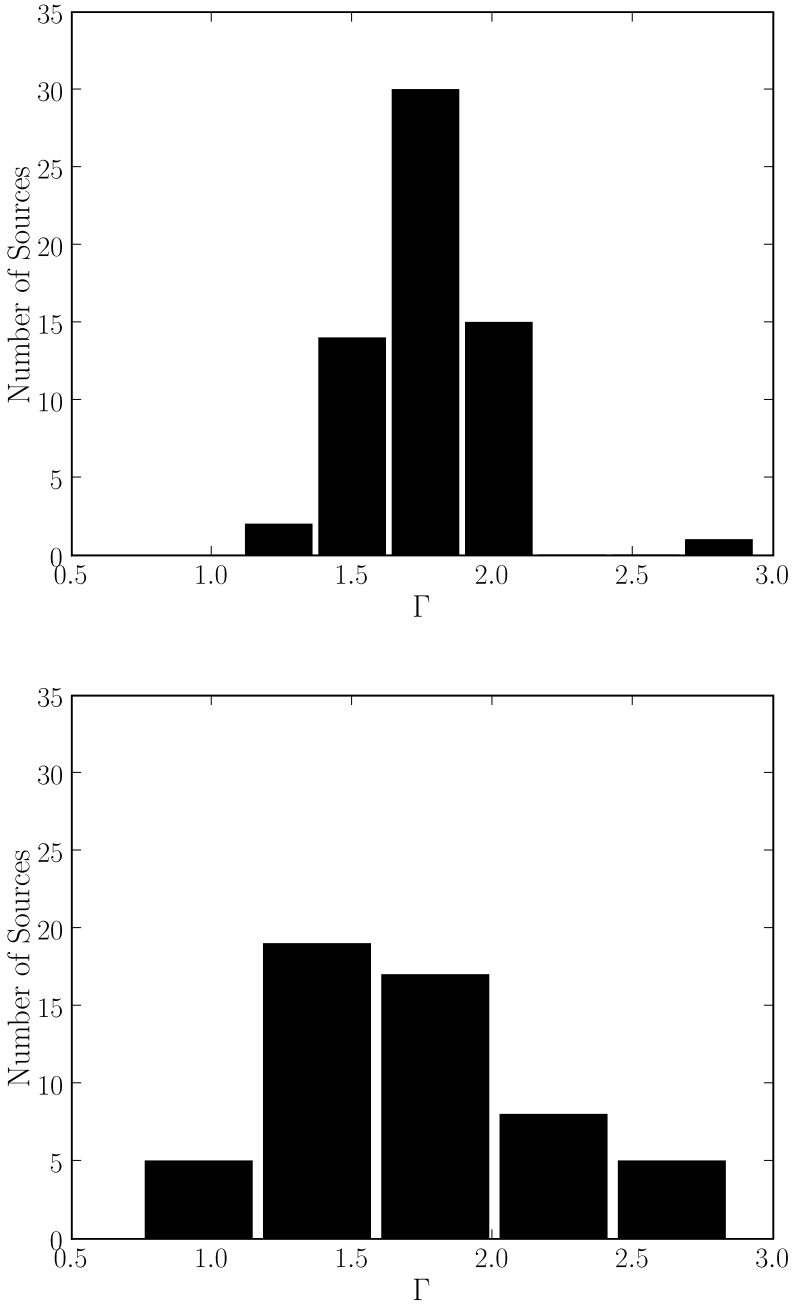

Figure 5.6: We plot the distribution of the spectral index, Γ, for our uniform sample of 102 sources. The top plot shows the simple model/power law sources, where the mean and standard deviation are $\mu = 1.78$ and $\sigma = 0.24$. The bottom plot shows the distribution of complex/partial covering/double power law sources, where the mean and standard deviation are $\mu = 1.73$ and $\sigma = 0.45$. The mean of the simple and complex models are very close, with only a 0.05 difference. If the partial covering model is an accurate physical model, all of the AGN have roughly the same power law description for their X-ray spectra.

tion for the complex partial covering model is $\mu = 1.73$ and $\sigma = 0.45$. There is a larger spread of values for the complex sources, compared to the simple power law model sources. However, there is only a slight difference in the average spectral index (0.05). This result is consistent with those of our representative sample in Chapter 4, which agrees with the average AGN photon indices reported in Mushotzky (1982) of ≈ 1.8 from HEAO-1 observations.

5.4.2 Distribution of $L^{corr}_{2-10keV}$ and $L^{corr}_{2-10keV}/L_{Edd}$

In this subsection, we test whether Sy 1 and Sy 2 sources have the same or different distributions of both hard band X-ray luminosity (2–10 keV) and accretion rate. Towards this end, we needed to compute an absorption independent measure of 2–10 keV luminosity as well as the Eddington luminosity. In terms of 2–10 keV luminosity, absorption has little to no affect on the unabsorbed luminosity for sources with $n_H < 10^{22}\,\mathrm{cm}^{-2}$. Therefore, for these sources we used the quoted 2–10 keV flux to compute $L^{corr}_{2-10keV}$ (absorption corrected 2–10 keV luminosity). For all luminosity calculations, we used $\Lambda = 0.7$ and $H_0 = 75\,\mathrm{km\,s^{-1}\,Mpc^{-1}}$. Above $n_H = 10^{22}\,\mathrm{cm}^{-2}$, absorption has a significant affect on the 2–10 keV flux. For these sources, we used `XSPEC` to calculate the unabsorbed 2–10 keV flux, which we then used to compute $L^{corr}_{2-10keV}$.

In Figure 5.7a, we plot our absorption corrected 2–10 keV luminosities versus the 14–195 keV luminosities. We find that the data is well fit ($R^2 = 0.85$) by a line: $\log L^{corr}_{2-10keV} = (1.06 \pm 0.05) \times \log L_{14-195keV} + (-3.08 \pm 2.16)$. Therefore, the relationship is linear ($L^{corr}_{2-10keV} \propto L_{14-195keV}$) showing the validity of our absorption corrected 2–10 keV luminosities. On the plot, we label the 5 sources which deviate the most from this relationship (sources with $1.7 \geq L_{14-195keV}/L^{corr}_{2-10keV} \geq 1.2$). A likely explanation for these sources (NGC 931, 2MASX J09180027+0425066, NGC

2992, NGC 5728, and NGC 6814) deviating from the linear fit is variability in the X-ray spectra, either in the BAT band or the 2–10 keV band. Indeed, the 64 day 14–195 keV light curves of each of these sources (Baumgartner et al. 2008) show variability by at least a factor of 2. See § 5.3, where we discuss the effects of time variability on hardness ratios. In Figure 5.7b, we plot the ratio of $L^{corr}_{2-10keV}/L_{14-195keV}$ versus the total luminosity in both bands. As shown, there is no relationship ($R^2 << 0.1$). We also indicate on the plot values of spectral index (Γ) for a constant ratio of $L^{corr}_{2-10keV}/L_{14-195keV}$, assuming that Γ is constant between both bands ($\Gamma^{corr}_{2-10keV} = \Gamma_{14-195keV}$).

To calculate the Eddington luminosity, we used the black hole mass computed from stellar 2MASS K magnitudes. In Mushotzky *et al.* 2008 (submitted), we calculated the stellar magnitude from the total 2MASS magnitude (obtained from NED) and a nuclear magnitude, calculated by using the IRAF task `qphot` to extract circular photometry from an aperture equal to the PSF FWHM of the 2MASS images. The stellar absolute magnitude was computed as: $M_{stellar} = 2.5\log(\chi/(\chi-1)) + M_{tot}$, where $\chi = F_{tot}/F_{nuc} = 10^{-0.4(M_{tot}-M_{nuc})}$. We then transformed the measured stellar 2MASS K magnitudes to mass using the relation set forward in Novak et al. (2006): $\log M_{BH} = 8.19 + 0.524 \times (M_{K(stellar)} - 23)$. The assumption made, in computing the mass, is that the K band stellar light is dominated by the bulge. Further details can be found in Mushotzky *et al.* 2008 (submitted), where we show that the derived stellar luminosity is not correlated with the X-ray luminosity (14–195 keV) but that the nuclear luminosities are.

Comparing these black hole masses to the results from reverberation mapping (Peterson et al. 2004), we find that the values agree within the quoted margin of error for the reverberation study (a factor of 3). L_{Edd} is then computed as $(M_{BH}/M_{\odot}) \times 1.3 \times 10^{38}$ ergs s^{-1}. As an estimate of accretion rate (L/L_{Edd}),

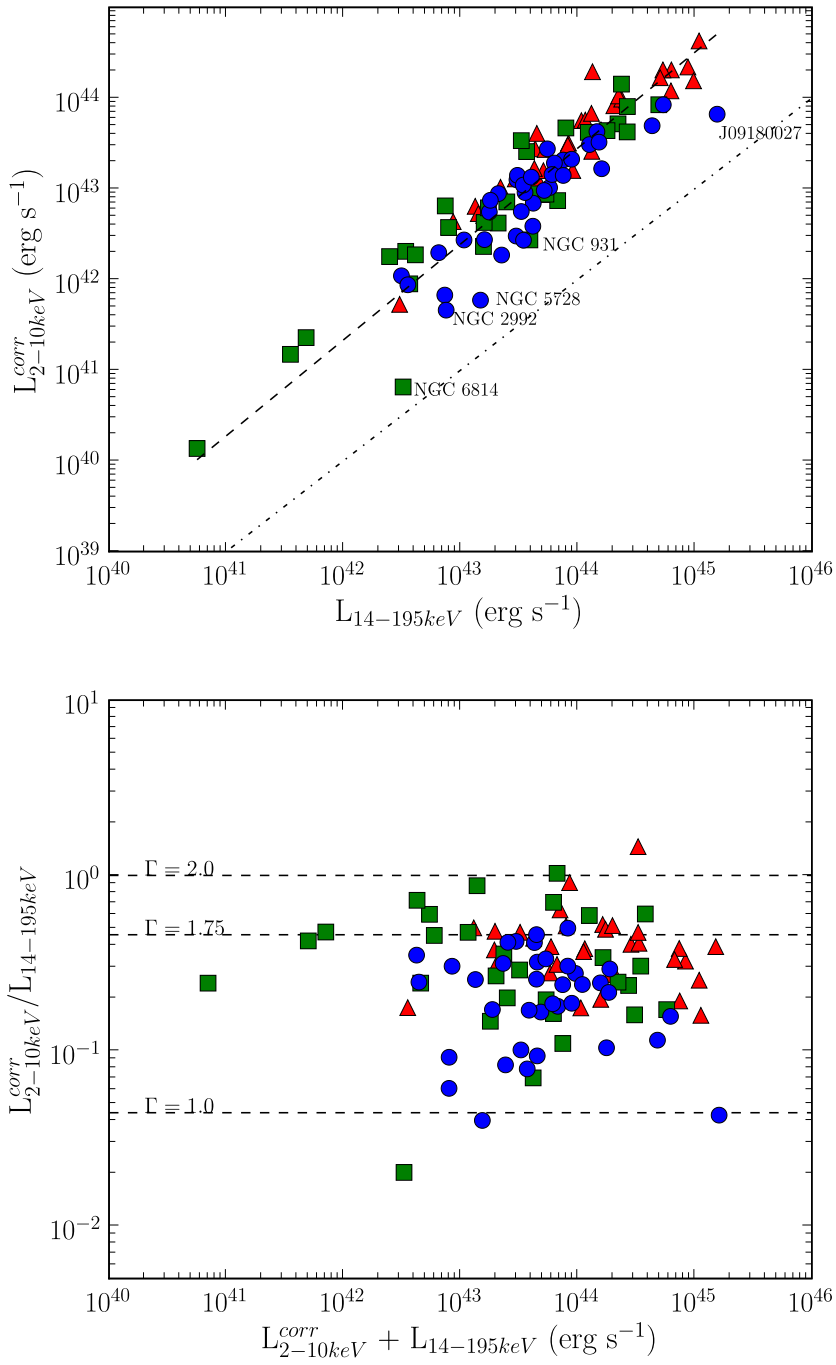

Figure 5.7: (top) We plot the absorption corrected 2–10 keV luminosity versus the 14–195 keV luminosity from BAT. The dashed line shows the best fit line to the data. The fit shows a linear relationship ($L^{corr}_{2-10} \propto L_{14-195}$) with high significance ($R^2 = 0.85$). The second line shows a slope of 2 in logarithmic space ($L^{corr}_{2-10} \propto 100 \times L_{14-195}$). The 5 sources which deviate the most from this fit are labeled in the plot and discussed in the text. (bottom) We plot the ratio of $L^{corr}_{2-10keV}/L_{14-195keV}$ versus the total luminosity in the 2–10 keV and 14–195 keV bands. The lines show values of constant Γ between both bands at constant ratios of $L^{corr}_{2-10keV}/L_{14-195keV}$.

we use the ratio of $L^{corr}_{2-10keV}/L_{Edd}$. These quantities are related by the bolometric correction, which could be as large as 100. Assuming a constant bolometric correction, however, $L^{corr}_{2-10keV}$ is proportional to L. We list both black hole mass and $L^{corr}_{2-10keV}/L_{Edd}$ in Table 5.1 for the 'uniform' sample.

In Figure 5.8, we plot the distribution of our accretion rate proxy, $L^{corr}_{2-10keV}/L_{Edd}$, for the 34 Sy 1–1.2s (red) and 32 Sy 2s (blue). We find that there is a clear difference in the distributions, with the Sy 2s having lower ratios of $L^{corr}_{2-10keV}/L_{Edd}$. To quantify this, the mean and standard deviations for the logarithm of accretion rate are $\mu = -2.92$ and $\sigma = 0.57$ for Sy 1–1.2s and $\mu = -3.53$ and $\sigma = 0.75$ for Sy 2s. Since we used unabsorbed luminosities to compute $L^{corr}_{2-10keV}$, this effect is not simply due to the Sy 2s being absorbed and therefore less luminous. We find that the difference in distributions also holds for luminosity alone, where $\mu = -2.92$ and $\sigma = 0.57$ for Sy 1–1.2s and $\mu = -3.53$ and $\sigma = 0.75$ for Sy 2s. Using the Kolmogorov-Smirnov test, we find that the differences in distributions are significant, both having a very small P value (< 0.001) or probability that the two samples are drawn from the same parent population.

The result of Sy 2s having lower hard X-ray luminosities than Sy 1s is not new, but the Eddington ratio result is. A lack of X-ray obscured sources at high luminosities was noted by Reichert et al. (1986) and Piconcelli et al. (2002). The results of Steffen et al. (2003) and Ueda et al. (2003) showed that the fraction of obscured AGN is lower at high luminosities. Our luminosity distribution results are new, however, in that the BAT AGN include the "hidden" sources which had not previously been identified as a class. Therefore, our study is much more unbiased with respect to absorption than the previous studies.

Also, more importantly, we show that it is not simply the 2 – 10 keV luminosities which are different but also the accretion rates, estimated by $L^{corr}_{2-10keV}/L_{Edd}$.

Table 5.1. K-band Derived Mass and $L^{corr}_{2-10keV}/L_{Edd}$

No.	Source	$M/M_\odot$ [1]	L_X/L_{Edd} [2]	No.	Source	$M/M_\odot$ [1]	L_X/L_{Edd} [2]
1	NGC 235A	8.76	-3.75	78	1RXS J112716.6+190914	9.00	-3.21
2	Mrk 348	7.97	-3.53	79	NGC 3783	8.21	-3.25
3	Mrk 352	7.26	-2.69	80	SBS 1136+594	7.53	-2.03
4	NGC 454	6.23	-2.08	81	UGC 06728	6.81	-3.22
5	Fairall 9	8.91	-3.13	82	2MASX J11454045-1827149	6.70	-1.36
6	NGC 526A	8.02	-2.75	83	CGCG 041-020	8.46	-3.32
7	NGC 612	8.47	-3.17	85	NGC 4051	7.27	-4.05
8	ESO 297-018	9.68	-4.66	86	Ark 347	8.12	-3.99
9	NGC 788	8.51	-3.71	88	NGC 4138	6.82	-3.79
10	Mrk 1018	8.94	-3.46	89	NGC 4151	7.69	-3.26
12	Mrk 590	8.87	-4.08	90	Mrk 766	7.85	-3.18
15	NGC 931	8.55	-4.25	91	NGC 4388	8.53	-4.24
16	NGC 985	8.94	-2.78	92	NGC 4395	5.30	-3.30
17	ESO 416-G002	9.02	-3.45	94	NGC 4507	8.39	-3.54
18	ESO 198-024	8.36	-2.85	95	ESO 506-G027	8.59	-3.51
20	NGC 1142	9.36	-4.01	96	XSS J12389-1614	8.88	-3.50
24	NGC 1365	8.88	-4.75	97	NGC 4593	8.61	-4.02
25	ESO 548-G081	8.94	-4.27	100	SBS 1301+540	7.54	-2.24
27	PGC 13946	8.75	-3.74	102	NGC 4992	8.56	-3.69
28	2MASX J03565655-4041453	8.64	-2.88	103	MCG -03-34-064	8.28	-3.56
29	3C 105	7.79	-2.00	105	MCG -06-30-015	7.36	-2.87
31	1H 0419-577	9.00	-2.83	106	NGC 5252	8.64	-3.91
32	3C 120	8.56	-2.71	108	IC 4329A	8.52	-3.05
34	MCG -01-13-025	8.06	-3.18	109	Mrk 279	8.62	-3.09
36	XSS J05054-2348	7.53	-2.04	110	NGC 5506	7.77	-3.12
38	Ark 120	8.74	-3.13	112	NGC 5548	8.42	-3.03
39	ESO 362-G018	9.00	-4.78	113	ESO 511-G030	8.66	-3.70
40	Pictor A	7.60	-2.30	115	NGC 5728	8.53	-4.90
45	NGC 2110	8.28	-3.94	116	Mrk 841	8.15	-2.88
47	EXO 055620-3820.2	8.44	-2.82	117	Mrk 290	7.68	-2.62
49	ESO 005-G004	7.89	-3.99	118	Mrk 1498	8.59	-3.10
50	Mrk 3	8.48	-3.66	124	1RXS J174538.1+290823	8.75	-2.70
51	ESO 121-G028	9.00	-3.81	125	3C 382	9.22	-3.05
53	2MASX J06403799-4321211	–	–	126	ESO 103-035	7.73	-3.12
55	Mrk 6	8.24	-3.44	127	3C 390.3	8.52	-2.58
56	Mrk 79	8.42	-2.95	129	NGC 6814	8.15	-5.47
60	Mrk 18	7.45	-3.76	133	NGC 6860	8.24	-3.75
61	2MASX J0904699+5536025	7.70	-2.64	136	4C +74.26	9.00	-2.51
62	2MASX J09112999+4528060	7.53	-2.83	137	Mrk 509	8.59	-2.70
64	2MASX J09180027+0425066	8.57	-2.88	138	IC 5063	7.68	-3.08
65	MCG -01-24-012	7.16	-2.26	139	2MASX J21140128+8204483	8.81	-2.72
66	MCG +04-22-042	8.49	-3.13	144	UGC 11871	8.34	-3.54
67	Mrk 110	7.80	-2.11	145	NGC 7172	8.31	-3.58
68	NGC 2992	8.04	-4.52	146	NGC 7213	8.63	-4.46
69	MCG -05-23-016	7.66	-2.70	147	NGC 7314	7.84	-3.73
70	NGC 3081	7.96	-3.66	148	NGC 7319	8.54	-3.55
71	NGC 3227	7.83	-4.02	151	MR 2251-178	8.76	-2.56
72	NGC 3281	8.62	-4.32	152	NGC 7469	8.64	-3.55
75	Mrk 417	8.04	-2.87	153	Mrk 926	8.95	-2.93
77	NGC 3516	8.13	-3.64	154	NGC 7582	8.31	-4.51

[1]The logarithm of $M/M_\odot$ where mass is derived from the 2MASS K-band stellar magnitudes (see Mushotzky *et al.* 2008).

[2]The logarithm of $L^{corr}_{2-10keV}/L_{Edd}$. Here, $L^{corr}_{2-10keV}$ is the value supplied in the X-ray spectral fitting tables for sources with $n_H < 10^{22}\,cm^{-2}$ and the calculated unabsorbed flux for the higher column density sources. The Eddington luminosity is calculated as $1.3 \times 10^{38} \times M/M_\odot$.

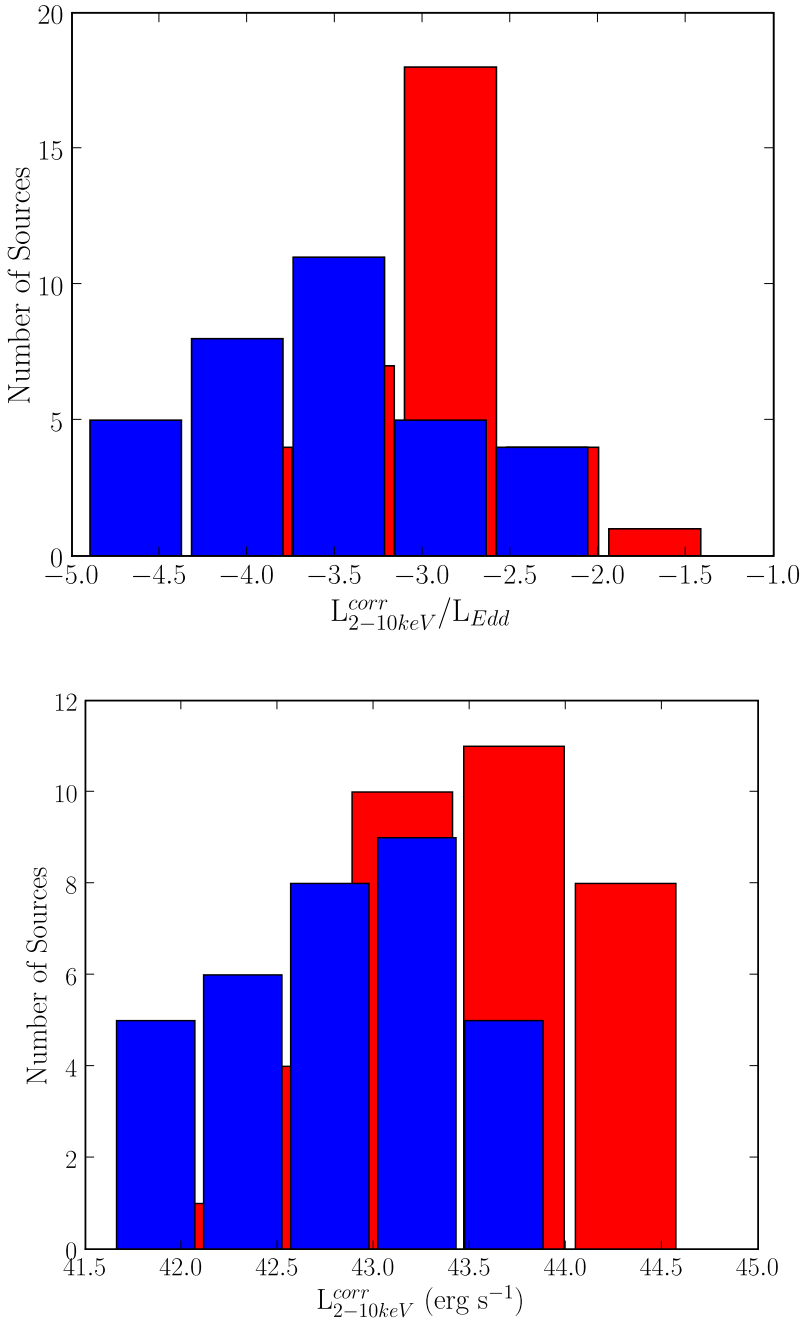

Figure 5.8: We plot the distribution of $L^{corr}_{2-10keV}/L_{Edd}$ (top) and unabsorbed L^{corr}_{2-10} (bottom) for our Seyfert 1 – 1.2 (red) and Seyfert 2 (blue) sources. From the plot, it is quite clear that the distribution of Seyfert 2s corresponds to lower $L^{corr}_{2-10keV}/L_{Edd}$. The X-ray luminosities are unabsorbed values and so the result is not merely a result of absorption. For both sets of distributions, we used a Kolmogorov-Smirnov test, finding a high probability of the distributions being different (the P values were < 0.001).

These results provide a challenge to the unified AGN model. If all AGN were essentially the same but viewed at different angles with respect to obscuring material, there would be no difference in the distributions of accretion rate or intrinsic luminosity. The fact that we are seeing these differences suggests that there is something fundamentally different besides the amount of obscuration. However, if the bolometric correction for hard X-ray luminosities varies between absorbed (correction of ≈ 85) and unabsorbed sources (correction of ≈ 35), as Barger et al. (2005) suggest, then our distributions of accretion rates would be the same. However, the unabsorbed X-ray luminosities would still differ and thus there is still a discrepancy with the unified model.

We are aware of at least three modifications to the unified model that can explain this difference in distributions between $\mathrm{L}^{corr}_{2-10keV}/\mathrm{L}_{Edd}$ in Sy 1s and Sy 2s. The first possibility is a luminosity dependent opening angle for the molecular torus, such as the receding torus model of Lawrence (1991). A second model is presented in Nicastro (2000), where the broad line region is produced from a wind from the accretion disk. The wind is produced at a boundary between radiation and gas dominated regions of the disk and its existence is dependent on reaching (or exceeding) a critical accretion rate. Our observation of a lower distribution of accretion rates in Sy 2s supports this claim. Their model also predicts that no hidden broad line regions should exist for low accretion rate sources. Such a test of the existence/non-existence of polarized broad line regions in the lowest accretion rate sources ($L_{bol}/L_{Edd} \leq 10^{-3}$ (Nicastro et al. 2003)), is beyond the scope of this thesis.

Another possibility is that, at lower luminosities, the host galaxy light is so much brighter than the emission from the broad line region that it is completely masked (Moran et al. 2002). Therefore, broad line galaxies should be brighter, as

we found. In Peterson et al. (2006), it is shown that the properties of high z objects may be modified by dilution of X-ray spectral features by star formation. Given the arc min resolution of ASCA, used for most of our spectra, this allows the blending of emission from star formation and other non-nuclear X-ray features. We expect this effect to be most pronounced for low luminosity sources, where the ratio of AGN emission to star formation/galaxy emission is lowest. We quantify the possible effects of this dilution in § 5.4.6.

5.4.3 Correlations of Γ with $L^{corr}_{2-10keV}$ and $L^{corr}_{2-10keV}/L_{Edd}$

Based on recent studies (Piconcelli et al. 2005; Porquet et al. 2004b; Shemmer et al. 2006), we wanted to test whether the X-ray power law index is correlated with the 2–10 keV luminosity or accretion rate. In Figure 5.9, we plot the photon index versus $L^{corr}_{2-10keV}$ (top left) and the ratio of $L^{corr}_{2-10keV}/L_{Edd}$ (bottom left). We see no evidence of a correlation between Γ and 2 – 10 keV luminosity or Eddington ratio, even among the Seyfert 1 sources which have smaller associated error bars on Γ. Based on previous studies, correlations between Γ and $L^{corr}_{2-10keV}$ have been seen in high-redshift samples (Dai et al. 2004; Saez et al. 2008), but not among the low-redshift sample ($z \leq 0.1$) of George et al. (2000). Thus, with our low redshift sample ($< z >= 0.03$), we confirm earlier results showing no correlation.

While we did not find a correlation between Γ and our Eddington ratio proxy on average in Chapter 4, we had found a correlation between luminosity and spectral index for individual sources. This correlation was found when we compared multiple X-ray observations from *XMM-Newton* and XRT. Similar results had been seen before for individual AGN (Mushotzky et al. 1993). Thus, these results show that while on average there is no relationship between Γ and a given Eddington rate, on a source by source basis, the photon index becomes steeper

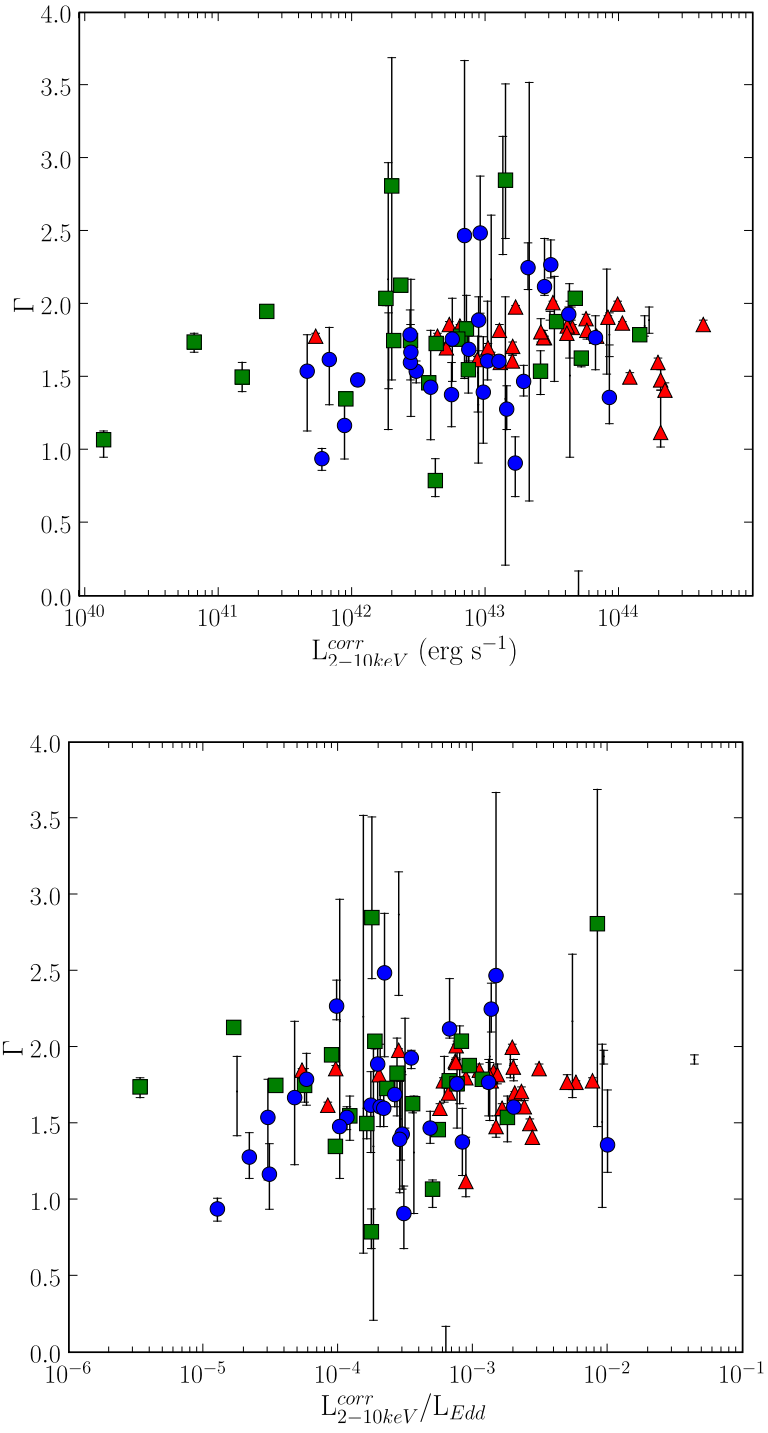

Figure 5.9: We plot the unabsorbed 2–10 keV luminosity versus power law index (top) and the ratio of unabsorbed 2–10 keV luminosity to Eddington luminosity versus power law index (bottom). Eddington luminosity is calculated from an estimate of the black hole mass using 2MASS K band photometry. We see no correlation between Γ and $L^{corr}_{2-10keV}$ or $L^{corr}_{2-10keV}/L_{Edd}$. Assuming that $L^{corr}_{2-10keV}$ is proportional to bolometric luminosity, our result shows no correlation between Γ and accretion rate, contrary to those of Shemmer et al. (2006). The triangles indicate optical Sy1–1.2 sources, the squares indicate Sy1.5–1.9 sources, and the circles indicate Sy2 sources.

with higher accretion rate. We interpret the fact that we do not see a correlation in the average plot as a result of each individual source having a broad range of luminosities and accretion rates which they vary between. Since the individual ranges overlap between the sources, the scatter is a natural result.

Comparing further with Shemmer et al. (2006), we see at least two possibilities for our different result. First, the 30 objects selected by Shemmer et al. (2006) are moderate to high luminosity RQQs. Our sample, however, includes lower luminosity sources not present in their sample. It may be that the correlation is only there for the most luminous AGNs. In this case, the more luminous AGN may be more similar, perhaps having the same trigger (like a large-scale merger event (Di Matteo et al. 2005)) which dictates a specific range of accretion rates. Our sample is more heterogeneous with a larger range in properties and possibly multiple triggers for AGN activity. Second, the Shemmer black hole masses are estimated from the width of the optical H-β line (Porquet et al. (2004b) and Piconcelli et al. (2005) use the luminosity at 5100Å) while we used the stellar K-band flux. It is possible that there is a bias in the Shemmer black hole mass determinations relative to ours. The H-β line width may have an explicit dependence on Γ (Laor et al. 1997), in addition to black hole mass and luminosity.

5.4.4 The Fe-Kα Feature

Yet another important feature of AGN spectra is the Fe Kα line. For 83/102 sources (81%), a measurement of the strength of this line, via the equivalent width (EW), was available. The missing objects include most of the XRT observed sources as well as some from the literature. For these sources, the data were not of sufficient quality to accurately measure the Fe K line strength. In Figure 5.10, we plot the Fe-Kα (6.4 keV) EW versus absorption corrected 2 – 10 keV luminos-

ity and our proxy for the Eddington ratio. We note that for three bright Seyfert 1 sources (Fairall 9, 3C 120, and 3C 382), the ASCA data show a strong, broad, Fe K-α line that is not seen in further observations. While we include the ASCA fit parameters, the high EWs for these sources cause these three points to be clear outliers.

The X-ray Baldwin/ "Iwasawa-Taniguchi" effect (Iwasawa & Taniguchi 1993) is the anti-correlation between Fe K-α and luminosity, quantified as $EW \propto L^{-0.17\pm0.08}$ by Page et al. (2004). Recently, this effect has been reported in radio quiet samples of Jiang et al. (2006) and Bianchi et al. (2007). In the top left panel of Figure 5.10, we see no evidence of the X-ray Baldwin effect. However, when we bin the sources by luminosity (excluding the 3 questionable measurements) we do find a correlation (middle left panel). This correlation is seen when we choose the average Fe K EW in each luminosity bin, with $\log EW = (-0.23 \pm 0.03) \times \log L^{corr}_{2-10keV} + (12.11 \pm 1.17)$, and is similar to the Page et al. (2004) measured slope. The significance of the anti-correlation, measured by a correlation co-efficient of $R^2 = 0.93$ (99% significance), seems to confirm the X-ray Baldwin effect. However, the results are deceiving. We find that when we alternatively use the median EW, the correlation becomes much weaker ($R^2 = 0.63$; lower left panel). This shows that the more absorbed, lower luminosity sources – among them, the hidden AGN clearly missed in other surveys – are skewing the results. Therefore, our data does not confirm the inverse Baldwin effect.

Jiang et al. (2006) suggested that the X-ray Baldwin effect is driven by a correlation of Fe K-α EW and Eddington ratio. Such an anti-correlation was found by Bianchi et al. (2007), who found that $EW \propto L_{bol}/L_{Edd}^{-0.19\pm0.05}$. In the top right panel of Figure 5.10, we plot the EW versus our proxy for Eddington ratio. As

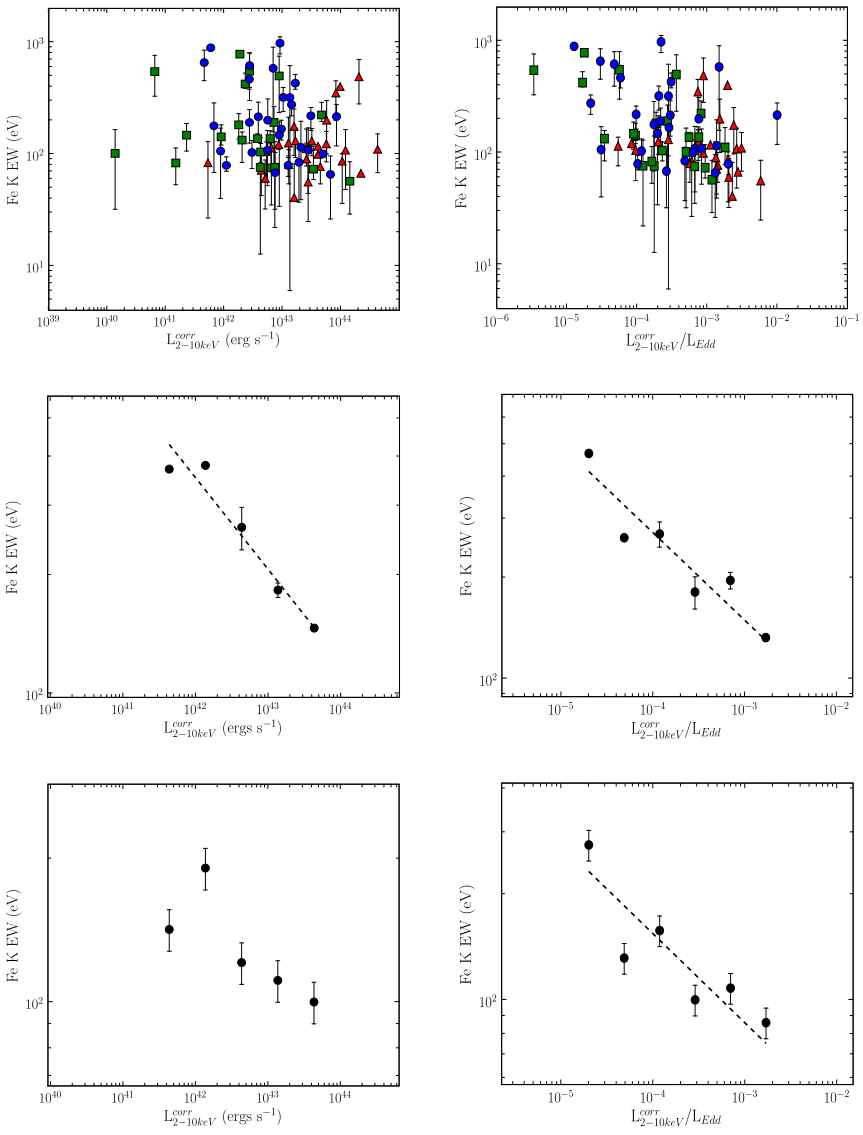

Figure 5.10: We plot the narrow Fe Kα line equivalent width (EW) versus unabsorbed 2 – 10 keV luminosity (left) and our proxy for Eddington rate (right). In the top panels, we plot the distribution for all of our sources. The triangles indicate optical Sy1–1.2 sources, the squares indicate Sy1.5–1.9 sources, and the circles indicate Sy2 sources. The mean EW for the 76 sources plotted is $\mu = 200$ eV with $\sigma = 203$ eV. In the remaining panels, we plot the distribution after binning the values by luminosity or $L^{corr}_{2-10keV}/L_{Edd}$ using the mean Fe K EW (middle) or median EW (bottom). While anti-correlations are seen in both sets of plots using the mean EW (middle), the relationship weakens substantially for the luminosity plot when the median EW is used (bottom left). Thus, our data does not show evidence of the X-ray Baldwin effect but does show an anti-correlation in the binned EW vs. Eddington ratio relation.

with the luminosity, we do not immediately find any correlation. However, when we again bin the values (excluding the 3 questionable measurements), we find an anti-correlation. Using the mean values of Fe K-α EW, we find that $\log EW = (-0.26 \pm 0.03) \times \log L^{corr}_{2-10keV}/L_{Edd} + (1.40 \pm 0.10)$, with $R^2 = 0.89$. Further, unlike in the luminosity plots, this relation also holds true when we use the median EW. Thus, our data shows no correlation with unabsorbed 2–10 keV luminosity but does show an anti-correlation with Eddington rate.

This suggests that the primary relationship causing the X-ray Baldwin effect is the relationship between Fe K EW and accretion rate. From Figure 5.8, we found that the distribution of $L^{corr}_{2-10keV}/L_{Edd}$ is different between absorbed and unabsorbed sources. The Sy 2s have lower accretion rates than Sy 1s. We also find this in Figure 5.11, where we plot the Eddington rate proxy and the Fe K EW versus hydrogen column density (n_H). In Figure 5.11 (top), we see that while there is a large range of accretion rates for a given column density, the higher column sources tend to have lower accretion rates. In Figure 5.11 (bottom), we find that the higher n_H sources also have higher Fe K EWs. This result is expected, particularly if some of the sources are Compton thick. However, since there are sources with higher EWs and lower n_H, there is no direct correlation between EW and column density.

Supporting the case that EW is correlated with accretion rate, Mattson et al. (2007) reported a correlation between Γ and Fe K EW. Their data sample consisted of 350 RXTE spectra of 12 Sy 1 – 1.2 sources, thus, as shown in their Figure 3, it appears that the anti-correlation (except for jet dominated 3C 273, where there is a correlation) is seen mostly for multiple observations of the same source. Since Γ steepens with increasing accretion rate, we claim that the primary relationship is again accretion rate and EW.

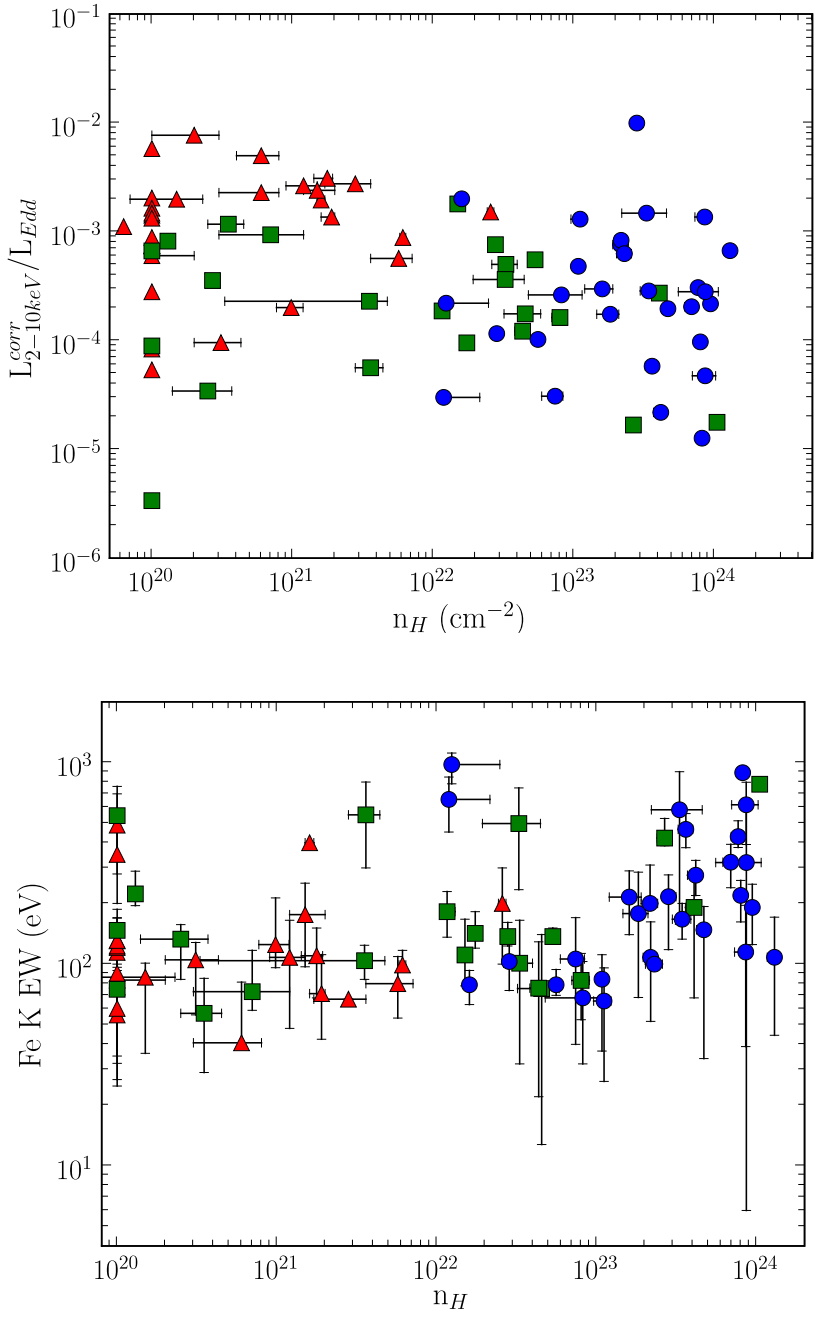

Figure 5.11: We plot $L^{corr}_{2-10keV}/L_{Edd}$ (top) and the narrow Fe Kα line equivalent width (EW) (bottom) versus the X-ray measured hydrogen column density. We find no correlation in either relation. Here, the triangles indicate optical Sy1–1.2 sources, the squares indicate Sy1.5–1.9 sources, and the circles indicate Sy2 sources.

5.4.5 Simple Power Law Model Sources

Nearly half, 46/102, of the uniform sample were well-fit by a simple absorbed power law model. As mentioned, none of these sources had X-ray column densities $\geq 10^{23}\,\mathrm{cm}^{-2}$. In this subsection, we detail additional properties of these sources. In particular, from the data available we can compare optical Seyfert type with the X-ray column density and examine the sources more closely for soft excesses. While we hoped to examine sources with warm absorbers in detail, given the non-uniform nature of analyses of warm absorbers in the literature, we defer this topic to a later study.

First, we discuss the optical versus X-ray type. For each of the simple model sources, an optical Seyfert type is listed in Table E.1. Most of the sources, 30/46 (65%), have optical classifications of Sy 1 – 1.2. The mean X-ray column density for these sources corresponds to a low column density, $\log \mathrm{n}_H = 20.7$. As expected, the Sy 1.5 – 1.9 sources (13/46 or $\approx 28\%$) have a higher mean column density of $\log \mathrm{n}_H = 21.8$. The 3 Sy 2 sources have a mean column density of $\log \mathrm{n}_H = 22.8$. Therefore, for the simple model sources, there is no large discrepancy between the X-ray and optical classifications. In the unified model of AGN, the presence/absence of optical broad emission lines is explained as an effect of viewing angle. Therefore, sources whose optical spectra show broad emission lines (Sy1s) would have little obscuring material blocking the central AGN emission while sources with no broad lines (Sy2s) would be more heavily obscured. Thus, our results agree, in general, with the unified model.

Next, we will examine the spectral fits in more detail. As a first step, we look at the goodness of fit for our sources through the χ^2 parameter. While a simple power law or power law and blackbody model was a better choice for

our sources than a more complex model (like the partial covering model), 4 of the simple model sources have χ^2/dof values of 1.3 or higher (in Tables E.2 and E.3). Of these, XSS J05054-2348 only had XRT data available. The number of data points for this source is small, so the high χ^2/dof value may be a product of poor statistics. Of the remaining sources, the source with the highest χ^2/dof value (2.2) is Mrk 841. For this source, XMM-Newton observations analyzed by Petrucci et al. (2007) showed an Fe line complex. In addition, this source is known to have a strong soft excess. These features were not well fitted by the simple models employed in this study. Additionally, Chandra observations of Mrk 279 reveal the presence of a weak absorbing outflow (Fields et al. 2007). Similarly, a high-quality XMM-Newton spectrum of NGC 4593 reveals an ionized warm absorber in addition to the soft excess, as well as cold and ionized Fe K lines (Brenneman et al. 2007).

In the spectral fits for our simple model sources, we allowed for the addition of a blackbody component to model the presence of a soft excess. In our uniform sample, 19/46 ($\approx 41\%$) of the sources required a blackbody for a statistically improved fit. This is slightly less than the 50% found in Chapter 4, but not significantly less. The mean blackbody temperature for our sources is $kT = 0.10$ keV with $\sigma = 0.07$ keV. This value agrees with the blackbody temperatures found for the PG quasars (Piconcelli et al. 2005; Porquet et al. 2004b) as well as those for type 1 AGN in the Lockman Hole (Mateos et al. 2005). We note that unlike the results of Gierliński & Done (2004), who found $< kT >= 0.12$ keV with $\sigma = 0.02$ keV for the PG quasars, we do see scatter in the values of kT (which becomes apparent in Figure 5.12). However, since they used two Comptonization models instead of a blackbody and power law model, it is hard to make a direct comparison.

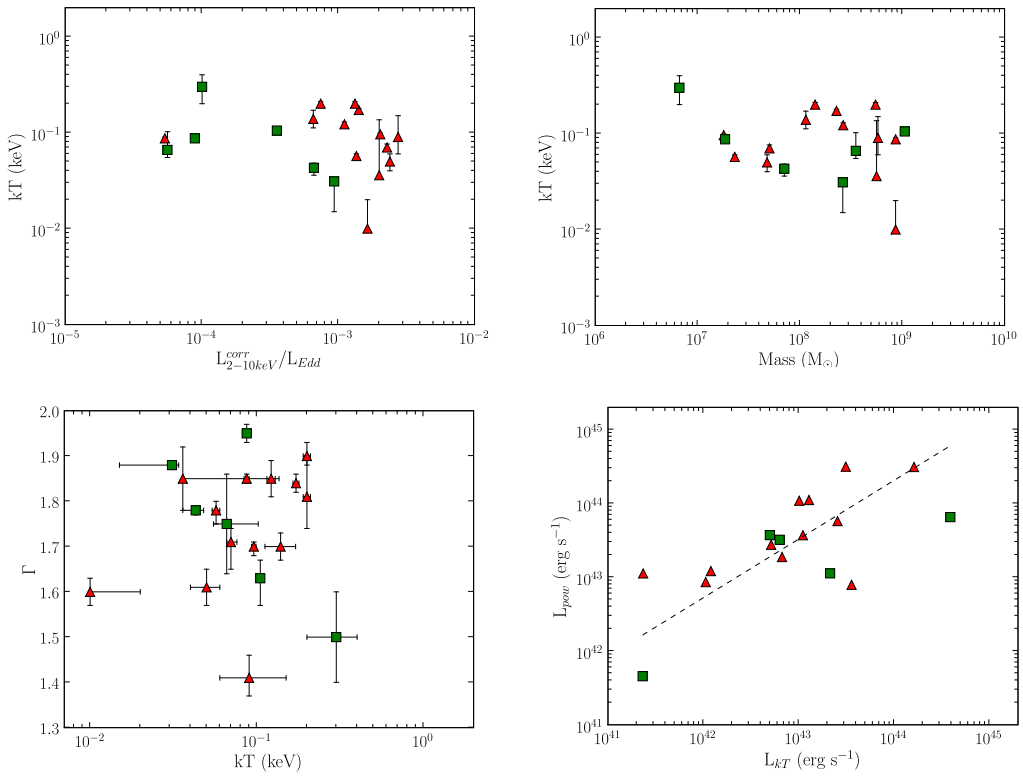

Figure 5.12: In the top row, we plot the blackbody temperature for the 19 simple model sources requiring a soft excess model versus $L^{corr}_{2-10keV}/L_{Edd}$ and black hole mass, respectively. There is no correlation between these parameters. Similarly, we find no correlation between the power law index and blackbody temperature (bottom left). However, there is a correlation between the unabsorbed luminosity in the power law component and that in the blackbody component (bottom right). Fitting a line to the data, we find that the relationship is nearly linear ($L_{pow} \propto L_{kT}$). Here, triangles represent Sy 1–1.2 sources and squares indicate Sy 1.5–1.9 sources.

For the sources with measured soft excesses, we wanted to test whether there was a relationship between the blackbody temperature (kT) and our proxy for Eddington rate, black hole mass, and the photon index (Γ). In Figure 5.12, we plot the results of these comparisons. As seen in the figure, there is no correlation of any of these values. We tested this by calculating the coefficient of correlation, R^2, which was < 0.10 for each comparison. Based on current understanding of the soft excess, we did not expect to find correlations for these

parameters. If the soft excess were the result of a thermal process, blackbody emission from a disk surrounding the black hole, we would see a correlation between black hole mass and the blackbody temperature ($T \propto M^{-1/4}\ {L/L_{Edd}}^{1/4}$). We do not find a correlation between kT and mass, kT and $L^{corr}_{2-10keV}/L_{Edd}$, or kT and ${L^{corr}_{2-10keV}/L_{Edd}}^{1/4} \times (M/M_{\odot})^{-1/4}$ (not shown in Figure 5.12).

In Figure 5.12, we also plot the luminosity in the power law component versus the luminosity in the blackbody component. Combining spectra from our own analysis with downloaded spectra of sources with soft excesses previously analyzed in the literature, we calculated unabsorbed fluxes for 17/19 sources in the 0.3–10 keV band for each component (power law and blackbody). As shown in the plot, we did find a correlation between the two values. The correlation is signficant, $R^2 = 0.48$, with $\log L_{pow} = (0.79 \pm 0.14) \times \log L_{kT} + (9.34 \pm 6.04)$. Thus, we find that $L_{pow} \propto L_{kT}$. Comparing the flux values F_{pow} and F_{kT}, we find that the correlation is still present with $R^2 = 0.50$ and $\log F_{pow} = (0.43 \pm 0.08) \times \log F_{kT} + (-5.79 \pm 0.90)$.

Such a relationship between L_{pow} and L_{kT} may provide a challenge to soft excess models where the excess is the result of an absorbing model, unless there is an explicit luminosity dependence between the absorbing wind and source emission. In terms of a reflection origin, where the soft excess is the result of emission from reprocessed disk emission, there is no implicit contradiction. However, in this case, our results indicate that since the reprocessed emission (L_{kT}) is on the same order as the input spectrum (L_{pow}) the process would need to be highly efficient, with the reprocessor occupying a large solid angle and a very high reprocessing efficiency.

5.4.6 Complex Sources

Slightly more than half of our sample ($\approx 55\%$) consists of sources whose X-ray spectra were not well-fit by a simple absorbed power law model. Here, we discuss the optical types of these sources. We also discuss the fraction of complex sources and the nature of the complexity.

As expected, the optical types for the complex sources are opposite those of the simple model sources. Here, only 4 sources are identified as Sy 1 – 1.2, where the complexity in their spectra is a result of complex absorption (e.g. IC 4329A is known to have at least 7 separate absorbers in the X-ray spectrum (Steenbrugge et al. 2005)). The majority of sources are Sy 2s (36/56 or 64%), with the remaining 16 sources Sy 1.5 – 1.9s (29%). As with the simple model sources, the optical types roughly matched the X-ray column densities. The mean values of $\log n_H$ corresponded to 22.0 (Sy 1 – 1.2), 23.2 (Sy 1.5 – 1.9), and 23.6 (Sy 2). Thus, we find no substantial discrepancy between our data and the standard unified AGN model for our entire uniform sample, with respect to X-ray/optical classifications.

One question remaining is the cause of the complexity. We fit the spectra in this category with a partial covering model, but this model is flexible and can be used to describe more than just a cloud or clouds of material blocking some of the AGN light. As already mentioned, one cause of complexity is complex absorption, e.g. warm absorption. The Seyfert 1–1.2 sources from our sample with complex spectra are known to fit in this category. Another possible cause of complexity is scattering of direct emission from an obscured region into our line of sight, accounting for the soft emission (< 2 keV). We can not easily test either of these theories with our data. Yet another cause of complexity could be that the soft emission is not from the AGN, but rather from X-ray binaries, star

formation, or hot ionized gas in the host galaxy. Since we do not expect this emission to exceed a few $\times 10^{41}$ ergs s^{-1} (Ranalli et al. 2003), we can automatically rule out this scenario for sources with higher luminosities in the soft emission.

In Figure 5.13 (top), we plot the distribution of soft X-ray luminosity in the 0.5–2.0 keV band for our complex sources. The mean luminosity is $\log L_{0.5-2.0keV} = 41$ with $\sigma = 0.94$. We find that only 13/54 sources have soft emission high enough to exclude a simple explanation of galactic emission ($\log L_{0.5-2.0keV} \geq 41.5$). For these sources, which include all of the 4 Sy 1s as well as 3 "hidden" AGN, it is unlikely that the soft emission is from the host galaxy. The fact that a few of the hidden sources can not be explained by this model suggests that an alternative model, like scattering or partial covering, is more favorable. However, for 75% of the complex sources, the luminosities are too low to exclude galactic emission. In Figure 5.13 (bottom), we plot the observed soft luminosity versus the observed hard luminosity. We would naively expect the two luminosities to be directly correlated if they are related and not due to galactic emission. Of course, the effects of obscuration in the 0.5–2 keV band have not been considered to make this plot, particularly since the nature of the soft emission is ill-determined. A strong correlation is not seen, but this does not rule out any of the possibilities. Unfortunately, the present data set has too low an angular resolution, on average, to distinguish galactic sources of soft emission from the AGN. We know that in some cases, e.g. Circinus, NGC 1365, and NGC 4151, the soft emission is due to X-ray binaries, hot gas from star formation, and extended emission from AGN cores, respectively. However, higher quality data with the superior spatial resolution of Chandra is needed to solve the problem of the origin of the soft emission. Even with the low fluxes of many of our sources, not very long (≈ 10 ks) Chandra exposures would be required to obtain images of the soft emission.

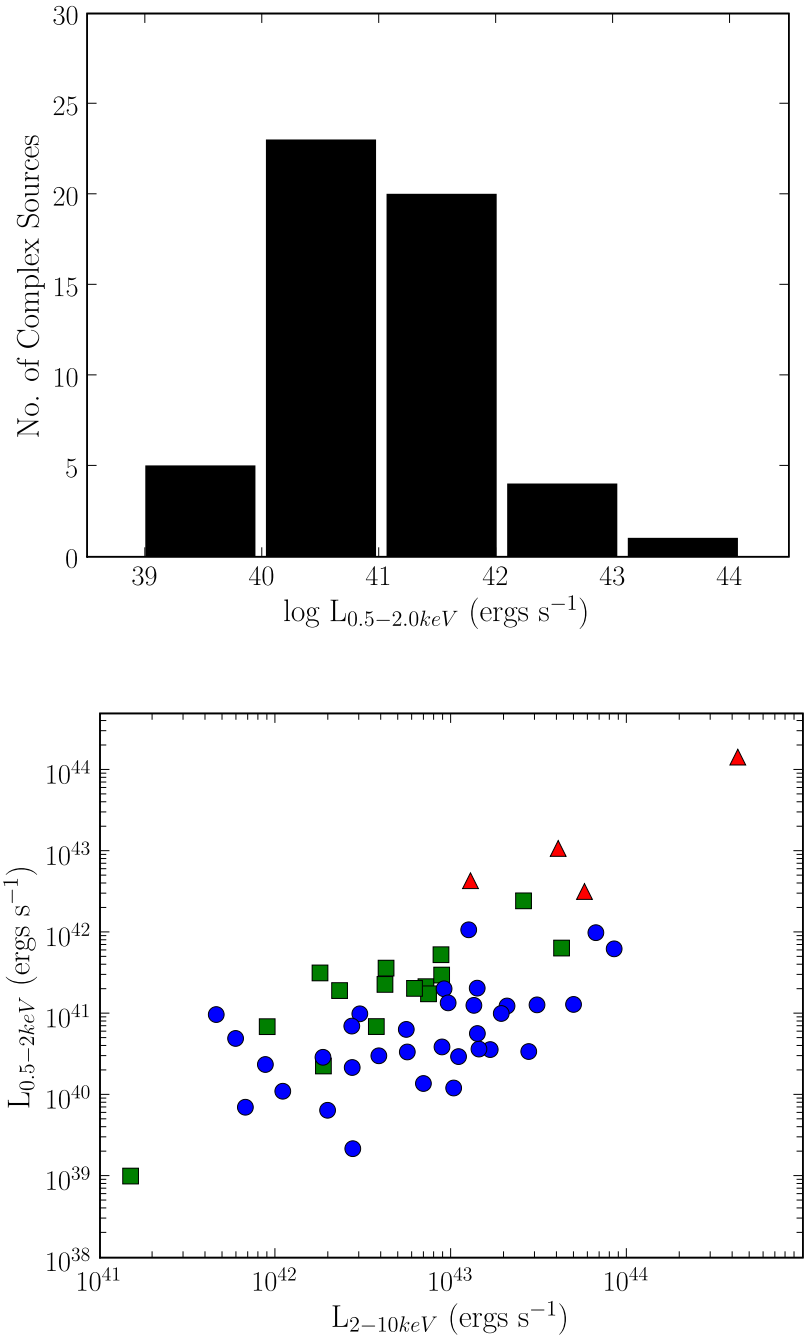

Figure 5.13: Plotted in the top panel is the distribution of soft band X-ray luminosity for sources with spectra best fit by a complex model. The mean value is $\log L_{0.5-2.0keV} = 41$ with $\sigma = 0.94$. This shows that for more than half of the sources the luminosities are low enough that we can not rule out the idea that the soft emission is from X-ray binaries/star formation/diffuse gas in the host galaxy. Plotted in the bottom panel, we show the soft X-ray observed luminosity versus the hard X-ray observed luminosity. A strong correlation is not seen, as indicated by $R^2 = 0.51$. This further suggests that we can not explain the soft emission as a simple extension of the hard power law emission.

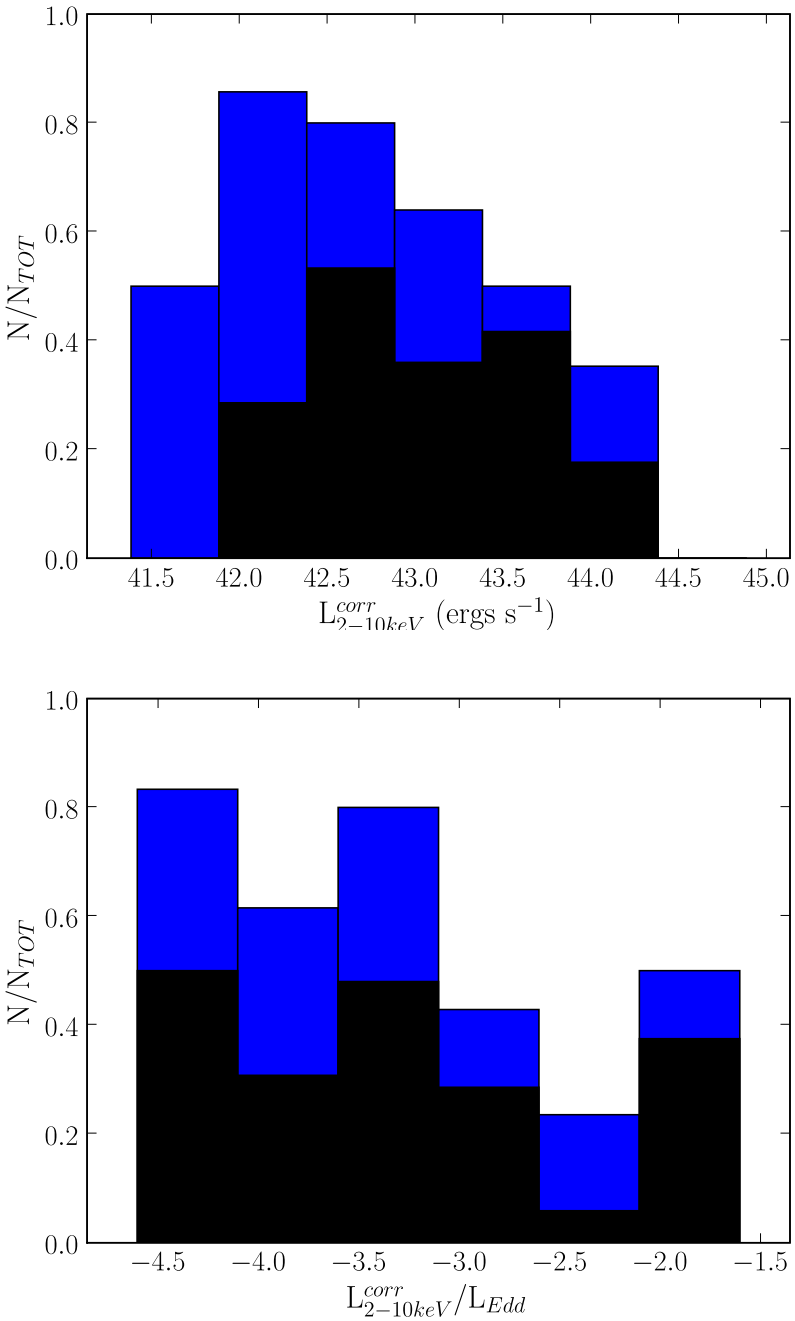

Figure 5.14: These plots show the fraction of absorbed sources in a given $L^{corr}_{2-10keV}$ bin (top) and accretion rate bin (bottom). N/N_{tot} is the number of absorbed sources in a given bin divided by the total number of sources in that bin. The black bins show the fraction of sources with $\log n_H \geq 23$. These are a subset of the sources with $\log n_H \geq 22$, pictured in blue. There are no high n_H sources in the highest $L^{corr}_{2-10keV}$ (unabsorbed) bin. Further, the fraction of obscured sources is lower at high luminosities. In the second plot, it is not clear that the fraction of obscured sources increases with lower accretion rate ($L^{corr}_{2-10keV}/L_{Edd}$). We find that 50% of the sources in the highest luminosity bin are absorbed, however, with only 8 sources in this bin, this could be the result of poor sampling.

Earlier, we had shown that the distribution of 2–10 keV luminosities and our Eddington ratio proxy ($L^{corr}_{2-10keV}/L_{Edd}$) was lower for Sy 2s than Sy 1s. Another important investigation that we can now make is the fraction of obscured AGN as a function of luminosity and accretion rate. In Figure 5.14, we show the results of the fraction of sources with column densities above $\log n_H = 22$ in each indicated 2–10 keV unabsorbed luminosity bin and $\log L^{corr}_{2-10keV}/L_{Edd}$ bin. We also show the subset fraction of sources with $\log n_H \geq 23$ (in black). These plots show us that there are clearly less obscured sources at high luminosity. The highest luminosity bin is composed entirely of unabsorbed sources. One interesting thing to note, however, is that the most absorbed sources ($\log n_H \geq 23$) are not more numerous at lower luminosity. Rather, they are merely a subset of the absorbed sources. Instead, the sources with $23 > \log n_H \geq 22$ dominate in the lowest luminosity bins. It is unclear what this result implies. However, our results clearly support previous studies which found the fraction of obscured sources low at high luminosities and higher at lower luminosities (Barger et al. 2005; Steffen et al. 2003; Ueda et al. 2003). Our results argue even more strongly that there must be a modification to the unified model which includes dependence on luminosity.

Our plot of the fraction of absorbed sources by binned accretion rate (Figure 5.14 (botom)), is more difficult to interpret. While absorbed sources do dominate at the lowest values of $\log L^{corr}_{2-10keV}/L_{Edd}$, the highest Eddington rate bin also shows a large fraction of absorbed sources. However, we find that this bin includes fewer sources (8), and the result could be a product of poor statistics. We do note that, as with luminosity, the fraction of the most heavily absorbed sources ($\log n_H \geq 23$) does not appear to increase with decreasing Eddington rate. Rather, it appears to remain nearly constant. Still, on the whole, the absorbed sources make up the largest fraction of sources at low Eddington rate and

a lower fraction at high Eddington rates.

Another important conclusion drawn from our analysis is that the fraction of "hidden" AGN, sources with low scattering fractions (≤ 0.03), is significant. These sources comprise 45% of the complex sources and 24% of our uniform sample. This highlights the importance of the BAT survey and its ability to find obscured sources, since these objects have no indication of AGN activity in the soft X-ray band. Now that these sources are firmly established as an important subset of local AGN, it is important to understand their properties. In Chapter 4, we had noted that fitting the sources with a reflection model is problematic. We were unable to constrain the reflection parameter or the cutoff energy, even with the addition of the BAT spectrum (14–195 keV). Further, while the partial covering model provides a decent fit, this model is very flexible. One probable explanation for the hidden/buried AGN, is that they are embedded in a very geometrically thick torus (Ueda et al. 2007).

Fabian et al. (1998) proposed a model in which low-luminosity AGN were obscured by nuclear starbursts. This is one possible origin for a geometrically thick torus. Following Ueda et al. (2007), we used the 60 μm and 100 μm fluxes from the *Infrared Astronomical Satellite*, obtained from NED, to estimate the far infrared luminosity of the hosts of the hidden sources. We found these values for 16/24. The mean value of $\log L_{FIR} = 43.76$ with $\sigma = 0.42$. We also computed the ratio of $L^{corr}_{2-10keV}/L_{FIR}$. Here, we find that the mean value is 0.26 with $\sigma = 0.26$. This value is consistent with ratios for AGNs in the local universe, as pointed out by Ueda et al. (2007). It is the sources with very small ratios, $<< 0.1$, which indicate the possibility of significant starburst activity. In our sample, only 6 sources fall into this category, with the lowest ratio (0.007) corresponding to NGC 7582, an object whose H and K band nuclear light is dominated by young supergiants

(Oliva et al. 1995). However, without higher quality IR observations of the nuclear region and an analysis which can separate out any AGN emission, little conclusions can be drawn from this data.

Yet another question remaining is how many sources are Compton-thick. This is not an easy question to answer, especially since different authors use different definitions. In general, the term has been used to apply to: (1) heavily obscured AGN ($n_H > 1.4 \times 10^{24}\,\mathrm{cm}^{-2}$), (2) spectra with a high EW Fe K line, (3) spectra with a flat power law continuum, and (4) spectra with a strong reflection hump. The last three criteria are all indications of a reflection dominated spectrum. If we take the Compton-thick definition to apply to sources whose column densities are $> 1.4 \times 10^{24}\,\mathrm{cm}^{-2}$, none of the BAT-detected sources are Compton-thick. There are, however, sources which come close (NGC 612, NGC 3281, NGC 1365, NGC 5728, NGC 6921, and NGC 7319), with $n_H \approx 10^{24}\,\mathrm{cm}^{-2}$. Without simultaneous data above 10 keV, it is extremely difficult to definitively discriminate between reflection models and partial covering models. Even with simultaneous data from Suzaku, we are finding it impossible for some sources (Winter *et al.*, in prep). However, this is not the case for all sources, for instance, NGC 5728 strongly prefers a reflection model and exhibits a strong iron K EW ($\approx 800\,\mathrm{eV}$). Therefore, it is clear that if other criteria are used we do find Compton-thick sources. For instance, we find that 6 sources exhibit a very flat spectrum ($\Gamma \leq 1.0$). Alternatively, 6 sources have strong Fe K equivalent widths ($EW \geq 600\,\mathrm{eV}$). From our data, we cannot test for the presence of a reflection hump, since the feature is predominant above 10 keV. However, with the BAT spectra such studies are forthcoming. Combining criteria, only 1 source shows both a flat continuum and a strong Fe K EW, NGC 5728. However, the column density is still below the strict Compton-thick limit. In this discussion, we have not considered the complicated spectra of Cen

A, NGC 1275, and the double nucleus NGC 6240, who may also have consistent properties with the various Compton thick definitions.

5.5 The Cosmic X-ray Background

The most recent synthesis models for the cosmic X-ray background (CXB) find that heavily obscured and Compton thick AGN are as important as unabsorbed AGN (Gilli et al. 2007). With an unbiased sample of AGN from the BAT, we can begin to understand the contributions of both types of AGN in the local Universe. In the previous section, we have presented the distribution of column densities and power law indices from the 0.1 – 12 keV X-ray bands for our unique uniform 14 – 195 keV X-ray sample. These properties will provide a valuable input to the CXB models for low redshift ($z \approx 0$) AGN. In addition, in this section we provide the 2 – 10 keV $\log N$-$\log S$ relationship. With this relationship, we will comment on the completeness of a very hard X-ray selected sample in the 2–10 keV band and its implications.

5.5.1 The Average X-ray Spectrum

Having compiled all of the properties of the 9-month BAT AGN sources, we present the average 0.6–10 keV X-ray spectrum for our uniform sample of 102 sources in Figure 5.15. Since the normalization values are not uniformly recorded in the literature, we could not simply add the spectra together. Instead, we construct the average spectrum using the shape of the spectrum (from the absorbed power law models) with 2–10 keV flux used to weight the contribution to the average spectrum.

To construct the average spectra, we have excluded three important AGN fea-

tures: blackbody components/soft excess, Fe K lines, and reflection. We do not include blackbody components since the $< kT > \approx 0.1$ keV components have very little spectral effects at $E > 0.6$ keV, the energy above which the CXB is well measured (McCammon et al. 2002). It is almost impossible to measure the diffuse background below this level because the Galaxy's soft X-ray background is very bright at $E < 0.7$ keV. A significant fraction of our spectra are from XRT observations, where one cannot constrain Fe K line emission or reflection. Also many of the ASCA, XMM, and other data sets were analyzed in many different ways with respect to reflection and without re-analyzing the entire data set in a uniform fashion one cannot model reflection correctly. In particular, we do not believe that the exclusion of reflection has a significant effect on the average spectrum < 10 keV, since the effect of reflection is typically rather small at these energies (for all but the largest reflection fractions). In fact, as Nandra & Pounds (1994) show, a $\Gamma = 1.7$ power law is almost a perfect match to a $\Gamma = 1.9$ power law with reflection in the 2–10 keV band.

The average spectrum was constructed as: $I(E) = \sum A_i \times F_i \times E^{1-\Gamma_i}$. For each source, F_i is the observed 2–10 keV flux. The measured spectral index was used as the main component of the AGN emission. Finally, A_i represents the absorbing column density. To apply the absorption term, we constructed a grid of `XSPEC` absorption models using an input power law with a spectral index of 1.73 (the average of the complex model sources). The models included simple absorption using `tbabs` with $\log N_H = 20, 20.5, 21, 21.5, 22, 22.5, 23$ and complex absorption using `pcfabs` with a partial covering fraction of 0.95 and $\log N_H = 21.5, 22, 22.5, 23, 23.5, 24$. The flux of the output `XSPEC` models corresponds to normalized photons cm^{-2} s^{-1} keV^{-1}. In order to compute A for each model, we divided the model by the power law contribution ($E^{1-1.73}$) and multiplied by

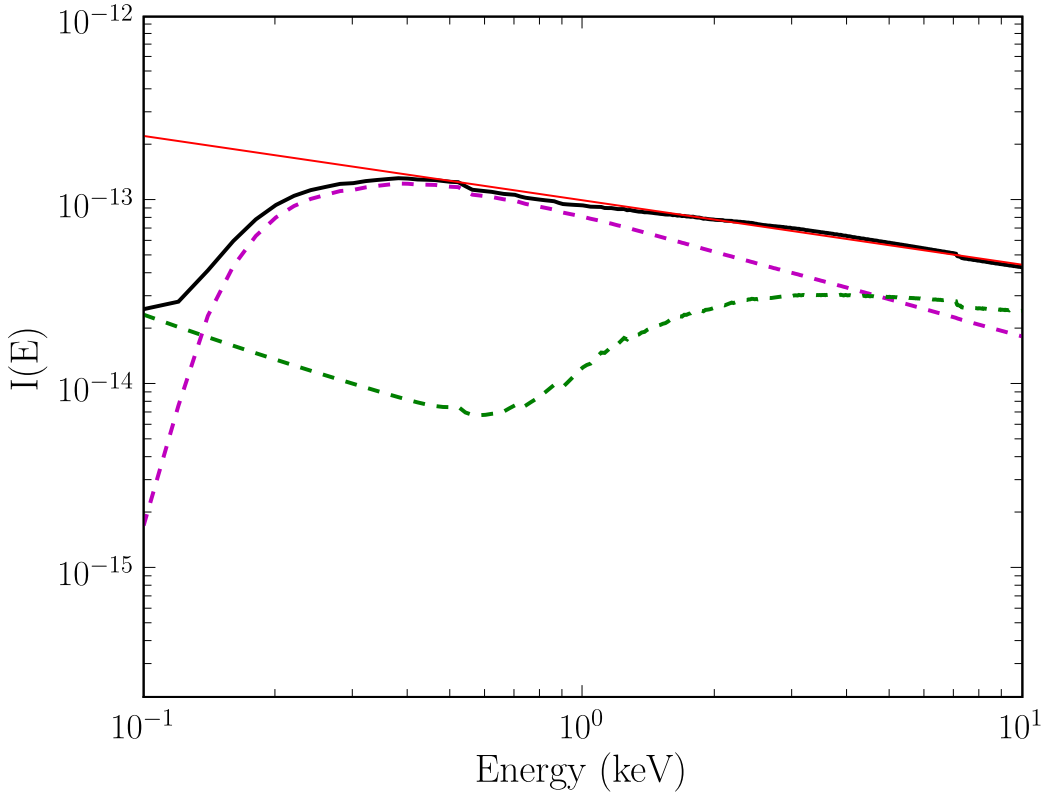

Figure 5.15: Shown here is the average spectrum constructed from the X-ray fits to our uniform sample of 102 AGN. The solid black curve is the average spectrum of the AGN sources. The dashed lines show the contribution from the simple absorption sources (magenta) and the complex absorption sources (green). We also show a line fit to the average spectrum from 0.6 – 10 keV. The slope of the line, $\Gamma = 1.369 \pm 0.004$, is consistent with the modeled CXB slope. The total flux from our sources corresponds to only 0.29% of the entire 2–10 keV CXB.

energy. We then applied the appropriate model for each of the sources based on N_H and the complexity flag.

In Figure 5.15, the contributions of the simple model and complex model sources are shown. We note that we chose to neglect additional soft emission and Fe K line signatures, as well as reflection. Fitting a line to our spectrum for energies above 0.6 keV, we find $\log I(E) = (-0.369 \pm 0.004) \log E + (-12.989 \pm 0.003)$, with $R^2 = 0.97$. Thus, we find $\Gamma \approx 1.37$. This result is quite remarkable. In 1980,

HEAO-1 found that the CXB could be modeled as a power law with $\Gamma = 1.4$, below 15 keV (Marshall et al. 1980). However, the narrow distribution of power law indices ($\Gamma \approx 1.7$) for AGN led to a "spectral paradox", where it was unclear how averaging over these dominant bright sources resulted in the flatter power law index fit to the CXB (Boldt 1987). The paradox was resolved theoretically by assuming that many AGN are absorbed, such that $\approx 85\%$ of their light is obscured (Fabian & Iwasawa 1999). With our simple estimate of the average X-ray spectrum from the SWIFT BAT-detected AGN, we have now observationally reproduced the measured CXB slope. The flux from these bright sources, with a total flux of 1.79×10^{-9}erg s^{-1} cm^{-2}over 74% of the sky, accounts for only 0.29% of the CXB (2.0×10^{-11}erg s^{-1} cm^{-2} deg^{-2} Revnivtsev et al. (2008)). However, if the distribution of source properties at $z \approx 1$, where most of the CXB originates, is similar to that of the BAT sources, the spectral paradox is resolved. A similar conclusion was reached by Sazonov et al. (2008), who calculated the 3–300 keV SEDs of local AGN using Integral and RXTE data.

5.5.2 The 2-10 keV Log N - Log S Relationship

Towards determining how complete a 14–195 keV survey is in the 2–10 keV band, we plotted the $\log N$-$\log S$ relationship for our uniform sample in the 2–10 keV band in Figure 5.16. Here, $\log N$ is the logarithm of the number of galaxies with a 2–10 keV flux above the associated $\log S$ value. We corrected this value for the BAT sky coverage by using the BAT sky coverage map from Tueller et al. (2008) and the 14–195 keV flux for each source. We found that the sample is complete in the 2–10 keV band to $\log S \approx -11$ ($F_{2-10keV} \approx 1 \times 10^{-11}$ erg cm^{-2} s^{-1}). To show this, we fit a line to the points above this threshold (shown in the plot). The fit is very significant, with $R^2 = 0.97$ and $\log N(S) = (-1.53 \pm 0.12) \times \log S -$

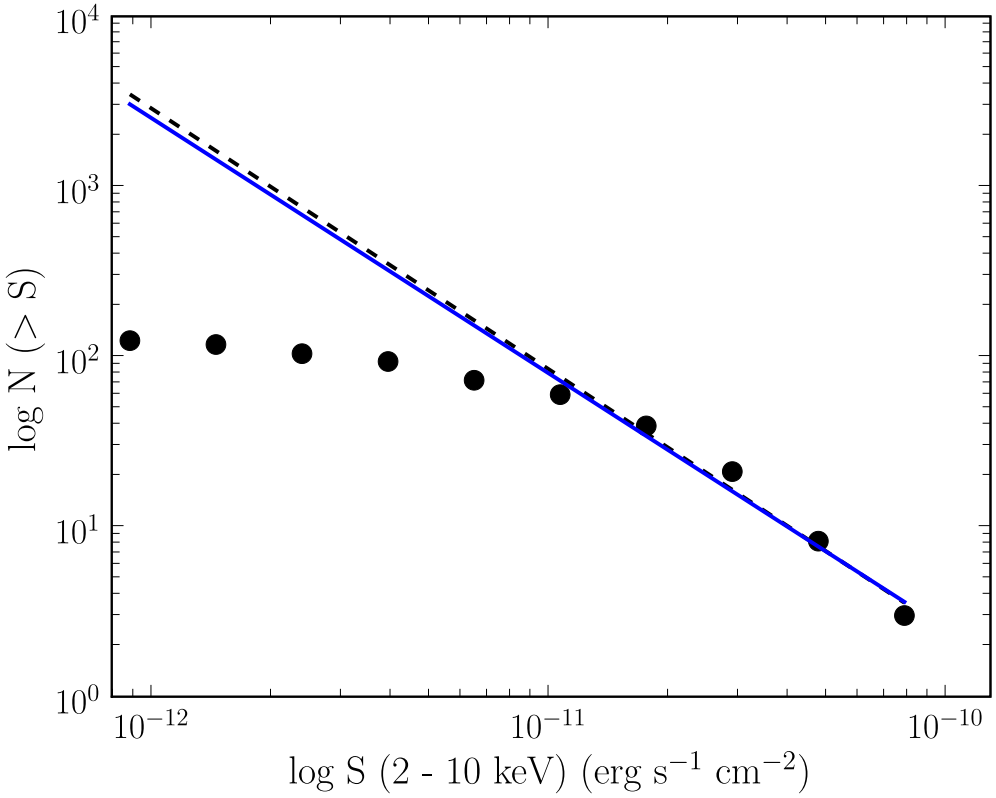

Figure 5.16: Here we plot the relation of $\log N$-$\log S$ for our entire uniform sample ($|b| \geq 15^\circ$ or 74% of the sky). The value $\log N$ corresponds to the number of AGN with 2 – 10 keV fluxes above the indicated $\log S$, corrected for sky coverage using the BAT sky coverage maps and 14–195 keV fluxes. The dashed line represents a fit to the points with $\log S \geq -11$. The slope of this line (-1.53 ± 0.12) is consistent with the cumulative distribution of a uniform density of objects (-1.5, shown as the solid line). This plot further suggests that we are missing many sources at fluxes below $\log S \approx -11$.

(14.93 ± 1.24). Thus, the measured slope of -1.53 ± 0.12 is consistent with the value -1.5 expected for a uniform density of objects. Our normalization, which corresponds to 1.17×10^{-15} (ergs cm^{-2} s^{-1})$^{-1}$ sr^{-1}, agrees very well with the normalization from the 2–10 keV $\log N$-$\log S$ relation of HEAO-1 for AGN ($2.2^{+0.3}_{-0.2} \times 10^{-15}$ (Piccinotti et al. 1982) for AGN).

This shows that above $\approx 1.0 \times 10^{-11}$ erg cm^{-2} s^{-1} (2 – 10 keV) we have a com-

plete sample, consisting of 51 sources. Only 9 of these AGN are Sy 2s while 28 are Sy 1 – 1.2s, showing that the brightest sources correspond mostly to less absorbed sources even in a very hard X-ray selected sample. Re-examining the average spectrum of this complete sample (with $F_{2-10keV} \geq 10^{-11}$erg s^{-1} cm^{-2}), we find that the shape is the same as the larger sample ($\log I(E) = (-0.41 \pm 0.005) \log E + (-13.019 \pm 0.003)$ with $R^2 = 0.973$). Thus, the average spectrum of these bright sources also replicate the measured CXB slope of $\Gamma \approx 1.4$. Of this complete sample, all have measured $N_H < 5 \times 10^{23}$ cm^{-2} and none are Compton-thick. In fact, most of the sources have much lower column densities (only 6 have $N_H \geq 10^{23}$ cm^{-2}). This suggests that there are no local Compton-thick objects with 2–10 keV fluxes above 1.0×10^{-11} erg cm^{-2} s^{-1}.

However, we also find that below this flux threshold we are far from complete. Particularly, towards $\log S = -12$ the plot suggests that we are missing close to 3000 sources. Could some of these missing sources be Compton-thick? From $\log N$-$\log S$ in Tueller et al. (2008), we know that the 9-month BAT AGN survey is complete in the 14 – 195 keV band above 2×10^{-11} erg cm^{-2} s^{-1}. Therefore, the missing sources in our sample must have 14 – 195 keV fluxes below 2×10^{-11} erg cm^{-2} s^{-1} and 2 – 10 keV fluxes from $\approx 1 - 10 \times 10^{-12}$ erg cm^{-2} s^{-1}. Since the ratio of $F_{14-195keV}/F_{2-10keV}$ for the majority of missing sources (near $\log S = -12$) is ≥ 10, it is likely that these sources are heavily absorbed. They may be an extension of the "hidden" AGN with higher column densities ($\log n_H \geq 24$). We can not determine whether or not some of these sources are Compton-thick.

5.6 Host Galaxy Properties

In this section, we present a simple analysis of the host galaxy properties of the uniform sample of BAT-detected AGN. Since the BAT AGN offer the first unbiased AGN sample with respect to absorption ($n_H \leq 10^{24}\,\mathrm{cm}^{-2}$), studying their host properties can provide major insight into the relationship between the AGN and host. This is particularly important since the exact trigger of activity around the black hole is not known.

Since the BAT AGN hosts are located nearby ($< z >= 0.03$), archived images are easily available from the Digital Sky Survey (DSS), Sloan Digital Sky Survey (SDSS), and 2MASS. For our study, we use these data as well as publicly available information from NED. First, we provide a simple comparison of the galaxy major axis/minor axis to the X-ray column density. We then discuss the host galaxy morphology types as well as the fraction in interacting galaxies.

5.6.1 Host Inclination

One of the questions left to be answered about AGNs is the nature of the obscuring material. Likely, there are many different answers to this question, depending on the host. In some cases, the obscuring material may largely be a product of looking through much of the gas and dust in the host galaxy. In such case, we can use the inclination of the host galaxy to determine how much of the obscuration can be simply attributed to the host. To test this, we found measurements of the major axis (a) and minor axis (b) in NED. These data were available for 85/102 sources in our uniform sample.

In Figure 5.17, we plot the ratio of minor to major axes (b/a) versus the X-ray derived column density. From the plot, we find that sources of all types (Sy 1 –

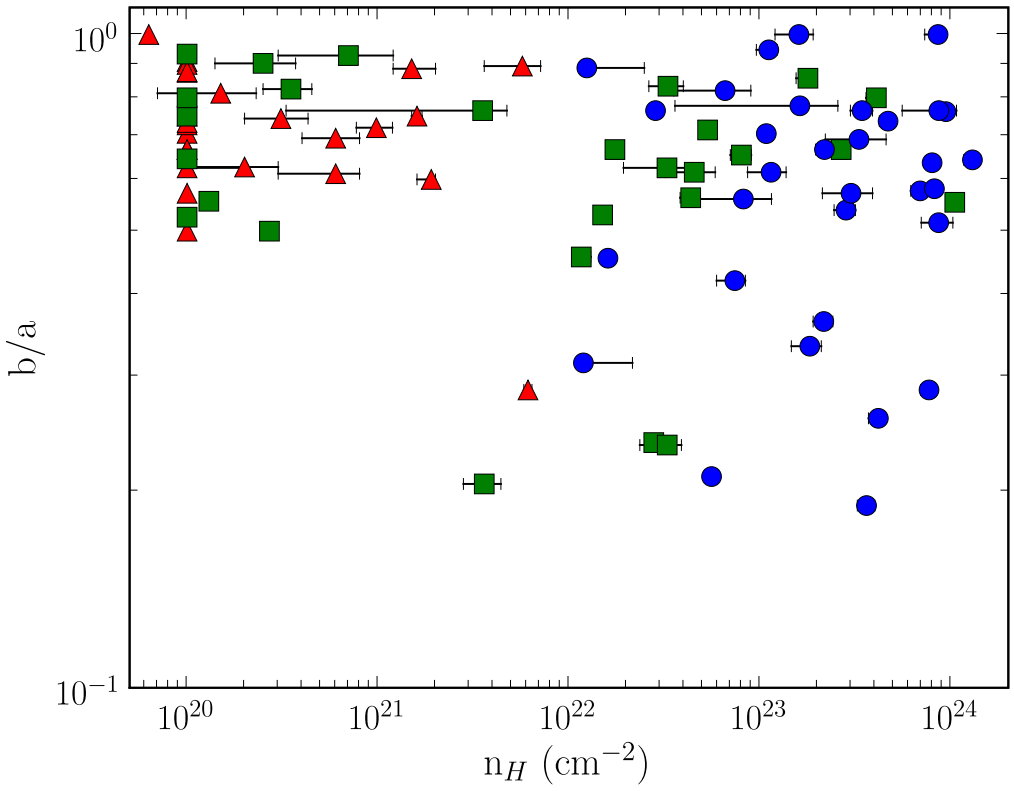

Figure 5.17: We plot the measured host galaxy minor axis/major axis (b/a) from NED versus the X-ray measured column density. As shown, only one Seyfert 1 (IC 4329A, a Sy 1.2) is in a highly inclined galaxy. However, this source has a higher X-ray column than most other Seyfert 1s. The hosts of Seyfert 2s span the entire range of b/a. Note that for sources requiring no additional absorption over the Galactic, we used a standard value of $n_H = 10^{20}\,cm^{-2}$. Here, triangles represent Sy 1–1.2 sources, squares indicate Sy 1.5–1.9 sources, and circles indicate Sy2s.

2) have similar distributions of b/a. We find that a face-on galaxy ($b/a = 1$) could host either a Sy 1 or Sy 2 source. However, the edge-on galaxies ($b/a \leq 0.4$) only host more absorbed AGNs. Among the 11 edge-on sources, only one is associated with a Sy 1. However, while IC 4329A is an optical Sy 1.2, the X-ray column density is high for a Sy 1 ($6 \times 10^{21}\,cm^{-2}$) and the X-ray spectrum is complex. In fact, the XMM-Newton spectrum of this source reveals signatures from 7 differ-

ent absorbing systems (Steenbrugge et al. 2005). We note that Kirhakos & Steiner (1990) found a deficiency of edge-on galaxies in their optically selected AGN sample, which they explained as a lack of obscured sources in the optical survey. Our results support this claim, since the unobscured sources are not associated with edge-on galaxies.

For the edge-on sources, it is possible that much of the X-ray obscuration is from the ISM in the host galaxy. In the Milky Way, we know that the column density looking towards the Galactic Center is a few $\times 10^{22}$ cm^{-2}. Therefore, this can be a plausible explanation for the 6 edge-on sources with X-ray columns below 10^{23} cm^{-2}. For the other 5 sources, however, the columns are simply too large to be attributed solely to the host galaxy.

Excluding the edge-on sources, we find the mean values for b/a as $\mu = 0.74$ and $\sigma = 0.13$ for Sy 1 – 1.2s, $\mu = 0.69$ and $\sigma = 0.14$ for Sy 1.5 – 1.9s, and $\mu = 0.70$ and $\sigma = 0.15$ for Sy 2s. This shows that the distributions are effectively the same, with a difference of only 0.04 in b/a between obscured and unobscured AGNs. Thus, we can not explain differences in obscuration simply through the inclination of the host galaxy for these sources. The fact that we see a range of b/a values causes us to disagree with Rigby et al. (2006), whose data on 9 optically active AGN (AGN showing optical emission lines) at $0.5 \leq z \leq 0.8$ led them to conclude that optically active AGN are only in the most face-on or spheroidal host galaxies. However, they also conclude that optically dull AGN (from a sample of 22 AGN) inhabit a range of b/a ratios, similar to our result for the entire sample. As for optically dull AGN in the 9-month BAT AGN sample, there are only two sources (NGC 612 and NGC 4992), both of which are intermediate between face-on and edge-on with $b/a = 0.64$ and 0.58, respectively.

5.6.2 Host Morphology

For our uniform sample, 74/102 sources had morphologies available from NED or LEDA (listed in Table E.1). For all of these sources, we expressed the morphology as a T-type, following the 2MASS large galaxy atlas (Jarrett et al. 2003) and the de Vaucouleurs method. Here, each morphology is assigned a numerical value (E = -1, S0 = 0, Sa = 1, Sab = 2, ..., Irr/Peculiars = 9.5). In Figure 5.18 (left), we plot the distribution of morphologies. For all of these galaxies, we also looked at the accompanying DSS images as confirmation of the NED classification. Additionally, these images are available for all of the 9-month surveys online at http://swift.gsfc.nasa.gov/docs/swift/results/bs9mon/ (Baumgartner et al. 2008).

From the plot of the distribution of morphologies, we find that our sample includes very few ellipticals ($\approx 8\%$). This is in direct contrast to deeper AGN surveys where the hosts are predominately in elliptical or red hosts. For instance, the $z \approx 1$ X-ray selected sample of Nandra et al. (2007) mostly have red colors consistent with early type galaxies (ellipticals and lenticulars). Meanwhile, our $< z >= 0.03$ sample includes a larger fraction of bluer hosts (spirals and peculiars). This suggests that there may be an evolutionary change in the host properties between local AGN and those at higher redshift. However, the SDSS results show a connection between Seyfert 2s and early type hosts but also young stellar populations at $0.02 < z < 0.3$ (Kauffmann et al. 2003). In order to compare more directly with both the SDSS and X-ray selected samples, we need more robust data including spectra and photometry. Thus, our results, based on NED classifications and DSS images, are preliminary and require higher quality images and photometry (Koss *et al.* in prep) as well as spectra (Winter *et al.* in prep) to

substantiate these findings. Our main goal from our simple analysis is to identify potentially interesting properties for further study.

In the morphology distribution plot, it is clear that a large fraction of the hosts (33%) are irregular/peculiars, with an equal percentage of Sy 1-1.2s, Sy 1.5-1.9s, and Sy2s with peculiar hosts. In some sense, the classification as peculiar in NED can be somewhat subjective. However, we looked through all of the DSS images to confirm the NED classifications. In a study of 256 nearby ($z \leq 0.035$), optically selected galaxies with HST, Malkan et al. (1998) found only $\approx 20\%$ of the hosts "normal" (i.e. axi-symmetric, a bulge with regular elliptical isophotes, a thin, planar disk). This suggests that even more than the 33% identified would fit within this category. In Figure 5.19, we show optical images of four representative cases. Some of these sources are quite famous and have high quality HST images available showing large dust lanes and other disturbances (i.e. Cen A, NGC 1275). In fact, many of these sources appear to be interacting with nearby galaxies (i.e. ESO 490-G026, ESO 511-G030) or are identified as the result of a merger (as for Cen A). More images can be seen at the indicated BAT 9-month survey website.

This leads to the most important result we have found in our analysis of the host galaxies. Namely, that a large fraction of the galaxies are interacting. In Table E.1, we included a note of Int or Int? to indicate sources that we classify as interacting or possibly interacting. Here, we use the term loosely to describe sources which, from the available DSS images, have a nearby companion galaxy or show a heavily distorted morphology, which has previously been identified as the result of a merger in the literature. We supplement the list with sources known to be the product of a merger (like Cen A and Cyg A). In addition to ESO 490-G026, Cen A, and ESO 511-G030, shown in Figure 5.19, more images of

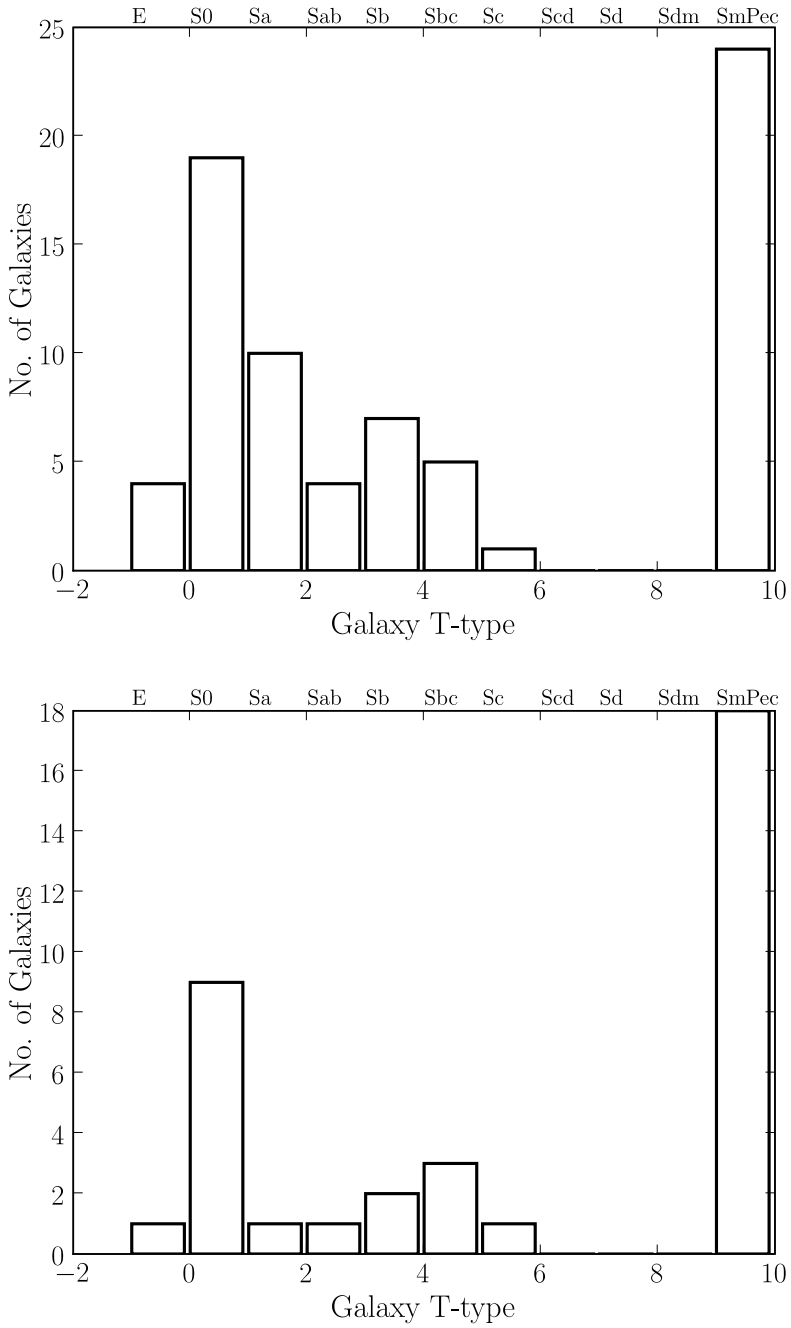

Figure 5.18: We plot the distribution of host galaxy type, from NED, for the uniform sample of BAT-detected AGNs (top). Also, we plot the distribution of host galaxy type for 'interacting' sources in our uniform sample (bottom). Clearly, there is no significant difference in the host type for these sources.

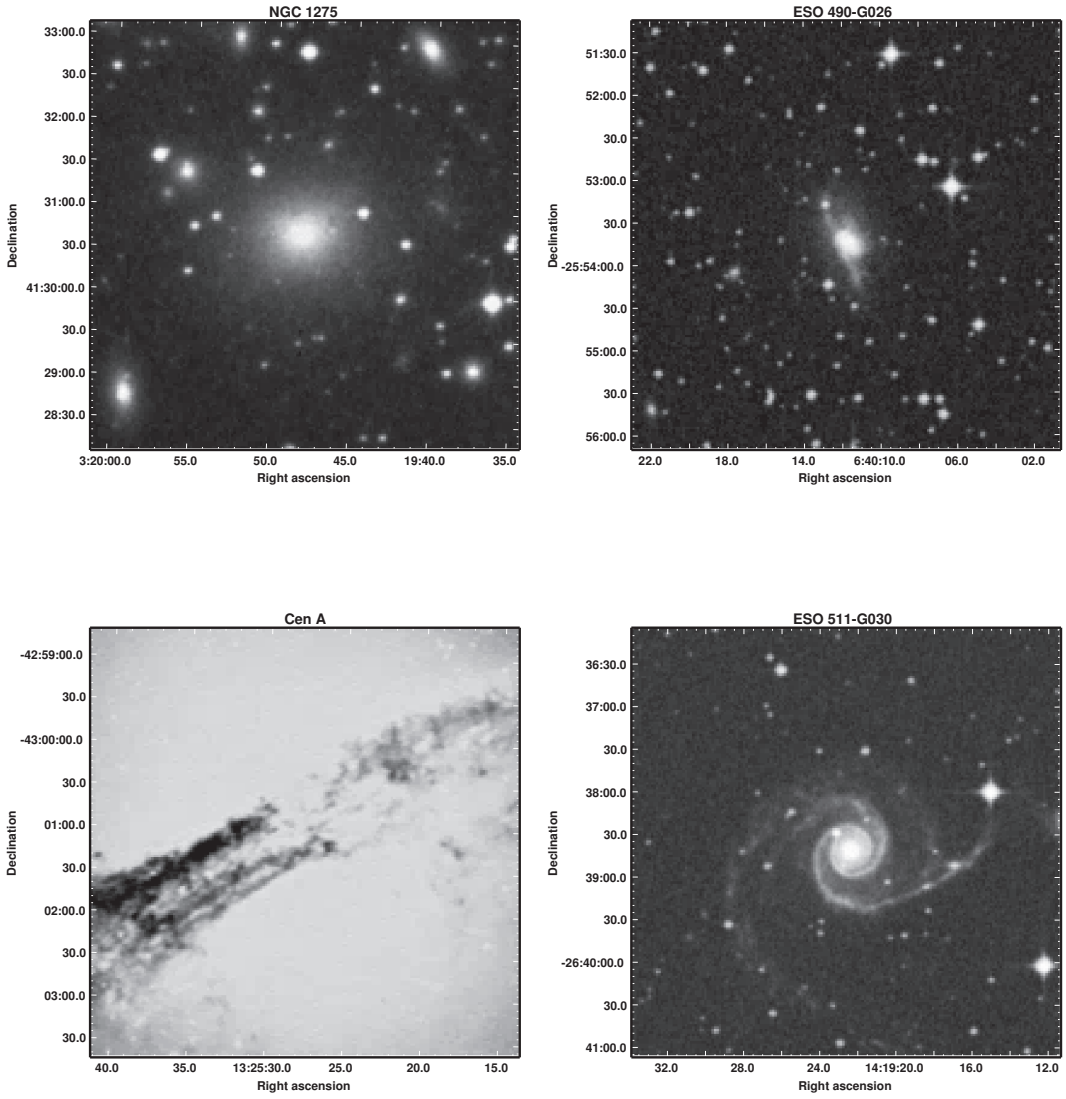

Figure 5.19: We show DSS images of 4 representative peculiar/irregular host galaxies. For all images, we plot a $5' \times 5'$ region. Both NGC 1275 and Cen A have available HST images which reveal in detail large dust lanes. However, even in the lower resolution DSS image, the dust lane in Cen A is clearly visible. Of the other sources, ESO 490-G026 is really two colliding galaxies and ESO 511-G030 is a spiral with a small nearby companion galaxy (outside the image).

interacting hosts are found in Tueller et al. (2008). All six of the sources shown in Figure 8 of that paper are classified as interacting. Additionally, NGC 454, NGC 6240, and NGC 7469 are interacting sources with HST images released in the recent "Cosmic Collisions Galore!" news release. Just from these available images, we account for 28% of the sources classified as interacting. Images of the additional sources are available online at the BAT 9-month survey website.

Of the sources with a known morphology (including those listed as S or S?), we classify 45 sources (54%) as interacting. The distinction between peculiars and interacting sources is somewhat arbitrary, since a merger galaxy would be expected to have a peculiar shape. However, not all of the classified peculiars are also classified as interacting, though a large fraction are (66%). If interactions cause disruptions to the galaxy, thereby making it peculiar, the percentage of interacting galaxies is even higher – including all of the peculiars. It is also important to note that not all interacting galaxies are peculiar. The distinction for these sources may be due to a companion that is much smaller than the AGN host or at a greater distance.

The important thing to note is that a large fraction of local AGN have companion galaxies or are the result of a merger (54%). This is significant considering that 12-33% of optically selected Seyferts (Rafanelli et al. 1995) and 15% of more distant X-ray selected AGN ($0.2 \leq z \leq 1.2$) (Pierce et al. 2007) are hosted in an interacting galaxy. It is possible that our high percentage of interacting galaxies indicates an evolutionary difference in AGN hosts. Another possibility is that our value is higher simply because we can see smaller companions at low redshift. Thus, the sources at $z \geq 0.1$ may have the same number of companions or merger galaxies like Cen A and Cyg A but the available images may not be of sufficient quality to distinguish this.

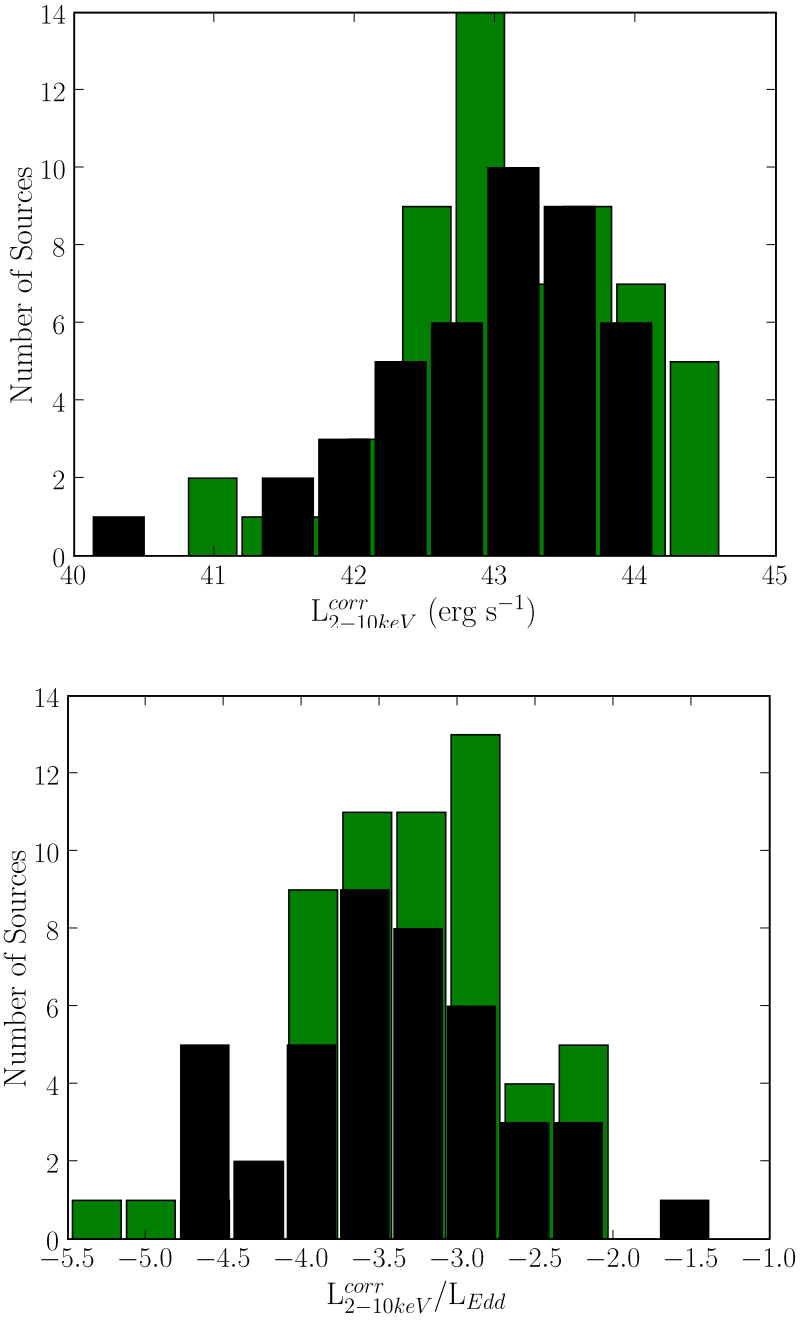

Figure 5.20: Here we plot the distributions of unabsorbed 2–10 keV luminosity and our Eddington ratio proxy for interacting (black) and non-interacting (green) systems. There is little difference between the two distributions, showing that AGN in galaxies with a close companion or which underwent a recent merger have the same luminosities and accretion rates as AGN in non-interacting galaxies.

Since such a large percentage of hosts are interacting, we wanted to test whether the distribution of luminosities and Eddington ratios were the same or different between AGN with interacting and non-interacting hosts. In Figure 5.20, we plot the results. We find no difference in the AGN unabsorbed 2–10 keV luminosity or the Eddington rate proxy ($L^{corr}_{2-10keV}/L_{Edd}$) between the two distributions. For interacting systems, $\mu = 42.97$ and $\sigma = 0.80$ for $\log L^{corr}_{2-10keV}$ while $\mu = -3.38$ and $\sigma = 0.76$ for $L^{corr}_{2-10keV}/L_{Edd}$. The non-interacting systems have a very similar distribution, with $\mu = 43.12$ and $\sigma = 0.81$ for $\log L^{corr}_{2-10keV}$ and $\mu = -3.29$ and $\sigma = 0.70$ for $L^{corr}_{2-10keV}/L_{Edd}$. Using the Kolmogorov-Smirnov test, the P values (0.65 for luminosity and 0.91 for Eddington ratio) are not small and therefore do not suggest a difference between the distributions.

Further, when we examine the morphologies of the interacting host galaxies, we find that they follow the same distribution as the larger sample (Figure 5.18 (bottom)). When we look at the distribution of optical Seyfert type within interacting galaxies, we find no preference for absorbed (Sy 2) systems. Broken down by optical type, 14 correspond to Sy 1 – 1.2, 13 in Sy 1.5 – 1.9, and 13 in Sy 2 sources. This is similar to the results of Rafanelli et al. (1995), who also found no difference in the percentage of interacting sources between Sy 1s and Sy 2s. However, this is somewhat confusing since we would expect optically-selected samples to find less of the interacting Sy 2s due to heavy absorption. Since the morphologies are a nearly even mix of Sy 1 – Sy 2 sources, it is not surprising that the mean 2–10 keV luminosities and Eddington ratio proxies are intermediate between the Sy 1 and Sy 2 values quoted in § 5.4.3 (for both interacting and non-interacting hosts).

Based on simple analyses of publicly available data on the host galaxies, we have found a few interesting results. We have found that the host inclination (ap-

proximated by b/a) does have an effect on the amount of obscuration we see in the X-ray band, but that the effect is slight. In particular, there are no unabsorbed sources hosted in an edge-on galaxy. However, there are heavily obscured AGN in face-on galaxies. This shows that for the bulk of the obscuring medium, the origin is most likely more local to the accreting black hole. This is further supported by HST observations of nearby AGN, which find Sy2s to be more likely to have dust lanes or irregular or disturbed dust absorption through the galactic nucleus (Malkan et al. 1998).

Also, we found that many of the hosts are in spirals and pecular/irregular galaxies. We find very few (5/74) in ellipticals, contrasting with the results of Nandra et al. (2007) who find red hosts for the majority of $z \approx 1$, X-ray selected AGN. This suggests an evolutionary change in AGN host properties, from red at $z \approx 1$ to blue at $z \approx 0.03$. However, high quality photometry is necessary to make a direct comparison with Nandra et al. (2007).

More than half of our sample is associated with a close companion or recent/ongoing merger. We find that Sy 1 and Sy 2 sources are equally likely to be hosted in interacting galaxies. Considering that optical surveys at similar redshift found between 12-33% (Rafanelli et al. 1995), it is tempting to attribute the difference to selection effect, i.e. the heavily obscured sources missed in the optical. However, we find that the hosts of the interacting systems are not dominated by absorbed sources.

We also find that the distribution of host morphologies are the same between interacting/non-interacting hosts. Further, the distributions of $\mathrm{L}_{2-10keV}^{corr}$ and $L_{2-10keV}^{corr}/L_{Edd}$ are also the same. Though, the reason for the similar distributions is unclear. Likely, mergers are not the sole trigger for our sample. The next step in understanding the differences between the interacting and non-

interacting systems is an in-depth source by source look at the local environments, with particular attention to star-formation and dust. This, however, is beyond the scope of this thesis.

5.7 Summary

In this chapter, we present the X-ray properties of a uniform sample of very hard X-ray (14 – 195 keV) selected AGN. We present a number of interesting results that highlight the many uses of an unbiased very hard X-ray survey. This study is complimentary to the 9-month AGN survey paper (Tueller et al. 2008), which presents the 14–195 keV properties of the sources. Additionally, this work confirms the results of our earlier study on *XMM-Newton* observations of a representative sample of the BAT AGN (Chapter 4). Among these, we show that: (1) the X-ray and optical classifications agree, i.e. Sy 1s have low X-ray column densities while Sy 2s are more obscured, (2) the average power law index, $\Gamma \approx 1.8$, agrees with the results from HEAO-1 (Mushotzky 1982), (3) "hidden" AGN are a significant fraction of local AGN, where we can now quantify this value as $\approx 24\%$, and (4) nearly half (45%) of local AGN are well-fit by a simple model (all with $\log n_H < 23$) while the remaining sources (55%) require a more complex model. In addition, this chapter presents a number of additional, important results.

Some of the most interesting results of the BAT AGN sample involve the nature of the host galaxy. From examining the host galaxy properties, we found that the majority of the X-ray obscuration is not simply from the host galaxy (by comparing host inclination (b/a) to X-ray column density). The most surprising results, however, were that many of the host galaxies are peculiar/irregular galaxies (33%). Further, an even larger fraction (54%) have either a close compan-

ion galaxy or are known mergers. This is observational proof that galaxy interactions may be driving activity in local supermassive black holes. However, we also find that the distribution of AGN 2–10 keV luminosities and accretion rates, as well as morphologies, are the same between interacting and non-interacting hosts. While, it is unclear what these results mean, however, there appears to be more than one trigger besides mergers for local AGN activity.

From our uniform sample (102 sources with $|b| \geq 15^{\circ}$), we found that the distributions of both unabsorbed 2 – 10 keV luminosity and accretion rate are significantly lower for Sy 2s than Sy 1s. While earlier studies found this connection in 2 – 10 keV luminosity (Steffen et al. 2003; Ueda et al. 2003), this is the first time it has been reported in accretion rate. We also showed that the fraction of obscured AGN is indeed larger for lower luminosities (absorption corrected $L^{corr}_{2-10keV}$) and accretion rates. However, we note that the most heavily obscured sources ($\log n_H \geq 23$) do not dominate this relationship. Since the unified model predicts differences between absorbed and unabsorbed sources are a product of viewing angle alone, our results provide a challenge, arguing in favor of a luminosity-dependent AGN model.

Another result involves the correlation between accretion rate and Γ. In Chapter 4, we had found indication of a connection between Eddington ratio (or 2 – 10 keV luminosity) and Γ using the spectral fits of multiple observations for individual sources. The fact that we did not observe a correlation in our larger sample seems to be a result of our sources having a larger range of Eddington ratios (or 2 – 10 keV luminosities). We suggest that previous studies, for instance by Shemmer et al. 2006, see this correlation because their samples have a narrower range of properties (being mid- to high luminosity AGNs). The primary correlation appears to be with accretion rate and not hard band luminosity. Such a correlation

should appear when comparing Γ to $L^{corr}_{2-10keV}/L_{Edd}$ for multiple observations of individual sources or for a sample of sources with a narrow range of accretion rates.

In a similar manner, we found that while our sample did not immediately confirm the X-ray Baldwin effect, binning the sources by luminosity, we were able to reproduce the anti-correlation between unabsorbed 2 – 10 keV luminosity and Fe K EW. The primary anti-correlation, however, again appears to be with Eddington rate. When we binned the values by our Eddington ratio proxy, we found that $EW \propto {L^{corr}_{2-10keV}/L_{Edd}}^{-0.26\pm0.03}$ (agreeing with the results of Bianchi et al. (2007)). Since both Γ and Fe K EW are dependent on accretion rate, this suggests that the Γ-EW correlation found by Mattson et al. (2007) is a result of the accretion rate dependences.

Having classified the X-ray spectra of our sample into simple and complex categories, we were able to examine the properties of the two sub-samples in more detail. For the simple model sources, we found that 41% of the sources exhibited a soft excess. Having modeled this parameter with a simple blackbody model, we found the average temperature to be $kT = 0.10$ keV. We also found that there was a significant amount of scatter in this value ($\sigma = 0.07$ keV), contrasting with the Gierliński & Done (2004) results for PG quasars. We found no correlation between the blackbody temperature and Eddington ratio, black hole mass, or photon index. However, we did find a correlation between the luminosity of the blackbody component and the luminosity in the power law. This relationship is linear ($L_{pow} \propto L_{kT}$) and may provide a challenge to the current soft excess models.

Examining the complex model sources, we found that the majority of these sources included absorbed AGN. Of the 4 Sy 1s in this category, all have complex

absorption features in their X-ray spectra. For these sources, we showed that the nature of the soft emission ($L_{0.5-2keV}$) for these sources is unclear. Over half have soft band luminosities low enough to be the result of galactic emission from star formation/X-ray binaries. However, of the sources with higher soft luminosities, 3 are "hidden"/buried AGN. This argues that the soft emission may be scattered AGN emission.

An important result we found is that the "hidden"/buried AGN, sources with a high covering fraction, are a significant fraction of local AGN. Among the complex sources, 45% are "hidden". For these sources, we found that the FIR luminosity is not consistent with an increased star formation rate, as suggested by Ueda et al. (2007). However, without higher quality X-ray spectra and multi-wavelength observations, we are unable to further explore the nature of these sources.

While BAT is quite good at finding heavily obscured sources, we found that none of the 9 month sources in our uniform sample have spectra consistent with heavily obscured Compton-thick objects ($n_H > 1.4 \times 10^{24}\,\mathrm{cm}^{-2}$). However, we do detect sources classified as Compton-thick in other studies based on a reflection dominated spectrum or strong Fe K EW (for instance 3C 452 and NGC 4945). Additionally, we did not include an analysis of the very complex source NGC 6240, which may also be classified as Compton thick. Since the Compton hump lies above 10 keV, spectral fits with and without reflection can be degenerate in the 0.1–10 keV band. Therefore, a full analysis of the Compton thick nature of the BAT sources must be deferred to future studies.

One remarkable result we found came from the average spectrum we constructed in the 0.1–10 keV band with the measured spectral properties of our uniform sample. Here, our data reproduce the measured slope of the CXB (≈ 1.4).

This highlights the importance of the BAT survey in selecting heavily absorbed sources. More importantly, this is observational proof that the combination of BAT-detected absorbed and unabsorbed local AGN replicate the shape of the CXB. If the distribution of source properties at $z \approx 1$, where much of the CXB originates, is the same as that of the BAT-detected AGN, the spectral paradox is resolved.

To test our completeness in the 2–10 keV band, we plotted the distribution of $\log N$-$\log S$ for the entire uniform sample. This showed that while the sample is complete in the 14–195 keV band (Tueller et al. 2008), we are only complete above $\log S = -11$ in the 2–10 keV band. Further, this distribution suggests that we are missing as many as 3000 sources at $\log S = -12$, requiring that these sources have 14–195 keV fluxes below the current flux limit of the BAT survey. Possibly these sources are "hidden" AGN with even higher X-ray columns ($\log n_H \geq 24$). Such sources must have a high ratio of $F_{2-10keV}/F_{14-195keV}$, like NGC 1068. Also, they may or may not contain Compton-thick sources, an answer to which our data can not supply. These results, in addition to the X-ray properties (including column densities and spectral indices) will provide important input for CXB models at low redshift ($z \approx 0$).

Chapter 6

Conclusions

In this dissertation, we have presented the results of X-ray surveys of accreting black holes external to our Galaxy. For both the ULXs and AGN, possible intermediate mass and super massive black holes, a great amount of energy is output at these high energies. Further, the photons are energetic enough to penetrate much of the gas and dust, which might otherwise hide the underlying black hole.

To understand the spectra of both ULXs and AGN, we employed a technique of fitting the source spectra with simple schematic models (i.e., a black body model, a power law model, absorption models, a gaussian line). It was important to use such models for a few reasons. First, the true physical model for these sources is not known. Therefore, any model that is used is an approximation on some level. Further, in many cases it is not possible to tell which model is the best fit to the data and the fits are often degenerate. For instance, we highlight this degeneracy when discussing various disk models applied to ULXs in Chapter 3 as well as in our discussion of the partial covering model versus double power law and reflection models in Chapter 4. With so many uncertainties in the "true models", it becomes necessary to choose some base model which can be applied to a large class of sources and be used as a comparison between the spec-

tra. Finally, since the data sample is not uniform (i.e. sources were observed with different instruments and/or for different exposure times), use of a base simple model allows for an easier comparison.

As presented in Chapters 2–5, a wealth of information can be obtained using these simple model analyses. In this chapter, we will detail the highlights of these surveys including a discussion of our contribution and future directions. In order to better facilitate the discussion, ULXs are discussed in § 6.1 and the BAT AGN Survey is discussed in § 6.2.

6.1 ULX Studies

6.1.1 Conclusions

The study of ULXs is a relatively new endeavor. As such, the breadth of research on these sources is not as extensive as the 40+ year history of AGN. When we began our survey in the summer of 2004, a few ULX surveys had been completed with ROSAT (Colbert & Ptak 2002; Liu & Bregman 2005; Ptak & Colbert 2004) and Chandra (Swartz et al. 2004). With Chandra, there is less of an issue of source confusion because of the superior sub-arcsecond angular resolution. These studies were aimed primarily at finding ULXs in galaxies. However, in order to conduct a comprehensive spectral survey, higher spectral resolution was needed.

Following upon the work of Miller et al. (2003), who found the disk temperatures of two ULXs consistent with intermediate mass black holes (IMBHs), our study sought to test another IMBH prediction. Namely, we used the superior spectral sensitivity of *XMM-Newton* to look for source spectra consistent with low/hard and high/soft state spectra; analogous to Galactic black hole systems.

As presented in Chapter 2, we did find sources consistent with low (16) and high state (26) ULXs. We also found a population of sources who were consistent with stellar mass black holes. Since a study of this kind had never before been conducted, our results are significant and provide further support of at least some of the ULXs as accreting IMBHs. In addition to providing a catalog of ULXs and the X-ray properties of ≈ 80 sources, we also provided other information useful to the community like the ratio of optical to X-ray flux for ULXs and the distribution of column densities and host galaxy star formation rates.

In Chapter 3, we presented the result of a more in-depth look at the highest quality *XMM-Newton* ULX spectra. We found, as in Chapter 2, that some ULXs have spectra consistent with IMBHs and others with stellar mass black holes at high accretion rates. We also found that we can use ULX spectra to probe the ISM of their host galaxies. The column densities of the ULXs were largely in agreement with H I studies, showing that only the M81 ULX required additional absorption more local to the source. Further, we found that all of the ULXs appeared to be in areas of roughly solar oxygen and iron abundances.

Recent work on ULXs appears to be centered along two tracks. The first involves applying different theoretical models (particularly disk or Comptonization models) to the ULX X-ray spectra, producing claims of sources having spectra consistent with either stellar mass black holes or IMBHs. The progress along this line appears to be hindered by the lack of higher quality spectra. Therefore, since many models can be used to fit the spectra without a clear statistical preference, it appears that further progress requires higher quality data. The second tract of ULX studies centers primarily on optical follow-ups of the sources. The studies involve either looking for a clear optical counterpart (i.e. the companion star) or the study of ionization nebulae. For a few ULXs, the discovery of a sur-

rounding ionization nebula has provided an exciting line of research and further support of the IMBH hypothesis. Still, the holy grail of ULX studies – observing an eclipsing ULX system and measuring the stellar mass function – continues to elude researchers.

6.1.2 Future Work

There are many unanswered questions involving ULXs. While it is clear that some sources are likely IMBHs, based on their X-ray spectra and the existence of ionization nebulae, we still do not know how IMBHs form. Further, how many ULXs are IMBHs versus stellar mass black holes and why/how long do they accrete matter at this rate? If the ULXs are associated with high galactic star formation rates, why are they not found in all star forming regions? Some future projects that may help to answer some of these questions are:

- *Studies of the local environments.* Particularly, a study aimed at obtaining local star formation rates for a large sample of ULXs, would provide valuable information on the local environments of ULXs. In Figure 2.10, we showed that galaxies with the most ULXs also have the highest far infrared luminosities (an indicator of star formation rate). However, we also found galaxies in our sample with high L_{FIR} and no ULXs. Further, we found ULXs in irregular galaxies with low L_{FIR}. Currently, we are involved in a project classifying ULXs as near/outside/inside H II regions based on *XMM-Newton* OM images (Berghea, Mushotzky, Weaver, Winter, in prep.). However, ground-based studies measuring SFR indicators in the IR at the ULX position and throughout the host galaxy would give direct information on whether or not ULXs are associated with heavy star formation. Further, with this information we could separate the various types of ULXs (stel-

lar mass and probable IMBHs) looking for any differences between the two sub-classes.

- *Absorbed ULXs?* From SWIFT and Integral, we know that there are a large number of obscured AGN. Integral is now finding a class of obscured Galactic X-ray binaries (Chaty 2008), which SWIFT will likely also detect. From our work and that of other authors, AGN studies are showing that there is likely a physical mechanism related to luminosity which creates the differences between obscured and unobscured sources. Assuming that there is a luminosity difference between obscured and unobscured IMBHs, we can look for obscured ULXs in really long XMM-Newton exposures. This would be yet another piece of evidence in favor of IMBHs. However, it may be difficult to tell whether the sources are IMBHs, stellar mass black holes, or background AGN.

6.2 SWIFT BAT-detected AGN Survey

6.2.1 Conclusions

As described in § 4.1, the BAT AGN survey is important because it is not affected by the selection effects plaguing other bands. Also, it is the first sensitive all-sky survey at 14–195 keV. With a larger field of view, it detects many more sources than Integral in a given amount of time. Therefore, with the continued lifetime of the SWIFT mission the potential for more complete studies of local AGN increases with $\sqrt{t}$.

In Chapter 4, we presented *XMM-Newton* follow-ups of 22 BAT sources from the 9-month catalog. As shown in Chapter 5, these sources are a representative

sample of the catalog. The statistical spectroscopic properties of the entire sample are presented in Chapter 5. However, Chapter 4, in addition to providing a first-look at the BAT AGN, provides a timing analysis of the *XMM-Newton* and SWIFT XRT spectra (on hour to month time scales).

From our AGN study, we have unveiled a number of interesting discoveries. Among these, we have quantified the fraction of "hidden" or buried AGN. This class had just recently been discovered through Suzaku follow-ups of SWIFT BAT-detected sources (Ueda et al. 2007). From our survey, we found that $\approx 20\%$ of our uniform sample had properties consistent with this class (i.e. a small fraction of scattered emission/direct emission). This shows that a significant fraction of local AGNs are only now being considered as a part of the general AGN zoo.

When we added the properties of these hidden sources, along with the unabsorbed and other absorbed sources, we reproduced the shape of the cosmic X-ray background ($\Gamma \approx 1.4$) (Marshall et al. 1980). This is quite remarkable since never before were there AGN X-ray observations which reproduced the CXB. However, the bulk of the CXB is believed to be produced in the $z \approx 1$ universe. Therefore, provided the spectral properties of our low redshift sources match the higher redshift sources, the CXB is resolved below ≈ 10 keV.

At higher energies, reflection becomes more important making it necessary to obtain high quality X-ray spectra above 10 keV. We have found this to be challenging for the fainter sources. While we have BAT spectra for all of the sources, the spectra currently available are 8 channel spectra and therefore difficult to use to constrain reflection. Further, the response files were constructed using the Crab spectrum as a basis (with a slope of ≈ 2), introducing error for spectra which deviate from this shape. Suzaku allows for simultaneous observations in the $\approx 0.2 - 600$ keV band, however, we find that the spectra of our faint sources

are only $\approx$ 2–3% above the PIN background level, yielding poor quality spectra. New background models have just been released, which will hopefully improve the signal of the high energy spectra.

Another important result which we have presented is that the fraction of obscured sources is larger at both low luminosity and low accretion rate. Other X-ray surveys had noted this effect in luminosity (Barger et al. 2005; Steffen et al. 2003; Ueda et al. 2003), but this is the first time the effect was also seen in accretion rate. This result strongly argues for a modification of the unified AGN model to include a dependence on luminosity/accretion rate. A physical explanation may include a luminosity dependent opening angle to the torus due to radiation pressure or a wind from the disk blowing matter away.

Since the BAT-detected AGN are mostly nearby sources ($z \approx 0.03$), they are close enough that we can study their host galaxy properties in detail. Using publicly available data, we found that many of the sources were hosted in peculiar galaxies (33%). Many, but not all, of these galaxies were classified as interacting systems. In total, 54% of the hosts had nearby companions or were classified as merger galaxies. This suggests that galaxy interactions are an important source of fuel for local AGNs. Since the host galaxies appear to be bluer than higher redshift AGN hosts, at $z \approx 1$ hosts are primarily red or ellipticals (Nandra et al. 2007), this suggests an evolutionary change in the hosts of AGNs.

The most distant AGN ($z >> 1$) are intensely powerful X-ray sources. These are believed to be fueled by large scale galaxy mergers – mergers between galaxies of roughly equal size – which not only fuel the central AGN, but also fuel a phase of active star formation (Di Matteo et al. 2005). Following this stage, the star formation is quenched by a wind from the AGN. With much of the AGN's fuel blown away, the accretion rate and luminosity lessens. Nandra et al. (2007)

find that their results of red/elliptical hosts at $z \approx 1$ are consistent with this stage of quenched star formation. Our results from the BAT-detected AGN suggest another step in this evolution. In this phase, smaller scale interactions and perhaps other as yet unknown triggers begin a new stage of star formation and AGN activity.

6.2.2 Future Work

The results of our study of the SWIFT BAT-detected AGN show that there is much to learn from an unbiased AGN survey. Further, they present direction towards a number of areas the BAT survey can present new understanding. For instance:

- *Optical Spectra of the BAT AGN.* Now that we have compiled the complete X-ray properties of the BAT AGN sample, an important next step is to compile the optical properties and make comparisons between the two bands. This is particularly important for the sources which were not previously found in the optical, the "hidden"/buried AGN. Towards this end, I had obtained (with Dr. Karen Lewis) optical spectra with the 2.1-m telescope at Kitt Peak Observatory for ≈ 40 sources (AGN and template galaxies). Additionally, ≈ 30 more BAT AGN have publicly available spectra from the Sloan Digital Sky Survey. The aim of this study will be subtracting the host galaxy from the AGN light to measure the prominent emission features. With the AGN lines, we will make diagnostic plots, estimate the amount of obscuration, and compare optical and X-ray properties (i.e. compare the H-β line to the X-ray slope).

- *Optical Photometry of the BAT AGN.* Based on our observations that the BAT AGN hosts are comprised of many spirals, peculiars, and interacting sys-

tems (Chapter 5), we are obtaining optical images of the 9-month sources (Koss et al., in prep). With this work, we will be able to quantify the claims in Chapter 5 for a uniform sample. One major part will be obtaining colors with which we can compare the BAT AGN hosts with those from SDSS (Kauffmann et al. 2003) and the AEGIS X-ray sample at $z \approx 1$ (Nandra et al. 2007; Pierce et al. 2007). This will tell us how the BAT hosts compare to optically selected and hard X-ray selected (2–10 keV) samples. We will be able to determine if there are differences between the hosts of obscured and unobscured sources and whether there is an evolutionary change between the hosts at higher redshifts (the X-ray sample) and our own low redshift sample.

Another interesting result will be quantifying the size and location of companion sources in our effort to understand the interacting nature of the host galaxies. From this, we can find if there is a difference in the type of interaction between obscured and unobscured sources. We will also find whether interactions are primarily between galaxies of similar size or a large host and small companion galaxy.

- *Multi-wavelength Observations.* As mentioned in Chapter 5, many more investigations are currently underway to unveil the properties of the BAT AGN. A Spitzer proposal has been approved for IR spectroscopy of many of our sources (led by Dr. Weaver). An HST proposal has been submitted for optical and IR imaging (PI, Dr. Weaver). Additionally, radio observations are also underway and a VLA proposal is in preparation (PI, Dr. Ulvestad). Further, optical polarimetry observations have been proposed for the hidden AGN sources (PI, Dr. Gandhi). Understanding these local AGN will require data from all available sources. However, with these observations,

we can test whether the findings of other AGN surveys are consistent with the properties of the BAT AGN. Since the BAT AGN are less biased towards obscuration, we hope that their properties will reveal the true properties of local AGN.

- *Interesting Sources.* In the BAT AGN survey, a number of new and interesting sources have been discovered. In Chapter 4, we mentioned two sources which had unusual spectra, NGC 6860 and ESO 362-G018. NGC 6860 had a complex spectrum which was flat both above and below 2 keV. We believe that this complex shape is due to complex absorption features. For ESO 362-G018, the prominent Fe K line seen in the *XMM-Newton* spectrum appeared to disappear in the much brighter XRT spectra. Such sources, and others like them, are excellent targets for higher signal-to-noise observations. In fact, for NGC 6860, we were approved for a 130 ks *XMM-Newton* spectrum to further investigate the spectrum with both RGS and EPIC.

Appendix A

Glossary

A.1 Abbreviations

2MASS: Two-micron all sky survey
A_V**:** total extinction in the optical V band
ASCA: the Advanced Satellite for Cosmology and Astrophysics, a Japanese X-ray satellite launched in 1993
AGN: active galactic nuclei
BAT: Burst Alert Telescope onboard SWIFT, sensitive in the 14–195 keV band
CCD: charge coupled device
CXB: cosmic X-ray background
Dec: declination
dof: degrees of freedom
E: energy; measured in keV for the X-ray band
E_{B-V}**:** selective extinction between the optical B and V bands ($A_B - A_V$)
EPIC: European photon-imaging camera; instrument onboard *XMM-Newton*
ESA: European Space Agency
F: flux; measured in ergs s^{-1} cm^{-2}
FITS: Flexible Image Transport System; standard astronomical data format endorsed by NASA and the IAU
FWHM: full-width half maximum
H I: neutral hydrogen; observed in the radio through the 21-cm emission feature
HEASARC: NASA's High Energy Astrophysics Science Archive Research Center
HST: Hubble Space Telescope
IMBH: intermediate mass black hole
IR: infrared
ISM: interstellar medium; the gas and dust between stars
kT: measurement of the accretion disk temperature in units of energy; the Boltzmann constant times the accretion disk temperature
L: luminosity; measured in ergs s^{-1}
$\mathbf{L}_{Edd}$**:** Eddington luminosity
M: mass
$\dot{M}$**:** mass accretion rate

MCD: multi-component disk; an accretion disk model consisting of black body emission from different temperature regions in the disk
MOS: type of CCD used on *XMM-Newton*
NASA: National Aeronautics and Space Administration
NED: NASA/IPAC Extragalactic Database
$\mathbf{n}_H$**:** column density of neutral hydrogen; measured in atoms cm^{-2}
OM: Optical monitor; optical/UV telescope onboard *XMM-Newton*
pn: type of CCD used on *XMM-Newton*
PSF: point spread function
QSO: Quasi-stellar object; designation for a type of AGN
RA: right ascension
RGS: Reflection grating spectrometer; detectors onboard *XMM-Newton*
SAS: Science Analysis System; data analysis software for *XMM-Newton*
SFR: star formation rate
Sy: Seyfert type; an optical classification scheme for AGN
- **Sy1:** shows optical broad emission lines and narrow emission lines
- **Sy1.5:** intermediary between a Sy1 and Sy2 source
- **Sy2:** shows only narrow optical emission lines

ULX: ultra-luminous X-ray source
UV: ultra violet
UVOT: Ultraviolet/optical telescope; onboard SWIFT
VLA: Very Large Array; an array of radio telescopes located near Socorro, NM
WHISP: Westerbork observations of neutral Hydrogen in Irregular and SPiral galaxies
XMM: X-ray Multi-mirror Mission
XRT: X-ray telescope; onboard SWIFT
XSPEC: A data analysis and spectral fitting program used in X-ray astronomy
z: redshift

A.2 Symbols

χ^2**:** a statistic used to compute goodness of fit for a model
η**:** efficiency factor for mass to energy conversion
Γ**:** photon spectral index measured from a power law model
μ**:** mean/average value
ν**:** degrees of freedom
σ**:** signal to noise; alternatively, the measured error/standard deviation or a cross section
τ**:** optical depth

A.3 Units

Å: Angstrom; a unit of length
: $1\mathring{\text{A}} = 10^{-10}$ m

Crab: a unit of intensity corresponding to the flux density of a bright X-ray source, the Crab nebula
: 1 Crab = 1060μJ
: 1 Crab = 2.5652×10^{-9}erg s^{-1} cm^{-2} keV^{-1}

erg: a unit of energy
: 1 erg = 10^{-7} J

eV: electron volt, a unit of energy
: 1 eV = $1.60217653(14) \times 10^{-19}$ J

Jy: Jansky; a unit of flux density
: 1 Jy = 10^{-23}erg s^{-1} cm^{-2} Hz^{-1}
: 1 Jy = 2.42×10^{-18}erg s^{-1} cm^{-2} keV^{-1}

$M_\odot$: solar mass
: $1M_\odot = 1.9891 \times 10^{30}$ kg

Mpc: Mega parsec; a unit of distance
: 1 Mpc = $3.08568025 \times 10^{24}$ cm or $1.91735281 \times 10^{19}$ miles

sr: steradian; SI unit of solid angle

A.4 Constants

c: speed of light in a vacuum; 2.99792458×10^8 m s^{-1}

G: Gravitational constant; $G = 6.67300 \times 10^{-11}$ m^3 kg^{-1} s^{-2}

H_0: Hubble's constant; we adopt $H_0 = 75$ km s^{-1} Mpc^{-1}

h: Planck's constant; $h = 6.626068 \times 10^{-34}$ m^2 kg s^{-1}

k: Boltzmann's constant; $8.617343(15) \times 10^{-5}$ eV K^{-1}

σ_T: Thomson cross section; 6.652×10^{25} cm^{-2}

Appendix B

Appendix to Chapter 2

B.1 Spectral Simulations

B.1.1 Two-component Model

In order to determine the number of counts required to distinguish whether a blackbody component is statistically significant for the sources fit with a two-component model, we simulated spectra based on that of some of the brightest sources. We chose to simulate spectra of bright two-component spectra exhibiting three different cases: (1) the flux from the blackbody dominates over the power law component at 2 kT, (2) an intermediary case, and (3) the flux from the power law dominates over the blackbody component at 2 kT . Such simulations would allow us to determine the uncertainty in our claims of a combined fit being a better descriptor of the data. This is necessary because there is no a priori model which predicts the relative intensities of the two components and, as we know from studies of Galactic black holes, these components show a wide variety of relative intensities. To this end, we simulated spectra using the best-fit absorbed blackbody and power

law model with the `fakeit` command in XSPEC. We chose (1) NGC 247 XMM1, (2) NGC 5408 XMM1, and (3) Holmberg II XMM1 as our seed observations. These objects all have very high signal-to-noise and thus the fits are robust. The respective ratios of powerlaw flux to blackbody flux contributions at 2 kT are: (1) $<< 1.0$, (2) 1.77, and (3) 3.52. All of these sources have comparable blackbody temperatures indicative of our high-state ULX candidates (roughly kT ≈ 0.15).

We simulated 500 spectra each, using the two-component model, for each of 2000 counts, 1000 counts, 400 counts, and 200 counts for the PN. Each simulated spectrum, based on the best-fit blackbody and power law model, was fit with an absorbed blackbody and powerlaw model as well as an absorbed pure-powerlaw model. We placed the constraint that the blackbody temperature must lie within the range of $0.07-4.0$ keV (the range at which it would be detectable in the *XMM-Newton* bandpass). We allowed the power law index to vary over the range $0 - 4$ for the power law component of the combined blackbody and power law model. However, we placed a constraint that the power law component must lie within the range $\Gamma = 1.5 - 2.0$ for the simple power law model to be consistent with our fits to the sources we claim are best fit by simple power laws. This constraint ensures that the spectral index would exhibit that of our classified "low-state" objects.

When analysing and classifying our real spectra, we declared a detection of the thermal disk component if the addition of this component (to a baseline powerlaw model) led to an improvement of the goodness of fit parameter by at least $\Delta\chi^2 = 8$. We can use the above simulations to address the detectability of a thermal disk component using this $\Delta\chi^2$

threshold as a function of the relative strength of the thermal component and the number of counts in the spectrum. For each simulation, we fit the spectrum with both a single absorbed power-law and a 2-component powerlaw and thermal disk model and compute the quantity $\Delta\chi^2 = \chi^2_{\rm pow} - \chi^2_{\rm pow+disk}$. In Fig. A1, we plot the distribution of $\Delta\chi^2$ from our 500 simulations for the weak and strong blackbody component for spectra with 400 counts and 2000 counts. It is clear that we cannot detect a weak thermal component in a 400 count spectrum — the vast majority of the simulations ($\approx 82\%$) result in $\Delta\chi^2 < 8$. However, even a weak thermal component is easily detected in a 2000 count spectrum (not a single simulation gave $\Delta\chi^2 < 8$). The strong blackbody case is detectable with high significance even in a 400 count spectrum ($< 1\%$ of the simulations resulted in $\Delta\chi^2 > 8$).

When we increase the upper limit of the range of the spectral index in XSPEC for the power law model to $\Gamma = 3.0$, our confidence levels decrease. For a weak thermal component with 400 counts, all of the simulations result in $\Delta\chi^2 < 8$. At 2000 counts, only $\approx 30\%$ of the simulations for a weak thermal component have $\Delta\chi^2 < 8$. For a strong thermal component, 20% of the simulations yield $\Delta\chi^2 < 8$ for 400 counts while, as was the case for $\Gamma = 2.0$, none of the simulations gave $\Delta\chi^2 < 8$ for 2000 counts.

Thus allowing the Γ to "float freely" or remain unconstrained further decreases the confidence levels. When the Γ parameter is allowed to float the spectra are fit with higher Γ values in order to compensate for the missing blackbody component. When the upper limit was instituted at 2.0 or 3.0, we found that all 500 simulated spectra were fit with a $\Gamma = 2.0$

or 3.0, respectively, for the simple power law model. This same affect is not seen in the Γ of the two-component model, where the value ranges between 1.4 and 4.0 with a peak in the distribution near that of the original model used to simulate the spectra. Thus, higher power law indices (> 3.0) can indicate the necessity of an added blackbody component. Since there are no Galactic black holes whose broad band spectra are well fit by steep power laws it seems that restricting the allowed power law indices is more consistent with the nature of Galactic black holes. In fitting our sources with the three "standard" models, we allowed the Γ to float, thus the problem of a missing blackbody component being compensated for by a steep power law should not have factored into our classification criteria.

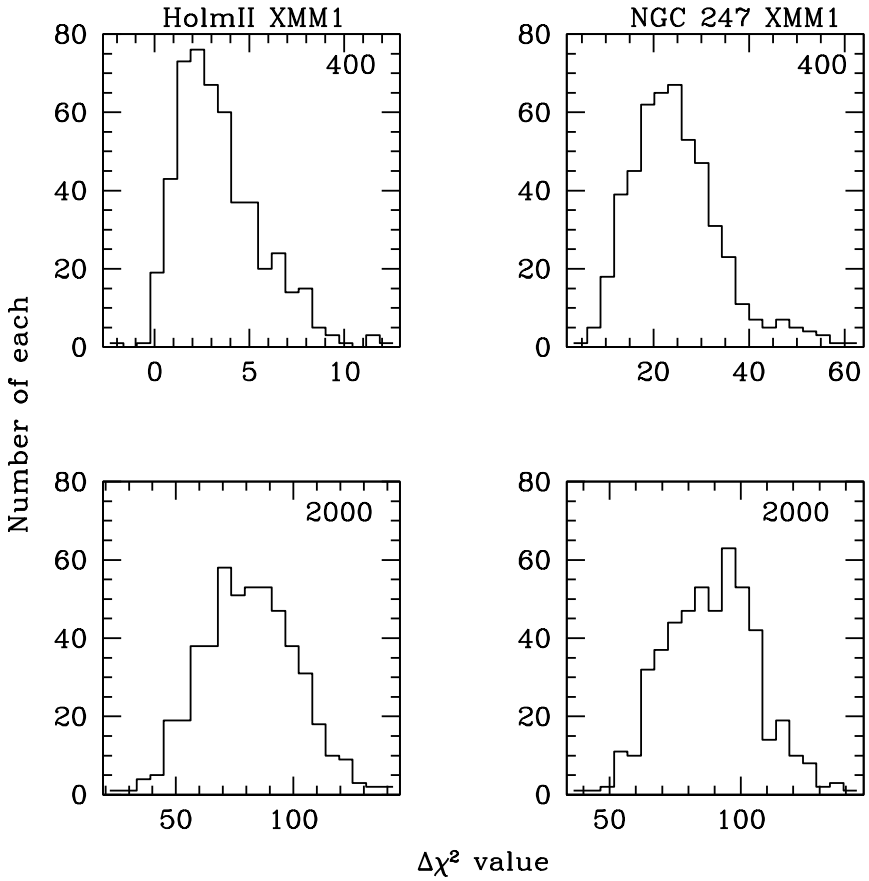

Figure B.1: Distribution of $\Delta\chi^2$ from simulations. The $\Delta\chi^2$ values represent the difference between the unreduced χ^2 of the absorbed power law model and the combined blackbody and power law model. The left panel shows the results for the "weak" blackbody component relative to power law for 500 simulated spectra at 400 counts (top) and 2000 counts (bottom). The right panel shows the results for the "strong" blackbody component. For a weak blackbody component at 400 counts, the thermal component is undetectable. However, it is able to be distinguished as the number of counts is increased. A strong blackbody component is easily distinguishable at 400 counts.

B.1.2 Simple Power Law Model

Our next set of simulations sought to determine our confidence in the simple power law fit being an adequate descriptor of the spectra. Binning provides a problem in distinguishing between a powerlaw and a curvature in the spectrum at the low energy range, since the binning procedure can wash out a low kT blackbody from the spectrum. For this reason, we chose to simulate unbinned PN spectra for a source we categorized as a low-state object, IC 0342 XMM1. IC 0342 XMM1 represents characteristics typical of our low-state candidates, namely it is within the proper luminosity range and it has a power law index of $\Gamma \approx 1.7$ (the median of the distribution for low-state objects is 2.03) and a hydrogen column density near the median of all the fitted values (where the median value is $\approx 3 \times 10^{21}\,\mathrm{cm}^{-2}$ and the value of IC 0342 X-1's column density is $5.8 \times 10^{21}\,\mathrm{cm}^{-2}$). We chose this source for these reasons and the high number of counts in its PN spectrum. Instead of using the χ^2 statistic (used for binned data), we chose to use the maximum-likelihood statistic, *C-stat*, in `XSPEC` (which uses unbinned data).

We simulated 500 spectra using the best-fit parameters for the simple power law fit using the `fakeit` command. We fit the simulated spectra with two models: the simple powerlaw and a combined blackbody and power law model and computed the change in the goodness of fit, $\Delta\chi^2$. For the two-component model, once again we placed the constraint that the blackbody temperature remain in the range that it would be detectable by *XMM-Newton*, 0.07 - 4 keV. We followed this procedure for 1000, 2000, and 4000 counts. At both the 1000 and 2000 count level, the

addition of a second component has no effect on the C-statistic (the distributions in C-space for both the power law fit and the two-component fit are indistinguishable).

At the 4000 count level, the C-statistic distributions for the two models separate such that there is an 26% confidence that the two-component model is a better fit to the data. We find, when we examine the model parameters, that the power law index (Γ) for the two-component model ranges between $1.19 - 2.12$ with the mean value ≈ 1.74. The mean value for all three count levels used clustered around this value, though the range in Γ increased as the counts decreased. The mean blackbody temperature for simulations with 4000 counts was 1.17 keV (with the range varying between the amount previously noted) with a median of 1.06 keV. For simulations with lower counts, the blackbody temperature becomes higher (1.24 keV for 1000 counts) with a higher median (1.83 keV for 1000 counts). This tells us that the fitting procedure tends to approximate a pure power law spectrum as a two-component spectrum with Γ equal to that of the true spectral index but with a blackbody temperature higher than those observed in our study (1.1 keV or higher) which in the *XMM* band can be approximated as a power law. If we found spectra in our sample that were best fit with a low spectral index and a high blackbody temperature, we might suspect that the spectrum's true nature is a power law. We also note that if the hydrogen column density is large, much $> 3 \times 10^{21}$ cm^{-2}, a low temperature (kT) blackbody component can be much more difficult to detect.

B.2 Additional Spectral Fits

The following sources were not best fit by the standard models employed in this study:

B.2.1 NGC300 XMM4

This source was classified as a super-soft X-ray source by Kong & Di Stefano (2003). We find that the standard single-component absorbed blackbody model is a much better model for this spectrum. In fact, the power law, bremsstrahlung, and combined models do not fit the data within the 90% confidence range. Fitting an absorbed blackbody, we find the best fit corresponds to the following parameters: $n_H = 1.38^{+0.27}_{-0.55} \times 10^{21}\,\mathrm{cm}^{-2}$, $kT = 0.059^{+0.007}_{-0.005}\,\mathrm{keV}$, and $\chi^2/dof = 74.5/45$. This fit yields an unabsorbed flux of $3.3 \times 10^{-13}\,\mathrm{erg\,cm^{-2}\,s^{-1}}$.

B.2.2 NGC4631 XMM4

The spectrum of this source clearly identifies it as a super-soft X-ray source. As with NGC300 XMM4, the standard models employed in this study did not adequately match the data. The best fitting model corresponds again to an absorbed blackbody. The corresponding parameters are as follows: $n_H = 6.2^{+0.26}_{-1.5} \times 10^{21}\,\mathrm{cm}^{-2}$, $kT = 0.07^{+0.01}_{-0.01}\,\mathrm{keV}$, and $\chi^2/dof = 142.3/74$. This fit yields an unabsorbed flux of 9.5×10^{-12} $\mathrm{erg\,cm^{-2}\,s^{-1}}$. The position of this source shows it to be coincident with a globular cluster associated with that galaxy. This source was identified as a bulge X-ray source, possibly powered by accretion, in a ROSAT study of NGC4631 (Vogler & Pietsch 1996).

B.2.3 NGC4631 XMM5

The spectrum of this source was best fit with an absorbed power law + an absorbed `vapec` model. This indicates the presence of hot gas, indicating a possible thermal X-ray source.

B.2.4 NGC4945 XMM5

The spectrum of this source was not adequately fit with any of the standard models used in this investigation. The spectrum exhibits a prominent Fe K line in the PN spectrum that is well fit by a gaussian (`zgauss`) at 6.4 keV. We find that the entire spectrum is best fit with a partial covering fraction absorption model (`pcfabs`) in combination with the normal absorption, a power law, and a gaussian. The best fit parameters yield: absorption column density, $n_H = 1.79 \times 10^{21}$ cm^{-2}, partial covering absorption, $n_H = 18.4 \times 10^{21}$ cm^{-2}, partial covering fraction $= 0.82$, $\Gamma = 1.6$, and $\chi^2/dof = 61.8/57$. The source is clearly located within the optical galaxy, and is thus unlikely to be a background AGN.

B.2.5 M51 XMM5

The spectrum and luminosity ($L_X \approx 1.9 \times 10^{42}$ erg s^{-1}) of this source suggests that it is an AGN. The location of the source, from the Digital Sky Survey, places it within the dwarf companion of M51 making a value of the optical flux hard to constrain. The best fit to this source was an absorbed blackbody + power law and the spectral parameters are listed in Table 2.4.

B.2.6 M83 XMM2

Like NGC4945 XMM5, this source was best fit by a partial absorption model. However, this source showed no evidence of an Fe K line. We fit this source's spectra using a partial covering fraction absorption model in combination with the normal absorption model and a power law. The best fit parameters yield: absorption column density, $n_H = 2.1 \times 10^{21}\,\mathrm{cm}^{-2}$, partial covering absorption, $n_H = 43.5 \times 10^{21}\,\mathrm{cm}^{-2}$, partial covering fraction $= 0.86$, $\Gamma = 2.95$, and $\chi^2/dof = 83.5/84$. The unabsorbed flux in the range of 0.3-10 keV equals $1.37 \times 10^{-12}\,\mathrm{erg\,cm^{-2}\,s^{-1}}$.

B.2.7 Inverse Compton Scattering Sources

Table B.4 includes the parameters for the "ULX" sources best fit by the `compST` model. A discussion of these sources and interpretation of the data is included in section 2.4.3.

B.3 Additional Tables

In this appendix we include additional tables containing supporting material for the text of the paper. In Table B.1 we list details of the XMM-Newton observations for all of the point sources examined in this study. Table B.2 lists information for bright sources that we excluded from our study, due to their classification as either foreground stars or background AGNs. Table B.3 includes single-component (absorbed power law) model fits for the sources listed in Table 2.4, while Table B.4 includes Comptonization model fit parameters for the sources mentioned in Section 2.4.3 (possible very high state stellar mass black holes with

luminosities in the ULX regime). Finally, Table B.5 includes the IR flux information for ULX host galaxies used to construct Figure 2.10.

Table B.1: Bright Point Sources Examined in the ULX Survey.

Source[1]	RA (h m s)	Dec (° ′ ″)	Total Counts	Count Rate[2]	ID	Location in galaxy[3]	XMM ref[7]
NGC247 XMM1	00 47 03.8	-20 47 46.2	3458, 1389, 1379	20.33, 5.8, 6.4	1RXS J004704.8-204743	sa	-
NGC247 XMM2	00 47 03.1	-20 37 02.5	-, 597, 600	-, 1.9, 1.4	-	sa	-
NGC253 XMM1	00 47 32.8	-25 17 52.6	-, 3156, 2985	-, 11.38, 9.9	NGC253 PSX-2[4]	near center	1
...	...	...	-, 12654, 12812	-, 8.7, 9.1	...	-	
NGC253 XMM2	00 47 22.4	-25 20 55.2	-, 825, 942	-, 2.8, 2.97	NGC253 PSX-5	sa	1
...	...	...	-, 10347, 10304	-, 8.2, 8.5	...	-	
NGC253 XMM3	00 47 35.2	-25 15 13.8	-, 870, 1065	-, 3, 3.41	NGC253 PSX-7	sa	1
...	...	...	-, 5988, 6131	-, 4.2, 4.6	...	-	
NGC253 XMM4	00 47 23.3	-25 19 06.5	-, 649, 703	-, 1.4, 1.3	-	sa	-
...	...	...	-, 3823,3738	-, 1.7, 1.95	-	-	
NGC253 XMM5	00 47 17.6	-25 18 12.1	-, 295, 313	-, 1.08, 1.04	NGC253 PSX-4	sa	2
...	...	...	-, 4199, 4303	-, 3.6, 3.8	...	-	
NGC253 XMM6	00 47 42.8	-25 15 05.5	-, 6081, 6407	-, 3.8, 4.4	NGC 0253 [VP99] X40	sa	1
NGC253 XMM7[5]	00 47 09.2	-25 21 21.7	-, 4300, 4454	-, 2.6, 3.0	-	sa	-
NGC300 XMM1	00 55 09.9	-37 42 13.9	6778, 2248, 2453	18.6, 4.9, 5.4	-	sa	-
NGC300 XMM2	00 55 10.6	-37 48 36.7	1364, 456, 463	3.1, 0.9, 0.9	-	edge sa?	-
NGC300 XMM3	00 54 49.7	-37 38 53.8	915, 442, 435	2.2, 0.9, 0.9	-	sa[6]	-
NGC300 XMM4	00 55 10.9	-37 38 53.8	745, 224, 233	1.9, 0.3, 0.4	XMMU J005511 -3749; SSS	sa	3
NGC300 XMM5	00 55 21.1	-37 29 19.5	750, 247, 250	1.7, 0.4, 0.5	-	out	-
NGC300 XMM6	00 54 44.2	-37 51 04.5	517, 187, 165	1.1, 0.3, 0.3	-	out	-
NGC625 XMM1[8]	01 35 06.8	-41 26 17.1	5832, 577, 2119	3, 0.6, 1.4	-	sa	-

Continued on Next Page...

Table B.1 – Continued

Source[1]	RA (h m s)	Dec (° ′ ″)	Total Counts	Count Rate[2]	ID	Location in galaxy[3]	XMM ref[7]
NGC1313 XMM1	03 18 19.9	-66 29 10.7	2876, 900, 810	8.6, 3.2, 2.8	NGC1313 [CPS95] X-1; IXO 07	sa	4,5
NGC1313 XMM2	03 17 38.8	-66 33 05.3	7568, 2357, 2108	25.4, 8.8, 7.8	NGC1313 [CPS95] X-3; SN 1978 K	edge sa	6
NGC1313 XMM3	03 18 22.5	-66 36 06.2	6960, 2179, 1793	23.3, 8.1, 6.6	NGC1313 [CPS95] X-2; IXO 08	edge sa?	4,5
NGC1313 XMM4	03 18 18.5	-66 30 05	2075, 659, 567	5.1, 1.8, 1.5	NGC1313 [SPC2000] X-8	near center	-
IC0342 XMM1	03 45 55.8	+68 04 54.5	1802, 1216, 1105	33.6, 12.4, 11.1	IC0342 [RW2000] X-1; IXO 22	sa	5, 7, 8
IC0342 XMM2	03 46 15.0	+68 11 11.2	1147, 541, 184	21.1, 5.5, 1.7	IC0342 [RW2000] X-3	sa	7, 8
IC0342 XMM3	03 46 48.6	+68 05 43.2	1186, 670, 606	21.7, 6.8, 6.0	IC0342 [LLJ2000] X-2	near center	7, 8
IC0342 XMM4	03 46 57.2	+68 06 20.2	551, 338, 377	9.5, 3.9, 3.6	IC0342 [RW2000] X-6	near center	7, 8
NGC1569[9]	...	...	...	...	...	...	...
NGC1705 XMM1	04 54 57.6	-53 24 23.5	1174, 400, 371	2.4, 0.6, 0.6	RX J0454.9-5324	out?	-
NGC1705 XMM2	04 54 19.6	-53 20 41.9	933, 375, 397	1.9, 0.6, 0.6	...	out?	-
NGC1705 XMM3	04 54 38.1	-53 18 16.2	698, 372, 418	1.4, 0.6, 0.6	WGA J0454.7-5318	out?	-
MRK71 XMM1	07 28 51.8	+69 07 27	832, 225, 207	3.9, 0.97, 0.9	-	out	-
NGC2403 XMM1	07 36 25.6	+65 35 40	-, 1199, 672	-, 1.0, 0.60	NGC2403 [RW2000] X-1	edge sa	-
NGC2403 XMM2	07 36 50.2	+65 36 02.1	1964, 729, 672	1.99, 0.63, 0.60	-	near center	-
NGC2403 XMM3	07 36 55.4	+65 35 40.3	1497, 489, 378	1.4, 0.40, 0.33	-	near center	-
NGC2403 XMM4	07 37 02.5	+65 39 35.2	1004, 274, 288	0.52, 0.15, 0.21	NGC2403 [RW2000] X-4	edge sa?	-
Hol II XMM1	08 19 28.8	+70 42 20.3	31052, 1257, 10807	272.2, 75.5, 72.7	Holm II X-1; IXO 31[10]	near center?	9
...	...	...	3853, 1361, 1452	78.3, 18.9, 20.5	...	-	
Hol I XMM1	09 41 30	+71 12 34	687, 768, 754	2.9, 2.7, 2.6	-	out?	-
Hol I XMM2	09 39 59.7	+71 06 40.2	575, 203, 224	2.5, 0.7, 0.7	1WGA J0940.0+7106	out?	-
Hol I XMM3	09 42 06.7	+71 04 45.3	452, 141, 141	1.7, 0.4, 0.4	-	out?	-

Continued on Next Page...

Table B.1 – Continued

Source[1]	RA (h m s)	Dec (° ′ ″)	Total Counts	Count Rate[2]	ID	Location in galaxy[3]	XMM ref[7]
M81 XMM1	09 55 32.9	+69 00 34.8	50788, -, 18988	51.1, -, 21.7	NGC3031 [RW2000] X-11	sa	-
...	...	...	-, 1227, -[11]	-, 12, 13.1	...	-	-
M81 XMM2	09 55 24.8	+69 01 11.7	17871, -, 4121	13.2, -, 4.4	SN 1993J	sa	10
M81 XMM3	09 55 10.6	+69 05 02.2	-, -, 1970	-, -, 1.5	NGC3031 [RW2000] X-05	sa	-
M81 XMM4	09 55 24.3	+69 10 00.2	-, -, 1197	-, -, 1.0	NGC3031 [RW2000] X-08	edge sa	-
M81 XMM5	09 55 49.2	+69 05 30.5	-, -, 2077	-, -, 2.3	-	sa	-
M82[12]	...	...	...	...	...	...	...
Hol IX XMM1	09 57 53.3	+69 03 48.7	14976, 6546, 6586	207.3, 64.3, 65	Hol IX X-1; IXO 34	?	4, 5
Sextans A XMM1	10 11 24.6	-04 42 17.2	3963, 1323, 1242	17.2, 5, 4.5	-	out	-
IC2574 XMM1	10 28 42.4	+68 28 17.8	1047, 673, 623	8.3, 2.6, 2.5	-	sa	-
IC2574 XMM2	10 26 33.5	+68 29 32.1	533, 335, 300	4.3, 1.3, 1.2	-	out	-
IC2574 XMM3	10 27 22.2	+68 18 47.6	538, 293, 301	4.2, 1.1, 1.2	-	out	-
NGC4214 XMM1	12 15 37.0	+36 19 29.4	434, 230, 225	2.9, 1.6, 1.5	NGC4214 [HSS2004] 11	sa	-
NGC4214 XMM2	12 15 58.2	+36 22 38.5	626, 160, 285	3.4, 0.6, 1.5	-	out	-
NGC4258 XMM1[5]	12 18 47.8	+47 20 51.7	828, 470, 444	7.0, 2.8, 2.8	-	sa	-
...	...	...	...	...	...	-	-
NGC4258 XMM2	12 18 57.8	+47 16 06.8	732, 337, 337	5.8, 2, 2.1	NGC4258 [RW2000] X-7	sa	-
...	...	...	716, 268, 290	1.8, 1, 1.0	...	-	
NGC4258 XMM3	12 18 56.5	+47 21 24.3	489, 182, 184	3.8, 0.9, 1.1	NGC4258 [RW2000] X-5	sa	-
...	...	...	-, 160, 142	-, 0.3, 0.3	...	-	
NGC4258 XMM4	12 19 23.2	+47 09 37.2	644, 277, 224	4.9, 1.3, 1.3	HELLAS 288	edge sa?	-
...	...	...	964, 410, 382	0.3, 0.2, 0.1	...	-	

Continued on Next Page...

Table B.1 – Continued

Source[1]	RA (h m s)	Dec (° ′ ″)	Total Counts	Count Rate[2]	ID	Location in galaxy[3]	XMM ref[7]
NGC4395 XMM1	12 26 01.5	+33 31 29	2162, 862, 921	15.5, 5.1, 5.6	NGC4395 [RW2000] X-1; IXO 53	sa	-
NGC4395 XMM2	12 25 25.3	+33 36 46.4	392, 252, 208	2.6, 1.5, 1.2	-	sa?	-
NGC4395 XMM3	12 25 32.6	+33 25 27.9	763, 277, 278	5.2, 1.5, 1.6	-	out?	-
NGC4395 XMM4	12 25 42.7	+33 40 00.1	516, 60, 40	3.1, 0.3, 0.2	-	out	-
NGC4449 XMM1	12 28 18	+44 06 30.9	1409, 608, 593	10.6, 3.6, 3.5	XRB?; NGC4449 [RW2000] X-7; Source 27[13]	sa	-
NGC4449 XMM2	12 28 09.3	+44 05 03.9	1503, 527, 586	11.3, 3.1, 3.5	SNR?; NGC4449 [RW2000] X-1; Source 10	sa	-
NGC4449 XMM3	12 28 11.1	+44 06 43.9	1094, 549, 404	8.3, 3.2, 2.3	SNR; Source 15	sa	-
NGC4490 XMM1	12 30 32.4	+41 39 14.6	746, 323, 393	6.0, 1.9, 2.2	NGC4490 [RW2000] X-1	sa	-
NGC4490 XMM2	12 30 36.5	+41 38 33.3	656, 299, 310	5.3, 1.7, 1.7	NGC4490 [RW2000] X-2	near center	-
NGC4490 XMM3	12 30 43.3	+41 38 11.5	832, 501, 461	5.8, 2.6, 2.2	NGC4490 [RW2000] X-4	sa	-
NGC4490 XMM4	12 30 31.1	+41 39 08.1	546, 291, 286	4.4, 1.7, 1.6	CXOU J123030.8 +413911	sa	-
NGC4490 XMM5	12 30 30.3	+41 41 40.3	413, 587, 482	2.7, 3.1, 2.3	NGC4485 [RW2000] X-1	sa	-
NGC4631 XMM1	12 41 55.8	+32 32 14	5093, 1969, 1762	13, 4.2, 3.8	NGC4631 [RW2000] X-1; IXO 68	sa	-
NGC4631 XMM2	12 41 57.5	+32 32 01	1273, 531, 400	3.3, 1.2, 0.9	NGC4631 [RW2000] X-2	sa	-
NGC4631 XMM3	12 41 58.2	+32 28 49.6	1271, 443, 457	2.8, 0.9, 0.9	CXOUSEXSI J124158.0+322851	out	-
NGC4631 XMM4	12 42 16.1	+32 32 48.8	957, 400, 429	2.3, 0.8, 0.8	[VP96] H13	sa	-
NGC4631 XMM5	12 42 11.2	+32 32 33.6	1626, 894, 866	3.9, 1.9, 1.8	[VP96] H12; [HFE2003] PSX-01	sa	-
NGC4736 XMM1	12 50 50.2	+41 07 12	713, 273, 227	6.7, 2.1, 1.7	NGC4736 X-4[14]	near center	-
NGC4945 XMM1	13 05 33.3	-49 27 36.3	1456, 646, 595	7.9, 2.9, 2.6	NGC4945 [GMB2000] X-2	sa	-
NGC4945 XMM2	13 05 38.4	-49 25 45.3	1393, 600, 523	7.6, 2.7, 2.3	NGC4945 [R97] X-3	sa	-
NGC4945 XMM3	13 05 18.8	-49 28 24	-, 357, 362	-, 1.6, 1.6	...	sa	-
NGC4945 XMM4	13 05 22.2	-49 28 26.3	731, 331, 332	4.0, 1.5, 1.5	NGC4945 [BIR96] X-1?	sa	-

Continued on Next Page...

Table B.1 – Continued

Source[1]	RA (h m s)	Dec (° ′ ″)	Total Counts	Count Rate[2]	ID	Location in galaxy[3]	XMM ref[7]
NGC4945 XMM5	13 05 25.7	-49 28 30.7	772, 267, 301	4.2, 1.2, 1.32	...	sa	-
NGC5204 XMM1	13 29 38.5	+58 25 03.6	9981, 3352, 3384	62.8, 17.7, 17.9	NGC5204 [RW2000] X-1; IXO 77	sa	11
...	...	...	9231, 2284, 2349	85.5, 24.7, 25.8	...	-	
NGC5204 XMM2	13 29 27.4	+58 25 31.8	573, 170, 231	3.4, 0.8, 1.2	-	edge sa	-
...	...	...	772, 161, 121	5.0, 1.7, 1.1	...	-	
M51 XMM1	13 29 40	+47 12 36.2	1102, 367, 409	6.2, 1.8, 2	NGC5194 [RW2000] X-1	sa	-
M51 XMM2	13 30 07.7	+47 11 04.8	514, 540, 549	2.6, 2.2, 2.2	IXO 81	sa	-
M51 XMM3	13 30 01.1	+47 13 41.4	1004, 315, 311	4.1, 1.1, 1.1	CXOU J133001.0 +471344; IXO 80	sa	-
M51 XMM4	13 30 06	+47 15 38.9	518, 183, 166	2.8, 0.9, 0.8	NGC 5195 [RW2000] X-1	sa	-
M51 XMM5	13 29 59.6	+47 15 54	1079, 359, 257	5, 1.5, 1	CXOU J132959.5 +471559	near center	-
M51 XMM6	13 29 57.5	+47 10 45.3	536, 206, 247	1.9, 0.6, 0.8	CXOU J132957.6 +471048	sa	-
M51 XMM7	13 29 53.6	+47 14 31.5	452, 141, 143	2.4, 0.6, 0.7	CXOU J132953.8 +471432	edge sa	-
M83 XMM1	13 37 19.8	-29 53 49.8	3074, 927, 987	12, 3.3, 2.5	RX J133719 -2953.6; IXO 82	sa	-
M83 XMM2	13 36 59.4	-29 49 57.2	1133, 371, 397	4, 1.3, 1	CXOU J133659.4 -294959	sa	-
M83 XMM3[15]	13 37 04.4	-29 51 24	1724, 576, 459	7.2, 2.3, 1.2	CXOU J133704.3 -295121	sa	-
M83 XMM4	13 37 01.5	-29 53 26	1289, 345, 401	4.9, 1.3, 1.0	CXOU J133701.4 -295326	sa	-
NGC5253[16]	...	...	...	...	...	...	...
M101 XMM1	14 03 14.7	+54 18 05	2690, 1449, 1417	10.3, 3.3, 3.3	CXOU J140313.9 +541811; XMM-2[17]	sa	12
M101 XMM2	14 03 03.8	+54 27 37	2825, 1623, 1551	10.3, 3.6, 3.3	XMM-1	edge sa?	12
M101 XMM3	14 04 14.6	+54 26 04.4	1460, 822, 717	5, 1.6, 1.3	CXOU J140414.3 +542604; XMM-3	edge sa?	12
M101 XMM4	14 02 28.5	+54 16 26.7	1505, 877, 757	5.1, 1.7, 1.5	CXOU J140228.3 +541626	sa	12
M101 XMM5	14 02 22.5	+54 17 58	516, 245, 289	1.8, 0.4, 0.6	CXOU J140222.2 +541756; XMM-6	sa	12

Continued on Next Page...

Table B.1 – Continued

Source[1]	RA (h m s)	Dec (° ′ ″)	Total Counts	Count Rate[2]	ID	Location in galaxy[3]	XMM ref[7]
NGC5408 XMM1	14 03 19.8	-41 22 59.3	5932, 2036, 2077	12.8, 3.2, 3.3	NGC5408 [KCP2003] X-1	sa	5
CIRCINUS XMM1[18]	14 12 54.2	-65 22 55.3	16220, 11452, -	14.5, 11.3, -	-	edge sa?	-
CIRCINUS XMM2	14 12 39.2	-65 23 34.3	8741, 2386, -	5.7, 1.9, -	-	edge sa?	-
CIRCINUS XMM3	14 13 28.3	-65 18 08.3	4873, 1031, -	1.8, 0.7, -	-	edge sa?	-

[1]Sources labeled *XMM-n* in order of apparent brightness from the first observation studied

[2]Count rate units of $\times 10^{-2}$ cts s^{-1} for the PN, MOS1, and MOS2 spectra

[3]Location specified as: inside the optical extent of the galaxy or in spiral arms (sa), near the center of the galaxy, at the edge of a spiral arm/ optical extent of galaxy, or outside the optical extent of the galaxy. Location based on DSS images.

[4]Identification for NGC0253 following Humphrey et al. (2003).

[5]Transient.

[6]Appears as an extended source in HST image.

[7]References to studies using *XMM-Newton* spectra

[8]Spectra too scattered to model.

[9]Bright sources coincide with nucleus (unresolvable star cluster and X-ray binaries), fore-ground star, and background AGN (Martin et al. 2002).

[10]IXO designation from Colbert & Ptak (2002).

[11]Spectrum from Hol IX observation.

[12]Bright source is too close to other sources.

[13]Chandra observations of point sources in NGC4449 published in Summers et al. (2003); Source 27 varied from ROSAT observations

[14]Three other sources near the nucleus are unresolveable in the XMM obs., but seen by Chandra (Eracleous et al. 2002).

[15]Unable to model sprectrum due to an error in χ^2-space

[16]Bright sources are too close, but resolvable by Chandra (Summers et al. 2004).

[17]Alternate ID from Jenkins et al. (2004).

[18]Bright sources near the nucleus are unresolvable, but seen by Chandra (Smith & Wilson 2001).

Table References:

(1) Pietsch et al. (2001); (2) Pietsch et al. (2003); (3) Kong & Di Stefano (2003); (4) Miller et al. (2004b); (5) Wang et al. (2004); (6) Schlegel et al. (2004); (7) Bauer et al. (2003a); (8) Kong (2003); (9) Lehmann et al. (2005); (10) Zimmermann & Aschenbach (2003); (11) Roberts et al. (2005); (12) Jenkins et al. (2004).

Table B.2. Bright, Identifiable Background and Foreground Sources

Galaxy	RA (h m s)	Dec (° ′ ″)	Identification
NGC 247	0 46 51.7	-20 43 30	QSO B044-2059
NGC 300	0 55 26.7	-37 31 25.6	HD 5403 (Star)
NGC 625	01 34 42.4	-41 36 15.2	QSO B0132-4151
NGC 1569[a]	04 31 16.9	+64 49 50	CXOU J043116.8+644950 (Star)
NGC 1569	04 31 14.2	+64 51 07.9	CXOU 043114.0+645107 (Star)
NGC 1569	04 31 25.4	+64 51 53.8	CXOU 043125.1+645154 (AGN)
NGC 1705	04 54 01.2	-53 21 12.3	WGA J0454.0-5320 (M star or elliptical galaxy)
NGC 2403	07 35 09	+65 40 27.5	HD 59581 (Star)
NGC 4258	12 18 08.9	+47 16 08.3	QSO J1218+472
M83	13 36 45.6	-29 59 13.9	2MASX J13364579-2959122 (Galaxy)
M83	13 36 13.9	-29 56 13	RX J133615-2957.8 (Galaxy)
NGC 5253	13 39 50.6	-31 34 11.1	CD-30 10790 (Star)
M101	14 02 30	+54 21 18.2	[WIP99] H13 (Star)[b]
NGC 5408	14 03 27.5	-41 25 18.5	(Star)

[a]identification for objects in NGC 1569 from Martin, Kobulnicky, & Heckman (2002)

[b]confirmed by K. Kuntz using HST ACS

Table B.3: *XMM-Newton* Power Law Fit for Best Fit Two-component Spectra (`wabs*pow`))

Source	n_H[a]	Γ	χ^2/dof	F_X[c]	L_X[d]
NGC247 XMM1	$9.5^{+1.6}_{-1.4}$	$8.52^{+1.14}_{-0.91}$	112.2/95	1900	2200
NGC253 XMM1	$3.4^{+0.3}_{-0.3}$	$1.77^{+0.06}_{-0.06}$	262.6/232	3.1	3.6
...	$6.9^{+0.4}_{-0.4}$	$1.98^{+0.05}_{-0.05}$	611.6/582	2.9	3.3
NGC253 XMM2 (obs 2)	$2.2^{+0.1}_{-0.1}$	$2.03^{+0.04}_{-0.04}$	507.4/500	1.2	1.4
NGC253 XMM3	$3.9^{+0.5}_{-0.4}$	$2.17^{+0.14}_{-0.11}$	91.9/83	0.73	1.2
...	$4.0^{+0.4}_{-0.3}$	$2.06^{+0.09}_{-0.07}$	381.8/409	0.98	1.6
NGC253 XMM4	$8.5^{+3.0}_{-2.3}$	$2.09^{+0.33}_{-0.28}$	73.6/59	0.52	0.85
...	$1.2^{+0.3}_{-0.3}$	$2.09^{+0.16}_{-0.15}$	321.4/293	0.29	0.48
NGC253 XMM5	$1.7^{+1.2}_{-0.9}$	$1.54^{+0.22}_{-0.20}$	31.8/25	0.32	0.53
...	$3.4^{+0.2}_{-0.2}$	$2.17^{+0.7}_{-0.7}$	283.8/298	1.1	1.3
NGC253 XMM6	$3.9^{+0.3}_{-0.3}$	$2.21^{+0.84}_{-0.80}$	435/409	0.93	1.5
NGC253 XMM7	$7.1^{+0.7}_{-0.7}$	$2.15^{+0.11}_{-0.11}$	357/342	1.3	2.2
NGC300 XMM1	$0.97^{+0.11}_{-0.11}$	$2.67^{+0.06}_{-0.06}$	469.8/422	0.81	0.6
NGC300 XMM2	$1.7^{+0.40}_{-0.40}$	$3.20^{+0.32}_{-0.24}$	133.98/99	0.27	0.21
NGC300 XMM3	$3.4^{+0.8}_{-0.6}$	$1.86^{+0.15}_{-0.13}$	101.9/81	0.19	0.15
NGC300 XMM5	0.311[e]	$2.29^{+0.15}_{-0.14}$	54.2/56	0.14	0.10
NGC300 XMM6	$?^{+?}_{-?}$	$2.05^{+0.17}_{-0.15}$	47.6/37	0.06	0.15
NGC1313 XMM1	$1.5^{+0.2}_{-0.2}$	$1.81^{+0.08}_{-0.09}$	219.8/203	0.42	0.88
NGC1313 XMM2	$2.8^{+0.16}_{-0.16}$	$2.48^{+0.07}_{-0.06}$	464.1/421	1.9	4.0
NGC1313 XMM3	$3.6^{+0.2}_{-0.2}$	$3.2^{+0.09}_{-0.09}$	778.3/426	3.3	6.9
IC0342 XMM3	$3.8^{+0.4}_{-0.4}$	$2.58^{+0.15}_{-0.14}$	185.8/109	1.7	3.1
NGC1705 XMM1	0.3[e]	$1.93^{+0.11}_{-0.10}$	61.9/88	0.12	0.37

Continued on Next Page...

Table B.3 – Continued

Source	n_H[a]	Γ	χ^2/dof	F_X[c]	L_X[d]
NGC1705 XMM2	$1.4^{+0.45}_{-0.41}$	$2.12^{+0.26}_{-0.15}$	91/76	0.078	0.24
NGC1705 XMM3	$0.6^{+0.36}_{-0.40}$	$1.36^{+0.12}_{-0.13}$	80.9/67	0.17	0.53
NGC2403 XMM1	$3.2^{+0.61}_{-0.55}$	$2.15^{+0.16}_{-0.15}$	92.2/81	2.2	3.6
NGC2403 XMM2	$2.7^{+0.37}_{-0.34}$	$2.07^{+0.11}_{-0.11}$	179.5/151	1.3	2.0
NGC2403 XMM3	$1.9^{+0.40}_{-0.36}$	$1.97^{+0.14}_{-0.13}$	92.6/107	0.81	1.3
HolmII XMM1 (obs 1)	$1.5^{+0.07}_{-0.07}$	$2.61^{+0.04}_{-0.04}$	1134.2/976	12	10
Holm I XMM1	$?^{+?}_{-?}$	$2.04^{+0.14}_{-0.07}$	102.8/95	0.48	1.7
M81 XMM1	$3.2^{+0.07}_{-0.07}$	$2.09^{+0.02}_{-0.02}$	1849.9/1245	4.5	7.0
...	$3.0^{+0.3}_{-0.3}$	$1.79^{+0.07}_{-0.07}$	224.9/208	4.3	6.7
M81 XMM2	7.3	6.13	1358.2/618	48.5	75.2
M81 XMM3	$0.97^{+0.25}_{-0.41}$	$1.58^{+0.18}_{-0.15}$	81.35/80	2.5	3.9
M81 XMM4	$?^{+?}_{-?}$	$0.88^{+0.11}_{-0.11}$	66.4/52	0.35	0.54
M81 XMM5	$1.0^{+0.4}_{-0.3}$	$1.52^{+0.11}_{-0.11}$	97.5/82	0.44	0.68
Holm IX XMM1	$1.7^{+0.08}_{-0.08}$	$1.84^{+0.03}_{-0.03}$	1000.9/882	9.4	15
Sextans A XMM1	$0.18^{+0.23}_{-0.16}$	$2.25^{+0.12}_{-0.07}$	271.4/275	0.56	0.13
NGC4214 XMM2	$0.2^{+0.5}_{-0.2}$	$2.03^{+0.43}_{-0.28}$	50.9/46	0.16	0.14
NGC4258 XMM1	$1.6^{+0.4}_{-0.4}$	$1.9^{+0.14}_{-0.13}$	101.4/78	0.06	0.04
NGC4258 XMM2 (obs 1)	$3.5^{+0.9}_{-0.7}$	$1.88^{+0.16}_{-0.15}$	97.5/63	0.43	2.6
NGC4395 XMM1	$3.7^{+0.5}_{-0.4}$	$4.93^{+0.34}_{-0.30}$	195.1/156	7.2	14
NGC4395 XMM3	$?^{+?}_{-?}$	$1.86^{+0.14}_{-0.09}$	55.9/58	0.25	0.48
NGC4449 XMM1	$6.3^{+0.9}_{-0.7}$	$2.22^{+0.14}_{-0.12}$	103/118	1.2	1.36
NGC4449 XMM3	$3.3^{+0.5}_{-0.4}$	$3.36^{+0.29}_{-0.23}$	154/89	1.3	1.5
NGC4490 XMM1	$0.83^{+0.14}_{-0.12}$	$2.53^{+0.17}_{-0.16}$	101.5/65	1.2	8.7

Continued on Next Page...

Table B.3 – Continued

Source	n_H[a]	Γ	χ^2/dof	F_X[c]	L_X[d]
NGC4490 XMM2	$6.3^{+1.3}_{-1.0}$	$2.36^{+0.19}_{-0.17}$	49.5/56	0.92	6.7
NGC4490 XMM3	$9.4^{+1.5}_{-1.2}$	$2.95^{+0.24}_{-0.20}$	76.7/80	1.5	11
NGC4631 XMM1	$2.3^{+0.16}_{-0.15}$	$2.13^{+0.06}_{-0.05}$	383.4/347	0.76	5.1
NGC4631 XMM2	$1.9^{+0.4}_{-0.3}$	$2.01^{+0.14}_{-0.12}$	119.5/99	0.23	1.5
NGC4631 XMM3	$0.63^{+0.3}_{-0.2}$	$1.53^{+0.1}_{-0.08}$	146/98	0.15	1.0
NGC4736 XMM1	$0.95^{+0.6}_{-0.5}$	$2.02^{+0.26}_{-0.25}$	62.8/53	0.36	0.80
NGC4945 XMM1	$5.8^{+0.8}_{-0.7}$	$1.88^{+0.08}_{-0.10}$	116/122	0.9	1.0
NGC4945 XMM2	$3.4^{+0.6}_{-0.5}$	$1.58^{+0.09}_{-0.10}$	114.5/115	0.71	0.82
NGC4945 XMM4	$5.2^{+0.8}_{-0.7}$	$2.59^{+0.19}_{-0.17}$	75.5/62	0.49	0.56
NGC5204 XMM1	$0.61^{+0.1}_{-0.1}$	$2.11^{+0.04}_{-0.04}$	592.1/561	2.0	5.5
...	$1.1^{+0.1}_{-0.1}$	$2.41^{+0.07}_{-0.07}$	533/498	3.0	8.3
M51 XMM1	$1.1^{+0.30}_{-0.27}$	$2.67^{+0.20}_{-0.16}$	110.5/82	0.34	2.8
M51 XMM2	$2.3^{+0.50}_{-0.30}$	$2.50^{+0.22}_{-0.20}$	75.2/70	0.52	3.3
M51 XMM5	2.7	3.08	256.0/72	0.43	2.7
M51 XMM6	$2.0^{+0.83}_{-0.72}$	$2.50^{+0.33}_{-0.25}$	40.97/43	0.13	0.83
M51 XMM7	$0.5^{+0.39}_{-0.46}$	$1.95^{+0.23}_{-0.18}$	37.8/31	0.11	0.66
M83 XMM1	$1.9^{+0.34}_{-0.31}$	$2.32^{+0.13}_{-0.12}$	210.9/211	0.64	2.8
M83 XMM4	$6.0^{+1.8}_{-1.3}$	$2.54^{+0.26}_{-0.23}$	91.4/91	0.4	1.8
M101 XMM1	$0.56^{+0.15}_{-0.14}$	$1.98^{+0.08}_{-0.08}$	303/233	0.45	2.9
M101 XMM2	$2.2^{+0.25}_{-0.23}$	$1.85^{+0.07}_{-0.07}$	288.8/263	0.81	5.3
M101 XMM3	$1.5^{+0.4}_{-0.3}$	$2.70^{+0.21}_{-0.17}$	148.9/133	0.51	3.4
M101 XMM4	$2.2^{+0.45}_{-0.42}$	$2.25^{+0.20}_{-0.17}$	165.7/140	0.38	2.5
M101 XMM5	$1.3^{+0.2}_{-0.3}$	$2.28^{+0.12}_{-0.11}$	47.9/46	0.12	0.8

Continued on Next Page...

Table B.3 – Continued

Source	n_H[a]	Γ	χ^2/dof	F_X[c]	L_X[d]
NGC5408 XMM1	$1.6^{+0.2}_{-0.1}$	$3.57^{+0.12}_{-0.11}$	396.8/339	7.04	19.4
CIRCINUS XMM1	$7.6^{+0.3}_{-0.3}$	$2.15^{+0.05}_{-0.04}$	762.9/863	4.6	8.8
CIRCINUS XMM2	$11.7^{+0.4}_{-0.7}$	$3.48^{+0.13}_{-0.06}$	517.9/432	2.7	5.2
CIRCINUS XMM3	$9.0^{+2.1}_{-1.0}$	$2.57^{+0.40}_{-0.17}$	285.2/262	0.32	0.61

[a]Total column density in units of 10^{21} cm^{-2}

[b]Improvement in χ^2 over the single-component power law model

[c]Unabsorbed flux in the 0.3-10 keV band in units of 10^{-12} erg cm^{-2} s^{-1}

[d]Unabsorbed luminosity in the 0.3-10 keV band, using the distances quoted in Table E.1, in units of 10^{39} erg s^{-1}

[e]Absorption level frozen at the Galactic level.

Table B.4. Best-Fit Absorbed Comptonization Model Parameters

ID	nH[a]	kT[b]	tau[c]	χ^2	F_X[d]
NGC 253 XMM2	$1.8^{+0.08}_{-0.16}$	$1.28^{+0.13}_{-0.12}$	$19.59^{+2.0}_{-1.6}$	464/498	1.47
NGC 2403 XMM1	$1.95^{+1.2}_{-0.6}$	$0.98^{+0.16}_{-0.15}$	$25.4^{+7.2}_{-8.3}$	82.8/85	1.4
NGC 4490 XMM1	$4.7^{+1.1}_{-2.1}$	$0.96^{+0.13}_{-0.16}$	$27.0^{+18.3}_{-4.9}$	66.5/64	0.66
NGC 4490 XMM2	$5.0^{+1.6}_{-1.4}$	$1.21^{+0.21}_{-0.31}$	$18.8^{+8.6}_{-9.7}$	45.7/55	0.67
M101 XMM2	$1.6^{+0.26}_{-0.24}$	$1.24^{+0.09}_{-0.15}$	$23.3^{+3.4}_{-2.8}$	256/262	0.65
M101 XMM3	$1.1^{+0.43}_{-0.40}$	1.13	15.2	128/132	0.41
Circinus XMM2	$6.8^{+1.3}_{-0.9}$	$0.62^{+0.08}_{-0.04}$	$29.7^{+8.1}_{-7.0}$	437.2/430	0.5
Circinus XMM3	$6.7^{+1.6}_{-2.4}$	$0.93^{+0.28}_{-0.24}$	$23.1^{+17.5}_{-5.2}$	273.1/261	0.17

[a]total column density in units of 10^{21} cm^{-2}

[b]temperature in keV

[c]optical depth

[d]unabsorbed flux in the 0.3-10 keV band in units of 10^{-12} erg cm^{-2} s^{-1}

Table B.5. *XMM-Newton* Galaxy Observations

Galaxy	S_{60} (Jy)	S_{100} (Jy)	F_{FIR}[a]	L_{FIR}[b]	No. of ULX
NGC247	7.93	27.32	0.602	0.687	1
NGC253	998.73	1861.67	55.92	93.10	3
NGC300	23.08	74.45	1.688	1.324	0
NGC625	5.09	9.08	0.280	0.230	0
NGC1313	35.97	92.00	2.329	4.845	2
IC0342	255.96	661.68	16.66	30.32	3
NGC1569	45.41	47.29	2.072	0.635	0
NGC1705	0.970	2.580	0.064	0.199	0
MRK 71	3.51	4.67	0.173	0.239	1
NGC2403	51.55	148.49	3.547	5.378	2
Holmberg II	1.15	2.62	0.070	0.061	1
Holmberg I	...	...	...	...	1
M81	44.73	174.02	3.647	5.655	1
M82	1271.32	1351.09	58.35	106.2	1
Holmberg IX	...	...	...	...	1
Sextans A	0.255	0.674	0.017	0.004	0
IC 2574	2.41	10.62	0.212	0.329	0
NGC 4214	17.87	29.04	0.947	0.826	1
NGC 4258	21.60	78.39	1.690	10.48	1
NGC4395	4.21	12.90	0.299	0.573	1
NGC4449	37.00	58.28	1.937	2.199	1
NGC4490	47.79	85.94	2.636	19.19	5
NGC4631	82.90	208.66	5.324	35.83	1
NGC4736	62.41	135.34	3.734	8.261	4
NGC4945	588.11	1415.5	36.95	42.49	0
NGC 5204	2.33	5.35	0.143	0.395	2
M51	108.68	292.08	7.213	44.74	5
M83	266.03	638.63	16.69	76.79	0
NGC5253	30.00	30.92	1.365	16.72	0
M101	88.04	252.84	6.048	39.63	4
NGC5408	2.825	2.958	0.129	0.356	1
Circinus	248.7	315.85	12.06	23.10	4

[a]flux in units of $10^{-9}\,\mathrm{erg\,cm^{-2}\,s^{-1}}$

[b]far-infrared luminosity in units of $10^{42}\,\mathrm{erg\,s^{-1}}$

Appendix C

Appendix to Chapter 3

C.1 Spectral Simulations

We conducted spectral simulations in order to: (1) determine the number of counts needed to measure the oxygen and iron abundances and (2) to verify the model independence of the galactic column density and abundances with respect to the `grad`, `diskbb`, and `bbody` models (seen in a comparison of Tables 3.2 and 3.4). Towards this end, we created simulated pn spectra based on the long Holmberg IX XMM1 observation's (0200980101) unbinned, pn spectrum. We used the base `(grad + pow)` model parameters as indicated in Table 3.2. We modeled both the Galactic column density (Dickey & Lockman (1990) value: $n_H = 4.0 \times 10^{20}\,cm^{-2}$) and host galaxy column density ($n_H = 1.9 \times 10^{21}\,cm^{-2}$) with individual `tbabs` models. Thus, all of the abundances were set to the solar Wilms values. We used the XSPEC command `fakeit` to create simulated spectra with 200000, 40000, 10000, 5000, and 2000 counts. The simulated spectra were binned with 20 cts/bin using `grppha`. We fit the binned simulated spectra with the mod-

els `tbabs*tbvarabs*(grad + pow)`, `tbabs*tbvarabs*(diskbb + pow)`, and `tbabs*tbvarabs*(bbody + pow)`. This allowed us to see the effects the different models have on the measured galactic hydrogen column density and abundances. The results for these fits are seen in Table C.1. The range that the oxygen and iron abundances were allowed to vary within was 0.0 (lower limit) to 5.0 (upper limit) with respect to the solar values.

In Figure C.1, the number of simulated counts versus the errors on the oxygen and iron abundances are plotted for the `tbabs*tbvarabs*(grad + pow)` model. Here, [O/H]$= 12 + \log(O \times 0.00049)$ and [Fe/H]$= 12 + \log(Fe \times 0.0000269)$, using the solar Wilms values for O/H and Fe/H. As seen in the plots, the errors in oxygen abundance are much smaller for a given number of counts compared to the errors in iron abundance. Further, the upper limits on the oxygen abundance continue to be meaningful through 2000 counts. This is not true for the iron abundances, where the error bars extend through the entire range of allowed values (from Fe/H = 0.0 - 5.0, or [Fe/H] up to 8.13). Thus, our simulations show us that the iron abundance (from measurements of the Fe L-shell edge at 851 eV with the `tbvarabs` model) requires at least 5000 counts to be detected. At 5000 counts the model derived value (Fe/H = 1.36) is meaningful, however, the errors extend throughout the entire allowable range (Fe/H = 0.0-5.0). The oxygen abundance (from measurements of the O K-shell edge at 542 eV with the `tbvarabs` model) is detected down to 2000 counts, but with large errors below 10000 counts.

From Table C.1, we find that the same trends described in Section 3.4.1

are present in our simulations. Namely, there is little variation between the model derived abundances and column densities. A comparison of the mean n_H and oxygen abundance values shows $\approx 2\%$ difference between the `grad` and `diskbb` model. The `bbody` n_H values are roughly 26% higher while the oxygen abundances are $\approx 11\,\%$ higher. Comparing the 40000 and 200000 count spectra for the iron abundance, we find that the `grad` and `diskbb` model values differ by $\approx 12\%$ while the `bbody` model results are larger by a factor of 50%. While the `bbody` model yields lower column densities and higher abundances, the `diskbb` and `grad` models are in agreement. The differences in the `bbody` results are low for the column density and oxygen abundance, but appeared significant for the iron abundance.

Table C.1. Spectral Fits to Simulated HolmIX XMM1 Spectrum

Counts[a]	n_H[b]	Oxygen abundance[c]	Iron abundance[c]	χ^2/dof
		`tbabs*tbvarabs*(grad + pow)`		
200000	$0.21^{+0.02}_{-0.02}$	$1.08^{+0.13}_{-0.15}$	$0.87^{+0.68}_{-0.76}$	1687/1727
40000	$0.19^{+0.04}_{-0.03}$	$1.15^{+0.26}_{-0.33}$	$0.97^{+1.41}_{-0.97}$	933/914
10000	$0.20^{+0.07}_{-0.06}$	$1.55^{+0.41}_{-0.52}$	$0.90^{+2.64}_{-0.90}$	340.5/401
5000	$0.16^{+0.13}_{-0.07}$	$1.37^{+0.75}_{-1.34}$	$1.36^{+3.64}_{-1.36}$	187.2/201
2000	$0.33^{+0.14}_{-0.19}$	$1.20^{+0.57}_{-1.20}$	$5.0^{+0.0}_{-5.0}$	71.9/89
		`tbabs*tbvarabs*(diskbb + pow)`		
200000	$0.21^{+0.02}_{-0.02}$	$1.09^{+0.15}_{-0.19}$	$0.99^{+0.94}_{-0.76}$	1691/1727
40000	$0.19^{+0.03}_{-0.03}$	$1.16^{+0.27}_{-0.35}$	$1.09^{+1.47}_{-1.09}$	934/914
10000	$0.19^{+0.03}_{-0.05}$	$1.58^{+0.43}_{-0.50}$	$1.01^{+2.80}_{-1.01}$	341/401
5000	$0.16^{+0.12}_{-0.08}$	$1.41^{+0.76}_{-1.16}$	$1.57^{+3.43}_{-1.57}$	187.5/201
2000	$0.32^{+0.18}_{-0.19}$	$1.23^{+0.59}_{-1.23}$	$5.0^{+0.0}_{-5.0}$	71.7/89
		`tbabs*tbvarabs*(bbody + pow)`		
200000	$0.17^{+0.02}_{-0.02}$	$1.24^{+0.16}_{-0.20}$	$1.65^{+0.85}_{-1.01}$	1702/1727
40000	$0.15^{+0.04}_{-0.02}$	$1.28^{+0.36}_{-0.40}$	$1.73^{+1.97}_{-1.72}$	937/914
10000	$0.15^{+0.07}_{-0.04}$	$1.77^{+0.61}_{-0.72}$	$1.22^{+3.78}_{-1.22}$	343.7/401
5000	$0.13^{+0.10}_{-0.07}$	$1.61^{+0.97}_{-1.61}$	$2.19^{+2.81}_{-2.19}$	187.5/201
2000	$0.21^{+0.19}_{-0.12}$	$1.16^{+0.92}_{-1.16}$	$5.0^{+0.0}_{-5.0}$	71.8/89

[a]Total number of photon counts for simulated pn spectrum. Simulated spectra created with the XSPEC `fakeit` command, using the model parameters and response files from the long HolmIX XMM1 observation.

[b]Hydrogen column density determined from `tbvarabs` in units of $10^{22}\,\mathrm{cm}^{-2}$. The Galactic value of n_H was fixed to the Dickey & Lockman (1990) value with the `tbabs` model.

[c]Element abundance relative to the Wilms solar abundance from the `tbvarabs` model

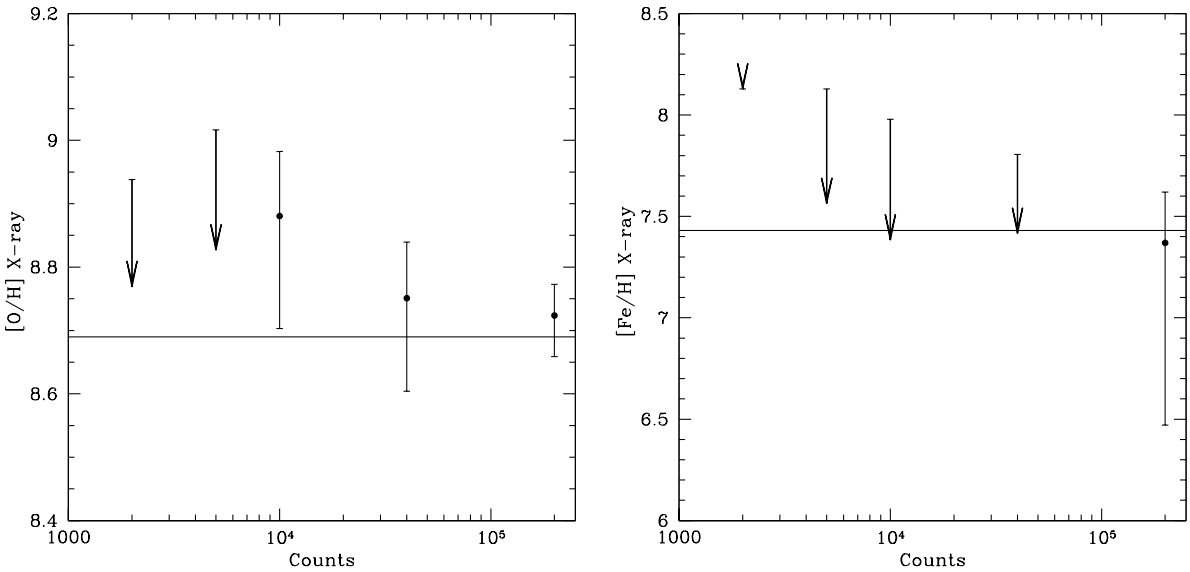

Figure C.1: The number of counts for simulated spectra versus the [O/H] value (left) and [Fe/H] value (right) from the `tbabs*tbvarabs*(grad + pow)`, where errors represent the 90% confidence rate. The horizontal lines represent the solar Wilms values ([O/H]$\approx$ 8.69 and [Fe/H]$\approx$ 7.43). Arrows are used to represent errors that extend below the range of the plot. The tip of the arrow point represents the [O/H] or [Fe/H] parameter from the XSPEC model (see Table C.1).

Appendix D

Appendix to Chapter 4

D.1 Details on Variability of Individual Sources

Below we describe the variability between observations for the AGN listed in Table 4.12. The low column density sources are those whose best-fit spectra were fit by a simple absorbed power law or a power law and blackbody model. The high column density/complex sources are those that we fit with the partial covering/double power law models. In the following discussion, XMM is used to denote the PN spectrum while XRT-1 denotes, for example, the first XRT observation for the source, as listed in Table 4.2.

D.1.1 Low Column Density Sources

MRK 352 – The PN and two XRT spectra for MRK 352 were not well fit until the flux was allowed to vary. A varying flux improved the fit by $\Delta\chi^2 \approx 6500$. The fit was then greater improved by allowing the column density to change ($\Delta\chi^2 = 320$). Changing the power law index and normalizations improved the fit by $\Delta\chi^2 = 30$, however, the

power law photon indices were the same within the errorbars. The best-fit `tbabs*tbabs*(pegpwrlw + bbody)` model is shown in Figure 4.9 where $\chi^2/dof = 1289.01/1189$. The black body and power law components were those seen in Table 4.6. Hydrogen column density changes between the observations as: 0.00 – 0.02 $\times 10^{21}\,\mathrm{cm}^{-2}$ (XMM), 0.83 – 1.04 $\times 10^{21}\,\mathrm{cm}^{-2}$ (XRT-1), 1.28 – 1.51 $\times 10^{21}\,\mathrm{cm}^{-2}$ (XRT-2). The flux errors from the pegged power law component were: 1.96 – 2.00 $\times 10^{-11}\,\mathrm{erg\,s}^{-1}\,\mathrm{cm}^{-2}$ (XMM), 1.37 – 1.47 $\times 10^{-11}\,\mathrm{erg\,s}^{-1}\,\mathrm{cm}^{-2}$ (XRT-1), and 0.98 – 1.05 $\times 10^{-11}\,\mathrm{erg\,s}^{-1}\,\mathrm{cm}^{-2}$ (XRT-2). Considering that the XRT observations were taken only a day apart, it is clear that this source varies considerably. Five months earlier, the XMM spectra show the source nearly twice as bright with no absorption.

SWIFT J0216.3+5128 – All of the observations for SWIFT J0216.3+5128 took place within the span of a month. While no variations were seen between the column densities and power law indices ($\Delta\chi^2 < 3$), the flux did vary. The flux errors from the pegged power law component were: 1.63 – 1.75 $\times 10^{-11}\,\mathrm{erg\,s}^{-1}\,\mathrm{cm}^{-2}$ (XMM), 2.25 – 2.52 $\times 10^{-11}\,\mathrm{erg\,s}^{-1}\,\mathrm{cm}^{-2}$ (XRT-1), 2.15 – 2.43 $\times 10^{-11}\,\mathrm{erg\,s}^{-1}\,\mathrm{cm}^{-2}$ (XRT-2), and 1.72 – 2.12 $\times 10^{-11}\,\mathrm{erg\,s}^{-1}\,\mathrm{cm}^{-2}$ (XRT-3). From the first two observations, the flux drops about 30% over two weeks and then remains at about the same level through the last two observations.

ESO 548-G081 – The spectra of ESO 548-G081 were found not to vary in column density. However, they did vary in both flux ($\Delta\chi^2 = 625$) and Γ ($\Delta\chi^2 = 60$). We fit this source with a `tbabs*tbabs*(pegpwrlw + bbody + zgauss)` model with χ^2/dof = 1428.1/1295. We note that the blackbody parameters were not fixed for observation XRT-2. This spectrum showed a soft excess that was fit with a blackbody much lower than the value for the XMM observation (see Table 4.6 with kT in the range of 0.034 – 0.049 keV. There were remaining residuals in this fit for XRT-2, leaving us unsure of the nature of this feature which could be the result of a hot pixel or the instrument. The higher energy spectrum (above 0.5 keV) appeared well fit by the model used. We found the error on the photon index as: 1.851 – 1.877 (XMM), 1.716 – 1.802 (XRT-1), and 1.930 – 2.002 (XRT-2). The flux errors from the pegged power law component were: 2.91 – 2.96 $\times 10^{-11}$ erg s^{-1} cm^{-2} (XMM), 3.76 – 4.04 $\times 10^{-11}$ erg s^{-1} cm^{-2} (XRT-1), and 4.13 – 4.33 $\times 10^{-11}$ erg s^{-1} cm^{-2} (XRT-2). It is unclear whether the changes between the XMM observation and XRT-1 reflect differences in the instruments or the source. Both observations were taken on the same day, nine hours apart. Two months later, the XRT-2 observation shows the source to have a steeper power law index and a higher flux.

ESO 490-G026 – Allowing flux, column density, and power law indices to vary between the four observations of ESO 490-G026 greatly improved the fit with $\Delta\chi^2$ values of 171, 21, and 62. We used an absorbed power law + blackbody model (kT set at the value in Table 4.6) with an Fe K line. Using the `pegpwrl` for a power law com-

ponent, the best fit gave χ^2/dof = 1281.8/1313. The errors on n_H were: 2.96 – 3.59 $\times 10^{21}$ cm^{-2} (XMM), 3.10 – 3.81 $\times 10^{21}$ cm^{-2} (XRT-1), 2.54 – 3.84 $\times 10^{21}$ cm^{-2} (XRT-2), and 4.12 – 6.74 $\times 10^{21}$ cm^{-2} (XRT-3). The errors on the photon index were: 1.66 – 1.71 (XMM), 1.88 – 2.00 (XRT-1), 1.63 – 1.86 (XRT-2), and 1.74 – 2.09 (XRT-3). Finally, the errors on the flux from the pegged power law component were: 3.23 – 3.32 $\times 10^{-11}$ erg s^{-1} cm^{-2} (XMM), 3.79 – 4.09 $\times 10^{-11}$ erg s^{-1} cm^{-2} (XRT-1), 3.53 – 3.97 $\times 10^{-11}$ erg s^{-1} cm^{-2} (XRT-2), and 2.71 – 3.37 $\times 10^{-11}$ erg s^{-1} cm^{-2} (XRT-3). Observation XRT-1 occurred about 3 months before the XMM observation. In this time, the power law index flattened while the flux decreased. The column density of the sources does not vary between the first three observations. However, between XRT-2 and XRT-3, 5 days apart, the column increased by nearly twice the previous amount with the flux decreasing.

SWIFT J0904.3+5538 – As with ESO 490-G026, all of the parameters (column density, flux, and power law photon index) varied for SWIFT J0904.3+5538. For this source, we fixed the parameters of the blackbody component to the best-fit values of the XMM PN observation. No Fe K line was required in this spectrum. The $\Delta\chi^2$ values allowing flux, n_H, and Γ to vary were 523, 12, and 20. Errors for column density were: 0.61 – 1.29 $\times 10^{21}$ cm^{-2} (XMM), 1.01 – 1.93 $\times 10^{21}$ cm^{-2} (XRT-1), and 1.37 – 2.41 $\times 10^{21}$ cm^{-2} (XRT-2). The errors on the photon index were: 1.80 – 1.97 (XMM), 1.45 – 1.69 (XRT-1), and 1.49 – 1.75 (XRT-2). Finally, the errors on the flux from the pegged power law component were: 0.94 – 1.02 $\times 10^{-11}$ erg s^{-1} cm^{-2} (XMM), 0.76 – 0.88 $\times 10^{-11}$ erg s^{-1} cm^{-2} (XRT-1),

and 0.60 – 0.69 $\times 10^{-11}$ erg s^{-1} cm^{-2} (XRT-2). Between XRT-1 and XRT-2, approximately a month apart, the source dimmed by $\approx 20\%$ and then brightened more than twice that amount 3 months later in the XMM observation. With the higher flux, the XMM observation showed less absorption and a steeper slope.

MCG +04-22-042 – MCG +04-22-042 was well-fit with a simple absorbed power law (`pegpwrlw`) with χ^2/dof = 1534.8/1190. This fit required flux and column density to vary between the XMM and XRT observations with $\Delta\chi^2$ of 938 and 298, respectively. Errors for column density were: 0.00 – 0.02 $\times 10^{20}$ cm^{-2} (XMM) and 1.77 – 3.36 $\times 10^{20}$ cm^{-2} (XRT-1). Though these values are small, there was clearly a change in column density, evidenced by the very significant change in χ^2. The errors on the flux for the pegged power law component were: 3.38 – 3.42 $\times 10^{-11}$ erg s^{-1} cm^{-2} (XMM) and 2.29 – 2.44 $\times 10^{-11}$ erg s^{-1} cm^{-2} (XRT-1). The two observations were approximately 5 months apart, showing that the flux and column changed while the photon index remained roughly the same. The flux increased (in the XMM obs.) while the column density decreased.

UGC 6728 – In the four UGC 6728 spectra, the only statistically significant variation is in flux ($\Delta\chi^2 = 680$). The absorbed pegged power law model yields a best-fit χ^2/dof of 855.3/863. This source varies by a high amount with errors in flux of: 1.15 – 1.19 $\times 10^{-11}$ erg s^{-1} cm^{-2} (XMM), 2.12 – 2.28 $\times 10^{-11}$ erg s^{-1} cm^{-2} (XRT-1), 1.40 – 1.60 $\times 10^{-11}$ erg s^{-1} cm^{-2} (XRT-2), and 1.53 – 1.89 $\times 10^{-11}$ erg s^{-1} cm^{-2} (XRT-3). Thus, the flux doubled between the four months from the XMM observation and XRT-1. It

then decreased by about 25% over 5 days, remaining at about the same level in the XRT-3 observation a week later.

WKK 1263 – The only significant change in χ^2 for the combined spectral fits to WKK 1263 was in flux ($\Delta\chi^2 = 150$). The best-fit pegged power law fit had χ^2/dof = 826.8/782. The errors on the flux from the pegged power law component were: 1.52 – 1.57 $\times 10^{-11}$ erg s^{-1} cm^{-2} (XMM), 1.18 – 1.39 $\times 10^{-11}$ erg s^{-1} cm^{-2} (XRT-1), and 1.07 – 1.21 $\times 10^{-11}$ erg s^{-1} cm^{-2} (XRT-2). The source was brighter (by as much as 50%) in the XMM observation taken about a month after the XRT observations.

MCG +09-21-096 – MCG +09-21-096 showed significant variation in χ^2 when allowing variations in flux and power law photon index ($\Delta\chi^2 = 797$ and 12). The model (`tbabs*pegpwrlw`) was a good fit with χ^2/dof = 1289.2/1334. Errors on Γ were: 1.78 – 1.79 (XMM), 1.77 – 1.82 (XRT-1), and 1.67 – 1.74 (XRT-2). The errors on the flux from the pegged power law component were: 2.77 – 2.81 $\times 10^{-11}$ erg s^{-1} cm^{-2} (XMM), 3.97 – 4.16 $\times 10^{-11}$ erg s^{-1} cm^{-2} (XRT-1), and 3.50 – 3.74 $\times 10^{-11}$ erg s^{-1} cm^{-2} (XRT-2). Between the XRT-1 and XMM observations, 7 months apart, the photon index is the same while the flux decreased by about 40%. Then, in the week between the XMM and XRT-2 observation, the source photon index flattened slightly while the flux increased to nearly the level in the XRT-1 observation.

D.1.2 High Column Density/Complex Sources

NGC 1142 – Since NGC 1142 has a strong Fe K line (see Table 4.8 for EW and normalization), we fixed the Fe K parameters for the three XRT observations to the best fit values for the PN spectrum. Allowing the flux to vary between these observations improved the fit by $\Delta\chi^2 = 130$. There is no evidence of variability in column density, however, varying power law components improved the fit by $\Delta\chi^2 \approx 30$. Fitting the spectra with a pegged power law model, the best-fit model has $\chi^2/\mathrm{dof} = 132.6/105$. Errors on the power law photon index, Γ, were: 1.54 – 2.29 (XMM), 2.34 – 3.85 (XRT-1), 2.15 – 3.98 (XRT-2), and 1.08 – 2.94 (XRT-3). Though the error bars for the photon index are large, due to the few counts for this heavily absorbed source, it is clear that observation XRT-1 has a steeper power law component than the XMM observation. The errors on the `pegpwrlw` flux were: 1.97 – 6.01 $\times 10^{-11}$ erg s^{-1} cm^{-2} (XMM), 10.87 – 322.3 $\times 10^{-11}$ erg s^{-1} cm^{-2} (XRT-1), 10.10 – 478 $\times 10^{-11}$ erg s^{-1} cm^{-2} (XRT-2), and 3.81 – 43.13 $\times 10^{-11}$ erg s^{-1} cm^{-2} (XRT-3). Once again, the XRT error bars are large due to the few counts. Noting that the XMM observation occurred 6 months before XRT-1, clearly the flux is higher in the XRT-1 observation while the photon index is steeper. No conclusions can be drawn from the final two XRT observations.

SWIFT J0318.7+6828 – SWIFT J0318.7+6828 showed no variability in column density or power law component between the XMM and two XRT observations ($\Delta\chi^2 < 3$ allowing each to vary). The variability was significant in flux with $\Delta\chi^2 \approx 40$ when a constant model was added. The errors on the `pegpwrlw` flux were computed as: 1.01 – 1.25 $\times 10^{-11}$ erg s^{-1} cm^{-2} (XMM), 0.76 – 1.00 $\times 10^{-11}$ erg s^{-1} cm^{-2} (XRT-1), and 0.79 – 1.04 $\times 10^{-11}$ erg s^{-1} cm^{-2} (XRT-2) with χ^2/dof$= 412.9/452$. Thus, the XRT observations, taken a week apart, did not vary. However, three months earlier the XMM observations show the source to be brighter by $\approx 30\%$.

ESO 362-G018 – As mentioned, the spectra of ESO 362-G018 showed more variability than any other source in this sample. The value $F_{max} - F_{min}/F_{avg}$ for this source was 1.64 in the soft band and 1.22 in the hard band. This source had a complex spectrum, described in the Detailed Spectral Fitting section. We fit the XMM and XRT spectra of this source with a partial covering and power law model. However, we added gaussian components to fit the strong Fe K line (in the XMM observation) and the helium-like oxygen edge. The best-fit model required flux, n$_H$, and Γ to vary ($\Delta\chi^2 =$ 1890, 254, and 40) with χ^2/dof = 538.4/445. The errors on column density were 24.54 – 31.23 $\times 10^{22}$ cm^{-2} (XMM), 6.47 – 269.3 $\times 10^{22}$ cm^{-2} (XRT-1), and 2.12 – 4.71 $\times 10^{22}$ cm^{-2} (XRT-2), with partial covering fractions of 0.91 – 0.93 (XMM), 0.10 – 0.91 (XRT-1), and 0.45 – 0.68 (XRT-2). Errors on the photon index were: 2.13 – 2.23 (XMM), 1.76 – 2.05 (XRT-1), and 1.69 – 1.99 (XRT-2). Finally, errors on flux for the pegged power law component were: 1.46 – 1.83 $\times 10^{-11}$ erg s^{-1} cm^{-2} (XMM), 2.17

– 7.69 $\times 10^{-11}$ erg s^{-1} cm^{-2} (XRT-1), and 2.25 – 2.95 $\times 10^{-11}$ erg s^{-1} cm^{-2} (XRT-2).

In Figure 4.10a, we show the normalized XMM and XRT spectra with best-fit model. It is clear from this figure that this source varied a great deal in these observations. Both XRT-1 and XRT-2, despite the large error bars on XRT-2, have similar spectra. These observations were taken approximately a month apart. Taken two months later, the XMM observation looks like a different source altogether. In this time, the column density increased by a factor of 10. Additionally, the photon index became steeper and the flux dropped by about 50%. Along with these changes, the Fe K line (not distinguishable in the XRT observations) became extremely prominent. One likely explanation for the appearance of the Fe K line is that it was simply too dim to be distinguishable at the higher flux levels exhibited in the XRT observations. This is illustrated in the unfolded spectrum shown in Figure 4.10b. In this plot, where the y-axis shows E^2 f(E), it is clear that if the Fe K line remained at the same flux level as in the XMM observation it would be completely dominated by the power law component.

NGC 6860 – As mentioned in the Detailed Spectral Fitting section, the spectrum of NGC 6860 is quite complex. Due to this complexity and a lack of signal to noise (especially considering that the PN data was corrupted), we are unsure of the true nature of this spectrum. Therefore, we decided to compare the XMM and XRT spectra with the `pcfabs*pow` model. This may not be the most valid description of the data, but it gives a basis to compare the spectra. Using this model, we fit both of the

MOS observations (with the parameters n_H and Γ tied together while the flux was allowed to vary) simultaneously with the XRT observation. Variations were statistically significant for flux, n_H, and Γ with $\Delta\chi^2 =$ 83, 56, and 15, respectively. The best-fit for the partial covering, pegged power law model yielded χ^2/dof of 513.3/430. Errors on the column density were 3.33 – 6.09 $\times 10^{22}\,\mathrm{cm}^{-2}$ (XMM) and 0.59 – 1.73 $\times 10^{22}\,\mathrm{cm}^{-2}$ (XRT) with covering fraction errors of 0.0 – 0.66 (XMM) and 0.73 – 0.92 (XRT). The photon index errors were: 0.64 – 0.88 (XMM) and 1.16 – 1.71 (XRT). Finally, errors on the flux from the pegged power law component were: 1.06 – 1.19 $\times 10^{-11}\,\mathrm{erg\,s}^{-1}\,\mathrm{cm}^{-2}$ (XMM MOS-1), 0.99 – 1.12 $\times 10^{-11}\,\mathrm{erg\,s}^{-1}\,\mathrm{cm}^{-2}$ (XMM MOS-2), and 1.44 – 1.88 $\times 10^{-11}\,\mathrm{erg\,s}^{-1}\,\mathrm{cm}^{-2}$ (XRT). These observations were taken 4 months apart. Interestingly, the XRT observation is well-fit by the partial covering model, giving photon index and covering fractions similar to the typical values seen in Table 4.8. However, the column density is much lower (by a factor of 10 from the other sources). Between the XRT and XMM observations, the column density seems to have doubled while the photon index flattened and the flux decreased by nearly half.

Appendix E

Appendix to Chapter 5

E.1 Additional Tables

In this appendix, we include several tables referred to in Chapter 5. Table E.1 includes all of the SWIFT BAT AGN from the 9-month catalog (Tueller et al. 2008). We include the optical type, host galaxy type, and X-ray observation details for each of these sources. The table is discussed in more detail throughout Chapter 5. Table E.2 includes the X-ray spectral fits to SWIFT XRT observations of sources with no other available data (or for which we could not easily obtain similar quality data to the rest of the survey sources). Table E.3 includes the X-ray spectral fits from the literature or our own analysis of ASCA data from the Tartarus database. Explanations of the analysis are included in § 5.2. Notes on individual sources are found in the following section (§ E.2).

Table E.1: X-ray Observation Details

No.	Source	RA (h m s)	Dec (° ′ ″)	Type[1]	Host Galaxy[1]	Obs.[2]	Obs ID/ref	Ct Rate	Exp Time
1	NGC 235A	00 42 52.8	-23 32 27.6	Sy2	S0 pec, Int	XRT	00035648001, 02	0.02196	21402
2	Mrk 348	00 48 47.1	31 57 25.2	Sy2	SA(s)0/a, Int	ASCA	Awaki et al. (2000)	0.027	28000
3	Mrk 352	00 59 53.3	31 49 36.8	Sy1	SA0	XMM	Winter et al. (2008)	7.3	9773
4	NGC 454	01 14 22.7	-55 23 55.0	Sy2	Pec, Int	XRT	00035244001, 02, 03	0.017	20290
5	Fairall 9	01 23 45.8	-58 48 20.5	Sy1	S, Int?	ASCA	Reynolds (1997)	1.001	22000
6	NGC 526A	01 23 54.4	-35 03 55.4	Sy1.5	S0pec?, Int	ASCA	Turner et al. (1997)	0.641	43000
7	NGC 612	01 33 57.7	-36 29 35.9	Gal	SA0+ pec, Int	XMM	Winter et al. (2008)	0.12	9744
8	ESO 297-018	01 38 37.2	-40 00 41.0	Sy2	Sa sp, Int	Suzaku			
9	NGC 788	02 01 06.5	-06 48 55.8	Sy2	SA(s)0/a	ASCA	77040000	0.03	1921
10	Mrk 1018	02 06 16.0	00 17 29.0	Sy1.5	S0, Int	XRT	00035166001	0.6109	4256
11	LEDA 138501	02 09 34.3	52 26 33.0	Sy1	?	XRT	00035246002	0.365	6435.5
12	Mrk 590	02 14 33.6	00 46 00.1	Sy1.2	SA(s)a	XMM	Longinotti et al. (2007)		71000
13	2MASX J02162987+5126246	02 16 29.8	51 26 24.7	?	–	XMM	Winter et al. (2008)	1.62	8921
14	[HB89] 0212+735	02 17 30.8	73 49 32.5	BL Lac	?	XRT	00035241002	0.08307	6485.4
15	NGC 931	02 28 14.5	31 18 42.1	Sy1.5	Sbc, Int	ASCA	Reynolds et al. (1995)	0.133	18900
16	NGC 985	02 34 37.8	-08 47 15.4	Sy1	SBbc? p (Ring)	Chandra	Krongold et al. (2005)	0.18	77000
17	ESO 416-G002	02 35 13.4	-29 36 16.9	Sy1.9	Sa	XMM	Gallo et al. (2006)		4269
18	ESO 198-024	02 38 19.7	-52 11 32.3	Sy1	N, Int	XMM	Porquet et al. (2004a)		22900
19	QSO B0241+622	02 44 57.7	62 28 06.6	Sy1	?	XRT	00036305001	0.4485	10618
20	NGC 1142	02 55 12.2	00 11 01.0	Sy2	S pec (Ring B), Int	XMM	Winter et al. (2008)	0.28	8921
21	2MASX J03181899+6829322	03 18 19.0	68 29 31.6	Sy1.9	?	XMM	Winter et al. (2008)	1.47	6578

Continued on Next Page…

Table E.1 – Continued

No.	Source	RA (h m s)	Dec (° ′ ″)	Type[1]	Host Galaxy[1]	Obs.[2]	Obs ID/ref	Ct Rate	Exp Time
22	NGC 1275	03 19 48.2	41 30 42.1	Sy2	cD;pec				
23	PKS 0326-288	03 28 36.5	-28 41 48.5	Sy1.9	?	none			
24	NGC 1365	03 33 36.4	-36 08 25.4	Sy1.8	(R′)SBb(s)b, Int	XRT	00035458001, 02	0.027	19434
25	ESO 548-G081	03 42 03.7	-21 14 39.8	Sy1	SB(rs)a pec?, Int?	XMM	Winter et al. (2008)	11.95	8924
26	RBS 476	03 49 23.2	-11 59 26.9	BL Lac	–	ASCA	Reeves & Turner (2000)		109000
27	PGC 13946	03 50 23.8	-50 18 35.6	?	?, Int	XRT	00035251003	0.02	8808
28	2MASX J03565655-4041453	03 56 56.5	-40 41 45.6	Sy1.9	?	XRT	00035600001, 02	0.0628	12579
29	3C 105	04 07 16.5	03 42 25.6	Sy2	?	XRT	00035625001, 02, 03, 04	0.007	22398
30	3C 111	04 18 21.3	38 01 35.8	Sy1	N	ASCA	Reynolds et al. (1998)	0.702	32800
31	1H 0419-577	04 26 00.8	-57 12 00.4	Sy1	?	ASCA	Turner et al. (1999)		24000
32	3C 120	04 33 11.1	05 21 15.5	Sy1	S0, Int?	ASCA	Grandi et al. (1997)	1.861	50000
33	2MASX J04440903+2813003	04 44 09.0	28 13 00.5	Sy2	S	XRT	00035175005, 06, 07	0.114	76404
34	MCG -01-13-025	04 51 41.5	-03 48 33.8	Sy1.2	SAB(s)0+ pec	XMM	Gallo et al. (2006)		2363
35	1RXS J045205.0+493248	04 52 05.0	49 32 45.2	Sy1	?	XRT	00035281002	0.95	2200
36	XSS J05054-2348	05 05 45.7	-23 51 14.0	Sy2	?	XRT	00035206004	0.12	3244
37	4U 0517+17	05 10 45.5	16 29 55.7	Sy1.5	?	XMM	not public		
38	Ark 120	05 16 11.4	00 08 59.3	Sy1	Sb/pec, Int	ASCA	72000000	1.248	47850
39	ESO 362-G018	05 19 35.8	-32 39 28.1	Sy1.5	S0/a, Int	XMM	Winter et al. (2008)	0.95	8921
40	Pictor A	05 19 49.7	-45 46 44.4	Sy1	(R′)SA0:pec	ASCA	Eracleous & Halpern (1998)	0.56	61877
41	ESO 362-G021	05 22 58.0	-36 27 31.0	BL Lac	N	ASCA	73055010	0.40	5133
42	PKS 0537-441	05 38 50.4	-44 05 08.9	BL Lac	?	XRT	00050150011	0.317	22570
43	[HB89] 0537-286	05 39 54.3	-28 39 55.8	Blazar	?	ASCA	Siebert et al. (1996)	0.04	29000

Continued on Next Page…

Table E.1 – Continued

No.	Source	RA (h m s)	Dec (° ′ ″)	Type[1]	Host Galaxy[1]	Obs.[2]	Obs ID/ref	Ct Rate	Exp Time
44	PKS 0548-322	05 50 40.8	-32 16 17.8	BL Lac	?, Int	ASCA	Sambruna & Mushotzky (1998)	1.70	31533
45	NGC 2110	05 52 11.4	-07 27 22.3	Sy2	SAB0-	ASCA	Turner et al. (1997)	0.319	36300
46	MCG +08-11-011	05 54 53.6	46 26 21.5	Sy1.5	SB0	ASCA	Grandi et al. (1998)	0.554	10000
47	EXO 055620-3820.2	05 58 02.0	-38 20 04.6	Sy1	?, Int	ASCA	Turner et al. (1996)		45000
48	IRAS 05589+2828	06 02 10.7	28 28 22.1	Sy1	?	XRT	00035255001	0.35	6446
49	ESO 005-G004	06 05 41.6	-86 37 54.8	Sy2	Sb	Suzaku			
50	Mrk 3	06 15 36.4	71 02 15.0	Sy2	S0	ASCA	Turner et al. (1997)	0.044	27300
51	ESO 121-G028	06 23 45.6	-60 58 44.4	Sy2	SB(l)0/a?, Int	XRT	00036296007	0.02	8716
52	ESO 490-G026	06 40 11.7	-25 53 43.4	Sy1.2	Pec, Int	XMM	Winter et al. (2008)	5.68	9192
53	2MASX J06403799-4321211	06 40 38.0	-43 21 20.9	?	?, Int	XRT	00035601001, 02	0.01	18897
54	2MASX J06411806+3249313	06 41 18.0	32 49 31.4	Sy2	?, Int	XMM	Winter et al. (2008)	0.25	10696
55	Mrk 6	06 52 12.2	74 25 37.6	Sy1.5	SAB0+	XRT	00035461003	0.114	5367
56	Mrk 79	07 42 32.8	49 48 34.9	Sy1.2	SBb	XMM	Gallo et al. (2005)	12.57	1680
57	SDSS J074625.87+254902.2	07 46 25.9	25 49 02.3	Blazar	?	XRT	00035422002	0.143	13365
58	IGR J07597-3842	07 59 41.0	-38 45 36.0	Sy1.2	?	XRT	00035223004	0.6055	7534
59	4C +71.07	08 41 24.4	70 53 42.4	Blazar	?	ASCA	Cappi et al. (1997)	0.30	10540
60	Mrk 18	09 01 58.4	60 09 06.1	Sy2	S?, Int	XMM	Winter et al. (2008)	0.50	9910
61	2MASX J0904699+5536025	09 04 36.9	55 36 02.5	Sy1	?, Int	XMM	Winter et al. (2008)	1.52	7142
62	2MASX J09112999+4528060	09 11 30.0	45 28 05.9	Sy2	?	XMM	Winter et al. (2008)	0.05 (mos)	11530
63	IRAS 09149-6206	09 16 08.9	-62 19 29.6	Sy1	?	XRT	00035233001	0.21	7399
64	2MASX J09180027+0425066	09 18 00.3	04 25 06.2	QSO2	?, Int?	Suzaku	702076010	0.029 (XIS0+3)	4989
65	MCG -01-24-012	09 20 46.2	-08 03 22.0	Sy2	SAB(rs)c, Int	XRT	00035262001	0.08	8522

Continued on Next Page…

Table E.1 – Continued

No.	Source	RA (h m s)	Dec (° ′ ″)	Type[1]	Host Galaxy[1]	Obs.[2]	Obs ID/ref	Ct Rate	Exp Time
66	MCG +04-22-042	09 23 43.0	22 54 32.4	Sy1.2	E?	XMM	Winter et al. (2008)	13.99	9012
67	Mrk 110	09 25 12.9	52 17 10.7	Sy1	S?, Int	ASCA	73091000	1.15	20747
68	NGC 2992	09 45 42.0	-14 19 35.0	Sy2	Sa pec, Int	ASCA	Turner et al. (1997)	0.039	27300
69	MCG -05-23-016	09 47 40.2	-30 56 56.0	Sy2	(RL)SA(l)	ASCA	Turner et al. (1997)	1.583	34000
70	NGC 3081	09 59 29.5	-22 49 34.7	Sy2	SAB(r)0/a	ASCA	74043000	0.03	34738
71	NGC 3227	10 23 30.6	19 51 54.0	Sy1.5	SAB(s) pec, Int	ASCA	73068000	0.42	34312
72	NGC 3281	10 31 52.1	-34 51 13.3	Sy2	SAB(rs+)a	ASCA	74058000	0.015	16959
73	2MASX J10384520-4946531	10 38 44.5	-49 46 57.4	Sy1	?	XRT	00035225003	0.087	16907
74	LEDA 093974	10 40 22.5	-46 25 25.7	Sy2	S0	XRT	00035345003	0.058	14377
75	Mrk 417	10 49 30.9	22 57 51.8	Sy2	Sa	XMM	Winter et al. (2008)	0.145	7437
76	Mrk 421	11 04 27.3	38 12 31.7	BL Lac	?	ASCA	70008000	2.20	32769
77	NGC 3516	11 06 47.5	72 34 07.0	Sy1.5	(R)SB(s)	ASCA	71007000	2.38	29842
78	1RXS J112716.6+190914	11 27 16.3	19 09 20.2	Sy1.8	?	XRT	00037088002	0.11	10062
79	NGC 3783	11 39 01.7	-37 44 19.0	Sy1	(R')SB(r)a	ASCA	74054010	1.71	18716
80	SBS 1136+594	11 39 09.0	59 11 54.6	Sy1.5	?	XRT	00035265001	0.34	8991
81	UGC 06728	11 45 16.0	79 40 53.4	Sy1.2	SB0/a, Int?	XMM	Winter et al. (2008)	4.25	7220
82	2MASX J11454045-1827149	11 45 40.5	-18 27 15.5	Sy1	Irr, Int	XRT	00035645001	0.72	9402
83	CGCG 041-020	12 00 57.9	06 48 23.0	Sy2	S?	XMM	Winter et al. (2008)	0.465	9777
84	IGR J12026-5349	12 02 47.6	-53 50 07.8	Sy2	SB0 pec, Int	chandra not public			
85	NGC 4051	12 03 09.6	44 31 52.7	Sy1.5	SAB(rs)bc	ASCA	70001000	0.917	25970
86	Ark 347	12 04 29.7	20 18 58.3	Sy2	S0: pec	XRT	00035599001, 02	0.013	21706
87	NGC 4102	12 06 23.1	52 42 39.2	LINER	SAB(s)b?	Chandra	too short?		

Continued on Next Page…

Table E.1 – Continued

No.	Source	RA (h m s)	Dec (° ′ ″)	Type[1]	Host Galaxy[1]	Obs.[2]	Obs ID/ref	Ct Rate	Exp Time
88	NGC 4138	12 09 29.8	43 41 07.1	Sy1.9	SA(r)0+	XMM	Cappi et al. (2006)		8856
89	NGC 4151	12 10 32.6	39 24 20.5	Sy1.5	(R′)SAB(rs)ab	ASCA	78001003	1.255	46006
90	Mrk 766	12 18 26.5	29 48 46.4	Sy1.5	(R′)SB(s)a	ASCA	71046000	0.819	32970
91	NGC 4388	12 25 46.8	12 39 43.6	Sy2	SA(s)b	ASCA	73073000	0.053	26040
92	NGC 4395	12 25 48.9	33 32 48.5	Sy1.9	SA(s)m, Int	ASCA	78009000	0.079	36084
93	3C 273	12 29 06.7	02 03 08.6	Blazar	?	ASCA	70023000	3.849	31964
94	NGC 4507	12 35 36.6	-39 54 33.5	Sy2	SAB(s)ab	ASCA	Turner et al. (1997)	0.1421	24800
95	ESO 506-G027	12 38 54.6	-27 18 28.1	Sy2	S pec sp	XMM	Winter et al. (2008)	0.27	8919
96	XSS J12389-1614	12 39 06.3	-16 10 47.6	Sy2	?	XRT	00035208002	0.103	6622
97	NGC 4593	12 39 39.4	-05 20 39.1	Sy1	(R)SB(rs)b	ASCA	71024000	1.478	21185
98	WKK 1263	12 41 25.7	-57 50 03.5	Sy2?	?	XMM	Winter et al. (2008)	2.72	8902
99	3C 279	12 56 11.2	-05 47 21.5	Blazar	?	ASCA	70026000	0.299	37195
100	SBS 1301+540	13 03 59.5	53 47 30.1	Sy1	?	XMM	Winter et al. (2008)	10.30	8408
101	NGC 4945	13 05 27.5	-49 28 05.5	Sy2	SB(s)cd	ASCA	Turner et al. (1997)	0.045	6100
102	NGC 4992	13 09 13.0	11 38 45.2	Gal	Sa	XMM	Winter et al. (2008)	0.137	12849
103	MCG -03-34-064	13 22 24.5	-16 43 43.0	Sy1.8	SB?, Int	ASCA	73029000	0.044	36174
104	Cen A	13 25 27.6	-43 01 09.1	Sy2	S0 pec, Int				
105	MCG -06-30-015	13 35 53.8	-34 17 44.2	Sy1.2	E-S0	ASCA	70016010	1.18	30026
106	NGC 5252	13 38 16.0	04 32 33.4	Sy1.9	S0	ASCA	Turner et al. (1997)	0.063	27300
107	4U 1344-60	13 47 24.0	-60 38 24.0	Sy1.5	S	XRT	00035284002	0.388	14065
108	IC 4329A	13 49 19.3	-30 18 34.6	Sy1.2	SA0+, Int	ASCA	70005000	2.025	27212
109	Mrk 279	13 53 03.5	69 18 29.5	Sy1.5	S0, Int	ASCA	72028000	1.342	21357

Continued on Next Page…

Table E.1 – Continued

No.	Source	RA (h m s)	Dec (° ′ ″)	Type[1]	Host Galaxy[1]	Obs.[2]	Obs ID/ref	Ct Rate	Exp Time
110	NGC 5506	14 13 14.9	-03 12 27.0	Sy1.9	Sa pec, Int?	ASCA	75033000	0.9316	39272
111	RBS 1366	14 17 56.7	25 43 26.4	BL Lac	?	XRT	00035270001	0.623	7930
112	NGC 5548	14 17 59.5	25 08 12.5	Sy1.5	(R′)SA(s)0/a	ASCA	76029000	2.633	21200
113	ESO 511-G030	14 19 22.4	-26 38 40.9	Sy1	SA(rs)c pec, Int	ASCA	76067000	0.467	16358
114	RBS 1399	14 28 32.7	42 40 20.6	BL Lac	?	ASCA	76053000	1.44	36000
115	NGC 5728	14 42 23.9	-17 15 11.5	Sy2	(R)SAB(r)a	Chandra	Zhang et al. (2006)		18700
116	Mrk 841	15 04 01.2	10 26 16.1	Sy1	E	XMM	Petrucci et al. (2007)	17.9	5861
117	Mrk 290	15 35 52.4	57 54 09.4	Sy1	E1?, Int?	ASCA	72027000	0.308	41018
118	Mrk 1498	16 28 04.1	51 46 31.4	Sy1.9	S?	XRT	00035271002	0.0613	19948
119	2MASX J16481523-3035037	16 48 15.2	-30 35 04.2	Sy1	?	XRT	00035348002	0.244	9203
120	NGC 6240	16 52 58.9	02 24 02.9	Sy	I0: pec, Int				
121	Mrk 501	16 53 52.2	39 45 36.7	BL Lac	E?	ASCA	76052000	5.55	5904
122	NGC 6300	17 16 59.5	-62 49 14.2	Sy2	SB(rs)b	XMM	Matsumoto et al. (2004)		
123	GRS 1734-292	17 37 24.3	-29 10 48.0	Sy1	?				
124	1RXS J174538.1+290823	17 45 38.3	29 08 22.2	Sy1	?	XRT	00035273001	0.237	9344
125	3C 382	18 35 02.2	32 41 50.3	Sy1	?	ASCA	Sambruna et al. (1999)	1.793	40500
126	ESO 103-035	18 38 20.3	-65 25 39.4	Sy2	SA0, Int	ASCA	Forster et al. (1999)	17.31	15700
127	3C 390.3	18 42 09.0	79 46 17.0	Sy1	?	ASCA	Sambruna et al. (1999)	0.528	19200
128	NVSS 193013+341047	19 30 13.3	34 10 46.9	Sy1	?	XRT	00035274001, 02	0.013	10247
129	NGC 6814	19 42 40.7	-10 19 24.6	Sy1.5	SAB(rs)bc	ASCA	70012000	0.032	39082
130	3C 403	19 52 15.8	02 30 24.5	Sy2	S0	Chandra	Kraft et al. (2005)		45900
131	Cyg A	19 59 28.3	40 44 02.0	Sy2	Sc, Int	ASCA	Sambruna et al. (1999)	0.911	21100

Continued on Next Page…

Table E.1 – Continued

No.	Source	RA (h m s)	Dec (° ′ ″)	Type[1]	Host Galaxy[1]	Obs.[2]	Obs ID/ref	Ct Rate	Exp Time
132	2MASX J19595975+6508547	19 59 59.9	65 08 54.6	BL Lac	E	XRT	00035025006	3.50	479.5
133	NGC 6860	20 08 46.9	-61 06 00.7	Sy1.5	(R′)SB(r)ab	XMM	Winter et al. (2008)	0.46	11815 (mos)
134	NGC 6921	20 28 28.9	25 43 24.3	Sy2	SA(r)0/a, Int	XMM	Winter et al. (2008)	0.255	8789
135	MCG +04-48-002	20 28 35.1	25 44 01.0	Sy2	Scd, Int	XMM	Winter et al. (2008)	0.096	8789
136	4C +74.26	20 42 37.3	75 08 02.4	Sy1	?	ASCA	74097000	0.615	21210
137	Mrk 509	20 44 09.7	-10 43 24.6	Sy1.2	S?	ASCA	71013000	1.96	40071
138	IC 5063	20 52 02.3	-57 04 07.7	Sy2	SA(s)0+	ASCA	Turner et al. (1997)	0.096	23900
139	2MASX J21140128+8204483	21 14 01.2	82 04 48.4	Sy1	?	XRT	00035624002	0.448	5179
140	IGR J21247+5058	21 24 38.1	50 58 58.1	Sy1	?	XRT	00035626002	0.708	6690
141	IGR 21277+5656	21 27 45.9	56 56 34.4	Sy1	?	XRT	00035215003	0.426	8372
142	RX J2135.9+4728	21 35 55.0	47 28 23.2	Sy1	?	XRT	00035628003	0.138	9115
143	PKS 2149-306	21 51 55.5	-30 27 54.0	Blazar	?	ASCA	Siebert et al. (1996)	0.24	19000
144	UGC 11871	22 00 41.4	10 33 08.6	Sy1.9	Sb, Int	XRT	00035278003	0.078	8928
145	NGC 7172	22 02 01.9	-31 52 11.3	Sy2	Sa pec sp	ASCA	Turner et al. (1997)	0.0066	14900
146	NGC 7213	22 09 16.2	-47 10 00.1	Sy1.5	Sa	ASCA	71026000	1.226	27091
147	NGC 7314	22 35 46.2	-26 03 00.7	Sy1.9	SAB(rs)bc, Int	ASCA	Turner et al. (1997)	0.9284	45300
148	NGC 7319	22 36 03.6	33 58 32.5	Sy2	SB(s)bc pec, Int	XRT	00035083004	0.012	14731
149	3C 452	22 45 48.8	39 41 15.7	Sy2	S?	Chandra			
150	3C 454.3	22 53 57.7	16 08 53.5	Blazar	?	XRT	00035030001	1.151	13668
151	MR 2251-178	22 54 05.8	-17 34 54.8	Sy1	?	ASCA	74028000	0.649	17760
152	NGC 7469	23 03 15.6	08 52 26.4	Sy1.2	(R′)SAB(rs)a, Int	ASCA	71028010	1.593	18707
153	Mrk 926	23 04 43.5	-08 41 08.5	Sy1.5	Sbc, Int	ASCA	75049000	1.218	37221

Continued on Next Page…

Table E.1 – Continued

No.	Source	RA (h m s)	Dec (° ′ ″)	Type[1]	Host Galaxy[1]	Obs.[2]	Obs ID/ref	Ct Rate	Exp Time
154	NGC 7582	23 18 23.5	-42 22 14.2	Sy2	(R′)SB(s)ab, Int	ASCA	Turner et al. (1997)	0.0906	17800

[1]AGN type is from Tueller et al. (2008). For AGN types, optical identifications are listed, where available. Where "Gal" is indicated, there are no optical emission lines indicative of the presence of an AGN. The optical spectrum looks like a galaxy spectrum. Additional host galaxy classifications were obtained from the NED and LEDA databases. Where "?" is indicated, there is no available classification.

[2]Observations were collected from archival or published work from ASCA, Chandra, XMM-Newton, Suzaku, and the SWIFT XRT instrument.

Table E.2: X-ray Fits of SWIFT XRT spectra

Source	$n_{H(Gal)}$ [1]	$n_{H(abs)}$	Cvr. Frac	Γ	χ^2/dof	F_X [2]	type
NGC 235A	0.014	$28.25^{+3.79}_{-3.37}$	$0.9975^{+0.0021}_{-0.0029}$	$2.85^{+0.40}_{-0.66}$	20.6/21	0.06, 2.92	C
NGC 454	0.026	$15.90^{+4.91}_{-3.64}$	$0.997^{+0.003}_{-0.004}$	$2.81^{+1.33}_{-0.88}$	19.7/15	0.023, 1.964	C
Mrk 1018	0.0258	$0.00^{+0.01}_{-0.00}$	–	$1.93^{+0.07}_{-0.05}$	99.5/99	8.73, 11.89	S
LEDA 138501	0.169	$0.030^{+0.040}_{-0.030}$	–	$1.812^{+0.094}_{-0.089}$	87.6/100	5.08, 11.38	S
[HB89] 0212+735	0.259	$0.350^{+0.220}_{-0.200}$	–	$1.376^{+0.259}_{-0.245}$	30.6/23	0.686, 5.54	S
QSO B0241+622	0.742	$0.100^{+0.070}_{-0.060}$	–	$1.733^{+0.083}_{-0.080}$	197.8/185	3.89, 25.82	S
NGC 1365	0.0142	104.8	$0.74^{+0.25}_{-0.15}$	$1.71^{+0.29}_{-0.23}$	55.0/43	0.40, 0.88	C
PGC 13946	0.0156	$14.4^{+7.4}_{-5.9}$	$0.94^{+0.05}_{-0.19}$	$1.35^{+1.14}_{-0.70}$	9/6	0.08, 2.96	C
2MASX J03565655-4041453	0.026	$3.27^{+0.92}_{-0.61}$	–	$1.94^{+0.42}_{-0.30}$	29.4/36	0.19, 5.58	S
2MASX J04440903+2813003	0.197	$3.39^{+0.31}_{-0.25}$	$0.98996^{+0.003}_{-0.003}$	$1.37^{+0.11}_{-0.08}$	329.8/331	0.02, 12.34	C
1RXS J045205.0+493248	0.531	$0.001^{+0.22}_{-0.001}$	–	$1.95^{+0.16}_{-0.11}$	110.1/86	11.4, 37.8	S
XSS J05054-2348	0.0228	$6.57^{+3.03}_{-2.39}$	–	$1.51^{+0.56}_{-0.51}$	21.9/16	0.15, 13.4	S
PKS 0537-441	0.0394	–	–	$1.78^{+0.03}_{-0.03}$	274.8/237	4.41, 7.57	S

Continued on Next Page…

Table E.2 – Continued

Source	$n_{H(Gal)}$[1]	$n_{H(abs)}$	Cvr. Frac	Γ	χ^2/dof	F_X[2]	type
IRAS 05589+2828	0.462	$0.00^{+0.04}$	–	$1.60^{+0.06}_{-0.06}$	106.4/98	3.95, 16.42	S
ESO 121-G028	0.0469	$16.19^{+12.6}_{-9.4}$	–	$2.20^{+1.55}_{-1.32}$	4/6	0, 2.97	S*
2MASX J06403799-4321211	0.0624	$16.13^{+10.0}_{-12.3}$	–	$1.79^{+1.41}_{-1.51}$	6.6/7	0.0006, 1.58	S*
Mrk 6	0.0623	$3.26^{+1.33}_{-1.19}$	$0.909^{+0.041}_{-0.075}$	$1.31^{+0.40}_{-0.37}$	31.6/26	0.44, 11.36	C
SDSS J074625.87+254902.2	0.04	$0.062^{+0.04}_{-0.03}$	–	$1.29^{+0.09}_{-0.08}$	95.8/84	1.63, 6.63	S
IGR J07597-3842	0.62	$0.0^{+0.03}$	–	$1.88^{+0.06}_{-0.05}$	185/181	6.47, 27.81	S
IRAS 09149-6206	0.189	$0.85^{+0.26}_{-0.17}$	–	$1.74^{+0.20}_{-0.14}$	75.7/68	1.81, 11.59	S
MCG -01-24-012	0.0355	$11.44^{+2.82}_{-2.27}$	–	$2.17^{+0.50}_{-0.44}$	26.8/29	0.04, 8.28	S*
2MASX J10384520-4946531	0.262	$1.55^{+0.56}_{-0.58}$	$0.880^{+0.064}_{-0.063}$	$1.44^{+0.18}_{-0.20}$	77.8/66	0.60, 6.17	C
LEDA 093974	0.141	$4.24^{+1.06}_{-1.00}$	$0.986^{+0.007}_{-0.014}$	$2.12^{+0.43}_{-0.40}$	57.7/35	0.16, 4.95	C
1RXS J112716.6+190914	0.017	$0.25^{+0.10}_{-0.08}$	–	$1.79^{+0.15}_{-0.15}$	58.4/48	1.38, 3.77	S
SBS 1136+594	0.0112	–	–	$1.94^{+0.05}_{-0.04}$	132.6/115	4.76, 6.15	S
2MASX J11454045-1827149	0.0349	–	–	$1.92^{+0.03}_{-0.03}$	212.7/214	10.37, 14.33	S
Ark 347	0.0236	$30.0^{+8.76}_{-8.88}$	$0.995^{+0.005}_{-0.017}$	$2.17^{+1.03}_{-0.80}$	6.3/13	0.03, 1.80	C

Continued on Next Page...

Table E.2 – Continued

Source	$n_{H(Gal)}$[1]	$n_{H(abs)}$	Cvr. Frac	Γ	χ^2/dof	F_X[2]	type
XSS J12389-1614	0.0369	$3.21^{+0.83}_{-0.71}$	–	$1.84^{+0.37}_{-0.35}$	19.2/30	0.30, 9.57	S
4U 1344-60	1.05	$1.45^{+0.20}_{-0.19}$	–	$1.69^{+0.09}_{-0.09}$	231.7/216	2.09, 29.20	S
RBS 1366	0.0167	$0.05^{+0.01}_{-0.01}$	–	$2.08^{+0.06}_{-0.06}$	195.1/176	9.26, 11.03	S
Mrk 1498	0.021	$17.84^{+2.37}_{-1.82}$	$0.990^{+0.005}_{-0.006}$	$1.92^{+0.29}_{-0.22}$	55.8/55	0.11, 7.20	C
2MASX J16481523-3035037	0.173	$0.24^{+0.06}_{-0.06}$	–	$1.72^{+0.10}_{-0.10}$	106.3/96	2.93, 9.95	S
1RXS J174538.1+290823	0.137	$0.02^{+0.07}_{-0.02}$	–	$1.85^{+0.07}_{-0.07}$	84.8/89	3.25, 6.20	S
NVSS 193013+341047	0.173	$27.47^{+20.37}_{-13.74}$	$0.926^{+0.065}_{-0.426}$	$0.958^{+1.56}_{-1.54}$	0.74/3	0.03, 2.22	C
2MASX J19595975+6508547	0.103	$0.07^{+0.04}_{-0.04}$	–	$1.93^{+0.11}_{-0.10}$	77.9/71	50.19, 91.75	S
2MASX J21140128+8204483	0.0736	$0.047^{+0.023}_{-0.021}$	–	$1.89^{+0.09}_{-0.09}$	99.9/96	6.27, 11.92	S
IGR J21247+5058	1.17	$1.30^{+0.23}_{-0.21}$	–	$1.33^{+0.09}_{-0.09}$	202.5/194	3.01, 63.18	S
IGR 21277+5656	0.806	$0.424^{+0.11}_{-0.11}$	–	$2.02^{+0.10}_{-0.10}$	141.9/144	4.29, 20.25	S
RX J2135.9+4728	0.385	$0.44^{+0.17}_{-0.15}$	–	$1.66^{+0.16}_{-0.15}$	52.1/56	1.37, 7.37	S
UGC 11871	0.0544	$2.39^{+0.71}_{-0.56}$	–	$1.53^{+0.27}_{-0.25}$	39.1/31	0.39, 6.35	S*
NGC 7319	0.083	$86.48^{+30.87}_{-20.55}$	$0.9965^{+0.0027}_{-0.0055}$	$2.87^{+0.53}_{-0.28}$	1.6/4	0.13, 1.49	C

Continued on Next Page...

Table E.2 – Continued

Source	$n_{H(Gal)}$[1]	$n_{H(abs)}$	Cvr. Frac	Γ	χ^2/dof	F_X[2]	type
3C 454.3	0.0645	$0.08^{+0.01}_{-0.01}$	–	$1.49^{+0.03}_{-0.03}$	446.7/407	14.31, 46.33	S

[1]Milky Way Galactic absorption obtained from the n_H FTOOL on HEASARC in units of 10^{22} cm^{-2}.

[2]Observed flux in the 0.5–2 keV and 2–10 keV bands in units of 10^{-12} erg s^{-1} cm^{-2}. The statistical errors on fluxes are very small and the systematic errors are dominated by model uncertainties.

Table E.3: X-ray Spectral Fits from the Literature/Suzaku XIS/*TARTARUS* Fits

Source	$n_{H(abs)}$	Γ	par$_{model}$[3]	Fe K E	Fe K EW	χ^2/dof	F$_X$[2]	model	type
Mrk 348	16^{+4}_{-3}	$1.69^{+0.36}_{-0.39}$	–	$6.27^{+0.08}_{-0.07}$	215^{+75}_{-75}	117.4/116	0.07, 4.84	double pow	C
Fairall 9	–	$1.91^{+0.01}_{-0.01}$	–	$6.37^{+0.11}_{-0.13}$	350^{+150}_{-100}	1283/1149	18.2,[4]19.0	pow	S
NGC 526A	$1.50^{+0.14}_{-0.14}$	$1.82^{+0.16}_{-0.14}$	32.5	6.4	111^{+33}_{-56}	1676/1586	3.5,[4]35.4	double pow	C
ESO 297-018	$41.71^{+4.70}_{-2.90}$	$1.28^{+0.14}_{-0.16}$	$0.993^{+0.004}_{-0.006}$	$6.38^{+0.02}_{-0.02}$	276^{+57}_{-51}	180.7/176	0.03, 3.26	pcfabs	C
NGC 788	$46.89^{+4.68}_{-4.47}$	$1.89^{+0.24}_{-0.16}$	$0.993^{+0.003}_{-0.005}$	$6.41^{+0.09}_{-0.12}$	148^{+114}_{-45}	1676/1586	0.11, 4.95	pcfabs	C
Mrk 590	–	$1.62^{+0.02}_{-0.02}$	–	$6.39^{+0.02}_{-0.02}$	121^{+11}_{-16}	948/964	4.4, 6.4	pow	S
NGC 931	$0.36^{+0.08}_{-0.08}$	$1.75^{+0.11}_{-0.11}$	$0.066^{+0.011}_{-0.036}$	$6.41^{+0.15}_{-0.15}$	550^{+250}_{-250}	342/365	1.14,[4]5.1	pow + bb	S
NGC 985	–	$1.60^{+0.03}_{-0.03}$	$0.010^{+0.01}_{-0.01}$	–	–	179/174	63, 54	pow + bb	S
ESO 416-G002	< 0.027	$1.63^{+0.06}_{-0.04}$	$0.105^{+0.006}_{-0.004}$	–	–	647/634	7.53	pow + bb	S
ESO 198-024	–	$1.84^{+0.02}_{-0.02}$	$0.172^{+0.007}_{-0.007}$	6.41	77^{+23}_{-23}	1667.9/1535	15.8, 11.0	pow + bb	S
RBS 476	–	$1.87^{+0.2}_{-0.2}$	–	–	–	47.2/50	10.30, 18.02	pow	S
3C 105	$28.16^{+1.41}_{-3.23}$	$1.36^{+0.18}_{-0.36}$	$0.973^{+0.005}_{-0.004}$	$6.42^{+0.04}_{-0.06}$	216^{+98}_{-61}	315.4/317	0.04, 2.08	pcfabs	C
3C 111	$0.62^{+0.03}_{-0.02}$	$1.72^{+0.03}_{-0.02}$	–	–	–	1653/1724	5.0, 35	pow	S
1H 0419-577	–	$1.48^{+0.07}_{-0.07}$	–	–	–	280/319	4.8, 9.4	pow	S
3C 120	$0.16^{+0.01}_{-0.01}$	$2.00^{+0.02}_{-0.02}$	–	$6.06^{+0.26}_{-0.21}$	> 400	139.9/126	23.5,[4]45.9	pow	S
MCG -01-13-025	< 0.0039	$1.70^{+0.03}_{-0.03}$	$0.139^{+0.027}_{-0.032}$	–	–	819.3/874	21.3	pow + bb	S
Ark 120	–	$1.90^{+0.02}_{-0.03}$	$0.20^{+0.01}_{-0.01}$	$6.46^{+0.06}_{-0.08}$	123^{+38}_{-36}	553/449	17.1, 27.8	pow + bb	S
Pictor A	$0.06^{+0.02}_{-0.02}$	$1.77^{+0.04}_{-0.05}$	–	–	–	113/106	6.97,11.33	pow	S
ESO 362-G021	–	$1.58^{+0.03}_{-0.03}$	–	–	–	365.6/336	4.65,11.02	pow	S
[HB89] 0537-286	–	$1.60^{+0.07}_{-0.07}$	–	–	–	142.8/140	0.57,1.75	pow	S
PKS 0548-322	$0.103^{+0.004}_{-0.004}$	$2.05^{+0.02}_{-0.02}$	–	–	–	862.9/846	25, 28	pow	S

Continued on Next Page…

Table E.3 – Continued

Source	$n_{H(abs)}$	Γ	par$_{model}$[3]	Fe K E	Fe K EW	χ^2/dof	F_X[2]	model	type
NGC 2110	$2.84^{+0.19}_{-0.16}$	$1.54^{+0.08}_{-0.07}$	$0.952^{+0.006}_{-0.002}$	6.4	103^{+29}_{-29}	628/682	0.86,[4]25.5	pcfabs	C
MCG +08-11-011	$0.25^{+0.016}_{-0.015}$	$1.64^{+0.03}_{-0.03}$	–	$6.43^{+0.08}_{-0.08}$	380^{+102}_{-83}	896/860	5.5, 20.3	pow	S
EXO 055620-3820.2	$2.57^{+0.14}_{-0.14}$	$1.82^{+0.06}_{-0.07}$	$0.966^{+0.005}_{-0.005}$	6.26	200^{+100}_{-100}	1177/1215	1.44, 22.47	pcfabs	C
ESO 005-G004	$5.58^{+0.16}_{-0.16}$	$1.48^{+0.04}_{-0.04}$	$0.984^{+0.002}_{-0.003}$	$6.39^{+0.05}_{-0.05}$	79^{+9}_{-15}	1316.1/1161	0.15, 10.41	pcfabs	C
Mrk 3	$1.24^{+5.67}_{-1.24}$	$2.94^{+0.55}_{-0.39}$	0.076	6.4	977^{+193}_{-137}	134.1/253	0.58,[4]2.15	double pow	C
Mrk 79	< 0.0063	$1.85^{+0.04}_{-0.04}$	$0.122^{+0.007}_{-0.007}$	$6.33^{+0.08}_{-0.09}$	$117^{+0.15}_{-0.15}$	436.8/480	42.75	pow + bb	S
4C +71.07	$0.11^{+0.03}_{-0.03}$	$1.45^{+0.05}_{-0.05}$	–	6.4	< 110	437.6/503	4.25, 14.0	pow	S
2MASX J09180027+0425066	$11.13^{+1.55}_{-1.18}$	$1.77^{+0.22}_{-0.15}$	$0.987^{+0.006}_{-0.005}$	$6.39^{+0.05}_{-0.05}$	$65.6^{+39.4}_{-30.2}$	310.6/333	0.02, 1.38	pcfabs	C
Mrk 110	$0.02^{+0.01}_{-0.01}$	$1.78^{+0.02}_{-0.02}$	–	–	–	484.4/451	16.55, 27.93	pow	S
NGC 2992	$1.19^{+2.21}_{-0.96}$	$1.54^{+0.41}_{-0.25}$	$0.476^{+0.209}_{-0.368}$	6.4	656^{+204}_{-191}	252/257	0.86,[4]3.51	pcfabs	C
MCG -05-23-016	$1.60^{+0.005}_{-0.006}$	$1.90^{+0.04}_{-0.04}$	139	6.4	79^{+16}_{-14}	1995/1744	7.84,[4]85.1	double pow	C
NGC 3081	$94.2^{+6.2}_{-7.2}$	$1.60^{+0.12}_{-0.17}$	$0.990^{+0.011}_{-0.002}$	$6.38^{+0.03}_{-0.05}$	191^{+66}_{-58}	303/245	0.18, 5.53	pcfabs	C
NGC 3227	$1.74^{+0.12}_{-0.09}$	$1.35^{+0.04}_{-0.04}$	$0.852^{+0.006}_{-0.010}$	$6.36^{+0.03}_{-0.06}$	142^{+22}_{-40}	488.1/445	2.44, 28.29	pcfabs	C
NGC 3281	$86.3^{+16.32}_{-16.12}$	$1.67^{+0.44}_{-0.50}$	$0.981^{+0.012}_{-0.025}$	$6.36^{+0.06}_{-0.06}$	617^{+225}_{-181}	153.6/135	0.01, 2.58	pcfabs	C
Mrk 421	$0.077^{+0.007}_{-0.007}$	$2.95^{+0.01}_{-0.01}$	–	–	–	621.1/439	61.22, 21.19	pow	S
NGC 3516	$0.353^{+0.32}_{-0.12}$	$1.73^{+0.01}_{-0.01}$	$0.99998^{+2e-5}_{-0.0462}$	$6.32^{+0.09}_{-0.02}$	104^{+20}_{-20}	584.2/413	2.44, 28.29	pcfabs, bb	C
NGC 3783	$0.57^{+0.21}_{-0.14}$	$1.60^{+0.04}_{-0.03}$	$0.722^{+0.107}_{-0.082}$	$6.34^{+0.07}_{-0.04}$	80^{+26}_{-29}	559.9/421	23.96, 70.49	pcfabs, bb	C
NGC 4051	–	$1.95^{+0.02}_{-0.02}$	$0.087^{+0.005}_{-0.003}$	$6.43^{+0.02}_{-0.02}$	147^{+41}_{-40}	509.7/434	24.11, 21.86	pow + bb	S
NGC 4138	$8.00^{+1.00}_{-1.00}$	$1.5^{+0.1}_{-0.1}$	$0.3^{+0.1}_{-0.1}$	6.4	83^{+30}_{-30}	408/408	0.06, 5.5	pow + bb	S*
NGC 4151	$5.32^{+0.07}_{-0.08}$	$1.46^{+0.02}_{-0.02}$	$0.959^{+0.002}_{-0.001}$	$6.36^{+0.01}_{-0.04}$	137^{+10}_{-14}	692/413	3.31, 129.36	pcfabs	C
Mrk 766	–	$1.78^{+0.01}_{-0.01}$	$0.043^{+0.007}_{-0.005}$	$6.38^{+0.07}_{-0.06}$	75^{+40}_{-32}	498.2/441	15.65, 20.09	pow + bb	S
NGC 4388	$36.17^{+3.81}_{-3.82}$	$1.79^{+0.17}_{-0.17}$	$0.954^{+0.013}_{-0.016}$	$6.44^{+0.04}_{-0.04}$	466^{+88}_{-92}	396.5/344	0.52, 5.90	pcfabs	C

Continued on Next Page…

Table E.3 – Continued

Source	$n_{H(abs)}$	Γ	par$_{model}$[3]	Fe K E	Fe K EW	χ^2/dof	F_X[2]	model	type
NGC 4395	$3.30^{+0.68}_{-0.67}$	$1.07^{+0.12}_{-0.06}$	$0.678^{+0.056}_{-0.062}$	$6.22^{+0.11}_{-0.16}$	101^{+69}_{-64}	318.6/359	0.51, 5.95	pcfabs	C
3C 273	–	$1.61^{+0.01}_{-0.01}$	$0.154^{+0.021}_{-0.013}$	–	–	574.06/452	57.44, 116.13	pow + bb	S
NGC 4507	$34.28^{+4.50}_{-4.57}$	$1.65^{+0.35}_{-0.38}$	66	6.4	167^{+34}_{-33}	564/490	0.51,[4]22.8	double pow	C
NGC 4593	$0.031^{+0.011}_{-0.012}$	$1.86^{+0.01}_{-0.02}$	–	$6.41^{+0.06}_{-0.08}$	105^{+49}_{-23}	583.8/444	21.11, 34.19	pow	S
3C 279	$0.020^{+0.017}_{-0.016}$	$1.78^{+0.04}_{-0.03}$	–	–	–	449.2/430	4.59, 8.06	pow	S
NGC 4945	$0.793^{+0.957}_{-0.495}$	$1.75^{+0.31}_{-0.14}$	$0.691^{+0.219}_{-0.590}$	6.4	1020^{+210}_{-298}	255/233	0.76,[4]2.91	pcfabs	C
MCG -03-34-064	$40.73^{+4.79}_{-4.30}$	$1.83^{+0.28}_{-0.23}$	$0.961^{+0.014}_{-0.008}$	$6.44^{+0.09}_{-0.10}$	191^{+123}_{-74}	306.9/261	0.41, 4.78	pcfabs, apec	C
MCG -06-30-015	$0.19^{+0.03}_{-0.01}$	$1.78^{+0.03}_{-0.02}$	$0.057^{+0.003}_{-0.003}$	6.41	71.4^{+29}_{-40}	488.2/450	20.41, 37.65	pow + bb	S
NGC 5252	$4.34^{+0.52}_{-0.42}$	$1.55^{+0.16}_{-0.13}$	$0.962^{+0.009}_{-0.009}$	6.4	76^{+54}_{-53}	483/478	0.173,[4]5.81	pcfabs	C
IC 4329A	$0.61^{+0.03}_{-0.03}$	$1.80^{+0.01}_{-0.01}$	$0.941^{+0.016}_{-0.015}$	6.40	99^{+123}_{-18}	862.8/452	21.91, 81.48	pcfabs	C
Mrk 279	< 0.013	$2.04^{+0.02}_{-0.02}$	–	6.4	223^{+28}_{-66}	644.9/447	22.01, 25.98	pow	S
NGC 5506	$2.78^{+0.05}_{-0.05}$	$1.76^{+0.03}_{-0.02}$	$0.9893^{+0.001}_{-0.001}$	6.40	137^{+14}_{-24}	426.4/413	2.81, 67.59	pcfabs	C
NGC 5548	$0.07^{+0.04}_{-0.05}$	$1.88^{+0.01}_{-0.01}$	$0.031^{+0.016}_{-0.003}$	6.41	73^{+14}_{-44}	502.3/423	40.34, 59.60	pow + bb	S
ESO 511-G030	$0.098^{+0.021}_{-0.021}$	$1.82^{+0.04}_{-0.04}$	–	6.41	125^{+29}_{-88}	384.5/388	6.26, 13.04	pow	S
RBS 1399	$0.102^{+0.007}_{-0.007}$	$1.95^{+0.01}_{-0.01}$	–	–	–	499.0/417	19.49, 33.79	pow	S
NGC 5728	$82.0^{+5.3}_{-5.0}$	$0.94^{+0.08}_{-0.07}$	0.011	$6.32^{+0.04}_{-0.04}$	890	16/16	0.30, 1.44	pcfabs	C
Mrk 841	–	$1.81^{+0.07}_{-0.09}$	$0.20^{+0.01}_{-0.01}$	6.25^{+15}_{-14}	90^{+210}_{-35}	548/244	16, 10	pow + bb	S
Mrk 290	$0.15^{+0.03}_{-0.05}$	$1.61^{+0.04}_{-0.04}$	$0.05^{+0.01}_{-0.01}$	6.4	176^{+79}_{-76}	523.3/440	4.84, 9.31	pow + bb	S
Mrk 501	$0.18^{+0.01}_{-0.01}$	$2.01^{+0.01}_{-0.01}$	–	–	–	523.8/416	74.96, 126.03	pow	S
NGC 6300	$21.5^{+0.8}_{-0.9}$	$1.83^{+0.08}_{-0.08}$	0.03	$6.43^{+0.01}_{-0.02}$	148^{+18}_{-18}	423.5/420	0.037, 8.6	**	C
3C 382	–	$1.12^{+0.10}_{-0.29}$	$1.94^{+0.24}_{-0.06}$	$6.30^{+0.21}_{-0.32}$	489^{+209}_{-210}	1011/982	18.00, 31.00	pow + brems	S
ESO 103-035	$21.6^{+2.6}_{-2.5}$	$2.08^{+0.29}_{-0.28}$	0.076	$6.363^{+0.270}_{-0.144}$	200^{+230}_{-110}	534/527	0.10,[4]24.10	double pow	C

Continued on Next Page…

Table E.3 – Continued

Source	$n_{H(abs)}$	Γ	par$_{model}$[3]	Fe K E	Fe K EW	χ^2/dof	F$_X$[2]	model	type
3C 390.3	$0.12^{+0.03}_{-0.03}$	$1.50^{+0.03}_{-0.03}$	–	$6.52^{+0.10}_{-0.10}$	108^{+60}_{-57}	807.8/792	7.48,19.4	pow	S
NGC 6814	–	$1.74^{+0.07}_{-0.06}$	–	6.4	545^{+217}_{-216}	221.8/250	0.53, 1.25	pow	S
3C 403	$45.0^{+7.0}_{-6.0}$	$1.76^{+0.2}_{-0.2}$	0.0044	$6.32^{+0.2}_{-0.2}$	244^{+20}_{-20}	31.1/50	0.05, 0.75[5]	double pow	C
Cyg A	$11.0^{+21.0}_{-6.0}$	$1.80^{+0.28}_{-0.43}$	–	–	–	969.3/932	16.0, 24.0	pow + R-S	C
4C +74.26	$0.177^{+0.035}_{-0.016}$	$1.86^{+0.03}_{-0.03}$	$1.00_{-0.091}$	6.4	110^{+42}_{-41}	413/405	6.67, 19.61	pcfabs	C
Mrk 509	$0.015^{+0.008}_{-0.008}$	$1.87^{+0.01}_{-0.01}$	–	6.4	86.1^{+50}_{-15}	573/445	28.32, 45.83	pow	S
IC 5063	$21.78^{+2.24}_{-2.06}$	$1.63^{+0.22}_{-0.22}$	63.1	6.4	108^{+56}_{-54}	526/461	0.26,13.1	double pow	C
PKS 2149-306	$0.07^{+0.02}_{-0.02}$	$1.57^{+0.05}_{-0.05}$	–	–	–	364.6/344	3.39,10.6	pow	S
NGC 7172	$8.19^{+3.42}_{-3.30}$	$1.69^{+0.08}_{-0.09}$	–	6.4	68^{+36}_{-35}	690/729	0.128,37.0	pow	S
NGC 7213	$0.025^{+0.011}_{-0.012}$	$1.75^{+0.02}_{-0.02}$	–	6.4	133^{+49}_{-24}	519.9/445	16.65, 31.18	pow	S
NGC 7314	$1.16^{+0.01}_{-0.14}$	$2.41^{+0.05}_{-0.02}$	18.5	6.4	182^{+46}_{-47}	1702/1561	7.35,35.6	double pow	C
3C 452	$22.98^{+2.78}_{-2.83}$	$-0.08^{+0.08}_{-0.25}$	$0.936^{+0.012}_{-0.034}$	6.4	100	135.5/110	0.01, 2.17	pcfabs	C
MR 2251-178	$0.28^{+0.11}_{-0.08}$	$1.41^{+0.04}_{-0.05}$	$0.09^{+0.03}_{-0.06}$	6.4	67	406.8/437	6.39, 27.24	pow + bb	S
NGC 7469	–	$1.98^{+0.01}_{-0.01}$	–	6.4	131^{+38}_{-39}	562.9/444	24.10, 32.55	pow	S
Mrk 926	$0.035^{+0.01}_{-0.01}$	$1.79^{+0.02}_{-0.02}$	–	6.4	57^{+28}_{-28}	574.3/416	15.70, 33.13	pow	S
NGC 7582	$7.39^{+1.46}_{-1.00}$	$1.38^{+0.23}_{-0.20}$	23.5	6.4	106^{+66}_{-64}	497/392	0.45,13.2	double pow	C

[1]Milky Way Galactic absorption obtained from the n_H FTOOL on HEASARC in units of 10^{22} cm^{-2}.

[2]Observed flux in the 0.5–2 keV and 2–10 keV bands in units of 10^{-12} erg s^{-1} cm^{-2}. Where only one number is shown, the value is the 0.3–10 keV flux. The statistical errors on fluxes are very small and the systematic errors are dominated by model uncertainties.

[3]This parameter accounts from extra components referred to in the model column. If the model includes: `bbody` then this is the temperature in

keV (kT), `double pow` then this is the ratio of normalizations between the first and second power law components, and `pcfabs` then this is the covering fraction.

[4]Estimate of 0.5-2 keV flux from Tartarus, only 2-10 keV flux was given in original paper.

E.2 Notes on Individual Sources

Here, we present notes on individual sources. These notes include complexities associated with the sources. Particularly, in notes to Table E.1, we include details on why sources needed to be excluded or why XRT observations were used instead of data available from other missions. Also, we include details on extra components added in order to model the X-ray spectra, corresponding to the XRT analysis (Notes to Table E.2) or the ASCA/*XMM-Newton*/Chandra/Suzaku analyses (Notes to Table E.3). Throughout, the sources are ordered in RA.

Notes to Table E.1

NGC 1275: This source is located within the Perseus cluster. As such, emission from the cluster is difficult to separate from the AGN emission. Therefore, we do not include an analysis of this source.

PKS 0326-288: The XRT observation of this source is too short to extract an X-ray spectrum.

NGC 1365: This source is a "changing-look" AGN, observed in both Compton-thin and Compton-thick states. The source has been observed extensively by XMM-Newton and Chandra with relevant papers – for instance Risaliti (2007) and Risaliti et al. (2005). For simplicity, we averaged the XRT observations, taken within a day of each other. However, the spectral parameters of this source, particularly column density, are quite variable.

4U 0517+17: The *XMM-Newton* observation of this source is not yet publicly available.

Mrk 6: This source is known to have a complex absorber, with ASCA and XMM-Newton spectra well modeled by a double partial covering model (Feldmeier et al. 1999; Immler et al. 2003). Due to its complex nature, we only include our XRT analysis with a simple model, for easy comparison with the other sources.

IGR J12026-5349: The Chandra observation of this source is not yet publicly available.

NGC 4102: The Chandra observation is too short to compare with the spectra of other sources in this survey.

Cen A: Cen A recently underwent a galaxy merger. The X-ray spectrum is extremely complicated, as presented in (Evans et al. 2004). Due to the complex form, we do not include an analysis of this source.

NGC 6240: This peculiar source hosts two active nuclei, as found by Chandra (Komossa et al. 2003). Therefore, we do not include an analysis of this source.

GRS 1734-292: This source is a Sy 1 seen through the Galactic plane in a heavily obscured region. Therefore, the exact hydrogen column is not known. An analysis of the spectrum of this source is not included.

Notes to Table E.2

NGC 1365: The spectral fit to this source also includes the addition of an `apec` model with kT of $0.74^{+0.07}_{-0.10}$ keV and an Fe K line at $6.54^{+0.08}_{-0.09}$ keV with EW ≥ 780 eV. The fitted column density has large errors.

2MASX J04440903+2813003: The residuals to this fit show clear evidence of an Fe K-α line ($\Delta\chi^2 = 20.9$). Adding a gaussian for this component, with σ fixed at 0.01 keV, we find E $= 6.41^{+0.05}_{-0.03}$ keV and EW=

$140^{+70}_{-54.6}$ eV.

1RXS J045205.0+493248: The model includes a significant ($\Delta\chi^2 = 23$) soft excess modeled with a blackbody (kT= $0.10^{+0.05}_{-0.03}$). The residuals indicate the presence of possible additional lines (including Fe K-α) in the spectrum, but a higher quality spectrum is necessary to fully resolve these features.

Mrk 6: The residuals to this fit show clear evidence of an Fe K-α line ($\Delta\chi^2 = 10.7$). Adding a gaussian for this component, we find E = $6.41^{+0.07}_{-0.06}$ keV, $\sigma = 0.09^{+0.10}_{-0.05}$ keV, and EW= 498^{+264}_{-250} eV.

SDSS J074625.87+254902.2: Sambruna et al. (2006) provide an analysis of the BAT + XRT spectra, however, we re-analyze an observation for comparison of the parameters from a fit without the BAT spectrum.

IRAS 09149-6206: An unabsorbed blackbody component was required ($\Delta\chi^2 = 100$) at soft energies, probably a foreground Galactic object given the AGN's position in the Galactic plane, with kT $= 0.13 \pm 0.02$ keV.

LEDA 093974: The residuals to this fit show evidence of an Fe K-α line ($\Delta\chi^2 = 5.4$). Adding a gaussian for this component, with σ fixed at 0.01 keV, we find E $= 6.46^{+0.09}_{-0.14}$ keV and EW= 297^{+326}_{-187} eV.

1RXS J112716.6+190914: A blackbody component was also added ($\Delta\chi^2 \approx 20$) with kT= 52^{+13}_{-12} eV. There are some residuals in the fit but a higher quality spectrum is necessary to investigate these features.

1RXS J174538.1+290823: We model a significant soft excess ($\Delta\chi^2 = 20$) is added with kT= $36.1^{+8.2}_{-9.6}$ eV.

NGC 7319: We also include an Fe K line in this fit with E fixed at 6.4 keV with $\sigma = 0.01$ keV. The resultant EW $= 319^{+313}_{-296}$ eV.

Notes to Table E.3

RBS 476: We found that the ASCA observation of RBS 476 had the wrong position in the ASCA catalog and that a large part of the emission was outside the observation's field of view. Using archived *XMM-Newton* data, we found that a broken power law is the best fit to the data, with the indicated fluxes recorded in the table.

EXO 055620-3820.2: We note that the authors (see Table 1 for the reference) suggest that an ionized partial covering absorber is a better physical explanation than neutral absorption.

ESO 005-G004: In addition to the partial covering model, a thermal model is also required (`apec`) at soft energies with kT $= 0.57^{+0.09}_{-0.12}$ keV.

Mrk 110: The spectrum is noted to be more complex in the XMM-Newton spectra analyzed by Boller et al. (2007). However, for our purposes a simple power law is a good fit.

NGC 3516: NGC 3516 has a very complex spectrum. A very significant ($\Delta\chi^2 \approx 600$) blackbody component was also added with kT$= 52.2^{+1.4}_{-2.0}$ eV and a normalization of 0.086. This source is extensively studied, particularly because of the complex absorption present.

NGC 3728: NGC 3783 has a complex spectrum, which has been observed with a 900 ks Chandra observation. A very significant ($\Delta\chi^2 = 214$) blackbody component was also added with kT$= 63.4^{+0.6}_{-0.7}$ eV and a normalization of 0.008.

NGC 4138: Alternatively, this source can be fit with a partial covering model with a high amount of scattering ($> 99\%$). Further, the blackbody component can alternatively be fit with an `apec` model of similar

temperature with no difference in χ^2.

MCG -03-34-064: The spectrum also has a significant ($\Delta\chi^2 = 34$) soft component, which we fit with an `apec` model with kT$= 0.82^{+0.11}_{-0.09}$ keV. A more complete analysis of this source is presented in Miniutti et al. (2007), where they model the spectra as reflection-dominated with thermal plasmas, a broad Fe K line, and additional Fe emission lines.

IC 4329A: This source has complex absorption, studied most recently in the *XMM-Newton* spectrum analyzed in Steenbrugge et al. (2005). They find signatures from 7 different absorbing systems.

NGC 5506: A full description of the X-ray history and properties of NGC 5506 is found in Bianchi et al. (2003) where BeppoSax observations are also presented (a strong reflection component is evident).

NGC 5728: Also included is a thermal model (`mekal`) with kT $= 0.15 \pm 0.01$ keV. A reflection model is also used, which is a worse fit to the data. We performed an independent analysis of the spectrum confirming these results.

Mrk 841: This source has complex iron features. The authors (see Table 1 for reference) get an acceptable fit when a relativistic disk line is included along with the narrow gaussian fit to Fe-Kα. The blackbody component is also an unacceptable approximation for the soft excess.

NGC 6300: In the analysis, the authors (see Table 1 for reference) model the soft and hard spectrum separately. The additional parameter is the ratio of the hard to soft power law flux.

Cyg A: For Cyg A, the authors include a Raymond-Smith model to describe the soft emission in the spectrum with $kT = 0.88^{+0.07}_{-0.11}$ keV, $Y = 0.53^{+4.57}_{-0.19}$.

3C 452: 3C 452 has an extremely flat spectrum which is much better fit with the addition of a reflection model (Evans et al. 2006). The values quoted are from our own analysis of the data with a simplistic model.

Bibliography

Anders, E., & Ebihara, M. 1982, Geochim. Cosmochim. Acta, 46, 2363

Anderson, S. F., Voges, W., Margon, B., Trümper, J., Agüeros, M. A., Boller, T., Collinge, M. J., Homer, L., Stinson, G., Strauss, M. A., Annis, J., Gómez, P., Hall, P. B., Nichol, R. C., Richards, G. T., Schneider, D. P., Vanden Berk, D. E., Fan, X., Ivezić, Ž., Munn, J. A., Newberg, H. J., Richmond, M. W., Weinberg, D. H., Yanny, B., Bahcall, N. A., Brinkmann, J., Fukugita, M., & York, D. G. 2003, AJ, 126, 2209

Antonucci, R. R. J., & Miller, J. S. 1985, ApJ, 297, 621

Arnaud, K. 1996, Astronomical Data Analysis Software and Systems V, 101, 5

Avni, Y. 1976, ApJ, 210, 642

Awaki, H., Ueno, S., Taniguchi, Y., & Weaver, K. A. 2000, ApJ, 542, 175

Barger, A. J., Cowie, L. L., Mushotzky, R. F., Yang, Y., Wang, W.-H., Steffen, A. T., & Capak, P. 2005, AJ, 129, 578

Barr, P., & Mushotzky, R. F. 1986, Nature, 320, 421

Bauer, F. E., Brandt, W. N., & Lehmer, B. 2003a, AJ, 126, 2797

Bauer, F. E., Vignali, C., Alexander, D. M., Brandt, W. N., Garmire, G. P., Hornschemeier, A. E., Broos, P., Townsley, L., & Schneider, D. P. 2003b, Astronomische Nachrichten, 324, 175

Baumgartner, W., Tueller, J., Mushotzky, R., Barthelmy, S., Cannizzo, J., Gehrels, N., Markwardt, C., Skinner, G., & Winter, L. 2008, The Astronomer's Telegram,

1429, 1

Baumgartner, W. H., & Mushotzky, R. F. 2006, ApJ, 639, 929

Begelman, M. C. 2002, ApJ, 568, L97

Belloni, T., Mendez, M., King, A. R., van der Klis, M., & van Paradijs, J. 1997, ApJ, 488, L109+

Bennert, N., Jungwiert, B., Komossa, S., Haas, M., & Chini, R. 2006, A&A, 459, 55

Bevington, P. R. 1969, Data reduction and error analysis for the physical sciences (New York: McGraw-Hill, 1969)

Bianchi, S., Balestra, I., Matt, G., Guainazzi, M., & Perola, G. C. 2003, A&A, 402, 141

Bianchi, S., Guainazzi, M., Matt, G., & Fonseca Bonilla, N. 2007, A&A, 467, L19

Boldt, E. 1987, Phys. Rep., 146, 215

Boller, T., Balestra, I., & Kollatschny, W. 2007, A&A, 465, 87

Brandt, W. N., & Hasinger, G. 2005, ARA&A, 43, 827

Braun, R. 1995, A&AS, 114, 409

Brenneman, L. W., Reynolds, C. S., Wilms, J., & Kaiser, M. E. 2007, ApJ, 666, 817

Burbidge, G., Burbidge, E. M., & Arp, H. 2003, A&A, 400, L17

Calzetti, D., Kinney, A. L., & Storchi-Bergmann, T. 1994, ApJ, 429, 582

Cappi, M., Matsuoka, M., Comastri, A., Brinkmann, W., Elvis, M., Palumbo, G. G. C., & Vignali, C. 1997, ApJ, 478, 492

Cappi, M., Panessa, F., Bassani, L., Dadina, M., Dicocco, G., Comastri, A., della Ceca, R., Filippenko, A. V., Gianotti, F., Ho, L. C., Malaguti, G., Mulchaey, J. S., Palumbo, G. G. C., Piconcelli, E., Sargent, W. L. W., Stephen, J., Trifoglio, M., & Weaver, K. A. 2006, A&A, 446, 459

Chaty, S. 2008, ArXiv e-prints, 805

Chen, W., Shrader, C. R., & Livio, M. 1997, ApJ, 491, 312

Colbert, E. J. M., & Ptak, A. F. 2002, ApJS, 143, 25

Comastri, A. 2004, in Astrophysics and Space Science Library, Vol. 308, Supermassive Black Holes in the Distant Universe, ed. A. J. Barger, 245–+

Crenshaw, D. M., Kraemer, S. B., & George, I. M. 2003, ARA&A, 41, 117

Cropper, M., Soria, R., Mushotzky, R. F., Wu, K., Markwardt, C. B., & Pakull, M. 2004, MNRAS, 349, 39

Czerny, B., Nikołajuk, M., Różańska, A., Dumont, A.-M., Loska, Z., & Zycki, P. T. 2003, A&A, 412, 317

Dai, X., Chartas, G., Eracleous, M., & Garmire, G. P. 2004, ApJ, 605, 45

Das, V., Crenshaw, D. M., Kraemer, S. B., & Deo, R. P. 2006, AJ, 132, 620

Di Matteo, T., Springel, V., & Hernquist, L. 2005, Nature, 433, 604

Dickey, J. M., & Lockman, F. J. 1990, ARA&A, 28, 215

Done, C., & Gierliński, M. 2003, MNRAS, 342, 1041

Ebisawa, K., Mitsuda, K., & Hanawa, T. 1991, ApJ, 367, 213

Ebisawa, K., Życki, P., Kubota, A., Mizuno, T., & Watarai, K.-y. 2003, ApJ, 597, 780

Eracleous, M., & Halpern, J. P. 1998, ApJ, 505, 577

Eracleous, M., Shields, J. C., Chartas, G., & Moran, E. C. 2002, ApJ, 565, 108

Evans, D. A., Kraft, R. P., Worrall, D. M., Hardcastle, M. J., Jones, C., Forman, W. R., & Murray, S. S. 2004, ApJ, 612, 786

Evans, D. A., Worrall, D. M., Hardcastle, M. J., Kraft, R. P., & Birkinshaw, M. 2006, ApJ, 642, 96

Fabian, A. C., Barcons, X., Almaini, O., & Iwasawa, K. 1998, MNRAS, 297, L11+

Fabian, A. C., & Iwasawa, K. 1999, MNRAS, 303, L34

Feldmeier, J. J., Brandt, W. N., Elvis, M., Fabian, A. C., Iwasawa, K., & Mathur, S. 1999, ApJ, 510, 167

Fields, D. L., Mathur, S., Krongold, Y., Williams, R., & Nicastro, F. 2007, ApJ, 666,

828

Forster, K., Leighly, K. M., & Kay, L. E. 1999, ApJ, 523, 521

Freedman, W. L., Hughes, S. M., Madore, B. F., Mould, J. R., Lee, M. G., Stetson, P., Kennicutt, R. C., Turner, A., Ferrarese, L., Ford, H., Graham, J. A., Hill, R., Hoessel, J. G., Huchra, J., & Illingworth, G. D. 1994, ApJ, 427, 628

Freeman, K. C., Karlsson, B., Lynga, G., Burrell, J. F., van Woerden, H., Goss, W. M., & Mebold, U. 1977, A&A, 55, 445

Gallo, L. C., Brandt, W. N., Costantini, E., & Fabian, A. C. 2007, MNRAS, 377, 1375

Gallo, L. C., Fabian, A. C., Boller, T., & Pietsch, W. 2005, MNRAS, 363, 64

Gallo, L. C., Lehmann, I., Pietsch, W., Boller, T., Brinkmann, W., Friedrich, P., & Grupe, D. 2006, MNRAS, 365, 688

García, J., Mendoza, C., Bautista, M. A., Gorczyca, T. W., Kallman, T. R., & Palmeri, P. 2005, ApJS, 158, 68

Garnett, D. R. 2002, ApJ, 581, 1019

George, I. M., Turner, T. J., Netzer, H., Nandra, K., Mushotzky, R. F., & Yaqoob, T. 1998, ApJS, 114, 73

George, I. M., Turner, T. J., Yaqoob, T., Netzer, H., Laor, A., Mushotzky, R. F., Nandra, K., & Takahashi, T. 2000, ApJ, 531, 52

Gierliński, M., & Done, C. 2004, MNRAS, 349, L7

Gilli, R., Comastri, A., & Hasinger, G. 2007, A&A, 463, 79

Goad, M. R., Roberts, T. P., Reeves, J. N., & Uttley, P. 2006, MNRAS, 365, 191

Gonçalves, A. C., & Soria, R. 2006, MNRAS, 371, 673

Grandi, P., Haardt, F., Ghisellini, G., Grove, E. J., Maraschi, L., & Urry, C. M. 1998, ApJ, 498, 220

Grandi, P., Sambruna, R. M., Maraschi, L., Matt, G., Urry, C. M., & Mushotzky,

R. F. 1997, ApJ, 487, 636

Grimm, H.-J., Gilfanov, M., & Sunyaev, R. 2002, A&A, 391, 923

—. 2003, MNRAS, 339, 793

Grogin, N. A., Conselice, C. J., Chatzichristou, E., Alexander, D. M., Bauer, F. E., Hornschemeier, A. E., Jogee, S., Koekemoer, A. M., Laidler, V. G., Livio, M., Lucas, R. A., Paolillo, M., Ravindranath, S., Schreier, E. J., Simmons, B. D., & Urry, C. M. 2005, ApJ, 627, L97

Gültekin, K., Miller, M. C., & Hamilton, D. P. 2004, ApJ, 616, 221

Gutiérrez, C. M., & López-Corredoira, M. 2005, ApJ, 622, L89

Hanawa, T. 1989, ApJ, 341, 948

Heger, A., & Woosley, S. E. 2002, ApJ, 567, 532

Hewett, P. C., & Foltz, C. B. 1994, PASP, 106, 113

Ho, L. C., Filippenko, A. V., & Sargent, W. L. W. 1997, ApJS, 112, 315

Holt, S. S., Mushotzky, R. F., Boldt, E. A., Serlemitsos, P. J., Becker, R. H., Szymkowiak, A. E., & White, N. E. 1980, ApJ, 241, L13

Humphrey, P. J., Fabbiano, G., Elvis, M., Church, M. J., & Bałucińska-Church, M. 2003, MNRAS, 344, 134

Immler, S., Brandt, W. N., Vignali, C., Bauer, F. E., Crenshaw, D. M., Feldmeier, J. J., & Kraemer, S. B. 2003, AJ, 126, 153

Iwasawa, K., & Taniguchi, Y. 1993, ApJ, 413, L15

Jarrett, T. H., Chester, T., Cutri, R., Schneider, S. E., & Huchra, J. P. 2003, AJ, 125, 525

Jenkins, L. P., Roberts, T. P., Warwick, R. S., Kilgard, R. E., & Ward, M. J. 2004, MNRAS, 349, 404

Jiang, P., Wang, J. X., & Wang, T. G. 2006, ApJ, 644, 725

Jones, C. 1977, ApJ, 214, 856

Jonker, P. G., & Nelemans, G. 2004, MNRAS, 354, 355

Juett, A. M., Schulz, N. S., & Chakrabarty, D. 2004, ApJ, 612, 308

Kalogera, V., Henninger, M., Ivanova, N., & King, A. R. 2004, ApJ, 603, L41

Karachentsev, I. D., Sharina, M. E., Dolphin, A. E., Grebel, E. K., Geisler, D., Guhathakurta, P., Hodge, P. W., Karachentseva, V. E., Sarajedini, A., & Seitzer, P. 2002, A&A, 385, 21

Kauffmann, G., Heckman, T. M., Tremonti, C., Brinchmann, J., Charlot, S., White, S. D. M., Ridgway, S. E., Brinkmann, J., Fukugita, M., Hall, P. B., Ivezić, Ž., Richards, G. T., & Schneider, D. P. 2003, MNRAS, 346, 1055

Kelson, D. D., Illingworth, G. D., Freedman, W. F., Graham, J. A., Hill, R., Madore, B. F., Saha, A., Stetson, P. B., Kennicutt, Jr., R. C., Mould, J. R., Hughes, S. M., Ferrarese, L., Phelps, R., Turner, A., Cook, K. H., Ford, H., Hoessel, J. G., & Huchra, J. 1996, ApJ, 463, 26

King, A. R., Davies, M. B., Ward, M. J., Fabbiano, G., & Elvis, M. 2001, ApJ, 552, L109

Kirhakos, S. D., & Steiner, J. E. 1990, AJ, 99, 1435

Komossa, S., Burwitz, V., Hasinger, G., Predehl, P., Kaastra, J. S., & Ikebe, Y. 2003, ApJ, 582, L15

Kong, A. K. H. 2003, MNRAS, 346, 265

Kong, A. K. H., & Di Stefano, R. 2003, ApJ, 590, L13

Kong, X., Zhou, X., Chen, J., Cheng, F., Jiang, Z., Zhu, J., Zheng, Z., Mao, S., Shang, Z., Fan, X., Byun, Y.-I., Chen, R., Chen, W.-p., Deng, L., Hester, J. J., Li, Y., Lin, W., Su, H., Sun, W.-h., Tsay, W.-s., Windhorst, R. A., Wu, H., Xia, X., Xu, W., Xue, S., Yan, H., Zheng, Z., & Zou, Z. 2000, AJ, 119, 2745

Körding, E., Falcke, H., & Markoff, S. 2002, A&A, 382, L13

Kraft, R. P., Hardcastle, M. J., Worrall, D. M., & Murray, S. S. 2005, ApJ, 622, 149

Krolik, J. H., & Begelman, M. C. 1988, ApJ, 329, 702

Krongold, Y., Nicastro, F., Elvis, M., Brickhouse, N. S., Mathur, S., & Zezas, A. 2005, ApJ, 620, 165

Kubota, A., & Makishima, K. 2004, ApJ, 601, 428

Kubota, A., Makishima, K., & Ebisawa, K. 2001, ApJ, 560, L147

Kuntz, K. D., Gruendl, R. A., Chu, Y.-H., Chen, C.-H. R., Still, M., Mukai, K., & Mushotzky, R. F. 2005, ApJ, 620, L31

Kuntz, K. D., Harrus, I., McGlynn, T. A., Mushotzky, R. F., & Snowden, S. L. 2008, ArXiv e-prints, 805

Laor, A., Fiore, F., Elvis, M., Wilkes, B. J., & McDowell, J. C. 1997, ApJ, 477, 93

Lawrence, A. 1991, MNRAS, 252, 586

Lehmann, I., Becker, T., Fabrika, S., Roth, M., Miyaji, T., Afanasiev, V., Sholukhova, O., Sánchez, S. F., Greiner, J., Hasinger, G., Costantini, E., Surkov, A., & Burenkov, A. 2005, A&A, 431, 847

Lewis, K. T., Eracleous, M., & Sambruna, R. M. 2003, ApJ, 593, 115

Lipari, S., Tsvetanov, Z., & Macchetto, F. 1993, ApJ, 405, 186

Liu, J.-F., & Bregman, J. N. 2005, ApJS, 157, 59

Liu, J.-F., Bregman, J. N., & Seitzer, P. 2002, ApJ, 580, L31

—. 2004, ApJ, 602, 249

Long, K. S., Charles, P. A., & Dubus, G. 2002, ApJ, 569, 204

Longinotti, A. L., Bianchi, S., Santos-Lleo, M., Rodríguez-Pascual, P., Guainazzi, M., Cardaci, M., & Pollock, A. M. T. 2007, A&A, 470, 73

Madau, P., & Rees, M. J. 2001, ApJ, 551, L27

Magdziarz, P., & Zdziarski, A. A. 1995, MNRAS, 273, 837

Maiolino, R., Marconi, A., Salvati, M., Risaliti, G., Severgnini, P., Oliva, E., La Franca, F., & Vanzi, L. 2001, A&A, 365, 28

Makishima, K., Kubota, A., Mizuno, T., Ohnishi, T., Tashiro, M., Aruga, Y., Asai, K., Dotani, T., Mitsuda, K., Ueda, Y., Uno, S., Yamaoka, K., Ebisawa, K., Kohmura, Y., & Okada, K. 2000, ApJ, 535, 632

Malizia, A., Bassani, L., Stephen, J. B., Malaguti, G., & Palumbo, G. G. C. 1997, ApJS, 113, 311

Malizia, A., Landi, R., Bassani, L., Bird, A. J., Molina, M., De Rosa, A., Fiocchi, M., Gehrels, N., Kennea, J., & Perri, M. 2007, ApJ, 668, 81

Malkan, M. A., Gorjian, V., & Tam, R. 1998, ApJS, 117, 25

Maloney, P. R., & Reynolds, C. S. 2000, ApJ, 545, L23

Markwardt, C. B., Tueller, J., Skinner, G. K., Gehrels, N., Barthelmy, S. D., & Mushotzky, R. F. 2005, ApJ, 633, L77

Marshall, F. E., Boldt, E. A., Holt, S. S., Miller, R. B., Mushotzky, R. F., Rose, L. A., Rothschild, R. E., & Serlemitsos, P. J. 1980, ApJ, 235, 4

Martin, C. L., Kobulnicky, H. A., & Heckman, T. M. 2002, ApJ, 574, 663

Masetti, N., Morelli, L., Palazzi, E., Galaz, G., Bassani, L., Bazzano, A., Bird, A. J., Dean, A. J., Israel, G. L., Landi, R., Malizia, A., Minniti, D., Schiavone, F., Stephen, J. B., Ubertini, P., & Walter, R. 2006, A&A, 459, 21

Mateos, S., Barcons, X., Carrera, F. J., Ceballos, M. T., Hasinger, G., Lehmann, I., Fabian, A. C., & Streblyanska, A. 2005, A&A, 444, 79

Mateos, S., Barcons, X., Carrera, F. J., Page, M. J., Ceballos, M. T., Hasinger, G., & Fabian, A. C. 2007, A&A, 473, 105

Matsumoto, C., Nava, A., Maddox, L. A., Leighly, K. M., Grupe, D., Awaki, H., & Ueno, S. 2004, ApJ, 617, 930

Matt, G. 2002, Royal Society of London Philosophical Transactions Series A, 360, 2045

Matt, G., Brandt, W. N., & Fabian, A. C. 1996, MNRAS, 280, 823

Matt, G., Fabian, A. C., Guainazzi, M., Iwasawa, K., Bassani, L., & Malaguti, G. 2000, MNRAS, 318, 173

Matt, G., Guainazzi, M., & Maiolino, R. 2003, MNRAS, 342, 422

Mattson, B. J., Weaver, K. A., & Reynolds, C. S. 2007, ApJ, 664, 101

McCammon, D., Almy, R., Apodaca, E., Bergmann Tiest, W., Cui, W., Deiker, S., Galeazzi, M., Juda, M., Lesser, A., Mihara, T., Morgenthaler, J. P., Sanders, W. T., Zhang, J., Figueroa-Feliciano, E., Kelley, R. L., Moseley, S. H., Mushotzky, R. F., Porter, F. S., Stahle, C. K., & Szymkowiak, A. E. 2002, ApJ, 576, 188

McClintock, J. E., Narayan, R., & Rybicki, G. B. 2004, ApJ, 615, 402

Meléndez, M., Kraemer, S. B., Armentrout, B. K., Deo, R. P., Crenshaw, D. M., Schmitt, H. R., Mushotzky, R. F., Tueller, J., Markwardt, C. B., & Winter, L. 2008, ArXiv e-prints, 804

Merloni, A., Fabian, A. C., & Ross, R. R. 2000, MNRAS, 313, 193

Miller, B. W. 1995, ApJ, 446, L75+

Miller, J. M., Fabbiano, G., Miller, M. C., & Fabian, A. C. 2003, ApJ, 585, L37

Miller, J. M., Fabian, A. C., & Miller, M. C. 2004a, ApJ, 614, L117

—. 2004b, ApJ, 607, 931

Miller, M. C., & Hamilton, D. P. 2002, MNRAS, 330, 232

Miniutti, G., Ponti, G., Dadina, M., Cappi, M., & Malaguti, G. 2007, MNRAS, 375, 227

Mitsuda, K., Inoue, H., Koyama, K., Makishima, K., Matsuoka, M., Ogawara, Y., Suzuki, K., Tanaka, Y., Shibazaki, N., & Hirano, T. 1984, PASJ, 36, 741

Miyamoto, S., Kimura, K., Kitamoto, S., Dotani, T., & Ebisawa, K. 1991, ApJ, 383, 784

Moran, E. C., Filippenko, A. V., & Chornock, R. 2002, ApJ, 579, L71

Morrison, R., & McCammon, D. 1983, ApJ, 270, 119

Mukai, K., Hellier, C., Madejski, G., Patterson, J., & Skillman, D. R. 2003, ApJ, 597, 479

Mushotzky, R. 2004, in Astrophysics and Space Science Library, Vol. 308, Supermassive Black Holes in the Distant Universe, ed. A. J. Barger, 53–+

Mushotzky, R. F. 1982, ApJ, 256, 92

Mushotzky, R. F., Done, C., & Pounds, K. A. 1993, ARA&A, 31, 717

Nandra, K., Georgakakis, A., Willmer, C. N. A., Cooper, M. C., Croton, D. J., Davis, M., Faber, S. M., Koo, D. C., Laird, E. S., & Newman, J. A. 2007, ApJ, 660, L11

Nandra, K., George, I. M., Mushotzky, R. F., Turner, T. J., & Yaqoob, T. 1997, ApJ, 476, 70

Nandra, K., & Pounds, K. A. 1994, MNRAS, 268, 405

Nicastro, F. 2000, ApJ, 530, L65

Nicastro, F., Martocchia, A., & Matt, G. 2003, ApJ, 589, L13

Novak, G. S., Faber, S. M., & Dekel, A. 2006, ApJ, 637, 96

Oliva, E., Origlia, L., Kotilainen, J. K., & Moorwood, A. F. M. 1995, A&A, 301, 55

Page, K. L., O'Brien, P. T., Reeves, J. N., & Turner, M. J. L. 2004, MNRAS, 347, 316

Pakull, M. W., & Mirioni, L. 2003, in Revista Mexicana de Astronomia y Astrofisica, vol. 27, Vol. 15, Revista Mexicana de Astronomia y Astrofisica Conference Series, ed. J. Arthur & W. J. Henney, 197–199

Paolillo, M., Schreier, E. J., Giacconi, R., Koekemoer, A. M., & Grogin, N. A. 2004, ApJ, 611, 93

Paturel, G., Fouque, P., Bottinelli, L., & Gouguenheim, L. 1989, A&AS, 80, 299

Peterson, B. M., Ferrarese, L., Gilbert, K. M., Kaspi, S., Malkan, M. A., Maoz, D., Merritt, D., Netzer, H., Onken, C. A., Pogge, R. W., Vestergaard, M., & Wandel, A. 2004, ApJ, 613, 682

Peterson, K. C., Gallagher, S. C., Hornschemeier, A. E., Muno, M. P., & Bullard, E. C. 2006, AJ, 131, 133

Petrucci, P. O., Ponti, G., Matt, G., Longinotti, A. L., Malzac, J., Mouchet, M., Boisson, C., Maraschi, L., Nandra, K., & Ferrando, P. 2007, A&A, 470, 889

Piccinotti, G., Mushotzky, R. F., Boldt, E. A., Holt, S. S., Marshall, F. E., Serlemitsos, P. J., & Shafer, R. A. 1982, ApJ, 253, 485

Piconcelli, E., Cappi, M., Bassani, L., Fiore, F., Di Cocco, G., & Stephen, J. B. 2002, A&A, 394, 835

Piconcelli, E., Jimenez-Bailón, E., Guainazzi, M., Schartel, N., Rodríguez-Pascual, P. M., & Santos-Lleó, M. 2005, A&A, 432, 15

Pierce, C. M., Lotz, J. M., Laird, E. S., Lin, L., Nandra, K., Primack, J. R., Faber, S. M., Barmby, P., Park, S. Q., Willner, S. P., Gwyn, S., Koo, D. C., Coil, A. L., Cooper, M. C., Georgakakis, A., Koekemoer, A. M., Noeske, K. G., Weiner, B. J., & Willmer, C. N. A. 2007, ApJ, 660, L19

Pietsch, W., Haberl, F., & Vogler, A. 2003, A&A, 402, 457

Pietsch, W., Roberts, T. P., Sako, M., Freyberg, M. J., Read, A. M., Borozdin, K. N., Branduardi-Raymont, G., Cappi, M., Ehle, M., Ferrando, P., Kahn, S. M., Ponman, T. J., Ptak, A., Shirey, R. E., & Ward, M. 2001, A&A, 365, L174

Pilyugin, L. S., Vílchez, J. M., & Contini, T. 2004, A&A, 425, 849

Porquet, D., Kaastra, J. S., Page, K. L., O'Brien, P. T., Ward, M. J., & Dubau, J. 2004a, A&A, 413, 913

Porquet, D., Reeves, J. N., O'Brien, P., & Brinkmann, W. 2004b, A&A, 422, 85

Predehl, P., & Schmitt, J. H. M. M. 1995, A&A, 293, 889

Protassov, R., van Dyk, D. A., Connors, A., Kashyap, V. L., & Siemiginowska, A. 2002, ApJ, 571, 545

Ptak, A., & Colbert, E. 2004, ApJ, 606, 291

Rafanelli, P., Violato, M., & Baruffolo, A. 1995, AJ, 109, 1546

Ranalli, P., Comastri, A., & Setti, G. 2003, A&A, 399, 39

Reeves, J. N., & Turner, M. J. L. 2000, MNRAS, 316, 234

Reichert, G. A., Mushotzky, R. F., & Holt, S. S. 1986, ApJ, 303, 87

Reilman, R. F., & Manson, S. T. 1979, ApJS, 40, 815

Remillard, R. A., & McClintock, J. E. 2006, ARA&A, 44, 49

Revnivtsev, M., Molkov, S., & Sazonov, S. 2008, A&A, 483, 425

Reynolds, C. S. 1997, MNRAS, 286, 513

Reynolds, C. S., Fabian, A. C., & Inoue, H. 1995, MNRAS, 276, 1311

Reynolds, C. S., Iwasawa, K., Crawford, C. S., & Fabian, A. C. 1998, MNRAS, 299, 410

Reynolds, C. S., Loan, A. J., Fabian, A. C., Makishima, K., Brandt, W. N., & Mizuno, T. 1997, MNRAS, 286, 349

Rigby, J. R., Rieke, G. H., Donley, J. L., Alonso-Herrero, A., & Pérez-González, P. G. 2006, ApJ, 645, 115

Risaliti, G. 2007, in Astronomical Society of the Pacific Conference Series, Vol. 373, Astronomical Society of the Pacific Conference Series, ed. L. C. Ho & J.-W. Wang, 458–+

Risaliti, G., Elvis, M., Fabbiano, G., Baldi, A., & Zezas, A. 2005, ApJ, 623, L93

Risaliti, G., Elvis, M., & Nicastro, F. 2002, ApJ, 571, 234

Roberts, T. P., Warwick, R. S., Ward, M. J., & Goad, M. R. 2004, MNRAS, 349, 1193

Roberts, T. P., Warwick, R. S., Ward, M. J., Goad, M. R., & Jenkins, L. P. 2005, MNRAS, 357, 1363

Ross, R. R., & Fabian, A. C. 2005, MNRAS, 358, 211

Saez, C., Chartas, G., Brandt, W. N., Lehmer, B. D., Bauer, F. E., Dai, X., & Garmire, G. P. 2008, AJ, 135, 1505

Sakai, S., & Madore, B. F. 1999, ApJ, 526, 599

Sakai, S., Madore, B. F., & Freedman, W. L. 1996, ApJ, 461, 713

Sambruna, R. M., Eracleous, M., & Mushotzky, R. F. 1999, ApJ, 526, 60

Sambruna, R. M., Markwardt, C. B., Mushotzky, R. F., Tueller, J., Hartman, R., Brandt, W. N., Schneider, D. P., Falcone, A., Cucchiara, A., Aller, M. F., Aller, H. D., Torniainen, I., Tavecchio, F., Maraschi, L., Gliozzi, M., & Takahashi, T. 2006, ApJ, 646, 23

Sambruna, R. M., & Mushotzky, R. F. 1998, ApJ, 502, 630

Sazonov, S., Krivonos, R., Revnivtsev, M., Churazov, E., & Sunyaev, R. 2008, A&A, 482, 517

Sazonov, S., Revnivtsev, M., Krivonos, R., Churazov, E., & Sunyaev, R. 2007, A&A, 462, 57

Schlegel, E. M., Kong, A., Kaaret, P., DiStefano, R., & Murray, S. 2004, ApJ, 603, 644

Searle, L. 1971, ApJ, 168, 327

Shapley, A., Fabbiano, G., & Eskridge, P. B. 2001, ApJS, 137, 139

Shemmer, O., Brandt, W. N., Netzer, H., Maiolino, R., & Kaspi, S. 2006, ApJ, 646, L29

Shimura, T., & Takahara, F. 1995, ApJ, 445, 780

Siebert, J., Matsuoka, M., Brinkmann, W., Cappi, M., Mihara, T., & Takahashi, T. 1996, A&A, 307, 8

Smith, D. A., & Wilson, A. S. 2001, ApJ, 557, 180

Sobczak, G. J., McClintock, J. E., Remillard, R. A., Bailyn, C. D., & Orosz, J. A. 1999, ApJ, 520, 776

Steenbrugge, K. C., Kaastra, J. S., Sako, M., Branduardi-Raymont, G., Behar, E., Paerels, F. B. S., Blustin, A. J., & Kahn, S. M. 2005, A&A, 432, 453

Steffen, A. T., Barger, A. J., Cowie, L. L., Mushotzky, R. F., & Yang, Y. 2003, ApJ, 596, L23

Stobbart, A.-M., Roberts, T. P., & Wilms, J. 2006, MNRAS, 368, 397

Stocke, J. T., Liebert, J., Gioia, I. M., Maccacaro, T., Griffiths, R. E., Danziger, I. J., Kunth, D., & Lub, J. 1983, ApJ, 273, 458

Strohmayer, T. E., Mushotzky, R. F., Winter, L., Soria, R., Uttley, P., & Cropper, M. 2007, ApJ, 660, 580

Summers, L. K., Stevens, I. R., Strickland, D. K., & Heckman, T. M. 2003, MNRAS, 342, 690

—. 2004, MNRAS, 351, 1

Sunyaev, R. A., & Titarchuk, L. G. 1980, A&A, 86, 121

Swartz, D. A., Ghosh, K. K., Tennant, A. F., & Wu, K. 2004, ApJS, 154, 519

Swaters, R. A., van Albada, T. S., van der Hulst, J. M., & Sancisi, R. 2002, A&A, 390, 829

Takano, M., Mitsuda, K., Fukazawa, Y., & Nagase, F. 1994, ApJ, 436, L47

Tolstoy, E., Saha, A., Hoessel, J. G., & McQuade, K. 1995, AJ, 110, 1640

Tosi, M., Sabbi, E., Bellazzini, M., Aloisi, A., Greggio, L., Leitherer, C., & Montegriffo, P. 2001, AJ, 122, 1271

Tremonti, C. A., Heckman, T. M., Kauffmann, G., Brinchmann, J., Charlot, S., White, S. D. M., Seibert, M., Peng, E. W., Schlegel, D. J., Uomoto, A., Fukugita, M., & Brinkmann, J. 2004, ApJ, 613, 898

Tueller, J., Mushotzky, R. F., Barthelmy, S., Cannizzo, J. K., Gehrels, N., Markwardt, C. B., Skinner, G. K., & Winter, L. M. 2008, ApJ, 681, 113

Tully, R. B. 1988, Nearby galaxies catalog (Cambridge and New York, Cambridge University Press, 1988, 221 p.)

Turner, T. J., George, I. M., Grupe, D., Nandra, K., Remillard, R. A., Leighly, K. M.,

Marshall, H. L., Kraemer, S. B., & Crenshaw, D. M. 1999, ApJ, 510, 178

Turner, T. J., George, I. M., Nandra, K., & Mushotzky, R. F. 1997, ApJS, 113, 23

Turner, T. J., Netzer, H., & George, I. M. 1996, ApJ, 463, 134

Ueda, Y., Akiyama, M., Ohta, K., & Miyaji, T. 2003, ApJ, 598, 886

Ueda, Y., Eguchi, S., Terashima, Y., Mushotzky, R., Tueller, J., Markwardt, C., Gehrels, N., Hashimoto, Y., & Potter, S. 2007, ApJ, 664, L79

Veilleux, S. 2002, in Astronomical Society of the Pacific Conference Series, Vol. 284, IAU Colloq. 184: AGN Surveys, ed. R. F. Green, E. Y. Khachikian, & D. B. Sanders, 111–+

Veilleux, S., Kim, D.-C., Sanders, D. B., Mazzarella, J. M., & Soifer, B. T. 1995, ApJS, 98, 171

Vogler, A., & Pietsch, W. 1996, A&A, 311, 35

Vogler, A., Pietsch, W., & Bertoldi, F. 1997, A&A, 318, 768

Walsh, J. R., & Roy, J.-R. 1997, MNRAS, 288, 726

Wang, Q. D., Yao, Y., Fukui, W., Zhang, S. N., & Williams, R. 2004, ApJ, 609, 113

White, R. L., Becker, R. H., Gregg, M. D., Laurent-Muehleisen, S. A., Brotherton, M. S., Impey, C. D., Petry, C. E., Foltz, C. B., Chaffee, F. H., Richards, G. T., Oegerle, W. R., Helfand, D. J., McMahon, R. G., & Cabanela, J. E. 2000, ApJS, 126, 133

Wilms, J., Allen, A., & McCray, R. 2000, ApJ, 542, 914

Winter, L. M., Mushotzky, R., & Reynolds, C. S. 2004, in Bulletin of the American Astronomical Society, Vol. 36, Bulletin of the American Astronomical Society, 1472–+

Winter, L. M., Mushotzky, R., Tueller, J., Lewis, K., & Reynolds, C. 2007a, in American Astronomical Society Meeting Abstracts, Vol. 211, American Astronomical Society Meeting Abstracts, 64.02–+

Winter, L. M., Mushotzky, R. F., & Reynolds, C. S. 2006a, in ESA Special Publication, Vol. 604, The X-ray Universe 2005, ed. A. Wilson, 377–378

Winter, L. M., Mushotzky, R. F., & Reynolds, C. S. 2006b, ApJ, 649, 730

—. 2007b, ApJ, 655, 163

Winter, L. M., Mushotzky, R. F., Tueller, J., & Markwardt, C. 2008, ApJ, 674, 686

Winter, L. M., Mushotzky, R. F., Tueller, J., Reynolds, C. S., & Markwardt, C. 2007c, in American Astronomical Society Meeting Abstracts, Vol. 210, American Astronomical Society Meeting Abstracts, 02.25–+

Winter, L. M., R. F. Mushotzky Collaboration, & C. S. Reynolds Collaboration. 2005, in Bulletin of the American Astronomical Society, Vol. 37, Bulletin of the American Astronomical Society, 1318–+

Zdziarski, A. A., & Gierliński, M. 2004, Progress of Theoretical Physics Supplement, 155, 99

Zhang, J. S., Henkel, C., Kadler, M., Greenhill, L. J., Nagar, N., Wilson, A. S., & Braatz, J. A. 2006, A&A, 450, 933

Zimmermann, H.-U., & Aschenbach, B. 2003, A&A, 406, 969